UNIVERSITY OF WOLLONGONG AUSTRALIA

University of Wollongong - Research Online

Thesis Collection

Title: Analytical and numerical investigations into belt conveyor transfers

Author: Shams Tamjeed Huque

Year: 2004

Repository DOI:

Copyright Warning
You may print or download ONE copy of this document for the purpose of your own research or study. The University does not authorise you to copy, communicate or otherwise make available electronically to any other person any copyright material contained on this site.
You are reminded of the following: This work is copyright. Apart from any use permitted under the Copyright Act 1968, no part of this work may be reproduced by any process, nor may any other exclusive right be exercised, without the permission of the author. Copyright owners are entitled to take legal action against persons who infringe their copyright. A reproduction of material that is protected by copyright may be a copyright infringement. A court may impose penalties and award damages in relation to offences and infringements relating to copyright material.
Higher penalties may apply, and higher damages may be awarded, for offences and infringements involving the conversion of material into digital or electronic form.

Unless otherwise indicated, the views expressed in this thesis are those of the author and do not necessarily represent the views of the University of Wollongong.

Research Online is the open access repository for the University of Wollongong. For further information contact the UOW Library: research-pubs@uow.edu.au

University of Wollongong
Research Online

University of Wollongong Thesis Collection | University of Wollongong Thesis Collections

2004

Analytical and numerical investigations into belt conveyor transfers

Shams Tamjeed Huque
University of Wollongong

Recommended Citation

Huque, Shams Tamjeed, Analytical and numerical investigations into belt conveyor transfers, Doctor of Philosophy thesis, University of Wollongong, School of Mechanical, Materials & Mechatronic Engineering, University of Wollongong, 2004. http://ro.uow.edu.au/theses/1820

Research Online is the open access institutional repository for the University of Wollongong. For further information contact Manager Repository Services: morgan@uow.edu.au.

NOTE

This online version of the thesis may have different page formatting and pagination from the paper copy held in the University of Wollongong Library.

UNIVERSITY OF WOLLONGONG

COPYRIGHT WARNING

You may print or download ONE copy of this document for the purpose of your own research or study. The University does not authorise you to copy, communicate or otherwise make available electronically to any other person any copyright material contained on this site. You are reminded of the following:

Copyright owners are entitled to take legal action against persons who infringe their copyright. A reproduction of material that is protected by copyright may be a copyright infringement. A court may impose penalties and award damages in relation to offences and infringements relating to copyright material. Higher penalties may apply, and higher damages may be awarded, for offences and infringements involving the conversion of material into digital or electronic form.

ANALYTICAL AND NUMERICAL INVESTIGATIONS INTO BELT CONVEYOR TRANSFERS

by

Shams Tamjeed Huque
Bachelor of Engineering (Mechanical), Graduate Certificate in Business

A thesis submitted in fulfilment of the
requirements for the award of the degree

Doctor of Philosophy

from

University of Wollongong
Faculty of Engineering, School of Mechanical, Materials & Mechatronic Engineering

December 2004

Abstract

The mining industry is an immense field with granular flows (e.g. coal) occurring in numerous areas. Accordingly there are a significant number of problems that arise, with a great number requiring solutions that are difficult to achieve by conventional industrial means. The modelling of granular flow using the numerical technique known as Distinct Element Method (DEM) has great potential in industry, particularly for solving transfer point problems. The advantage of DEM for transfer applications is that an entire system can be simulated using the single numerical technique, as opposed to the existing situation where a myriad of design techniques are required (e.g. analytical solution for one component and graphical solution for another). DEM involves solving the equations of motion for the trajectory/rotation/orientation of each particle and modelling each collision between particles and between particles and boundary objects.

The research presented a comprehensive overview of all of the available analytical processes available to design chute system components, such as material trajectory calculations, impact plate models, and gravity flow chute aspects. To the author's knowledge, this was the first such review in the literature. A detailed comparison between the most common analytical design methods was conducted, recommendations for which method to use were established, and areas of weakness and further study were identified. It was found that: most areas apart from the prediction of the initial material discharge and trajectory were lacking in design method; often the few available design methods for chute components, such as impact plates and gravity flow chutes, were lengthy and often difficult to implement.

A computer code was developed during the course of the research to simulate bulk material using the Distinct Element Method (DEM). A background into DEM and its application to modelling material flow at transfer points was presented. One major drawback found in the recent transfer studies was the lack of quantification of the velocity distributions obtained using the DEM against existing analytical design theories. Contour coloured particulate simulations have also been recently produced by a number of companies (e.g. Overland Conveyor Company Inc.) however the flow

regimes observed from the relevant simulation screen captures were not adequately scrutinised. All the DEM mathematical formulation and numerical methods utilised for the current work were comprehensively described and relevant computational aspects were also detailed, such as the coding of a pre-processor and post-processor allowing animations of the DEM particles. A series of tests was conducted to gauge the validity of the computer code, and this produced satisfactory results.

The DEM code was also applied to simulate two separate transfers originally designed by The Gulf Group using their EasyFlow™ technology, and currently in operation in industry in Lithgow, Australia. By observing animation screen captures the current research confirmed the advantage of maintaining particle speed through the system when using curved chute elements. Quantitative DEM velocity data were compared to the velocities predicted by the most favourable analytical methods. It was found that DEM generally produced velocity regimes close to those of the analytical techniques. However it also provided the additional benefit of providing data on stream characteristics such as impact forces and velocities in the vicinity of the hood and spoon elements, which are difficult to examine in detail using analytical methods. An analysis of the micro dynamics of individual particles also identified that there are differing scales of contact during the flow through a chute. Although the analytical methods do not allow closer scrutiny of the flowing stream at the micro scale, they have the advantage of providing much faster solutions and are good for chute designs for free flowing material transfers.

Disclaimer

I, Shams T. Huque, declare that this thesis, submitted in fulfilment of the requirements for the award of Doctor of Philosophy, in the School of Mechanical, Materials & Mechatronic Engineering, Faculty of Engineering, University of Wollongong, is wholly my own work unless otherwise referenced or acknowledged, as defined by the University's policy on plagiarism, and that I may have received assistance from others on style, presentation and further formatting aspects. The document has not been submitted for qualifications at any other academic institution.

Shams T. Huque

16 December 2004

Acknowledgements

The author would like to specially thank his supervisor through the four years, Associate Professor Peter Wypych for his unflagging support and endorsement of the research. His expertise, advice and general supervisory role allowed the project to progress at moments of stagnation and indecision, and he always had time to discuss any issues raised, both professional and personal.

The author would like to thank Michael Walsh, Projects Manager of Engineering Services, ANSTO (Australian Nuclear Science and Technology Organisation), for his helpful discussions on general computational coding aspects and debugging, and his time spent with the author on the project. This was of significant assistance during the course of the project. Thanks to Allan Tapp of Stephen-Adamson Inc., Canada, for providing a complimentary copy of the most recent CEMA manual, and copies of a number of technical papers that were difficult to locate or obtain. Without his support in this regard the literature overview of recent DEM transfer station studies in Chapter Four would not have been as comprehensive.

Appreciation is given to the University of Wollongong for providing significant financial support by means of an Australian Postgraduate Award (APA), and also to Gulf Conveyor Holdings Pty. Ltd. who provided both a top-up scholarship and funds for project consumables. Thanks must be given to key contacts at Gulf, including Chief Executive Officer Colin Benjamin for initialising the project, and General Managers Andrew Burleigh (Operations), Dennis Pomfret (Engineering), Lena Plambeck (Technology and Systems), and Peter Jones (Engineering), and Quality Manager Paul Bryant for insightful discussions regarding industrial aspects of the project.

Thanks to Anton Fuchs of Graz University of Technology, Austria, for translating an important paper for the literature review from German to English and Tajeen Huque of University of Wollongong for typing the translated document. Thanks are also extended to the technical staff of the Key Centre for Bulk Solids and Particulate Technologies, for their thoughts in all particulate testing discussion and assistance in the initial

experimental developments. Thanks to the staff of the Engineering Enquiries Centre for always assisting with non-research related issues, and the Inter-Library Loans personnel for tracking down many articles and conference proceedings from overseas institutions.

Finally, the author would like to thank his parents Sobhana and Sheikh Huque, and his sister Tajeen Huque for giving their support throughout the candidature.

Contents

Appendices

Tables

Figures

Nomenclature

The author attempted to use symbols as close to common interpretations as possible in the thesis (for example, *g* is frequently used to represent gravitational acceleration and is therefore used similarly here). However due to this and the number of symbols required, some overlapping did occur. Therefore in the following nomenclature the symbol {♣} represents the interpretation as used in Chapters Two and Three, and {♠} represents the interpretation as used in Chapters Four and Five.

ARABIC LETTERS

a	{♣} Acceleration along the tangent {$= \ddot{s} = \dot{v}$} (ms^{-2}); {♠} Index allowing for differing loading and unloading paths {NFD model}
A	Total cross-sectional area of bulk solid in flowing stream (m^2)
A_0	Initial cross-sectional area of the flowing stream at the point of entry of the chute (m^2)
$A_{1,2}$	Cross-sectional areas {rectangular portion, circular segment} of bulk solid in flowing stream (m^2)
A_a	Cross-sectional area of material stream at exit to 'flow-round' zone (m^2)
A_b	Area of trapezoidal {3 idler system} or triangular {2 idler system} area (m^2)
A_{BC}	Non-dimensional cross-sectional area factor
ac	Y-axis intercept of the perpendicular to the chord between successive points on the arc
A_i	Cross-sectional area of free-falling stream (m^2)
am	Gradient of the perpendicular to the chord between successive points on the arc
A_p	Cross-sectional area of material stream at entrance to 'flow-round' zone (m^2)
A_s	Area of segment (m^2)
A_T	Total area of material on the belt in the troughed portion (m^2)

a_w	Proportionality factor for air drag
$A(\kappa)$	Function that describes cross-sectional area of flow stream on impact plate (m^2)
b	{♣} Width of belt (m); {♠} Fixed parameter, often set to 1/3 to agree with Mindlin's frictional sphere theory {TFD model}
B	Width of rectangular chute (m)
B_0	Width of entry for converging chute (m)
b_s	Mean width of material stream on the belt prior to discharge (m)
b_t	Thickness of belt (m)
bw_2	Width of material on flattened belt {troughed belts only} (m)
c	{♣} Cohesive stress (kNm^2); {♠} Y-intercept of straight line
C	Constant of integration
$C_{1,2\&3}$	Constants used during calculation of the load cross-sectional area
C_{grav}	Distance from belt surface to centre of mass (m)
C_l	Inverse velocity Coulomb drag coefficient
C_s	Intergranular stress constant (s^2m^{-2})
D	Horizontal distance from discharge point to impact point (m)
D_{base}	Base particle diameter (m)
d_{ij}	Sum of contacting sphere radii (m)
D_{max}	Maximum particle diameter (m)
D_{min}	Minimum particle diameter (m)
D_{mono}	Mono-sized particle (m)
dn	Displacement between particles (m)
D_{var}	Variance between particle sizes (m)
dx	Horizontal displacement difference between particles (m)
dy	Vertical displacement difference between particles (m)
E	Young's modulus (Nm^{-2})
E_{ij}	Equivalent elastic modulus (Nm^{-2})
E_T	Total energy of a particle (J)
$E_{1,2}$	Parameters in Equation (2.116)
f_0	Friction value of motion at the initial point of the chute
F_D	Drag force (N)
F_n	Normal force in Distinct Element Model (N)

F_N	Normal force in gravity flow chute theory (N)
F_n^{max}	Maximum force ever experienced by the contact (N)
F_t	Tangential force in Distinct Element Model (N)
F_t^*	Value of the tangential force F_t whenever the magnitude changes from increasing to decreasing, or vice versa (N)
F_v	Velocity dependent drag force (N)
f_φ	Friction value of motion at any angle φ around chute
F_μ	Coulomb frictional drag force (N)
F_mag_t	Magnitude of tangential force (N)
F_x_t	Horizontal component of tangential force (N)
$F\_x_{t,u}$	Horizontal component of unit vector (N)
F_y_t	Vertical component of tangential force (N)
$F\_y_{t,u}$	Vertical component of unit vector (N)
g	Acceleration due to gravity (ms^{-2})
G	Shear {or rigidity} modulus (Nm^{-2})
G_{ij}	Equivalent shear modulus (Nm^{-2})
h	Material drop height (m)
H	Flowing stream thickness (m)
H_0	Initial stream thickness (m)
$H_{1,2}$	Stream thickness {rectangular portion, circular segment} (m)
h_a	Thickness of material stream at exit of 'flow-round' zone (m)
h_b	Thickness of material on belt prior to discharge (m)
h_p	Thickness of material stream entering 'flow-round' zone (m)
h_φ	Stream thickness at any angle φ around curved chute (m)
I	Moment of inertia (kgm^2)
K	Constant of proportionality usually between 1.11 – 1.42
k_{EO}	Effective linear pressure gradient down the wall surface at zero velocity
k_i	Number of particles in contact with particle i
k_{max}	Largest inter-particle spring stiffness (Nm^{-1})
K_n	Some normal stiffness coefficient (Nm^{-1})
K_{n1}	Normal stiffness coefficients for the (loading stage) (Nm^{-1})
K_{n2}	Normal stiffness coefficients for the (unloading stage) (Nm^{-1})

K_t	Some tangential stiffness coefficient (Nm^{-1})
K_t^0	Initial tangential stiffness (Nm^{-1})
K_T	Effective incremental tangential stiffness (Nm^{-1})
k_v	Coefficient relating lateral pressure at the chute wall to the average normal pressure during flow
L	Distance between periodic boundaries (m)
L_{BC}	Contact perimeter of material burden on discharging belt (m)
m	Particle mass (kg) / gradient of straight line
$\dot{m}$	Mass flow rate of material (kgs^{-1})
m_{ij}	Effective mass of particles *i* and *j* acting in series (kg)
m_{min}	Mass of smallest particle in system (kg)
n	Parameter that is a function of the total number of particles in the system
N	Number of particle in system
N_{grid}	User defined term that specifies the maximum number of particles to be allowed in one cell
n_s	Number of time steps between searches
P_n	Pressure in normal direction (kPa)
Q_m	Flowrate (th^{-1})
r	Non-dimensional parameter representing ratio between outside and central idler contact
R	{♣} Pulley radius; radius of curvature of curved chute (m); {♠} Radius of sphere (m)
R_0	Radius of the conveying stream midpoint at the start of the chute (m)
r_1	Radius of interior sphere in Verlet neighbour list (m)
r_2	Radius of exterior sphere in Verlet neighbour list (m)
R_b	Distance from centre of discharge pulley to outer surface of belt (m)
R_c	Radius of curvature of discharge trajectory (m)
R_e	Distance from discharge pulley centre to material centre of mass (m)
R_{fz}	Radius of the ‘flow-round’ zone (m)
R_{ij}	Relative contact curvature (m)
R_m	Distance from centre of pulley to top of material upon belt (m)
R_{min}	Radius of smallest sized particle in the system (m)
R_p	Radius of curved impact plate (m)

s	Displacement along tangent (m)
S	{♣} Distance between end of 'flow-round zone' and bottom of the plate (m); {♠} An empirically determined model parameter
$S_{flowround}$	Portion of curved impact plate in contact with material stream (m)
S_p	Length of impact plate {flat or curved} (m)
s_v	Vertical fall distance (m)
t	Time (s)
U_{max}	Maximum particle velocity (ms^{-1})
v	Velocity {$= \dot{s}$} (ms^{-1})
v_0	{♣} Initial velocity of the flowing stream at the point of entry of the chute (ms^{-1}); {♠} Relative velocity of approach (ms^{-1})
$v_{0,S}$	Velocity of stream parallel to chute surface after impact (ms^{-1})
v_1^*	Velocity of stream before impact (ms^{-1})
v_2^*	Velocity of stream after the first deflection (ms^{-1})
v_3^*	Velocity of stream after second deflection (ms^{-1})
v_4^*	Velocity of stream after impact for a single deflection (ms^{-1})
v_a	Exit velocity of material leaving 'flow-round' zone (ms^{-1})
v_b	Conveyor belt velocity (ms^{-1})
v_c	Critical velocity (ms^{-1})
v_d	Discharge velocity (ms^{-1})
v_e	Exit velocity from bottom of flat impact plate (ms^{-1})
v_{f0}	Vertical component of bulk solid discharging velocity (ms^{-1})
v_i	Velocity of impact with the curved chute (ms^{-1})
v_1	Velocity of stream before impact (ms^{-1})
v_p	Material velocity at entrance to 'flow-round' zone (ms^{-1})
v_t	Tangential velocity; velocity of load stream centre (ms^{-1})
$v(\kappa)$	Velocity of stream at angle κ in 'flow-round' zone (ms^{-1})
$v(\psi)$	Discharge velocity at angle ψ (ms^{-1})
v_∞	Terminal velocity (ms^{-1})
x	General x-coordinate (m)
$\dot{x}$	Velocity in x-direction (ms^{-1})
$\ddot{x}$	Acceleration in x-direction (ms^{-2})

$x1$	First x-coordinate of line / arc (m)
$x_{1,2,3,4}$	Four x-coordinates representing a boundary (m)
$x2$	Second x-coordinate of line / arc (m)
$x3$	Third x-coordinate of line / arc (m)
$x4$	Fourth x-coordinate of line / arc (m)
Xc	X-coordinate of arc centre (m)
x_h	Height of material bed on belt (m)
X_{len}	Width of calculation space (m)
y	General y-coordinate (m)
$\dot{y}$	Velocity in y-direction (ms^{-1})
$\ddot{y}$	Acceleration in y-direction (ms^{-2})
$y1$	First y-coordinate of line / arc (m)
$y_{1,2,3,4}$	Four y-coordinates representing a boundary (m)
$y2$	Second y-coordinate of line / arc (m)
$y3$	Third y-coordinate of line / arc (m)
$y4$	Fourth y-coordinate of line / arc (m)
Yc	Y-coordinate of arc centre (m)
Y_{len}	Height of calculation space (m)
$y(x)$	Function that describes the trajectory of free fall (m)
$z_{1,2,3,4}$	Four z-coordinates representing a boundary (m)

GREEK LETTERS

α	Angle of convergence for chute side walls (°)
α_b	Conveyor belt inclination angle before discharge (°)
α_d	Bulk solid stream discharge angle measured from the vertical (°)
α_r	Angle at which material starts to slip on discharge pulley (°)
β	Impact plate inclination angle (°)
β_i	Angle of idler roll (°)
β_v	Viscous drag coefficient (s^{-1})
Δm	Elementary mass of bulk solid (kg)

δ_n	Normal overlap {relative displacement of the centres of the two spheres} (m)
$\dot{\delta}_n$	Rate of change of the distance between centres of the colliding particles (ms^{-1})
δ_{n0}	Residual displacement after complete unloading {the value where the unloading curve goes to zero} (m)
δ_r	Residual tangential displacement (m)
Δr_x	Horizontal component of change in relative position vector (m)
Δr_y	Vertical component of change in relative position vector (m)
δ_t	Tangential overlap between particles (m)
Δt	Time step (s)
Δt_c	Critical time step (s)
$\Delta\delta_t$	Incremental tangential displacement (m)
$\Delta\delta x_t$	Horizontal component of relative surface displacement vector (m)
$\Delta\delta y_t$	Vertical component of relative surface displacement vector (m)
ε	Coefficient of restitution
ϕ	{♣} Wall friction angle used in gravity flow chute work {$= tan^{-1}\mu$} (°); {♠} Angle from horizontal {line} / angle from horizontal of the perpendicular to the chord between successive points {arc} (°)
Φ	Poisson's ratio (ν) dependent parameter for Rayleigh Wave speed critical time step determination
Φ_{ij}	Angle of the particle with reference to the arc during contact (°)
ϕ_w	Kinematic angle of wall friction between material and conveyor belt (°)
γ	Specific weight of the material being conveyed {$= \rho g$} (kNm^{-3})
γ_1	Start angle of an arc (°)
γ_2	Finish angle of an arc (°)
γ_n	Damping constant
φ	Chute slope angle for Korzen's work {$= 90 - \theta$}(°)
φ_0	Angle of chute to horizontal at impact (°)
κ	Angle of impact to horizontal {for flat plates}; angle the tangent to the end of the plate makes with the horizontal {for curved plates} (°)

λ	Angle of surcharge of material (°)
λ_{bottom}	Angle tangent to end of curved plate makes with the vertical (°)
μ	{♣} Coefficient of internal friction used in flat impact plate model {= $tan\zeta$}; coefficient of wall friction used in gravity flow chute work {= tanϕ}; {♠} Coefficient of friction
μ_E	Equivalent coefficient of friction
μ_k	Kinematic friction coefficient between material and belt {= tanϕ_w}
μ_s	Static friction coefficient
ν	Poisson's ratio
θ	{♣} Chute slope angle for Roberts' work {= dy/dx} (°); {♠} General rotation (radians)
$\dot{\theta}$	Angular velocity (rads^{-1})
$\ddot{\theta}$	Angular acceleration (rads^{-2})
θ_1	Angle of incoming stream relative to chute surface (°)
θ_2	Angle after impact of material stream relative to chute surface (°)
θ_3	Angle of incoming stream relative to chute surface {for double deflection of material stream} (°)
θ_a	Angle from horizontal made by incoming material stream to impact plate (°)
θ_c	Corrected angle of entry of material on a curved impact plate (°)
θ_{co}	Optimum cutoff angle for curved chute (°)
θ_f	Limiting angle for maintenance of 'fast' flow (°)
θ_i	Instantaneous angle of impact (°)
θ_s	Angle opposite arc length $S_{flowround}$ (°)
ρ	{♣} Bulk density (kgm^{-3}); {♠} Particle density (kgm^{-3})
σ_1	Normal stress corresponding to conditions on the belt prior to discharge (kPa)
σ_a	Adhesive stress (kPa)
τ	Shear stress (kPa)
ω	Angular velocity
ξ	{♣} Percentage admissible relative deviation for the estimation of the k-th value of v_a {impact plate model}; tolerated relative deviation for the

	estimation of the k-th value of $v(\varphi)$ {gravity flow chute model}; {♠}
	Percentage overlap or overlap ratio of two contacting particles
ψ	Wrap angle around discharge pulley (°)
ζ	Effective angle of internal friction (°)

SUBSCRIPTS

i	Particle number i
j	Particle / boundary number j
$\|\|$	Denotes parallel component
$\perp$	Denotes perpendicular component
old	Denotes previous time step

SUPERSCRIPTS

N	Time t^N
N+1	Time t^{N+1}
N-1	Time t^{N-1}
N+1/2	Time $t^{N+1/2}$
N-1/2	Time $t^{N-1/2}$
line	Represents line
arc	Represents arc

VECTOR QUANTITIES

$\mathbf{F}_n$	Normal contact force
$\mathbf{F}_t$	Tangential contact force
g	Gravitational vector
i	Denotes x-direction
j	Denotes y-direction

$\mathbf{k}$	Denotes z-direction
$\hat{\mathbf{k}}_{ij}$	Unit vector in normal direction between particles
$\mathbf{r}$	Position vector for a particle
$\mathbf{r}_{ij}$	Relative position vector between two particles
$\mathbf{R}$	Radius vector
$\hat{\mathbf{t}}_{ij}$	Unit vector in the direction of the virgin loading
$\mathbf{T}_{ij}$	Torque
$\mathbf{v}$	Velocity vector for a particle
$\dot{\mathbf{x}}$	Velocity vector in x-direction
$\dot{\mathbf{y}}$	Velocity vector in y-direction
$\Delta\mathbf{r}_{ij}$	Change in the relative position vector during the last time step
$\Delta\boldsymbol{\delta}_{\tau}$	Relative surface displacement vector

Chapter One
INTRODUCTION

1.1 A Current Challenge in Materials Handling

The study of particulate flows is of great importance in the materials handling industry, particularly mining, with economic factors, environmental considerations and safety issues being of great relevance. Some experimental methods are available to study granular flows. These include high-speed camera measurements (Vemuri et al. 1998, Vu-Quoc et al. 2000), insertion of fibre optical probes (Vemuri et al. 1998, Vu-Quoc et al. 2000), magnetic resonance imaging (MRI) (Vemuri et al. 1998, Vu-Quoc et al. 2000), and capacitance and resistance tomography (Vemuri et al. 1998). Most of the conventional experimental methods can supply reliable information on the surface of granular flows, but obtaining the information inside the flow domain is much more difficult and expensive (Vu-Quoc et al. 2000). High-speed camera measurements can only supply limited information on material flows, such as the velocity distribution on the boundaries of the flow domain. Insertion of probes into the material flow modifies the local behaviour of the flow, or could be damaged in coarse particle conveying. The other experimental methods listed are not yet widely available, have a restricted measurement range, and are expensive (Vu-Quoc et al. 2000).

Major statutory limitations are also an impedance, with the policy in Australian mines of the total restriction of contraband underground. Modified equipment subject to approval may be allowed but even then still has the limitations detailed above. Building a full-sized test rig is expensive for many companies, with time and monetary resources taken away from the major priority of material production. Scale modelling has problems with regards to correctly modelling materials. Computer simulations are hence a useful tool for understanding flow behaviour of granular solids, especially at the micro scale and for underground applications. The Distinct Element Method (DEM) is one such numerical technique that is gaining in popularity.

1.2 An Introduction to Transfer Chutes

Transfer points are widely recognised as critical areas within a bulk solids handling facility (Benjamin 1999, 2001, Benjamin & Nemeth 2001, Benjamin et al. 1999a, 1999b). They can be found in a wide range of industries, including mining, mineral processing, chemical processing, thermal power plants and other industries that deal with bulk commodities. To facilitate the transfer, a *chute* system is used to direct bulk material from a discharge point to a receiving point, usually from a conveyor belt to another conveyor belt or into a process component. A transfer chute system can be composed of a combination of elements including a curved 'Hood', curved 'Spoon', a rock-box, an impact plate or a U-form chute. The primary aim of a chute system is to control the flow of material through the transfer process.

The failure of chutes to perform reliably can be costly, especially in mining operations where large quantities of bulk commodity are handled and the sequence of continuous production is considered of utmost importance. Poorly designed and maintained transfer stations can cause 'bottleneck' problems in terms of plant capacity. For example, there are considerable costs associated with a problematic transfer chute in a coal mining facility. These include the cost of a new transfer chute design (ranging from $15k to $50k) (Jones, P. 2004, pers. comm., 25 March), the fabrication of the transfer chute (ranging from $50k to $300k) (Jones, P. 2004, pers. comm., 25 March), the installation of the chute system (cost depends upon the number of personnel involved), the chute commissioning stage (again, the cost depends upon the number of personnel involved), and of course, lost production (approximately $600/minute = $36k/hour) (Kervroeden, J. 2000, pers. comm., 23 March). All costs are in Australian dollars. A single downtime for a complicated transfer arrangement can easily cost a mining company millions of dollars, and if the new transfer to be installed has not been sufficiently designed, within a short period of time the downtime will be repeated. Financial losses of such magnitude are unsustainable for most companies, so a well designed transfer is imperative.

In addition to economic factors, environmental considerations and safety issues are also of great relevance and concern and ultimately dependent upon the performance of a

transfer chute system. It is clear that a good transfer design from the outset can negate the costs associated when the chute and/or conveyor belt needs to be replaced or repaired on a regular basis due to bad design principles. If the velocity profile of the material stream flowing through the transfer at a number of critical locations can be correctly predicted at the design stage, the potential for a successful chute design is greatly increased (Burleigh, A. 2001, pers. comm., 15 January). A colliery will thus benefit from minimised downtime losses, higher product yields and improved product quality.

1.3 Background and Objectives

The work encompassed in the thesis is a new research direction for the Key Centre for Bulk Solids and Particulate Technologies, in the School of Mechanical, Materials and Mechatronics Engineering, Faculty of Engineering, University of Wollongong, with the current thesis to provide the foundation for future DEM studies. The two-dimensional computer code was developed from fundamentals as commercial software offered little upgradeability or potential to develop further, considering the purchasing cost. Also, non-commercially developed codes, such as those found at research institutions were not obtainable. Thus the research was started from basics. Gantt charts for the project are presented in Appendix I.

Initially it was envisaged that the project would be a combined experimental-numerical examination of the transfer point. During the early stages of the research a full sized transfer system was desired, with a number of local collieries contacted to seek permission for on-site testing. This was unsuccessful due to possible stoppages required for the testing and hence lost production so the feasibility of setting up a transfer system at the university was explored. Ultimately this idea was also abandoned due to financial constraints, however during this period, the owner/consultant from OreFlow^{TM} in Perth offered the services of their 1:10 scale model transfer system, complete with conveyors, and after experiencing personal difficulties, offered to sell this facility for a fraction of its value. During this development stage, significant background work was completed based upon the author's sponsoring company receiving the facility at a nominated time.

A range of drawings was developed for a scale model chute system, along with obtaining associated fabrication quotes. Since the scale model system required semi-permanent housing, storage facilities were also contacted. The experiments were to provide a means of validating the DEM code that was in process of development, and also allow observations of flow patterns, material stagnation points, and other material transfer related phenomena. The physical modelling of a transfer chute was to be based upon the earlier investigations of Low (2000) and Low & Verran (2000). Unfortunately the specifics of the transaction consumed a large amount of time, and when the time came for initial payments, the owner of the facility declined to sell, and ultimately resulted in a significant amount of time and resources being wasted. By the end of the whole process, little time was remaining to progress in an experimental direction, and the experimental component of the work was fully abandoned. The aims of this research have thus been changed and are as follows:

1. To comprehensively review and compare current transfer chute design procedures, which is lacking in literature;
2. To develop and qualitatively test DEM computer code to model particulate simulations;
3. Develop an interface to facilitate simple input of parameters (pre-processor) into the DEM and develop software to allow animations of the particulate interactions taking place (post-processor);
4. To quantitatively compare the velocity regimes obtained from DEM transfer chute simulations to those obtained from existing theories that have been experimentally validated;
5. Implement the DEM to model material flow through a transfer chute system and examine the resulting velocity profiles throughout the chute system.

1.4 Thesis Overview

The thesis is structured as follows. Chapter Two provides a review of current transfer chute design literature. Aspects of conveyor-to-conveyor transfer technology are identified. Prominent areas of belt conveyor transfers, especially the various models and

design methods available to calculate or predict the relevant parameters (e.g. material discharge velocities, material trajectories, dynamics of material impact, air entrainment) are presented. Chapter Two is limited to providing descriptions and an overview.

Chapter Three examines the major transfer chute components, all of which have a multitude of design techniques. Existing models that are inaccurate in predicting the relevant transfer point aspects and areas where the available literature is insufficient are identified. Chapter Three will also compare those methods and conclude by recommending the technique best suited for utilisation for each transfer chute component.

In Chapter Four a review is given on the background to Distinct Element Modelling and current applications in industry. The application of DEM to transfer chutes is particularly examined with the available literature reviewed. The governing equations and additional mathematical formulations used for the current work are described in detail, such as particle and boundary definitions and contact force models in the normal and tangential directions.

Chapter Five describes the numerical methods used for solving the Distinct Element Modelling equations, with a brief overview of the methods available in literature. The numerical time integration scheme employed for the work is described, and the contact detection algorithm for particle-particle and particle-boundary interactions is developed. The selection of critical time step is also detailed. Finally, the background to the supplement modules used in the work, namely the pre-processing (parameter input) and post-processing (graphics and animation) coding, are described.

Chapter Six details three sets of tests to qualitatively check the computer code and ensure the DEM and numerical procedures have been implemented correctly. The computational analyses used to test the DEM code include single contact tests between particle pairs and particles and walls, multiple particle tests to observe the influence of various parameters, and a stability test that examines the conservation of system energy.

Chapter Seven introduces two separate chute systems currently in operation in industry for analysis. All preliminary work pertaining to utilising the Distinct Element Method to

model the particulate flow through the chute systems will be described. Particular areas of concern regarding memory concerns and coding the relevant animation particulate flow aspects will be highlighted. A number of analytical methods will be used in Chapter Eight to model the velocity distribution as a means of comparison, and therefore the particular design techniques will also be specified here.

Chapter Eight qualitatively and quantitatively examines in detail the velocity distributions through the two chutes introduced in Chapter Seven and also micro dynamics of individual particles in the systems. The graphical processes developed will be used to animate the particulate flow. The material stream paths resulting from the analytical methods are compared to the paths of the DEM particle stream. Further areas of interest identified in the literature or from industrial experience/observations are explored.

Chapter Nine encapsulates the work in the thesis. The author's conclusions and recommendations for further work are summarised. Chapter Ten details all literature referred to in the current work. A bibliography is also detailed where all texts utilised for developing the relevant parts of the computer code are listed. Appendices are provided for supplementary items, such as project Gantt charts, drawings, and examples of DEM input files.

Chapter Two
TRANSFER CHUTE LITERATURE OVERVIEW

2.1 Introduction

This chapter will examine current transfer chute design literature. The elements in a transfer chute and the problems associated with badly designed chutes will be introduced and the models and design methods available to calculate or predict material flow aspects at each major component of a transfer point such as material discharge velocities, material trajectories, dynamics of material impact, air entrainment and free fall, and flow through chutes will also be reviewed. Note that the thesis will investigate only those works that have been frequently referred to in transfer chute literature to date, and those popular in industry. Obscure amalgamations of methods such as those observed by the author in many industrial facilities will not be examined.

2.2 Attributes of Conveyor-to-Conveyor Transfers

Figure 2.1 illustrates the major areas of analysis when examining the transfer of materials between belt conveyors. These are: discharge models (exit velocity vector); material trajectory; impact models (dynamics of flow stream impacting on the impact plate or 'Hood' section); sliding models (flow through 'Hood' section); free fall models; impact models (dynamics of flow stream impacting on the U-form curved chute or 'Spoon' section); and sliding models (flow through 'Spoon' section). One or a combination of these is usually used in directing and controlling the material flow at transfer points, usually via a single transfer chute, or a combination 'Hood-Spoon' arrangement. Ideally, the upper element turns the material stream downwards in a controlled manner to be captured and turned again by the lower element to load onto the receiving belt, preferably at the belt's conveying speed.

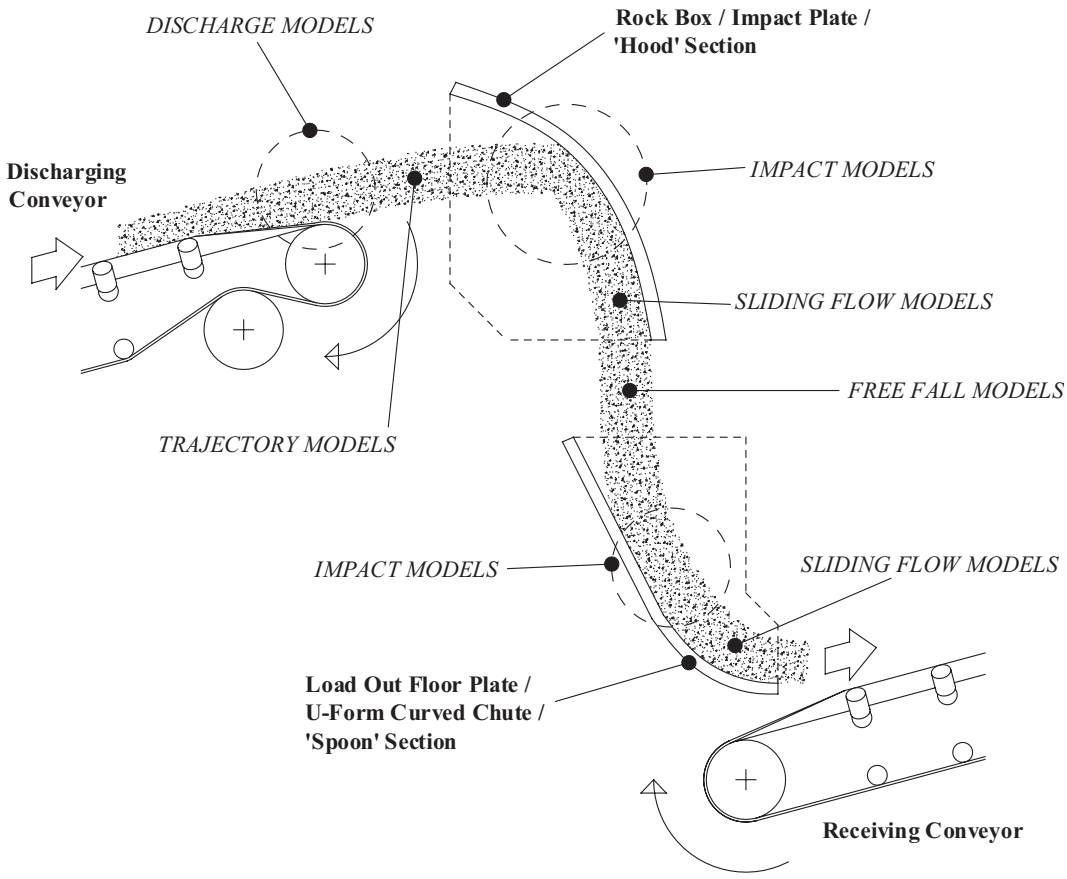

Figure 2.1 Schematic of conveyor-to-conveyor transfer

2.3 Problems Occurring At Transfer Points

Unfortunately, a transfer chute component is usually chosen based upon immediate cost effectiveness rather than for the long term. It must be noted here that with production and rapid material conveyance as the major priority for a mining facility, quick solutions are preferred. However, serious problems can occur if transfer stations are poorly designed and maintained. Identified transfer chute problems include, but are not limited to, the following (adapted from Sabina et al. 1984, 1992):

- Spillage and hence loss of material;
- Dust generation and control, hence more loss of material;
- Load centering;
- Material degradation;

- Impact and abrasive chute wear;
- Belt damage from large lumps;
- Belt wear, abuse and damage;
- Material buildup/blockage;
- Noise generation;
- Belt tracking due to non-central or non-ideal loading.

Those in industry have traditionally addressed these problems by means of trial and error. Successful problem solving has been dependent on past experience and a thorough understanding of bulk material behaviour. Due to the large number of variables (system physical restraints, material properties, conveyor belt attributes), there has now been an increasing use of computer and mathematical modelling to address problems related to transfer points. The aim must be to ensure the components within a transfer system compliment each other. For example, if either the trajectory or impact issues are not sufficiently designed, problems will occur when the material drops onto the lower section of the transfer. Also, a transfer chute design that considers the system variables such as discharge conveyor geometry and material characteristics is significantly closer to eliminating most of the problems listed above than one that does not.

2.4 Material Discharge and Trajectory Techniques

2.4.1 Introduction to Material Discharge

Material discharge is one of the most critical aspects in transfer chute design as it determines the exact point at which the material leaves the belt. A number of different methods exist in the literature for modelling material discharge, such as the works of Arnold & Hill (1989, 1990a, 1990b, 1991a, 1991b, 1993), Booth (1934), BFGoodrich (n.d.), BTR (n.d.), C.E.M.A. (1997), Colijn & Conners (1972), Dunlop (1982), Golka (1993a), Goodyear (1976), Korzen (1984b, 1989), M.H.E.A. (1986, 1989), S-A 66 (n.d.), Roberts (1997b, 2001) and Roberts et al. (1987).

As shown by Arnold (1993) and Arnold & Hill (1990a, 1991a, 1991b), derivations for material discharge can be divided into two areas: slow discharge, where the material wraps around the head pulley to some extent before discharging; and fast discharge, where the material will discharge at the point of tangency between the belt and head pulley. An important aspect of accurate trajectory prediction is the determination of the wrap angle (α_d) and discharge velocity. Korzen (1989) and Roberts (1997b, 2001) provide the most comprehensive method of determining whether a conveyor belt is running in the high or slow speed condition. In their work, a belt can be described as high-speed if it meets the condition shown in Eq. (2.1):

$$\frac{v_b^2}{R_e g} - \frac{\sigma_a}{\gamma h_b} \geq \cos\alpha_b \tag{2.1}$$

A belt can be described as slow-speed if the condition in Eq. (2.2) is met:

$$\frac{v_b^2}{R_e g} - \frac{\sigma_a}{\gamma h_b} < \cos\alpha_d \tag{2.2}$$

Other condition methods are available and shall be described in Sections 2.4.4 to 2.4.13 though these generally do not include the term containing the adhesive stress component.

Once the bulk solid stream has separated from the conveyor belt, it undergoes a period of free fall until it hits the impact plate. Prediction of the trajectory path for bulk materials has been presented in the papers of Arnold (1993), Arnold & Hill (1989, 1991a), Booth (1934), Golka (1992, 1993a), Korzen (1986, 1989), Page (1991), Roberts (2001), Roberts et al. (1987), Rozentals (1991), and Snow (1991), as well as in the published recommendations and manufacturer's conveyor belt manuals of Arnold & Hill (1991b), BFGoodrich (n.d.), BTR (n.d.), C.E.M.A. (1997), Dunlop (1982), Goodyear (1976), M.H.E.A. (1986) and S-A 66 (n.d.). The relatively large amount of literature available for this aspect of chute design stems from the fact that a close approximation of the material trajectory off the head pulley of the conveyor system is among the first steps towards designing a dependable transfer chute. Evidenced from

citations in literature and the primary author's industrial experience, the concepts of discharge and material trajectory prediction outlined in the papers of Booth (1934), Golka (1993a), and Korzen (1989), and published manuals BFGoodrich handbook (n.d.), BTR (n.d.), C.E.M.A. (1997), Dunlop (1982), Goodyear (1976), M.H.E.A. (1986, 1989), and S-A 66 catalogue (n.d.) are the most popular and shall be reviewed in greater detail here. Drag effects for trajectories can be considered, though Arnold & Hill (1991b) suggest that air drag effects should be investigated only if the material is to be thrown greater than 5 metres.

2.4.2 Material Height Calculations

The material height upon the belt prior to discharge is required as this is the starting point for the upper trajectory limit. Techniques of calculating material height were absent in some of the available work such as the trajectory prediction methods of Booth (1934), BF Goodrich (n.d.), BTR (n.d.), Dunlop (1982), Golka (1993a), Goodyear (1976) and S-A 66 (n.d.). In Korzen's (1989) work the height of the material upon the belt prior to discharge at high-speed conditions is given by:

$$h_b = \frac{\dot{m}}{\rho b_s v_b} \tag{2.3}$$

For slow speed conditions, the belt velocity v_b is replaced by the discharge velocity v_d in Eq. (2.3). It is ideal however to use the comprehensive theory detailed in Arnold & Hill (1991b) and Powell's (1995) work, which is based upon theory in the two M.H.E.A. (1986, 1989) and C.E.M.A. (1997) guides, to calculate material height upon the belt. Major aspects of this work are outlined below. An understanding of the geometry involved for calculating the material height and centroid of material is important and shall now be described.

The volumetric capacity of material on a conveyor belt is dependent upon the belt's velocity and the material load cross-sectional area. Certain techniques like that of Korzen (1989) base their area calculations upon the material's bulk density, which is not an accurate method by which to calculate the cross-sectional area due to material densities varying during conveying operations. A prime example is the mining industry,

where particulate matter can range between raw coal with lumps to finished product, possibly causing variations in the bulk density for a particular conveyor.

Powell (1995) recommends the belt load cross-sectional area be calculated from a material's surcharge angle and the geometry of the conveyor. The calculations for determining the cross-sectional area are based upon two assumptions. The first is a constant volumetric flow rate enabling the use of a constant edge distance. This is the distance from the edge of the belt to the edge of the material loaded on the belt. The second assumption is that the free surface of the material burden on the belt is to represent an arc of a circle whose ends are tangent to the material surcharge angle at the edge of the load.

The derivation of load cross-sectional area for troughed (3 idlers) and flat (single idler) conveyor belt configurations can be found in the C.E.M.A. (1997) manual. The derivation for troughed (2 idlers) was devised by Powell (1995). The derivation for troughed (5 idlers) is not detailed in literature, and has not been considered here. However the equations can be derived from conveyor geometry after an analysis is conducted upon five-equal-roll troughing idler systems to determine edge distances for high and slow-speeds, and also idler/belt length proportional ratios. Additionally, the calculations can be somewhat simplified if it is assumed that the material load upon the belt is centrally applied and hence the two sets of outer idlers are inclined at approximately the same angle.

The load cross-section on troughed belts with only two idlers can be broken into two portions as shown in Figure 2.2, the upper circular segment area and the lower triangular area.

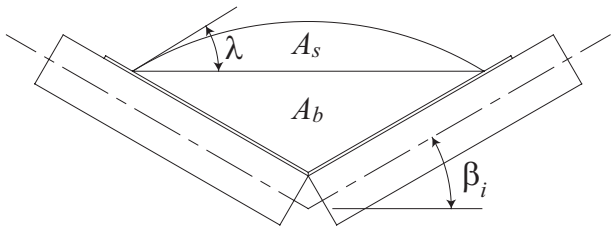

Figure 2.2 Load cross-section area on a 2 idler belt.

The circular segment area is found from:

$$A_s = \left(\frac{(0.455b - C_1)\cos\beta_i}{\sin\lambda} \right)^2 \cdot \left(\frac{\pi\lambda}{180} - \frac{\sin 2\lambda}{2} \right) \tag{2.4}$$

The area of the lower triangular portion is found from:

$$A_b = \left((0.455b - C_1)\cos\beta_i\right)^2 \cdot \tan\left(\tan\beta_i\right) \tag{2.5}$$

The constant $C_1 = 0.023$ for $v_b < 3.5$ ms^{-1} and $C_1 = 0.048$ for $v_b > 3.5$ ms^{-1}. The total area is calculated from the combination of the two areas, given by:

$$A_T = A_s + A_b \tag{2.6}$$

The load cross-section on troughed belts with three idlers can be broken into two portions as shown in Figure 2.3, the upper circular segment area and the lower trapezoidal area.

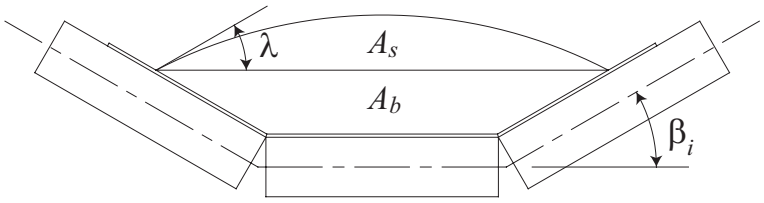

Figure 2.3 Load cross-section area on a 3 idler belt.

The circular segment area is found from:

$$A_s = \left(\frac{0.1855b + C_2 + (0.2595b - C_2)\cos\beta_i}{\sin\lambda} \right)^2 \cdot \left(\frac{\pi\lambda}{180} - \frac{\sin 2\lambda}{2} \right) \tag{2.7}$$

The area of the lower trapezoidal portion is found from:

$$A_b = \left(0.371b + 0.00635 + \left(0.2595b - C_2\right) cos\,\beta_i\right) \cdot \left(\left(0.2595b - C_2\right) sin\,\beta_i\right) \quad (2.8)$$

The constant $C_2 = 0.026$ for $v_b < 3.5$ ms^{-1} and $C_2 = 0.051$ for $v_b > 3.5$ ms^{-1}. The total area is calculated from the combination of the two areas, given by:

$$A_T = A_s + A_b \quad (2.9)$$

The load cross-section area on flat belts is made up of only one section, that of the segment of a circle, and is illustrated in Figure 2.4.

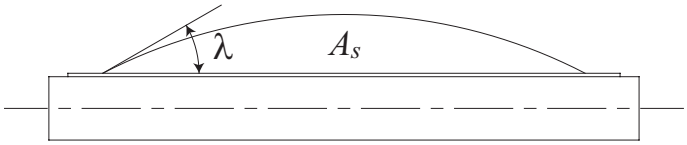

Figure 2.4 Load cross-section area on a flat belt.

The total area can be calculated from:

$$A_T = A_s = \left(\frac{\left(0.455b - C_1\right)}{sin\,\lambda}\right)^2 \cdot \left(\frac{\pi\lambda}{180} - \frac{sin\,2\lambda}{2}\right) \quad (2.10)$$

The constant $C_1 = 0.023$ for $v_b < 3.5$ ms^{-1} and $C_1 = 0.048$ for $v_b > 3.5$ ms^{-1}.

The material centre of gravity and height of the material upon the belt is dependent on the conveyor design also. These can be calculated once the load area of material has been calculated. The formulas presented are reproduced from the work of Powell (1995). An iterative approach is used to calculate the centre of gravity and material height for troughed belts (2 and 3 idlers). Eq. (2.11) is firstly minimized:

$$f(x_h) = 3x_h^3 + 4x_h bw_2 - 6A_T bw_2 \tag{2.11}$$

to obtain:

$$f'(x_h) = 9x_h^2 + 4bw_2 \tag{2.12}$$

Eq. (2.13) is then iterated to find the final value of the height of material on the belt (x_h):

$$x_h = x_h - \left(\frac{f(x_h)}{f'(x_h)} \right) \tag{2.13}$$

The centre of gravity of the material on the belt is calculated from:

$$C_{grav} = \frac{bw_2^3}{12A_T} - \sqrt{\left(0.5x_h + \frac{bw_2^2}{8x_h} \right)^2 - \frac{bw_2^2}{4}} \tag{2.14}$$

The centre of gravity for flat belts can be calculated by solving:

$$C_{grav} = \frac{(0.89b - C_3)^3}{12A_T^2} - \left(\frac{0.445b - C_1}{sin\,\lambda} \right) \cdot cos\,\lambda \tag{2.15}$$

The constant $C_3 = 0.046$ for $v_b < 3.5$ ms^{-1} and $C_3 = 0.096$ for $v_b > 3.5$ ms^{-1}. Roberts (2000, 2001, 2004) also provides a method to calculate height of material upon the belt prior to discharge with the theory as follows. Referring to Figure 2.5, assuming a three-idler system and parabolic surcharge profile the load cross-sectional area is given by:

$$A_T = A_{BC} + L_{BC} \tag{2.16}$$

where A_{BC} is a non-dimensional cross-sectional area factor and L_{BC} is the contact perimeter found from:

$$L_{BC} = L_B + 2L_C \tag{2.17}$$

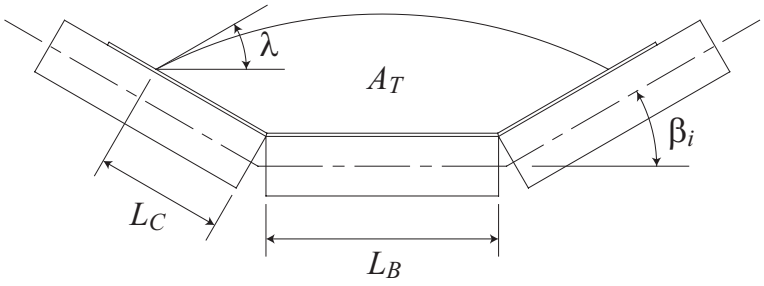

Figure 2.5 Cross-section of troughed belt

The cross-sectional area factor can be found from:

$$A_{BC} = \frac{1}{(1+2r)^2}\left\{ r\sin\beta + \frac{r^2}{2}\sin 2\beta + \frac{\tan\lambda}{6}\left[1 + 4r\cos\beta + 2r^2(1+\cos 2\beta)\right]\right\} \tag{2.18}$$

where:

$$r = \frac{L_C}{L_B} \tag{2.19}$$

The height of the material prior to discharge is approximated from:

$$h_b = \frac{A_T}{L_B + L_C} \tag{2.20}$$

Once the material height prior to discharge is calculated, the discharge characteristics and trajectory can be calculated. Each prediction method shall now be reviewed.

2.4.3 Method of Korzen

The method of Korzen (1989) provides the most thorough and detailed analytical method of all the choices available in literature. The method is particularly useful for

materials possessing high amounts of adhesion as it is the only model available that uses the concept of adhesion and inertia of the material on the belt and allowance is made for the variation in static and kinematic friction.

Using Eq. (2.2) and replacing the discharge angle α_d with the belt inclination angle α_b it can be determined whether the slow-speed belt condition has been met. When this is the case the angle at which the material slips α_r on the belt as it begins to wrap around the discharge pulley can be found from:

$$\alpha_r = tan^{-1}\,\mu_s \pm sin^{-1}\left[sin\left(tan^{-1}\,\mu_s\right)\cdot\left(\frac{v_b^2}{R_e g} - \frac{2\sigma_a}{\gamma h_b}\right)\right] \tag{2.21}$$

The positive or negative signs depend upon the belt inclination. A '+' is used for descending belts and a '–' for an ascending belt. A value for the static friction coefficient can be estimated from (Arnold & Hill 1991b):

$$\mu_s = \frac{K\sigma_1 \tan\phi_w}{\left(\sigma_a + \sigma_1\right)} \tag{2.22}$$

The normal stress σ_1 can be found by approximating conditions on the belt with a hydrostatic case namely (Arnold & Hill 1991b):

$$\sigma_1 = \rho g h_b \tag{2.23}$$

The separation angle and discharge velocity can be determined from:

$$v^2(\psi) = Ce^{4\mu_k\psi} + \frac{2R_e g}{1+16\mu_k^2}\left[\left(4\mu_k^2 - 1\right)cos\,\psi - 5\mu_k\, sin\,\psi\right] \tag{2.24}$$

The integration constant C can be found by substituting the initial conditions into Eq. (2.24) which are:

$$\psi = \alpha_r \quad \Rightarrow \quad v(\psi) = v_b \tag{2.25}$$

Once a value for C has been obtained from substituting the initial conditions, and expression for the discharge velocity $v(\alpha_d) = v_d$ can be obtained from Eq. (2.24) and is given by:

$$v_d = \sqrt{R_e g \cos \alpha_d} \tag{2.26}$$

The method measures discharge velocity from half the material stream height, which is not as accurate as other methods such as that detailed in the C.E.M.A. (1997) handbook. The method provides formulas to calculate material stream height and cross sectional area but requires knowledge of the mass flow rate. One drawback is that it does not include belt transition effects.

The discharge velocity given in Eq. (2.26) gives the velocity of the material stream centerline, which is fine to use as the initial velocity of the upper and lower material stream limits at high speed-conditions. To calculate the initial velocities used for the upper and lower trajectories at slow-speed conditions, Korzen provides Eq. (2.27) and Eq. (2.28) for the upper and lower limits respectively:

$$v_{d,upper} = v_d \cdot \frac{R + h_b}{R + 0.5h_b} \tag{2.27}$$

$$v_{d,lower} = v_d \cdot \frac{R}{R + 0.5h_b} \tag{2.28}$$

Korzen provides an extensive analysis on air drag effects in his work, if air drag is a factor. The effects of air drag are included in his theory to help describe the trajectory after the material has left the belt. A multi-step approximation method is used to solve the expressions developed by Korzen for air drag. Properties including particle solid density, equivalent diameter, correction factors allowing for the effect of grain shape on the air drag coefficient as well as properties of the atmospheric air must be obtained. A value for the coefficient of air drag can then be obtained using this information.

2.4.4 Method of Booth

The method of Booth (1934) is essentially a combined analytical-graphical approach. The method provides a chart from which the angle of material discharge can be found, though it doesn't provide calculations to determine material height at discharge point. Booth proposed taking material slippage into consideration but the technique does not take into account the inertia of the particle or any adhesion the particles may have with the belt. For fast belts, a more traditional approach is used that concentrates only on belt velocity. The conditions for slow-speed belts are met when Eq. (2.29) holds:

$$\frac{v_b^2}{R_b g} < cos\,\alpha_b \tag{2.29}$$

When this is the case, the angle at which the material begins to slip on the belt as it begins to wrap around the discharge pulley can be found from:

$$cos\,\alpha_r - \frac{v^2}{gR_b} = \frac{sin\,\alpha_r}{\mu_s} \tag{2.30}$$

which simplifies to:

$$\alpha_r = tan^{-1}\,\mu_s \pm sin^{-1}\left[sin\left(tan^{-1}\,\mu_s\right) \cdot \frac{v_b^2}{R_b g} \right] \tag{2.31}$$

Eq. (2.31) is basically the same as Eq. (2.21) without the adhesion term and using the distance measured from the centre of the discharge pulley to the top surface of the belt in place of the corresponding distance to the material's centroid. The separation angle and the discharge velocity can be found from:

$$\frac{v^2(\psi)}{2gR_b} = \frac{\left(2\mu_k^2 - 1\right)cos\,\psi - 3\mu\,sin\,\psi}{\left(4\mu_k^2 + 1\right)} + Ce^{2\mu_k\psi} \tag{2.32}$$

The integration constant *C* can be found by substituting the initial conditions into Eq. (2.32) which are:

$$\psi = \alpha_r \quad \Rightarrow \quad v(\psi) = v_b \tag{2.33}$$

An expression for the discharge velocity $v(\alpha_d) = v_d$ and separation angle α_d can be obtained by simultaneously solving Eq. (2.32) and Eq. (2.34):

$$v_d = \sqrt{R_b g \cos\alpha_d} \tag{2.34}$$

Booth only illustrates how to plot the inner edge of the material stream. The method doesn't analytically provide the method to plot the outer edge of the material stream, a feature which is required with emphasis in industry on designing chutes for efficiency and cost effectiveness. Also, the characteristics of the material stream pattern are not mentioned i.e. whether it expands along its flight path, it remains parallel, or contracts.

2.4.5 Method of Golka

Golka (1993a) attempted to simplify discharge trajectories by presenting formulas in Cartesian equation format for varying belt discharge velocity scenarios. His method however only used the concept of centripetal acceleration. It defines a critical speed as:

$$v_c = \sqrt{gR\cos\alpha_d} \tag{2.35}$$

Golka's method doesn't provide a procedure to calculate the height of material at the discharge point for fast conditions. For slow-speed conditions formulas are provided for the material height based on continuity-flow relationship, but still require the original material height for it to work. Golka also introduced 'divergent coefficients' to represent the influence of air resistance, size distribution, permeability, particle segregation, the effect of the wind in an open area, and other factors on the theoretical path of the material trajectory, though no mention is made of how to obtain the coefficient values.

2.4.6 Method of Dunlop

The method of Dunlop (1982) is essentially a graphical approach that is straightforward to implement, and parallels the analytical method by Booth (1934); hence the results are very similar to Booth's method. The concept of friction acting between the material and the belt is used.

Despite the Dunlop manual providing formulas to calculate belt transition distances it doesn't provide calculations to determine material height at the discharge point. The manual provides a chart from which the angle of material discharge can be found for slow conveyors. The technique doesn't take into account: inertia effects of the material on the belt, material adhesion characteristics, belt thickness, belt width, material surcharge angle, load shape on the belt, and edge distances. Also, the method is limited to pulleys equal to or larger than 312 mm in diameter. For fast belts, a more traditional approach is used that concentrates only on belt velocity.

Similar to Booth's technique, The Dunlop method only illustrates how to plot the inner edge of the material stream, and doesn't analytically provide the method to plot the outer edge of the material stream. The manual states that material density, grain size, and wind currents influence the trajectory, but no calculations or modifying factors are provided. Also, the characteristics of the material stream pattern are not mentioned: whether it expands along its flight path, it remains parallel, or contracts, although the example drawings imply contraction.

2.4.7 Method of Goodyear

The Goodyear (1976) manual only uses the concept of centripetal acceleration in its analysis. If the condition given in Eq. (2.36) holds, high-speed conditions result, otherwise slow-speed is assumed:

$$\frac{v_b^2}{gR_e} > cos\,\alpha_b \tag{2.36}$$

For slow-speed conditions, the left hand term of Eq. (2.36) is set to equal to the cosine of α_d to determine the wrap angle. The method of Goodyear doesn't provide calculations to determine material load height at the point of discharge, and doesn't consider the effects of material interaction with the belt. The method only provides the trajectory of the material at one-half load depth.

2.4.8 Method of M.H.E.A. (Early Version)

The first M.H.E.A. (1986) guide fundamentally uses a graphical approach. Tables are provided for the most common arrangements of belt width, trough angle, and material surcharge angle, to obtain the distance from the centre of mass to the pulley centre line. Tables are also provided to determine the angle factor, tension factor and specific modulus and the corresponding formula to calculate the transition distance.

The method does not consider the effects of material interaction with the belt. Only the concept of centripetal acceleration is used in the analysis. If the term on the left in Eq. (2.37) below is greater than 1, high-speed conditions result, otherwise slow-speed conditions result and the wrap angle α_d must be determined:

$$\frac{v_t^2}{gR_e} = cos\,\alpha_d \tag{2.37}$$

The guide illustrates how to plot both the inner and outer edges of the material stream. The angle at which the outer trajectory begins can be calculated from:

$$cos\,\alpha_d = \frac{v_b^2}{gR} \cdot \frac{R_m}{R} \tag{2.38}$$

2.4.9 Method of C.E.M.A.

The C.E.M.A. (1997) guide describes an approach that is essentially the same as that of the first M.H.E.A. (1986) guide. It addresses five aspects when examining material discharge: centre of mass, velocities, start of trajectory, load shape, and separation angle.

Almost all standard combinations of belt width, troughing idlers and bulk material characteristics are accounted for. Tables are provided to calculate the load height and centre of gravity of the material. Formulas are also provided to calculate the distance from the pulley centre to material stream centre of mass. Using this distance and the pulley rotational speed the tangential velocity is calculated.

The technique does not consider the effects of material interaction with the belt, namely frictional forces between the material and belt, inertia effects of the material on the belt, and adhesive properties of the material, rather it only uses the concept of centripetal acceleration in its analysis. For slow-speed conditions the following results:

$$\frac{v_t^{\,2}}{gR_e} = cos\,\alpha_d \tag{2.39}$$

The guide suggests that the plot of the material trajectory yields a parallel path for the upper and lower trajectory limits, though if the material is light and fluffy, or discharged from a very high-speed belt a slightly divergent path will result.

2.4.10 Method of M.H.E.A. (Updated Version)

The second M.H.E.A. (1989) guide provides a table to calculate the material load height at the discharge pulley. Discussions are provided on adjustments for material discharge, namely pulley height and belt sag, and belt edge materials. Tables are provided for determining approximate values for the critical velocity and discharge angles. Charts are also provided for determining the critical velocity and discharge angle for slow-speed belts.

The pulley rotational speed is used to calculate the load stream velocity that is assumed to be approximately equal to the belt velocity. The fast or slow-speed belt condition is determined by comparison to a critical velocity v_c, shown as Eq. (2.40). If the belt velocity $v_b > v_c$ then the conveying conditions are deemed high-speed, otherwise they are considered slow-speed.

$$v_c = \sqrt{gR_e \cos\alpha_b} \tag{2.40}$$

For slow-speed belts, the slightly modified formula shown by Eq. (2.41) is proposed to account for particle velocity increases under gravity and lifting material departure point. The method does not consider the effects of material interaction with the belt, and the concept of centripetal acceleration is used as its basis.

$$\cos\alpha_d = \sqrt[3]{\frac{v_b^2 \cos^2\alpha_b}{gR_e}} \tag{2.41}$$

The M.H.E.A guide provides a method to incorporate the effects of lumps in the trajectory plot though does not analytically provide the method to plot the outer edge of the material stream. The discharge velocity can be calculated from:

$$v_d = \frac{v_b \cos\alpha_b}{\cos\alpha_d} \tag{2.42}$$

2.4.11 Method of BTR

The method outlined in the BTR (n.d.) Conveyor Belt Manual combines a theoretical and graphical method similar to many of the techniques discussed. For this method, high-speed conditions occur when Eq. (2.43) is satisfied:

$$\frac{v_b^2}{gR_e \cos\alpha_b} > 1 \tag{2.43}$$

If the factor on the left side of the Eq. (2.44) below is less than 1, then a slow-speed condition exists where the material wraps around the pulley to some extent. This wrap angle α_d can be calculated from:

$$\frac{v_b^2}{gR_e} = \cos\alpha_d \tag{2.44}$$

Only a method to plot the underside of the trajectory path is shown.

2.4.12 Method of BFGoodrich

The BFGoodrich (n.d.) Engineering Handbook describes an identical method to the BTR (n.d.) Conveyor Belt Manual for determining discharge characteristics and also plotting the trajectory.

2.4.13 Method of S-A 66

The S-A 66 (n.d.) Catalogue uses a combined theoretical and graphical technique where the high and slow-speed conditions are only determined by the speed of the belt. For all conditions the material stream is assumed to traject at the point of tangency between the belt and the head pulley. A high-speed condition results if the theoretical stream does not intersect the pulley as it is plotted away from the point of trajection. Slow-speed condition results when the theoretical trajectory cuts into the belt and it is assumed that the material wraps around the head pulley for a distance. To find the point at which the theoretical trajectory will leave the belt, a line must be drawn from the pulley centre through the point on the current trajectory closest to the pulley centre. The point at which this line crosses the top of the belt is the point of trajection. Also, the method assumes that the maximum point of trajection occurs at 45 degrees from the vertical from the centre of the pulley which the author's experience has shown to be incorrect. This technique only discusses plotting the underside of the material stream.

2.5 Material Impact and Flow – Upper Chute Element

2.5.1 Introduction to the Upper Chute Element

Impact plates/rebound boards, rock-boxes, or 'Hood' elements, are used in transfer points to intercept the material trajectory from the upper conveyor, and direct the material downwards to be met by a curved chute section, or 'Spoon' element. During the literature survey, a few relevant technical papers focusing on material impact have been found including those of Benjamin et al. (1999a, 1999b), Colijn & Conners (1972),

Korzen (1980, 1988), Lonie (1989), Page (1991), Roberts (2001), Roberts & Wiche (1999), Rozentals (1991), Scott (1997), Scott & Choules (1993a, 1993b) and Sundstrom & Benjamin (1993), although only two of these (Korzen 1980, 1988) dealt comprehensively with the interaction between the flow stream and its impact with the upper chute element.

One of the major types of ore-on-ore impact arrangements used in mining and quarrying operations is the rock box with the concept detailed in a number of papers (Page 1991, Scott 1997, Scott & Choules 1993a, 1993b). It basically uses a ledge to form a single pocket of ore to redirect the material stream, hence reducing wear on most structural elements. Rock boxes are used to train the flow of material after receiving it from the belt conveyor, and are particularly useful for abrasive materials. Generally they are not used for material with high cohesion to prevent material build-up leading to flow blockages. For an angled transfer with variable ore properties and also differing belt speeds, it is critical that the horizontal component of the velocity, which in most cases is unpredictable (Scott & Choules 1993b), is removed from the material stream. This cannot be achieved by rock boxes, only by impact plates or 'Hood' sections, hence their use. The problem common to both rock boxes and impact plates is that material is not allowed to flow naturally; rather, they obstruct the free motion of the material stream, which can cause a multitude of problems. Schematics showing the use of an impact plate, or rock box are shown in Figures 2.6 (a) and 2.6 (b) respectively.

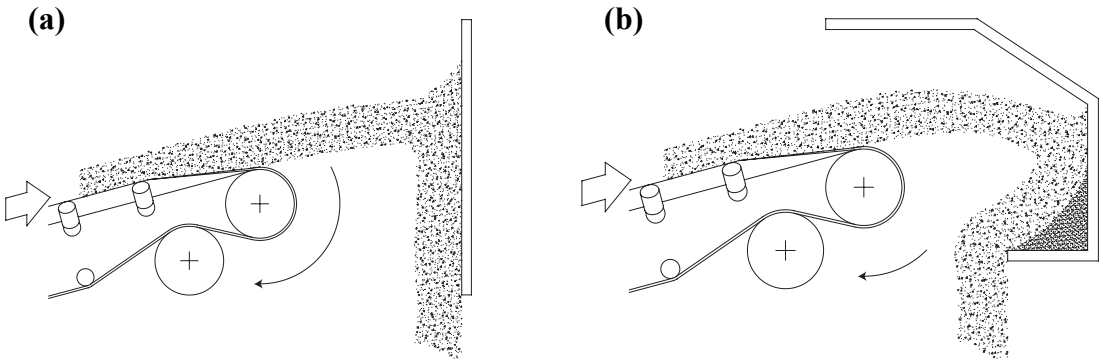

Figure 2.6 **(a)** Impact Plate; **(b)** Rock box

If time and budget permit, a curved element such as a curved plate or a 'Hood' enclosure is usually designed and fabricated for use in the upper section of the transfer. The aim when designing a 'Hood' type element is to basically ensure that there is unrestricted flow through the system, hence the use of a curved profile.

Based on experimental work, Korzen (1988) suggested the behaviour of the bulk material on impact with an impact plate (or upper element) to follow that presented in Figure 2.7. The stream of bulk material slides against a curved plane formed by a region of static material build-up just above the stream impact location. The abrasive contact region is also known as the 'flow-round' zone. This phenomenon has also been identified by Lonie (1989).

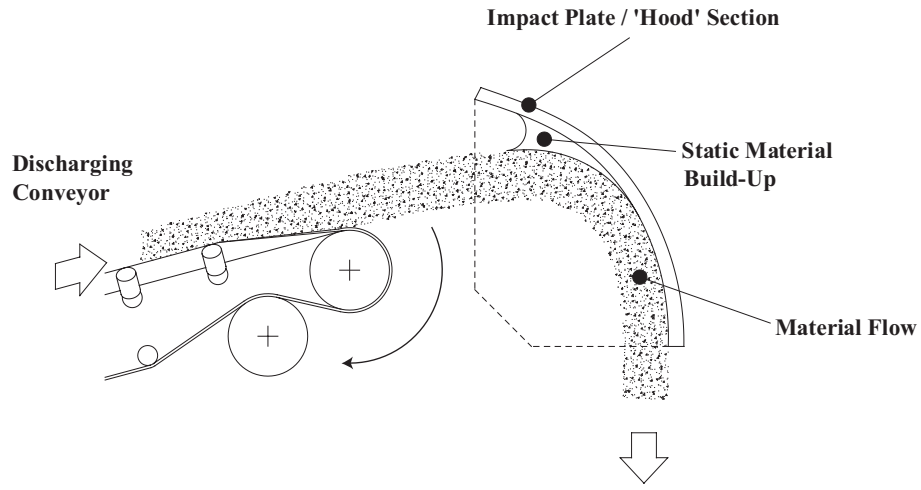

Figure 2.7 Schematic diagram of bulk solids behaviour upon impact with the rebound board/'Hood' section

Using this conclusion, Korzen's subsequent mathematical analyses allow for the discharge velocity vector from the material flow impact with the rebound board to be calculated. Following this iterative procedure, simple sliding flow mechanics are used to determine the exit velocity vector from the upper transfer chute element. Korzen also suggested two models for the dynamics of the bulk solids stream against the impact plates, one based on the material behaviour being cohesionless, and the other based on a cohesive material. Marcus et al. (1996) practically confirmed the work of Korzen and

suggested that there are three basic parameters that influence the effectiveness of impact plates. These are the angle of inclination, the tilting angle and the distance from the discharge drum axis.

2.5.2 Cohesive Impact upon a Flat Plate

For materials with high cohesion or those that cannot satisfy the conditions set for cohesionless materials, Korzen (1988) proposed a multi-step approximation procedure. This can be time consuming to apply as a result of the lengthy equation that must be used and subsequent iterative process. One aspect of note is that there is no actual rebound: the velocity vector defined by Korzen is actually tangential to the rebound board surface, indicated in Figure 2.8. For best prediction using the impact model, the initial conditions should be calculated from Korzen's (1989) paper on material discharge.

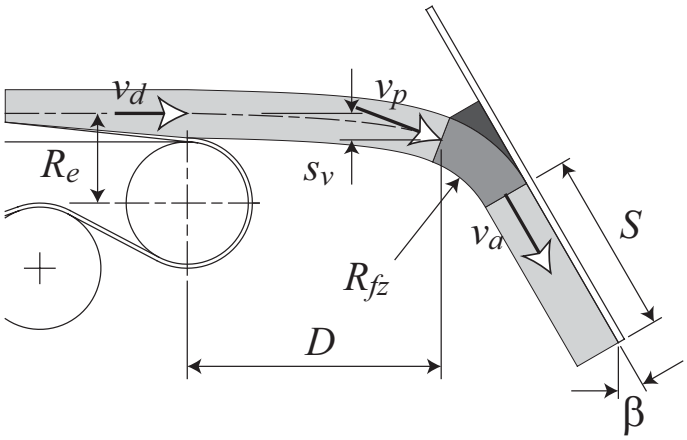

Figure 2.8 Cohesive impact upon a flat plate

The differential equation used as the basis for the cohesive impact model of Korzen is given by:

$$\frac{dv^2}{d\kappa} + 4\mu v^2 = 2gR_{fz}\left[\sin\kappa + \mu\cos\kappa - \frac{cb_s}{\gamma A(\kappa)}\right] \tag{2.45}$$

which yields the solution:

$$v^2(\kappa) = Ce^{-4\mu\varphi} + \frac{2R_{fz}g}{1+16\mu^2}\left[5\mu\sin\kappa + \left(4\mu^2 - 1\right)\cos\kappa\right] - \frac{cb_s R_{fz}}{2\mu\rho A(\kappa)} \tag{2.46}$$

where:

$$\kappa = \begin{cases} \dfrac{\pi}{2} - \beta & \text{for a plate inclined as shown in Figure 2.8} \\ \dfrac{\pi}{2} & \text{for a vertical plate} \\ \dfrac{\pi}{2} + \beta & \text{for a plate inclined opposite to that shown in Figure 2.8} \end{cases} \tag{2.47}$$

The constant of integration C can be found by substituting the initial conditions below into Eq. (2.46):

$$\kappa = \theta_a \tag{2.48}$$

$$v(\kappa) = v(\theta_a) = v_p \tag{2.49}$$

$$A(\kappa) = A(\theta_a) = A_p = \frac{\dot{m}}{\rho v_p} \tag{2.50}$$

$$R_{fz} = h(\kappa) = h_p = \frac{\dot{m}}{\rho v_p b_s} \tag{2.51}$$

Once the value for the constant of integration has been found a multi-step approximation procedure is used to find a value for v_a the exit velocity of the material stream from the 'flow-round' zone. So at the first step:

$$R_{fz} = R_{fz1} = h_p \tag{2.52}$$

$$A(\kappa) = A_{a1} = A_p = \frac{\dot{m}}{\rho v_p} \quad \Rightarrow \quad v_a = v_{a1} \tag{2.53}$$

In the second step of the approximation:

$$R_{fz} = R_{fz2} = \frac{h_p + h_{a1}}{2} \tag{2.54}$$

$$A(\kappa) = A_{a2} = \frac{\dot{m}}{\rho v_a} \quad \Rightarrow \quad v_a = v_{a2} \tag{2.55}$$

$$h_{a2} = \frac{\dot{m}}{\rho v_{a1} b_s} \tag{2.56}$$

The multi-step approximation procedure is followed until convergence results and the condition in Eq. (2.57) holds:

$$\left| \frac{v_{a(k)} - v_{a(k-1)}}{v_{a(k)}} \right| \cdot 100 \leq \xi \tag{2.57}$$

2.5.3 Non-Cohesive Impact upon a Flat Plate

Burnett (2000a, 2000b) identified that the model of Korzen (1988) for non-cohesive material impact has limitations owing to its use of the cosine rule in defining the exit velocity vector magnitude. The main drawback is the possibility of negative numbers occurring, rendering the model ineffective. The cohesive model though has no such constraints. Burnett identified that by substituting a cohesion stress of 0 kN/m^2 a non-cohesive state could be modelled. This compares favourably with the original cohesionless impact model.

If using the suggestions of Burnett, the cohesionless model requires a multi-step approximation procedure to find the exit velocity. This is fairly straightforward to use, as the equations are relatively simple. However, Arnold & Hill (1991a, 1991b) provided an estimate of the material's velocity on a flat plate for non-cohesive material, where the original model's problem is not present (no possibility of taking the square root of a negative number) when calculating the exit velocity. An iterative procedure is not required for this model, and the parameters required are illustrated in Figure 2.9.

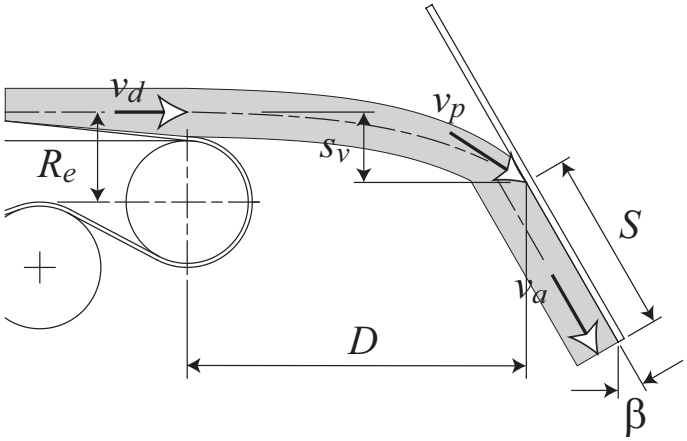

Figure 2.9 Non-cohesive impact upon a flat plate

Arnold & Hill (1991b) detailed how an estimate of the material's velocity on a flat plate may be obtained at the point immediately after the material has passed through the 'flow-round' zone from:

$$v_a = v_p \left[sin\left(\theta_a + \beta\right) - \mu cos\left(\theta_a + \beta\right) \right] \tag{2.58}$$

The condition in Eq. (2.59) must hold for Eq. (2.58) to be successfully used:

$$\left(\theta_a + \beta\right) > tan^{-1}\,\mu \tag{2.59}$$

Referring to Figure 2.9, v_p is given by:

$$v_p = \sqrt{2gs_v + v_d^2} \tag{2.60}$$

where the material stream drop s_v can be found from:

$$s_v = D\left(tan\,\alpha_d + \frac{gD}{2v_d^2\, cos^2\,\alpha_d} \right) \tag{2.61}$$

The angle θ_a the material impinges on the impact plate with can be found from:

$$\theta_a = cos^{-1}\left(\frac{v_d\, cos\,\alpha_d}{v_p}\right) \tag{2.62}$$

The reader is directed to the works by Arnold & Hill (1991a, 1991b) for further details regarding formulas and corresponding conditions.

2.5.4 Sliding Flow upon a Flat Plate

After exiting the 'flow-round' zone or at the point where the velocity vector is tangential to the plate, the material will increase its velocity as it slides down the flat plate or free-falls. Once the exit velocity from the impact plate is determined the material trajectory can be plotted exactly as it is for belt conveyors. The velocity of the material stream from the bottom of the impact plate can be estimated from (Arnold & Hill 1991b):

$$v_e = \sqrt{v_a^2 + 2gS\left(cos\,\beta - \mu\, sin\,\beta\right)} \tag{2.63}$$

where:

$$\beta = \begin{cases} 0 \text{ if the plate is vertical or tilted towards the incoming material stream } (^o) \\ \text{angle of plate to the vertical if plate is tilted away from incoming material stream } (^o) \end{cases} \tag{2.64}$$

2.5.5 Impact upon a Curved Plate

Korzen (1988) only examined material impact upon flat plates. Arnold & Hill (1991b) applied the approach used by Korzen in determining the exit velocity after cohesionless material impact with a flat plate to the case of a curved plate. The relevant terms are detailed in Figure 2.10.

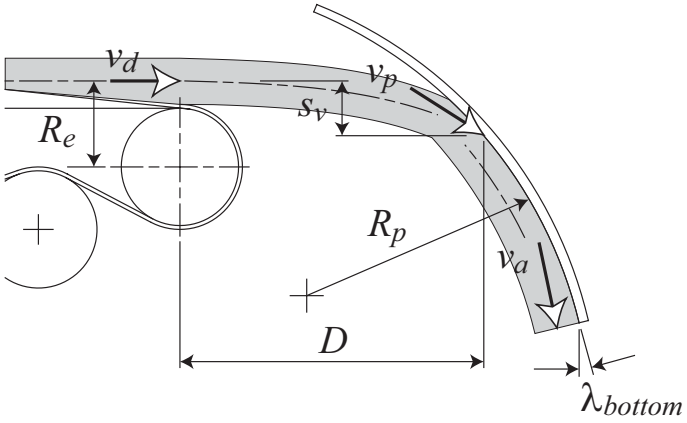

Figure 2.10 Impact upon a curved plate

The cohesion term was omitted and the 'flow-round' zone radius was replaced with the radius of the plate, resulting in Eq. (2.65). Their curved plate model requires knowledge of the plate dimensions though. A multi step approximation procedure is not needed for the curved plate model.

$$v^2(\kappa) = Ce^{-4\mu\varphi} + \frac{2R_p g}{1+16\mu^2}\left[5\mu \sin\kappa + \left(4\mu^2 - 1\right)\cos\kappa\right] \tag{2.65}$$

where:

$$\kappa = \begin{cases} \dfrac{\pi}{2} - \lambda_{bottom} & \text{case where material exits plate travelling in same horizontal direction as incoming material stream} \\ \dfrac{\pi}{2} & \text{vertical exit velocity} \\ \dfrac{\pi}{2} + \lambda_{bottom} & \text{case where material exits plate travelling in opposite horizontal direction to the incoming material stream} \end{cases} \tag{2.66}$$

In order to solve for the integration constant C the same initial conditions are substituted into Eq. (2.65) as used in Eq. (2.46):

$$\kappa = \theta_a \tag{2.67}$$

$$v(\kappa) = v(\theta_a) = v_p \tag{2.68}$$

As the stream is forced to follow the curvature of the plate the initial conditions in Eq. (2.67) and Eq. (2.68) are not ideal, because the impact angle of the material stream θ_a bears no relationship to the curve of the plate, unlike Eq. (2.46) where the incoming velocity vector is tangential to the curvature of the 'flow-round' zone. Arnold & Hill proposed a corrected angle of entry θ_c to be used. The concept is illustrated in Figure 2.11.

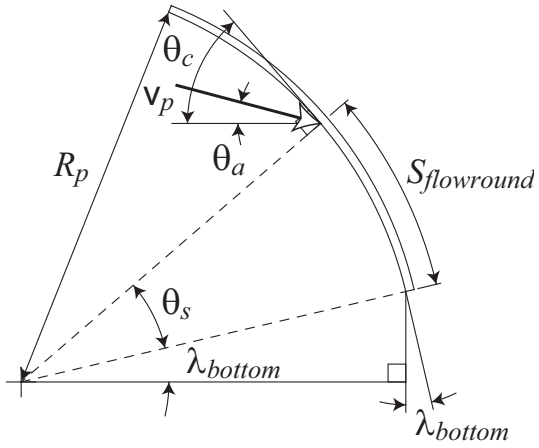

Figure 2.11 Defining the corrected angle of entry when examining impact upon a curved plate

This could be calculated from the point where the centre of mass of the material stream intersects the plate. It is assumed the velocity change between the two angles is negligible i.e.

$$v(\theta_c) = v_p \tag{2.69}$$

This leads to an alternative set of initial conditions for Eq. (2.65):

$$\kappa = \theta_c \tag{2.70}$$

$$v(\varphi) = v(\theta_c) = v_p \tag{2.71}$$

Roberts also examined curved upper chute elements. He applied the theories created for gravity flow U-form chutes to the investigation of flows through the upper chute element or 'Hood' section in his works (Roberts 1997b, 1997c, 2001, 2004, Roberts & Wiche 1999). The concept of material impact was not addressed analytically though mention is made of the impact process. Further discussions on U-form transfer chute sections are presented in Section 2.7. Roberts gives the radius of curvature of the discharge trajectory as:

$$R_C = \frac{\left[1 + \left(\frac{gx}{v_b^2 \cos^2\theta}\right)^2\right]^{3/2}}{\left(\frac{g}{v_b^2 \cos^2\theta}\right)} \tag{2.72}$$

For contact to be made with a curved impact plate of constant radius, the radius of curvature of the trajectory at the point of contact must be such that:

$$R_C \geq R \tag{2.73}$$

where R is the chute radius (m). The aim is to create a chute profile where the radius of curvature of the impact plate equals the material stream path curvature at the point of impact. Using $\theta = dy/dx$ as the chute slope, the radius of curvature of the chute can be found from:

$$R = \frac{\left[1 + \left(\frac{dy}{dx}\right)^2\right]^{3/2}}{\left(\frac{d^2y}{dx^2}\right)} \tag{2.74}$$

Note in this work, the horizontal axis is given by 'y' and the vertical axis is designated by 'x'. The flow of the material through the chute or around the impact plate must now be considered. Referring to Figure 2.12 and noting that $F_D = \mu_E N$, it may be shown that the relevant differential equation is given by (Roberts 2001):

$$-\frac{dv}{d\theta}+\mu_E v=\frac{gR}{v}\left(cos\,\theta+\mu_E\,sin\,\theta\right) \tag{2.75}$$

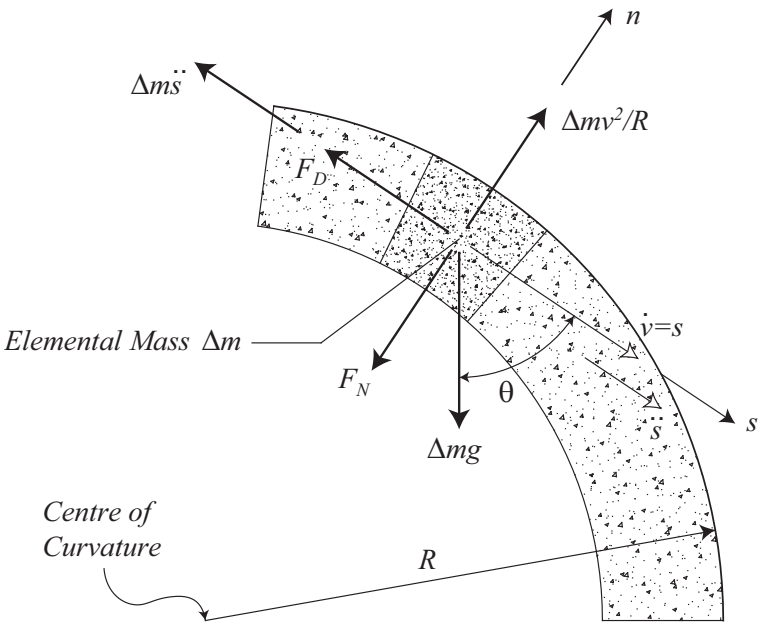

Figure 2.12 Inverted curved chute model (adapted from Roberts 2001)

For a constant radius R and assuming μ_E is constant at an average value for the material stream, the solution of Eq. (2.75) is:

$$v=\sqrt{\frac{2gR}{4\mu_E^2+1}\left[sin\,\theta\left(2\mu_E^2-1\right)+3\mu_E\,cos\,\theta\right]+Ce^{2\mu_E\theta}} \tag{2.76}$$

The constant C can be found from the initial conditions:

$$\theta=\theta_0 \quad \Rightarrow \quad v=v_0 \tag{2.77}$$

leading to:

$$C = \left\{ v_0^2 - \frac{2gR}{4\mu_E^2 + 1}\left[3\mu_E \cos\theta_0 + \left(2\mu_E^2 - 1\right)\sin\theta_0\right]\right\} e^{-2\mu_E\theta_0} \tag{2.78}$$

Eq. (2.77) and Eq. (2.78) apply for the following condition (Roberts 2001):

$$\frac{v^2}{Rg} \geq \sin\theta \tag{2.79}$$

Comparisons between the analytical techniques of Korzen, Arnold & Hill, and Roberts are presented in Chapter Three.

2.6 Material Free Fall

2.6.1 Air Entrainment Overview

As the material undergoes free fall, the concept of air *entrainment* becomes a significant issue, especially for great material drops between conveyors. Air entrainment can play a role in altering the freefall profile of the material stream, with dust generation as one phenomenon that occurs. This is an important aspect in materials handling because of several issues including: dust emissions that are hazardous to workers, dust damage to pulleys and idlers; and economic aspects like product losses (spillage) to consider. Projects undertaken by the author in industry have revealed that up to 70% of dust generation can be reduced through a transfer by utilisation of a well designed chute system. Nonetheless, the current work will briefly examine some of the work performed in dust generation and air movement. Air entrainment aspects are illustrated in Figure 2.13.

Dust control and related fugitive material problems in conveyor transfers are not described here, where the reader is referred to the works of Binzon (1985), Colijn & Conners (1972), Firstbrook (1983), Gibor (1997), Goldbeck (1996), Goldbeck & Marti (1996), Maynard (2003), Morrison (1971), Ove & Michael Brunius (1995), *Quarry Management* (1993), Rappen (1986, 1994), Rozentals (1991), Sabina et al. (1984),

Stahura (1992), Swinderman (1994), Thomas (1993), Tooker (1985), Weakly (2000) and Weiss (1992).

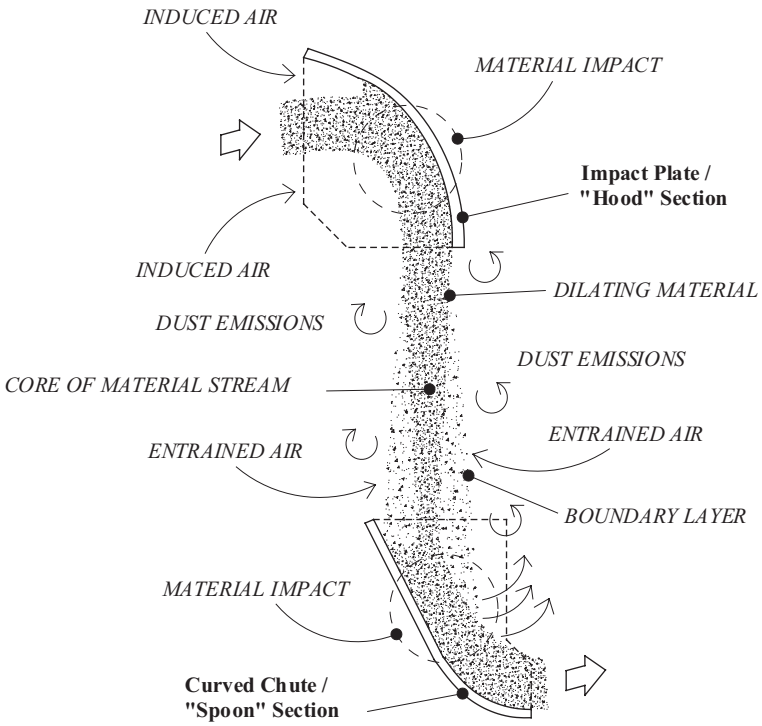

Figure 2.13 Schematic of a falling material stream involving air entrainment and fugitive dust generation. In addition to directing the flow, curved 'Hood' and 'Spoon' elements minimise dust emissions

Fugitive dust generation in bulk material handling transfer operations was investigated by Tooker (1992), who considered the bulk material particle motion mainly as flow in the fully turbulent regions of Reynolds numbers. The work of Hemeon (1962) provided the basis for his work, with Tooker introducing new concepts to give air entrainment predictions of greater accuracy.

The work of Cooper and Arnold (1995) presented experimental results for air entrainment and dust generation by a stream of alumina falling from a hopper under steady state conditions. They discussed 3 simple analytical models of the air

entrainment process: the single particle model by Hemeon, the massive particle model, and the miscible plume model. This work deduced that the miscible plume model provided the best correlation of the experimental air entrainment data. The drawback of this work is that the analysis covers only vertical material streams; hence the theory is limited with regard to 'non-vertical' transportation of material as occurring in certain conveyor transfer situations, such as material trajectory off the head pulley at high-speeds.

Based upon the work described above, Liu et al. (1999) provided a review of the available dust generation and air entrainment mechanisms in bulk handling operations. In further work, Liu et al. (2001) described an experimental investigation of the velocity distribution within air induced to move by a falling stream of bulk material. The topic has application to belt conveyor transfers as its relevance is to the design of dust control systems involving free falling bulk solids. The review paper by Ullmann & Dayan (1998) thoroughly examined dust emissions from belt conveyor transfer points. They considered transfer points enclosed within containment structures. Different formulas and current design methods of exhaust volume models i.e. the models depicting air flow rate that must be drawn from an enclosure to prevent dust emission, were reviewed, compared and analysed. This work however made assumptions with regards to particle size distribution and also catered for only a particular shape of enclosure.

The lack of supplementary literature to that mentioned suggests the area of air entrainment requires further research. In most cases air entrainment issues are not considered during the chute design phase, due to analytical complexity and hence timing issues. The author's industrial experience has shown that to counter large material drop heights, often a straight chute is used that extends from below the head pulley at a constant angle down to the lower chute element. This has been successful for a number of applications.

2.6.2 Air Resistance and Drag Overview

The aspect of air *resistance* in conveyor transfers has been ignored by most researchers, with very few papers in the literature including air resistance calculations within their respective models, for example see Roberts (1997a, 1997c, 2000, 2001) and Roberts &

Wiche (1999). This is due in part to the large tonnage of coarse granular materials being conveyed, which are not prone to air drag. Hence the associated drag calculations are usually not required.

The work by Korzen (1989) is the only available paper in the literature concentrating on conveyor transfers that details comprehensively the effects of air drag on individual bulk solid particles. He suggested a method of modelling the effect of air drag on the bulk material stream during free fall. The model assumes that particles less than 1 gram in mass will be dependent on air drag. The trajectory of inclined free fall of a bulk material particle subject to air drag is given by:

$$y(x) = x\tan\alpha_d - \frac{g}{2v_d^2\cos^2\alpha_d}x^2 - \frac{a_w g}{3\Delta m v_d^2\cos^2\alpha_d}x^3 - \ldots \tag{2.80}$$

Korzen illustrates that if air drag is neglected, ie for $a_w = 0$, Eq. (2.80) reduces to the known formula for the trajectory of inclined free fall of a material in vacuum:

$$y(x) = x\tan\alpha_d - \frac{g}{2v_d^2\cos^2\alpha_d}x^2 \tag{2.81}$$

For belt speeds of less than or equal to 0.5 ms^{-1}, Roberts (1997a, 2000) provides a relationship between the height of material drop h and the velocity of impact with the curved chute v_i if air resistance is to be taken into account, shown by:

$$h = \frac{v_\infty^2}{g}\log_e\left[\frac{1-\frac{v_{f0}}{v_\infty}}{1-\frac{v_i}{v_\infty}}\right] - \left(\frac{v_i - v_{f0}}{g}\right)v_\infty \tag{2.82}$$

For free falling materials, Roberts (1997c) gives the displacement as a function of time:

$$y(t) = \frac{1}{\beta_v}\left[v_i - v_\infty\right]\left[1 - e^{-\beta_v t}\right] + v_\infty t \tag{2.83}$$

and the velocity as:

$$v = y'(t) = \left[v_i - v_\infty\right] e^{-\beta_v t} + v_\infty \tag{2.84}$$

The assumption used for these relations is that there are no inter-particle collisions. An iterative procedure using Eq. (2.83) is used to calculate the time t to fall through the drop height. Eq. (2.84) can then be solved using this value of t. The terminal velocity is given by (Roberts 1997c):

$$v_\infty = \frac{g}{\beta_v} \tag{2.85}$$

2.7 Material Impact and Flow – Lower Chute Element

2.7.1 Material Impact Aspects

After the material stream has undergone free fall from the impact with the 'Hood' section or trajects directly off the head pulley, it impacts on a lower chute element, or 'Spoon' section. There are two papers available in literature that examined material impact upon the lower chute element. Roberts (2004) considers the falling stream impacting on a surface as illustrated in Figure 2.14 (a).

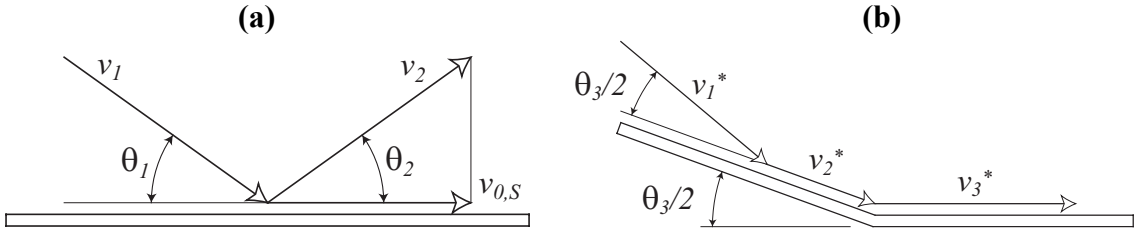

Figure 2.14 **(a)** Impact model proposed by Roberts (2004); **(b)** impact model proposed by Stuart-Dick & Royal (1991, 1992)

The ratio of velocities after and before impact is given by:

$$\frac{v_{0,S}}{v_1} = cos\,\theta_1 - (1-\varepsilon)\mu\, sin\,\theta_1 \tag{2.86}$$

Stuart-Dick & Royal (1991, 1992) have shown that such a method can often reduce the material velocity, and for a particular combination of angle of incidence θ_1 and wall friction angle ϕ the velocity after impact may even reduce to zero. They proposed an arrangement where the material stream is deflected twice through half-angles, as illustrated in Figure 2.14 (b) and hence allows a greater proportion of the velocity to be maintained. The ratio of velocities after first impact is given by:

$$\frac{v_2^*}{v_1^*} = cos\frac{\theta_3}{2} - sin\frac{\theta_3}{2}tan\,\phi \tag{2.87}$$

and the ratio of velocities after second impact is given by:

$$\frac{v_3^*}{v_2^*} = cos\frac{\theta_3}{2} - sin\frac{\theta_3}{2}tan\,\phi \tag{2.88}$$

The ratio of the velocity after the double deflection to the original velocity is (Stuart-Dick & Royal 1991, 1992):

$$\frac{v_3^*}{v_1^*} = cos^2\frac{\theta_3}{2} - sin\,\theta_3\, tan\,\phi + sin^2\frac{\theta_3}{2}tan^2\,\phi \tag{2.89}$$

For a single deflection through the angle θ_1 (similar to that presented by Roberts (2004) described above), the ratio of velocities after and before impact is:

$$\frac{v_4^*}{v_1^*} = cos\,\theta_1 - sin\,\theta_1\, tan\,\phi \tag{2.90}$$

The impact process upon lower chute element has also been explored by Maynard (2003), Rabindra Nath Ojha (1993), Roberts & Wiche (1999), and Royal & Craig (2001), though without the numerical detail required to sufficiently design the section with great confidence. A comprehensive technique similar to that of Korzen (1980, 1988) for the impact in the upper element or 'Hood' (discussed in Section 2.5) would be ideal. Certain papers (Burnett 2000a, 2000b) do apply the same impact models as used in the upper 'Hood' section to the lower 'Spoon' section. This in essence should work unless great drop height exists and the falling material has entrained a significant amount of air, resulting in a material stream whose cross-sectional area has increased during the free fall. After impact, provided the impact plate is sufficiently long, the material stream undergoes sliding flow.

A number of papers (Lonie 1989, Page 1991, Scott 1997, Scott & Choules 1993a) suggest the use of a V-shaped load out floor plate in the lower portion of a transfer chute. As material impacts and flows over the plate, a dead zone is created, similar to a rock box, over which the material continues to flow. Choking of the outlet can occur if the material becomes excessively cohesive (Scott 1997). The outlet plate is also difficult to adjust to cater for variations in material cohesiveness with the changing rill angle (Scott 1997). The process is shown in Figure 2.15.

2.7.2 Gravity Flow Chute Overview

Based on the volume of literature available though, the majority of the work performed in transfer chutes has been the development of U-form or gravity flow feed chutes. This type of chute transfers the material in a continuous sliding action, in which the material remains in continuous contact with the chute work as it is taken from the discharge point to the receiving conveyor. The flow of non-cohesive bulk solids through such discharge or transfer chutes has been studied in some detail (Bingham & Wikoff 1931, Choda 1965, Choda & Willis 1967, Korzen 1984a, McCurdy & Buelow 1963, Parbery & Roberts 1986, Roberts 1967, 1969, 1979, Roberts & Arnold 1971, Roberts & Scott 1981, Savage 1979, Trees 1962, Wolf & Von Hohenleiten 1945, 1948). Many of the earlier investigations in this field (Bingham & Wikoff 1931, McCurdy & Buelow 1963, Trees 1962, Wolf & Von Hohenleiten 1945, 1948) looked at a qualitative study for the

particular installations or looked at the derivation of empirical relationships for expressing material flow rate in terms of the transfer chute's dimensional characteristics.

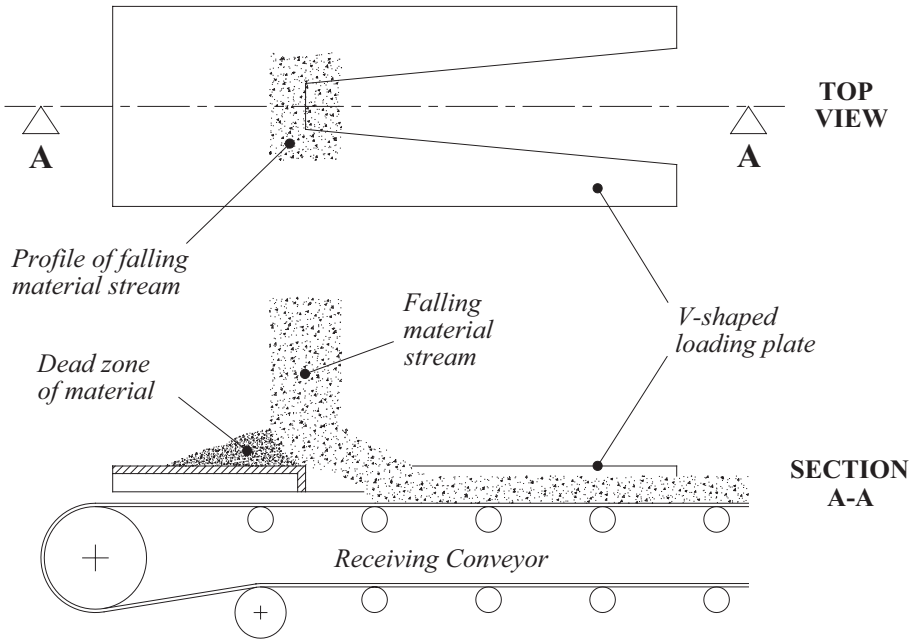

Figure 2.15 Top and section views of material impact and flow upon V-shaped load out floor pate

Choda's (1965) work was based entirely on experimental observations. This work showed how two conditions of flow were established: 'fast' flow and 'slow' flow. In general, the 'fast' or accelerated flow mode occurs when the material flows in contact with the chute bottom and side walls without contact with the top. Today, this is the situation proposed for most 'spoon' elements. In the 'slow' flow mode the chute is completely filled with the material flowing adjacent to all surfaces. The experimental work performed by Choda (1965) and Choda & Willis (1967) indicated how the influences of chute shape variation determined fast and slow flow characteristics, a significant step in chute flow analysis. Roberts (1967) followed Choda's work by proposing an approximate theory based on dynamic analysis. The resulting generalised flow equations were solved for a range of geometrical chute profiles, including straight, circularly curved, parabolic and cycloidal. To account for the drag on the side walls and chute bottom, an equivalent friction coefficient was introduced. The computations

performed were based on an assumed constant average value for the friction, though the friction coefficient was found to vary with the flowing stream thickness. Roberts (1967) stated that using the assumption of a constant mean value for μ_E for the theoretically computed results has been a satisfactory one for predicting chute performance for 'fast' flow conditions.

Roberts (1969) extended this work by taking into account the effect of the varying equivalent friction coefficient in the solution of the flow equations, resulting in improved accuracy of the models. The paper though only dealt with chutes of rectangular cross-section and no allowance was made for the influence of intergranular motion. Roberts & Arnold (1971) and Roberts & Scott (1981) extended the work of Roberts (1969) to include chutes of circular cross-section. For this application, the concept of an equivalent friction coefficient was introduced. The chute design theory of Roberts & Scott (1981) was based on a lumped parameter dynamic model. Parbery & Roberts (1986) examined in greater detail the concept of the equivalent friction model for rectangular cross-sectioned chutes, then extended the model to chutes of circular cross-section. Solutions of the chute flow equations were presented.

Many papers (Charlton & Roberts 1970, Charlton et al. 1975, Chiarella & Charlton 1972) use a single particle model to simulate the gravity assisted discharge from chutes. This has been shown by Roberts (1967, 1969) to be adequate, assuming fast flow conditions. As a result of being highly analytical in nature, they tend to lean towards theoretical use, rather than practical. These papers investigated the concept of optimum flow, where the aim is to find a chute profile to optimise some flow property such as transit time or exit velocity. The research presented provided methods that could be employed in such optimisation problems. Optimum flow was also investigated by Chiarella et al. (1974a, 1974b), Montagner et al. (1974), and Roberts & Montagner (1975).

There are also several other papers that investigate U-form transfer chute aspects (Augenstein & Hogg 1978, Burnett 2000a, 2000b, Colijn & Conners 1972, Golka 1993b, Marcus et al. 1996, Maynard 2003, M.H.E.A. 1989, Nordell 1994, Nordell & Van Heerden 1995, Roberts 1988, 1990, 1997a, 1997b, 1997c, 1998a, Roberts & Wiche 1999, Royal & Craig 2001, Rozentals 1983, Stuart-Dick & Royal 1991, 1992) though

without the analytical depth of (Korzen 1984a, Parbery & Roberts 1986, Roberts 1967, 1969, 1998b, Roberts & Scott 1981).

2.7.3 Method of Roberts

The pioneering work of Parbery & Roberts (1986), Roberts (1967, 1969, 1998b, 2000), Roberts & Arnold (1971), Roberts & Scott (1981) for chutes of rectangular cross-section shall be briefly presented. It should be noted that the work of Parbery & Roberts (1986), Roberts (1998b), Roberts & Arnold (1971) and Roberts & Scott (1981) also consider chutes of circular cross-section, however these are not utilised in industry due to the vastly greater degree of manufacturing expense. Chutes of approximate rectangular cross-section are manufactured using flat plates which are easy to design, draft, fabricate and line, and are thus preferred. Chutes of circular cross-section also need careful consideration regarding maintenance of stable fast flow conditions. Ideally for fast flow conditions, it is desirable that the chute ends at an optimum cut-off angle from the vertical (to be explained in the next section); otherwise a choked-flow condition may result, which would be disastrous for a mining facility, say. Utilisation of such an optimum cut-off angle would mean the material exiting the chute would most probably have a component of velocity in the direction perpendicular to the belt that is undesirable. However this must be tolerated to ensure there is a sufficient chute slope to ensure flow at the specified rate under all conditions and to prevent flow blockages due to material holding-up on the chute bottom or side walls. The reader is referred to the relevant works for the derivations for chutes of circular cross-section.

2.7.3.1 Straight Chutes

Roberts (1998b) describes how for straight inclined chutes, ‘fast’ flow is automatically achieved provided the chute slope is sufficient to permit accelerated flow in the presence of various drag forces. The material will flow with increasing velocity until some terminal velocity is reached. The corresponding stream thickness variation is one which shows a gradual thinning down the chute until steady state constant thickness is reached corresponding to the terminal velocity.

2.7.3.2 Curved Chutes

Ideally, for stable 'fast' flow conditions in a curved profile chute, it is desirable that the chute be terminated at the 'optimum' cutoff angle θ_{co} (Roberts 1998b) illustrated in Figure 2.16 (a). The optimum cutoff angle corresponds to the point of maximum velocity and minimum stream thickness. If the chute continues beyond the optimum cutoff angle, the stream thickness will increase toward the end of the chute, as shown in Figure 2.16 (b). Slow flow modes are usually not desired in industry and were hence not discussed.

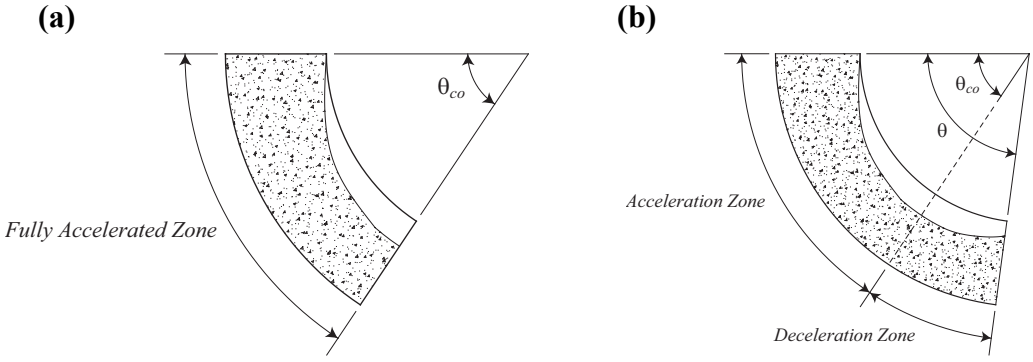

Figure 2.16 Modes of chute flow: **(a)** fast flow, ideal case; **(b)** fast flow, general case (adapted from Roberts 1998b)

It is important that for the maintenance of fast flow the cutoff angle should not be greater than the limiting angle θ_f (Roberts 1998b). This angle depends on the frictional properties of the material on the chute surfaces.

2.7.3.3 Lumped Parameter Model

The lumped parameter model depicted in Figure 2.17 may be used to describe the motion (Roberts 1969).

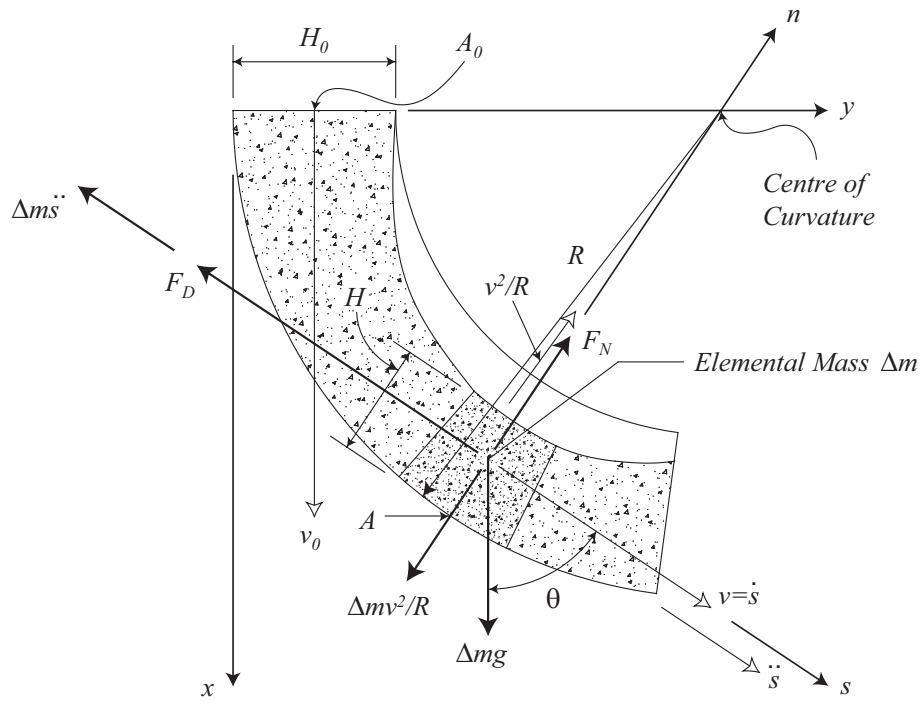

Figure 2.17 Chute flow model (adapted from Parbery & Roberts 1986). The dimensions in the figure have been exaggerated for clarity

The objective in design is to determine an appropriate chute geometry to provide stable flow without the possibility of flow blockages occurring. Certain assumptions can be made to simplify the analysis. If the material is free-flowing and the material stream thickness is small in relation to the radius of curvature of the chute, then it can be assumed that the material behaves as a continuum with a constant mass flow rate throughout the flow. Under these conditions the main factors governing flow are the chute curvature and frictional drag along the internal chute walls. The interactionary effects between particles are considered to be negligible. All equations unless otherwise specified can be utilised for straight chutes also, in addition to those of curved profile.

Referring to Figure 2.17, a moving coordinate system is chosen in this case with tangential '*s*' and normal '*n*' components. With constant curvature chutes commonly used in industry the use of such a coordinate system is particularly relevant. Resolving the forces in the tangential direction, and using:

$$\ddot{s} = v\frac{dv}{ds} \tag{2.91}$$

then the relevant equation of motion becomes:

$$\frac{dv}{ds} = \frac{g}{v}cos\theta - \frac{F_D}{v\Delta m} \tag{2.92}$$

The radius of curvature is given by:

$$R = \frac{\left[1+\left(\frac{dy}{dx}\right)^2\right]^{3/2}}{\left(\frac{d^2y}{dx^2}\right)} \tag{2.93}$$

2.7.3.4 Continuity of Flow

Assuming uniform mass flow, the equation for continuity of flow is (Roberts & Scott 1981):

$$Q_m = \rho Av = constant \tag{2.94}$$

The variation with depth of the bulk density ρ at any section of the flowing stream is small, and it is convenient to assume a constant average value. Then from Eq. (2.94) it follows that:

$$Av = constant \tag{2.95}$$

or

$$Av = A_0 v_0 \tag{2.96}$$

For a given cross-section of the chute, the stream thickness is a function of the area A:

$$H = f(A) \tag{2.97}$$

then from Eq. (2.92) together with Eq. (2.97) the stream thickness variation can be determined.

2.7.3.5 Drag Force

The drag force F_D may be considered to be composed of two components (Roberts & Scott 1981). The first is that due to Coulomb friction, and is given by (Roberts 1998b):

$$F_\mu = \mu_E F_N = \mu_E \left(\frac{v^2}{R} + g \sin\theta \right) \Delta m \tag{2.98}$$

The second is that due to velocity dependent resistance resulting from air drag on the surface of the flowing stream and air permeation through the mass. Assuming viscous drag, which is consistent with the magnitudes of velocities experienced in chute flows (Roberts 1998b), the velocity dependent drag force can be expressed as:

$$F_v = \beta_v v \Delta m \tag{2.99}$$

The overall drag coefficient is thus:

$$F_D = F_\mu + F_v = \left\{ \mu_E \left(\frac{v^2}{R} + g \sin\theta \right) + \beta_v \right\} \Delta m \tag{2.100}$$

2.7.3.6 Equivalent Friction Coefficient

The pressure distribution around the boundaries of a chute of rectangular cross-section is depicted in Figure 2.18.

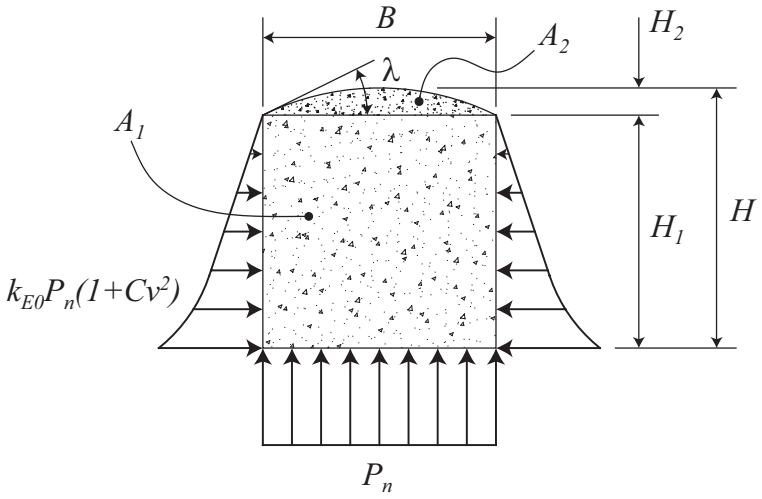

Figure 2.18 Pressure distributions around chute boundary and cross-section of flowing stream (adapted from Roberts & Scott 1981). The dimensions in the figure have been exaggerated for clarity

Referring to Figure 2.18, Roberts & Scott (1981) showed that the equivalent friction coefficient for a chute of rectangular cross-section may be expressed in terms of the height H of the flowing stream, the breadth B of the chute and the velocity v. The expression derived for μ_E is given by (Roberts & Scott 1981):

$$\mu_E = \mu\left[1 + k_{E0}\frac{H}{B}\left(1 + C_s v^2\right)\right] \tag{2.101}$$

Roberts (1998b) presented an alternative form of Eq. (2.101) for cohesive bulk solids. A coefficient k_v is used that relates the lateral to depth pressure:

$$k_v = \frac{1 - \sin\zeta}{1 + \sin\zeta} \tag{2.102}$$

Thus, the expression for μ_E is given by (Roberts 1998b):

$$\mu_E = \mu\left[1 + k_v\frac{H}{B}\right] \tag{2.103}$$

For a chute that converges in the direction of material flow as illustrated in Figure 2.19, the equivalent friction coefficient is given by (Roberts 2004):

$$\mu_E = \mu\left[1 + k_v\left(\frac{H}{B_0 - 2s\tan\alpha}\right)\left(1 + \frac{\tan\alpha}{\mu}\right)\right] \tag{2.104}$$

where k_v is given by Eq. (2.102).

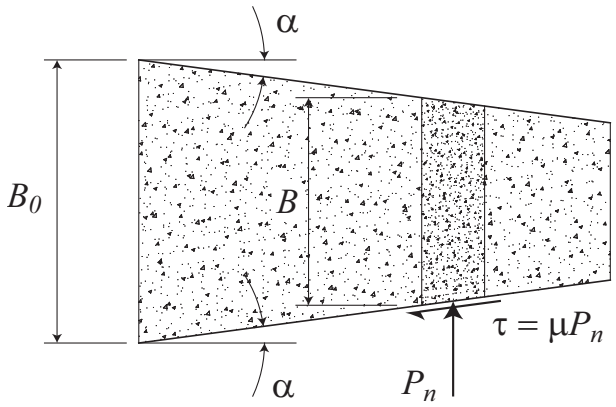

Figure 2.19 Top view of the parameters needed for the design of a converging chute (adapted from Roberts 2004). The parameter $B = B_0 - 2s\tan\alpha$ represents the width of the elemental mass at any distance s from the chute entry.

2.7.3.7 Stream Thickness Variation

Figure 2.18 illustrates the cross-section of the flowing stream through the rectangular chute. Assuming a parabolic surcharge with surcharge angle λ, an expression for the cross-sectional area may be obtained (Roberts & Scott 1981):

$$A = A_1 + A_2 = BH_1 + \frac{B^2\tan\lambda}{\lambda} \tag{2.105}$$

and total stream thickness:

$$H = H_1 + B\tan\lambda \tag{2.106}$$

The surcharge angle λ may be positive or negative depending on whether the surcharge is positive {convex} or negative {concave} (Roberts 1998b). The height of the rectangular portion of the stream cross-section can be calculated from:

$$H_1 = \frac{Q_m}{\rho v B} \tag{2.107}$$

Note that for the assumption of uniform mass flow, the stream thickness varies inversely with velocity (Roberts 1969):

$$\frac{H}{H_0} = \frac{v_0}{v} \tag{2.108}$$

Now, the combination of the computed velocity distribution $v = f(s)$, together with the appropriate equations for A and H enables the following ratio to be determined:

$$\frac{H}{H_0} = f(s) \tag{2.109}$$

For stable 'fast' flow, it is most desirable that $H/H_0 < 1$ and that H/H_0 decreases as s increases.

2.7.3.8 Approximate Closed Form Solutions of Flow Equations

In the case of short length chutes, it can be assumed that μ_E is constant and $F_v = 0$ (Roberts & Scott 1981). The flow is assumed to be fully accelerated. The drag force can be expressed as:

$$F_D = \mu_E \Delta m \left(g \sin\theta + \frac{v^2}{R} \right) \tag{2.110}$$

The generalised flow equation from Eq. (2.92) can thus be expressed as:

$$\frac{dv}{ds} = \frac{g}{v} \cos\theta - \frac{\mu_E}{v} \left(g \sin\theta + \frac{v^2}{R} \right) \tag{2.111}$$

For straight inclined chutes with $R = \infty$, Eq. (2.111) becomes:

$$\frac{dv}{ds} = \frac{g}{v} \left(\cos\theta - \mu_E \sin\theta \right) \tag{2.112}$$

Here θ is constant and represents a particular chute inclination. A closed form solution of the form $s = f(v)$ is readily available for the following case (Roberts 1998b):

$$\mu_E = \mu \left(1 + \frac{C_l}{v} \right) \tag{2.113}$$

for

$$v_0 \geq \frac{\mu C_l \sin\theta}{\left(\cos\theta - \mu \sin\theta \right)} \tag{2.114}$$

where

$$C_l = k_{EO} \frac{v_0 H_0}{B} \tag{2.115}$$

In Eq. (2.115) the value C_l is the inverse velocity Coulomb drag coefficient. Substituting in Eq. (2.111) and solving gives the following expression (Roberts 1969):

$$s = \frac{v^2 - v_0^2}{2E_1} + \frac{E_2}{E_1^2}(v - v_0) + \frac{E_2}{E_1^3} ln\left[\frac{E_1 v - E_2}{E_1 v_0 - E_2}\right] \tag{2.116}$$

where:

$$E_1 = g(cos\,\theta - \mu\, sin\,\theta) \tag{2.117}$$

$$E_2 = \mu g C_l\, sin\,\theta \tag{2.118}$$

The factor E_1 represents the acceleration of a single particle down the chute. Now, assuming μ_E is constant, the acceleration down the straight inclined chute is constant and the velocity distribution is given by (Roberts & Scott 1981):

$$v = \sqrt{v_0^2 + 2gs(cos\,\theta - \mu_E\, sin\,\theta)} \tag{2.119}$$

For the circularly curved chute, assuming μ_E constant and re-writing Eq. (2.111):

$$\frac{d\dot{\theta}}{d\theta} = -\mu_E \dot{\theta} - \frac{g}{R\dot{\theta}}(\mu_E\, sin\,\theta - cos\,\theta) \tag{2.120}$$

Roberts (1969) has shown this equation has the same form as Bernoulli's equation, for which a known solution exists. The solution of Eq. (2.120) noting that $v = R\dot{\theta}$, is (Roberts & Scott 1981):

$$v = \sqrt{\frac{2gR}{4\mu_E^2 + 1}\left[sin\,\theta(1 - 2\mu_E^2) + 3\mu_E\, cos\,\theta\right] + e^{-2\mu_E\theta}\left[v_0^2 - \frac{6\mu_E Rg}{4\mu_E^2 + 1}\right]} \tag{2.121}$$

Using this equation, the velocity at any angle θ around the chute can be determined. For a non-inclined conveyor belt, the aim when designing the chute is to match as closely as possible the horizontal component of the exit velocity to the belt speed.

2.7.4 Method of Korzen

The work of Korzen (1984a) shall also be presented, albeit in compressed form. Korzen's analysis differs from that of Roberts in that a multi-step approximation procedure is used to calculate parameters such as stream thickness and velocity at each point of the chute that requires examination. Korzen also examined trapezoidal cross-sections which are less prone to material blockages though such shapes are not ideal for centrally loading bulk material onto a receiving conveyor belt.

2.7.4.1 Methodology

Korzen (1984a) presented a detailed examination of feed chutes of both rectangular and trapezoidal cross-sections, and was the only other paper in literature to comprehensively analyse U-form or gravity flow chutes. His work examined both straight and curved chutes. A brief overview of Korzen's work for curved chutes is as follows, with the conditions of motion of the stream of bulk material on the chute depicted in Figure 2.20.

Korzen assumes both the mass flow rate through the chute and density to be constant, similar to Roberts' work outlined above. The stream thickness at the start of the chute is based upon the conditions of impact, and can be calculated from (Korzen 1984a):

$$h_0 = \frac{\dot{m}}{\rho v_0 B} \tag{2.122}$$

where the velocity at the start of the flow v_0 is based upon the impact velocity v_i of the falling material stream:

$$v_0 = v_i \sqrt{\frac{A_i}{A_0}\left[cos^2(\theta_i - \varphi) - \mu\, sin^2(\theta_i - \varphi)\right]} \tag{2.123}$$

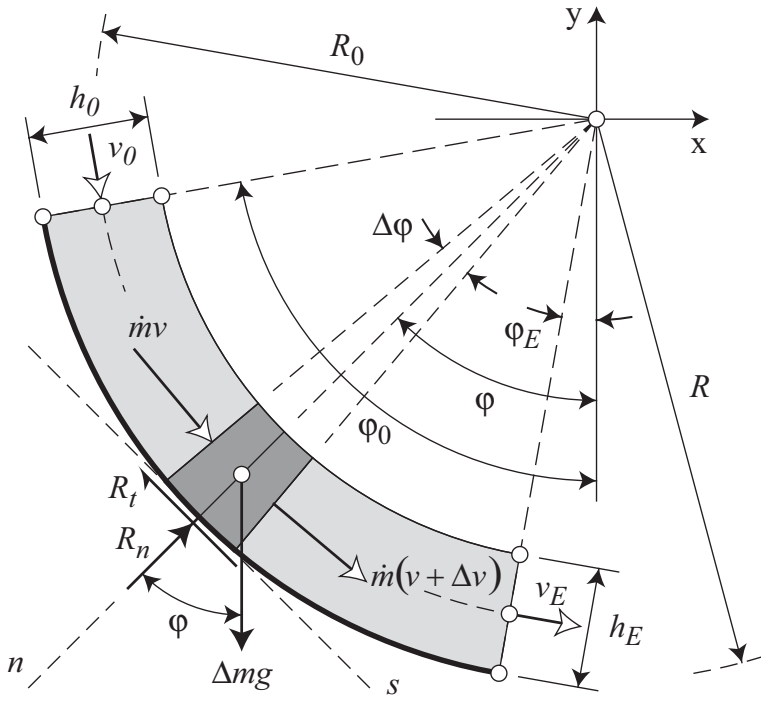

Figure 2.20 Conditions of motion of the stream of bulk material in a curved chute (adapted from Korzen 1984a)

The term A_0 is dependent on h_0, and so a multi-step approximation procedure can be used to calculate its value. For a chute with minimal impact conditions, such as material falling into a curved chute with a horizontal entry point, the velocity v_0 can be assumed to be equal to the velocity of the falling material stream. The velocity at any point through the chute can be represented by the following differential equation (Korzen 1984a):

$$\frac{dv^2}{d\varphi} + f_\varphi v^2 - 2R_\varphi g\left(\sin\varphi - f_\varphi \cos\varphi\right) = 0 \tag{2.124}$$

which is a special case of a Bernoulli differential equation that is not homogenous and non-linear for the variable v^2. The solution of Eq. (2.124) is (Korzen 1984a):

$$v(\varphi)=\sqrt{Ce^{-2f_\varphi\varphi}-2R_\varphi g\sqrt{\frac{1+f_\varphi^2}{1+4f_\varphi^2}}\cos\left[\varphi+\tan^{-1}\left(\frac{f_\varphi}{1+2f_\varphi^2}\right)\right]} \tag{2.125}$$

The integration constant C can be obtained by substituting the boundary conditions below into Eq. (2.125):

$$\varphi=\varphi_0;\ v=v_0;\ R=R_0;\ f_\varphi=f_\varphi(h_0)=f_0 \tag{2.126}$$

thus giving:

$$C=e^{2f_0\varphi_0}\left\{v_0^2+2R_0g\sqrt{\frac{1+f_0^2}{1+4f_0^2}}\cos\left[\varphi_0+\tan^{-1}\left(\frac{f_0}{1+2f_0^2}\right)\right]\right\} \tag{2.127}$$

where:

$$R_0=R-\frac{h_0}{2} \tag{2.128}$$

2.7.4.2 Multi-Step Approximation Procedure

Due to the variability of the parameters R_φ and f_φ as a function of the angle coordinate φ, the velocity $v = v(\varphi)$ can be estimated using a multi-step approximation procedure, as follows. In the first approximation step

$$h_\varphi=h_0;\ R_{\varphi(1)}=R-\frac{h_0}{2}=R_0;\ f_{\varphi(1)}=\mu \tag{2.129}$$

$$v(\varphi)_1=\sqrt{C_1e^{-2\mu\varphi}-2R_0g\sqrt{\frac{1+\mu^2}{1+4\mu^2}}\cos\left[\varphi+\tan^{-1}\left(\frac{\mu}{1+2\mu^2}\right)\right]} \tag{2.130}$$

$$C_1=e^{2\mu\varphi_0}\left\{v_0^2+2R_0g\sqrt{\frac{1+\mu^2}{1+4\mu^2}}\cos\left[\varphi_0+\tan^{-1}\left(\frac{\mu}{1+2\mu^2}\right)\right]\right\} \tag{2.131}$$

For a chute with rectangular cross-section:

$$h_{\varphi(1)} = \frac{A_0 v_0}{B v(\varphi)_1} \tag{2.132}$$

In the second approximation step:

$$R_{\varphi(2)} = R - h_{\varphi(1)};\ f_{\varphi(2)} = f_{\varphi}\left(h_{\varphi}\right) \tag{2.133}$$

$$v(\varphi)_2 = \sqrt{C_2 e^{-2 f_{\varphi(2)}\varphi} - 2R_{\varphi(2)} g \sqrt{\frac{1+f_{\varphi(2)}^2}{1+4f_{\varphi(2)}^2}}\, cos\left[\varphi + tan^{-1}\left(\frac{f_{\varphi(2)}}{1+2f_{\varphi(2)}^2}\right)\right]} \tag{2.134}$$

$$C_2 = C \tag{2.135}$$

$$h_{\varphi(2)} = \frac{A_0 v_0}{B v(\varphi)_2} \tag{2.136}$$

And so on until in the r^{th} approximation step we get:

$$R_{\varphi(r)} = R - h_{\varphi(r-1)};\ f_{\varphi(r)} = f_{\varphi}\left(h_{\varphi(r-1)}\right) \tag{2.137}$$

$$v(\varphi)_r = \sqrt{C_r e^{-2 f_{\varphi(r)}\varphi} - 2R_{\varphi(r)} g \sqrt{\frac{1+f_{\varphi(r)}^2}{1+4f_{\varphi(r)}^2}}\, cos\left[\varphi + tan^{-1}\left(\frac{f_{\varphi(r)}}{1+2f_{\varphi(r)}^2}\right)\right]} \tag{2.138}$$

$$C_r = C \tag{2.139}$$

$$h_{\varphi(r)} = \frac{A_0 v_0}{B v(\varphi)_r} \tag{2.140}$$

The approximation in the k^{th} step (k = 1, 2... r) is sufficient if the following relation is valid:

$$\frac{v(\varphi)_k - v(\varphi)_{k-1}}{v(\varphi)_k} \cdot 100 \le \xi \tag{2.141}$$

where ξ is the tolerated relative deviation for the k^{th} estimation (%).

Both Roberts' and Korzen's work make assumptions regarding material flow limiting the analyses to free-flowing materials. Korzen's work takes time to implement however due to its iterative procedure to calculate the velocity throughout the chute. Roberts' work has been experimentally validated for free flowing materials, and shall hence be used as a reference to which Korzen's work will be compared. Chapter Three describes a comparison between both analytical models.

2.8 Further Comments and Summary

This chapter presented the various techniques available to design chute components. The methods available have been developed primarily for industrial use, hence the lack of analytical complexity. The author's experience has shown the more theory intensive techniques, such as Korzen's (1988) analysis for material impact and flow on the upper chute element and Roberts' work for gravity flow chutes (Parbery & Roberts 1986, Roberts 1967, 1969, 1998b, 2000, Roberts & Arnold 1971, Roberts & Scott 1981), has been neglected as they have been considered too time consuming to implement. These issues will be explored in Chapter Three, as will comparisons between discharge and trajectory prediction methods, the impact and flow methods for impact plates, and the U-form gravity chute flow analysis described here, all for random sets of parameters.

Chapter Three

CHUTE DESIGN TECHNIQUE COMPARISONS

3.1 Introduction

This chapter shall present comparisons between design techniques for certain chute components identified in Chapter Two. The three primary areas to consider are the material trajectory, material impact and flow around the upper chute element, and material impact and flow around the lower chute element. As certain derivations have been experimentally validated, these will be used as a reference point in determining the ideal design method for the chute component. Air entrainment issues will not be examined, as the area is complex in nature and can embody an individual piece of research in itself, and it is also not a factor for relatively small drop heights when using coarse bulk material.

3.2 Material Discharge and Trajectories

3.2.1 Overview of Trajectory Design Methods

The eleven trajectory prediction models presented in Chapter Two are readily available in published work. The most comprehensive technique available in the literature was that described by Korzen (1989), which was the only model available that used the concept of adhesion and inertia of the material on the belt and allowance was made for the variation in static and kinematic friction. Booth (1934) included the effects of friction between the particle and the belt, but did not include adhesive effects in the analysis. These two techniques require iterative procedures to obtain results. Similar to Booth, Dunlop (1982) used the concept of friction acting between the material and the belt. The work of Golka (1993a), Goodyear (1976), the C.E.M.A. (1997) and two M.H.E.A. (1986, 1989) guides, and the manuals of BTR (n.d.), BF Goodrich (n.d.) and S-A 66 (n.d.) all essentially only use the concept of centripetal acceleration in their

work, however these are relatively straightforward to implement and use, hence their popularity in industry. If friction and/or adhesive effects are prominent between the material and conveyor belt they will have an influence on the discharge process and associated trajectory, so the method to use must be carefully chosen.

The discharge angle, or separation angle of the material stream with the belt (α_d) can be determined in a number of ways, as outlined for each method from Section 2.4.3 to Section 2.4.13 in Chapter Two, and is plotted in Figure 3.1 for a range of belt velocities. There is a difference of up to 27 degrees at the very slow belt velocities between the methods of Booth and Dunlop compared to those of Golka, M.H.E.A. (1986), Goodyear and C.E.M.A., with a greater difference if Korzen's method is considered. There is a difference of up to 10 degrees if the comprehensive work of Korzen, Booth and Dunlop is compared to the second M.H.E.A. (1989) guide which uses a modified discharge formula. The differences will shortly be highlighted with a comparison for high and slow-speed conveying conditions between these major published prediction methods, however a few brief comments must be made.

At first glance it would seem that the methods of Korzen, Booth and Dunlop are superior to those of Golka (1993a), Goodyear (1976), the C.E.M.A. (1997) and two M.H.E.A. (1986, 1989) guides, and the manuals of BTR (n.d.), BF Goodrich (n.d.) and S-A 66 (n.d.). Some of these techniques however, such as the C.E.M.A. and M.H.E.A. guides have superior elements in their derivations of the discharge process compared to Korzen, Booth or Dunlop. These include material centre of mass calculations and determination of the cross-sectional area of the material stream, which are derived from the conveyor geometry rather than the conveying material's properties and was explored in Section 2.4.2 in Chapter Two.

Arnold & Hill (1989, 1990a, 1990b, 1991a, 1991b, 1991c) and Arnold (1993) also made comparisons and recommendations regarding a number of the methods described here. However many of the techniques described here such as Golka (1993a), Goodyear (1976), BTR (n.d.), BF Goodrich (n.d.) and S-A 66 (n.d.) were not featured, and the actual specifics of the comparisons (e.g. type of software used, experimental data to plot relevant figures) were not sufficiently detailed. The next few sections will describe the comparisons made between trajectory prediction methods.

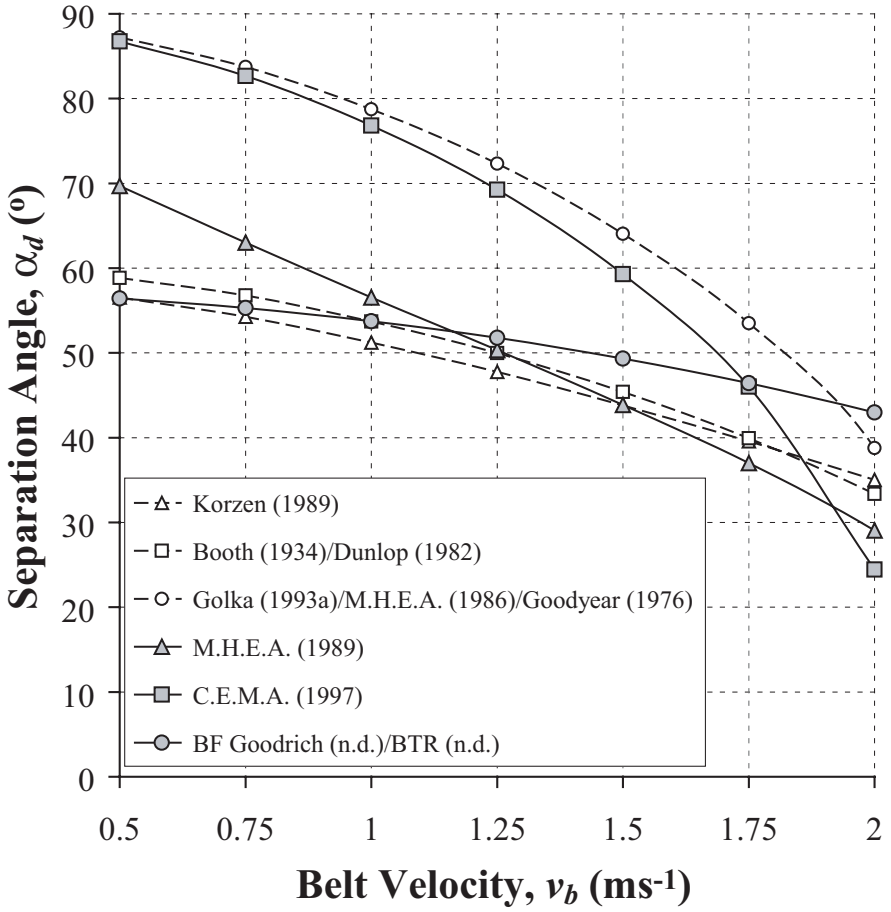

Figure 3.1 Separation angle α_d vs. Belt Velocity v_b for the major discharge prediction techniques. Parameters used include mass flow rate ($\dot{m}$): 768 kgs^{-1}; bulk Density (ρ): 900 kgm^{-3}; adhesive stress (σ_a): 0.11 kPa; wall friction angle (ϕ_w): 25 degrees; pulley radius (R): 0.5 m; belt thickness (b_t): 0.025 m; belt width (b): 1.5 m; inclination angle (α_b): 0 degrees; idlers @ (β_i): 30 degrees; surcharge angle (θ): 20 degrees; and proportionality constant (K): 1.25

3.2.2 Spreadsheet Setup

There are various permutations of conveying conditions in industry, and naturally all cannot be explored. Therefore for the trajectory comparisons the material parameters and major conveyor attributes have been left identical throughout the simulations, with only the belt speed conditions varied to facilitate a noticeable difference between the high and slow-speed conditions. The simulations were conducted at belt velocities (v_b)

of 6 ms^{-1} and at 1 ms^{-1}, satisfying both the high and slow-speed conditions respectively of each particular method and also the comprehensive technique of Korzen (1989) shown in Equations (2.1) and (2.2). The author's industrial experience has shown these to be common conveying velocities used in industry. Other than the belt velocity, identical parameters and material properties were used to plot trajectories for both high and slow-speed conditions including the mass flow rate ($\dot{m}$): 768 kgs^{-1}; bulk density (ρ): 900 kgm^{-3}; adhesive stress (σ_a): 0.11 kPa; wall friction angle (ϕ_w): 25 degrees; pulley radius (R): 0.5 m; belt thickness (b_t): 0.025 m; belt width (b): 1.5 m; inclination angle (α_b): 0 degrees; idler inclinations (β_i): 30 degrees; surcharge angle (θ): 20 degrees; and proportionality constant (K): 1.25.

Microsoft® Excel was used to plot the upper and lower limits of the relevant trajectories, one advantage being that the more complicated prediction methods available requiring iterative procedures (for example Korzen's (1989) work) could be modelled with ease. As described for all methods, the material was assumed to traject at the point of tangency between the belt and head pulley for high-speed conditions. For slow-speed belts, the material wraps around the head pulley to some extent before discharging. The wrap angles and discharge velocities corresponding to this were calculated using the discharge calculation techniques outlined by each of the relevant methods. For the slow-speed condition the angle of trajection from the vertical for the S-A 66 S-A 66 (n.d.) method was calculated within a separate spreadsheet.

To accurately compare the various methods available of calculating the trajectory in the literature, adjustments needed to be made to the way in which certain methods plotted the material stream path. The methods of Booth (1934), Dunlop (1982), M.H.E.A. (1989), C.E.M.A. (1997), BTR (n.d.), and S-A 66 (n.d.) only presented the lower limit of the trajectory, while Goodyear (1976) presented the trajectory of the material stream centre line. For high-speed belt conditions, the discharge velocity was assumed to be equal to the belt speed as defined by Arnold & Hill (1991b). Hence, for the techniques where only the inner edge of the material stream was presented, the outer limit of the stream was plotted parallel to the inner limit of the stream. For the technique that only presented the centre line of the material stream, the inner and outer limits were plotted parallel to the material stream centre line. For the case of slow-speed belts, the inner and

outer limits of the trajectory were plotted using the technique described by Arnold & Hill (1991b). Obviously, no adjustments were needed for those methods that provided techniques of plotting both the outer and inner material stream trajectories.

For the comparisons a horizontal conveyor belt ($\alpha_b = 0$) with a 3 idler system is used, with the outside idler inclinations at 30^o and a surcharge angle of 20^o. Note that factors such as the transition correction angle and edge material correction angle have not been considered in the trajectory calculations. Air drag has also not been considered. These factors have been discussed in detail in the works of Arnold & Hill (1991b) and Powell (1995).

Using suggestions outlined by Arnold & Hill (1989, 1990b), a 'Hybrid' trajectory prediction method was also developed and plotted. They stated that the best material trajectory prediction results when the C.E.M.A. guide and Booth or Dunlop methods are combined. For high-speed conditions the inner edge of the trajectory is determined by the Booth/Dunlop method for and the outer edge of the trajectory is drawn parallel to the inner edge. For slow-speed conditions the inner edge of the trajectory is also determined by the Booth/Dunlop method however the outer edge of the trajectory is drawn at the velocity of the centre of mass to give a slightly divergent material stream. For adhesive material, the magnitude of the adhesive stress and friction coefficient value should be determined by testing and Korzen's (1989) method used instead. Based upon these conclusions, the discharge and trajectory calculations were calculated using Korzen's (1989) iterative technique and the material stream cross-section and material height calculations prior to discharge were determined from the work of Powell (1995). Arnold & Hill (1991b) confirmed the closeness of the upper and lower limit approximations given by this combination for high and slow-speed conditions with full scale experiments. Therefore all other trajectories will be compared to those generated by the Hybrid method.

3.2.3 Comparisons for High–Speed Conveying Conditions

A plot showing the comparison between the trajectories produced by the various methods for high-speed belt conditions is shown in Figure 3.2. A number of the trajectory prediction methods yield identical paths in the high-speed domain, and these

were grouped together in the plots for clarity. The results were denoted Method H1 to Method H5. Method H1 represents the methods of Korzen (1989), Booth (1934), Dunlop (1982), Goodyear (1976), S-A 66 (n.d.), BF Goodrich (n.d.) and BTR (n.d.); Method H2 represents Golka (1993a); Method H3 represents M.H.E.A. (1989); Method H4 represents the C.E.M.A. (1997) and M.H.E.A. (1986); and Method H5 represents the Hybrid.

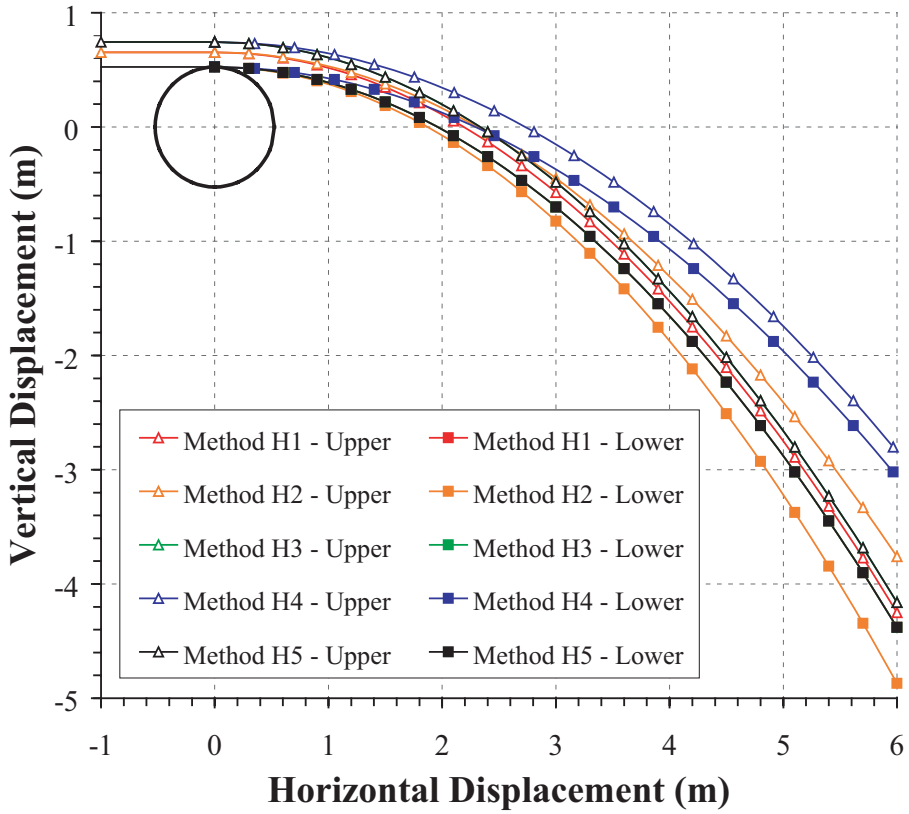

Figure 3.2 Trajectories generated by the various methods at $v_b = 6$ ms^{-1}

The differences between the prediction methods are not so apparent for the high-speed case. C.E.M.A./M.H.E.A. (1986) trajects further than all other trajectories. Golka's upper and lower trajectory paths diverge while all other techniques give converging upper and lower limits, or at the very least parallel for high-speed belts, however the approximate centre line of the predicted trajectory follows that of Korzen/Booth/Dunlop/Goodyear, S-A 66, BF Goodrich and BTR. Note that in Figure

3.2 the lower limit of the Korzen trajectory path is identical to that of Hybrid, and the M.H.E.A. (1989) and Hybrid trajectories are identical.

Burnett (2000a, 2000b) suggests the use of the C.E.M.A. (1997) and M.H.E.A. (1986) guides to predict the material trajectory path. However both of these guides recommend that the material's velocity be calculated from its centre of mass position, which leads to the excessive throw of the material stream shown in Figure 3.2. This phenomenon has been identified by others (Arnold & Hill 1990a, 1991a, Arnold 1993). Experiments performed by Arnold & Hill (1991b) on high-speed belts showed this was not the case though, and the trajectories should be calculated based on the belt velocity. The latter work published by the M.H.E.A. (1989) corrected this problem as shown in Figure 3.2.

Another aspect of interest is the material height upon the belt prior to discharge, which is significantly greater in the M.H.E.A. and C.E.M.A. trajectories than those that utilized the theory of the Korzen or Golka methods. This is due to the M.H.E.A. and C.E.M.A. guides providing a superior method of calculating the material height than the other techniques, specifically those of Korzen and Golka. This has also been identified by a number of sources (Arnold & Hill 1991b).

When using an impact plate in high-speed belt conditions the minor differences between the techniques in predicting the material trajectory is not critical. It is clear from Figure 3.2 that with an impact plate or a chute wall only located a metre or two from the discharge pulley, any trajectory differences are of small magnitude and hence the method to choose is at the user's discretion. Therefore taking into consideration the material height calculation techniques used by each method for high-speed belts, and the ease of implementing the discharge equations, the recommended technique for plotting the trajectory is to use the M.H.E.A. (1989) guide. Even if adhesive forces are present, Korzen's (1989) technique assumes these to play no part for high speed conditions.

3.2.4 Comparisons for Slow–Speed Conveying Conditions

Plots showing the comparison between the trajectories produced by the various methods for slow-speed belt conditions are shown in Figure 3.3, Figure 3.4 and Figure 3.5. Three

separate figures have been used for reasons of clarity. As for the high-speed comparisons, the techniques that have identical trajectories have been grouped together for clarity. Method S1 represents the method of Korzen (1989); Method S2 represents Booth (1934) and Dunlop (1982); Method S3 represents Golka (1993a); Method S4 represents the M.H.E.A. (1989); Method S5 represents the C.E.M.A. (1997); Method S6 represents the earlier M.H.E.A. (1986); Method S7 represents Goodyear (1976); Method S8 represents BFGoodrich (n.d.) and BTR (n.d.); Method S9 represents S-A 66 (n.d.); and Method S10 represents the Hybrid.

It can be clearly seen that the trajectories predicted by each of the methods at slow-speed conveying conditions have a greater variance than those at high-speed due mostly to the differing separation angles (α_d) calculated. The trajectory that results from the method of Golka diverges, or fans, the most. The lower limit of Booth/Dunlop trajects further than either Korzen or Hybrid, due to the lack of an adhesive component. The method of Korzen has an unrealistically thick material stream due to a large material

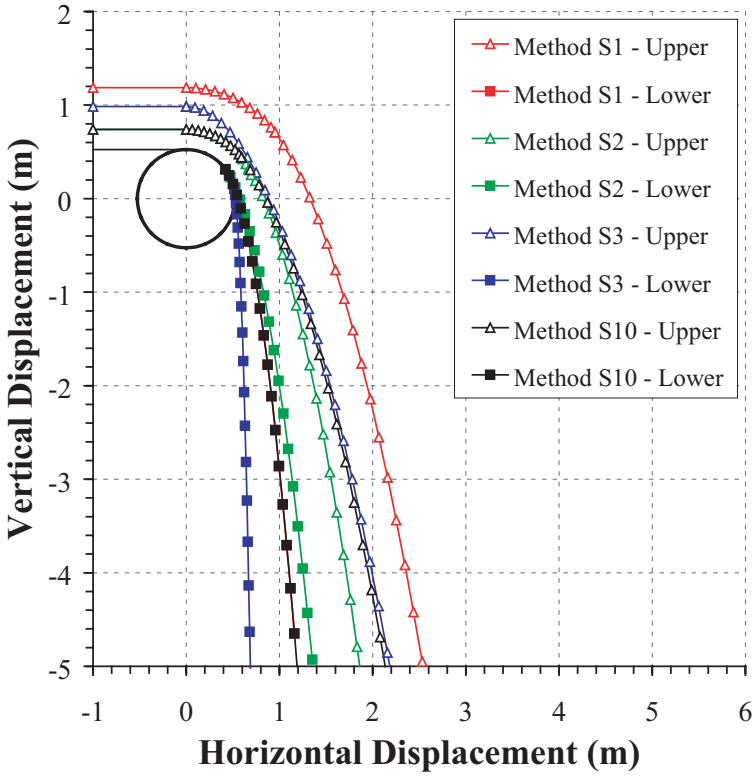

Figure 3.3 Trajectories generated by methods S1, S2, S3 and S10 at $v_b = 1$ ms^{-1}

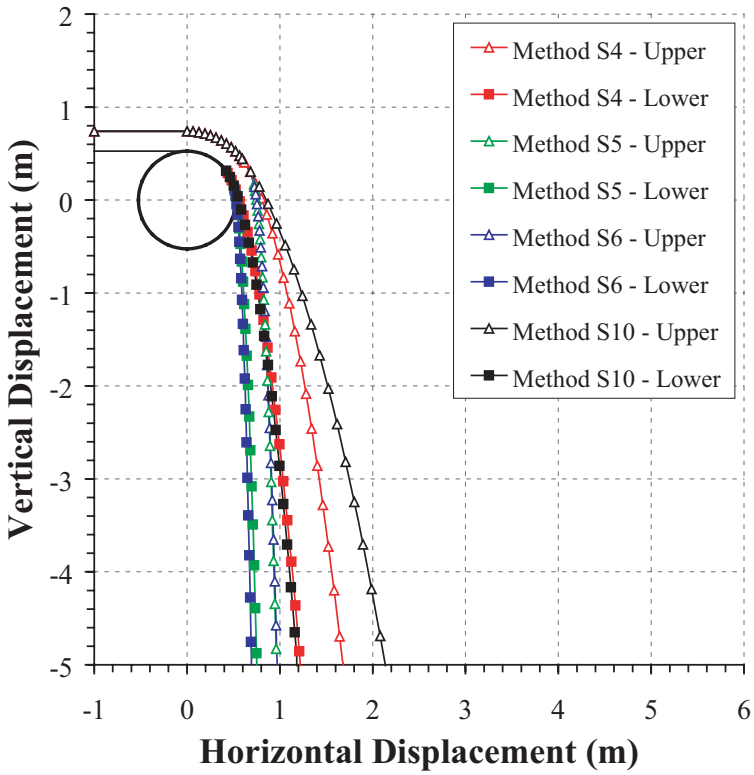

Figure 3.4 Trajectories generated by methods S4, S5, S6, and S10 at $v_b = 1$ ms^{-1}

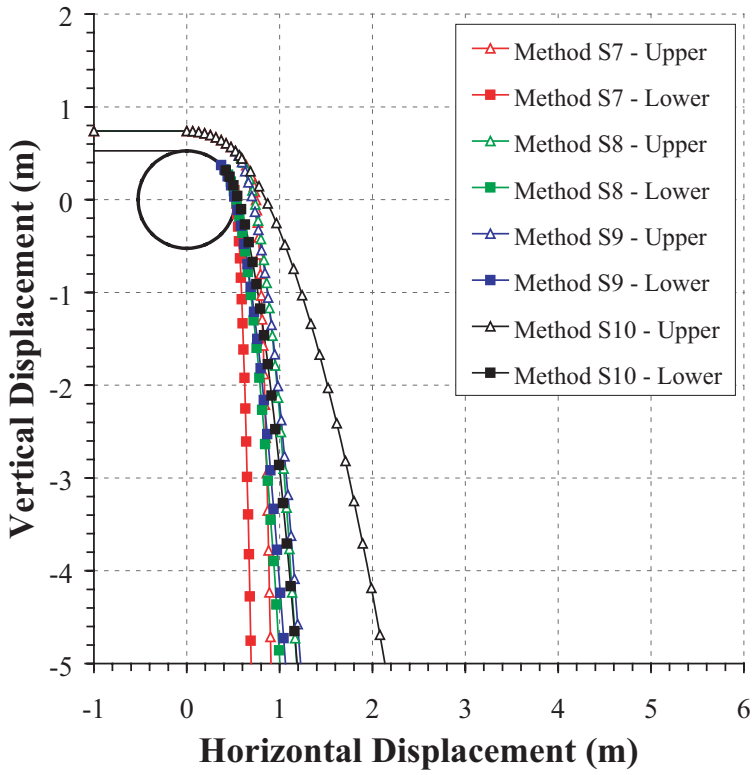

Figure 3.5 Trajectories generated by methods S7, S8, S9 and S10 at $v_b = 1$ ms^{-1}

burden height. M.H.E.A. (1989) predicts a trajectory stream that is narrow compared to that of the Hybrid. C.E.M.A. predicts the upper and lower trajectory limits to be relatively parallel. M.H.E.A. (1986) provides a trajectory prediction where the upper limit is close to that of C.E.M.A., and the lower limit trajects a little less than C.E.M.A. Goodyear, BF Goodrich, BTR, and S-A 66 all provide predictions whose upper and lower limits flow vertically downwards. Note that in Figure 3.3 the lower limit of the Korzen trajectory path is identical to that of Hybrid.

If the upper transfer chute element is designed using a trajectory that predicts the material throw to be less than it actually is, serious problems will occur, including possible blockages, spillage, excessive impact wear, abrasive wear, significant dust generation, and noise pollution. If the chute element is designed using a trajectory that predicts the material throw to be greater than it actually is, the material stream may not even come in contact with the chute but rather free fall onto the lower chute element and receiving belt, causing problems such as spillage, impact wear, dust generation, and posing significant safety concerns. There is also the added cost of having wasted resources on designing and fabricating an upper chute element that is ineffectual. The problems mentioned are exacerbated if complex angled transfers are utilised in the conveying system, or a passive dust suppression system that depends upon an accurate chute design is considered.

The Korzen (1989) method trajects the material at a slightly greater discharge angle (measured from the vertical) relative to that of the Booth (1934) and Dunlop (1982) combined trajectory, due to the adhesive stress component used in its calculations. The material height calculation of Korzen is significantly high and obviously incorrect, illustrating the deficiency of calculating burden height using material properties rather than conveyor geometry. In the Golka (1993a) upper and lower trajectory paths, the material stream fans more than any of the other prediction techniques described. The divergent coefficients described by Golka in the calculations contribute to plotting the material trajectory but techniques for determining these were not described in his work. The value used for each coefficient was identical to that used in Golka's papers. If the divergent coefficients were calculated correctly for the particular situation used in Figure 3.3, perhaps the trajectories would have been consistent with those remaining. It can be observed that Golka's technique of calculating material height is also incorrect.

Figure 3.5 illustrates that the methods of Goodyear (1976), S-A 66 (n.d.), BF Goodrich (n.d.) and BTR (n.d.) provide trajectories that do not correlate well with those of Korzen or Booth/Dunlop and are hence assumed to be inaccurate. The upper and lower limits generated by all these techniques have too great a discharge angle and as a result fall almost vertically down.

Burnett (2000a, 2000b) again suggests the use of the M.H.E.A. (1986) and C.E.M.A. (1997) guides to predict the material trajectory path. Using these techniques would result in a predicted trajectory that is less than it would actually go, and also little material spread or fanning of the material compared to the work of Korzen, Booth or Dunlop which could lead to difficulties and expense if unplanned impingements occur. This is evident from Figure 3.4. This has been identified by Arnold & Hill (1990a, 1991a) and Arnold (1993), and confirmed from full scale experiments by Arnold & Hill (1991b). The later work by the M.H.E.A. (1989) provides a trajectory more consistent with that of Korzen, Booth and Dunlop for the parameters used, however the degree of fanning is reduced due to its different upper limit velocity allocation. Further discrepancies may result for a different set of parameters, particularly for a combination of very slow belt speed (see Figure 3.1) and adhesive forces present. Arnold & Hill (1989) have shown using computer modelling that methods relying on the physical interaction between the belt and material such as Korzen's and Booth's (and hence the Dunlop manual) predict better trajectories at slow speed conditions than those that model the material discharge as a case of projectile motion of the material from the belt. This has also been confirmed by Arnold & Hill (1991a, 1991b) and Arnold (1993). Hence the M.H.E.A. guide may predict inaccurate trajectories for sticky or cohesive materials.

3.2.5 Material Discharge and Trajectory Summary

A comparison was just described between the major methods available to predict material trajectories off belt conveyor head pulleys. Methods that required multi-step approximation procedures such as Korzen (1989) were difficult to implement without the use of computers, so a commercial spreadsheet package was used to calculate and plot the various trajectories. It was found that the existing modelling techniques that are independent of adhesive or slippage aspects are optimal for a selected range of conveyor

belt speeds, with great differences occurring at very slow belt speeds. These methods are however simpler to implement rendering them attractive for industry purposes. The so-called Hybrid method has been identified in literature as providing the most accurate prediction, and is therefore considered the ideal method to use.

3.3 Material Impact and Flow – Upper Chute Element

3.3.1 Spreadsheet Setup

For the two works found in the literature that examined impingement upon flat plates, Korzen (1988) and Arnold & Hill (1991b), the parameters and material properties used above for the trajectory prediction off high-speed belt conveyors were used as the initial conditions for the impact plate trajectory predictions. The works of Arnold & Hill (1991b) and Roberts (2001) were the only literature found examining curve plates with similar initial conditions. Only the approximate centre line velocity of the material stream was used due to the complicated nature of plotting the inner and outer limits of the material stream during the impact process. The exit velocity from both the flat and curved impact plates was estimated using the procedure outlined in the work of Arnold & Hill Arnold & Hill (1991b). Korzen's work for cohesive and non-cohesive material impact required an iterative procedure to solve, and hence Microsoft® Excel was used to create a spreadsheet to allow successive approximation steps to be simply applied. Roberts did not examine material impact aspects but rather a method of analysing the velocity profile around a curved impact plate, therefore the material stream path is identical to that of Arnold & Hill (1991b) until the end of the impact plate where the different exit velocities take effect. Non-dimensional velocities were used so that differences between the methods were clear. The non-dimensional velocities are simply the stream velocity divided by the initial discharge velocity v_d.

The parameters used for analysis of the flat impact plate were the belt velocity (v_b): 6 ms-1; discharge angle (α_d): 0 degrees; horizontal distance to impact plate (D) {flate, curved}: 0.9, 0.8 m; plate inclination angle (β) {flat}: 12 degrees; plate length (S_p) {flat, curved}: 1.4, 0.9 m; impact plate radius (R_p) {curved}: 0.6 m; angle of plate-end tangent (λ_{bottom}) {curved}: 4 degrees; coefficient of wall friction (μ): 0.5; and equivalent

coefficient of friction (μ_E) {curved}: 0.4. All other relevant parameters were identical to those used for the high-speed trajectory comparisons.

3.3.2 Comparisons for Impact upon a Flat Plate

A plot showing the comparison between the material stream paths and non-dimensional velocities produced by the Korzen (1988) and Arnold & Hill (1991b) methods for material impinging on a flat impact plate is shown in Figure 3.6. For the analysis of flat plate impacts, 'Stream Path 1' and 'Non-Dimensional Velocity 1' corresponds to Korzen (1988) cohesive model; 'Stream Path 2' and 'Non-Dimensional Velocity 2' corresponds to Korzen (1988) non-cohesive model; and 'Stream Path 3' and 'Non-Dimensional Velocity 3' corresponds to Arnold & Hill (1991b) non-cohesive model.

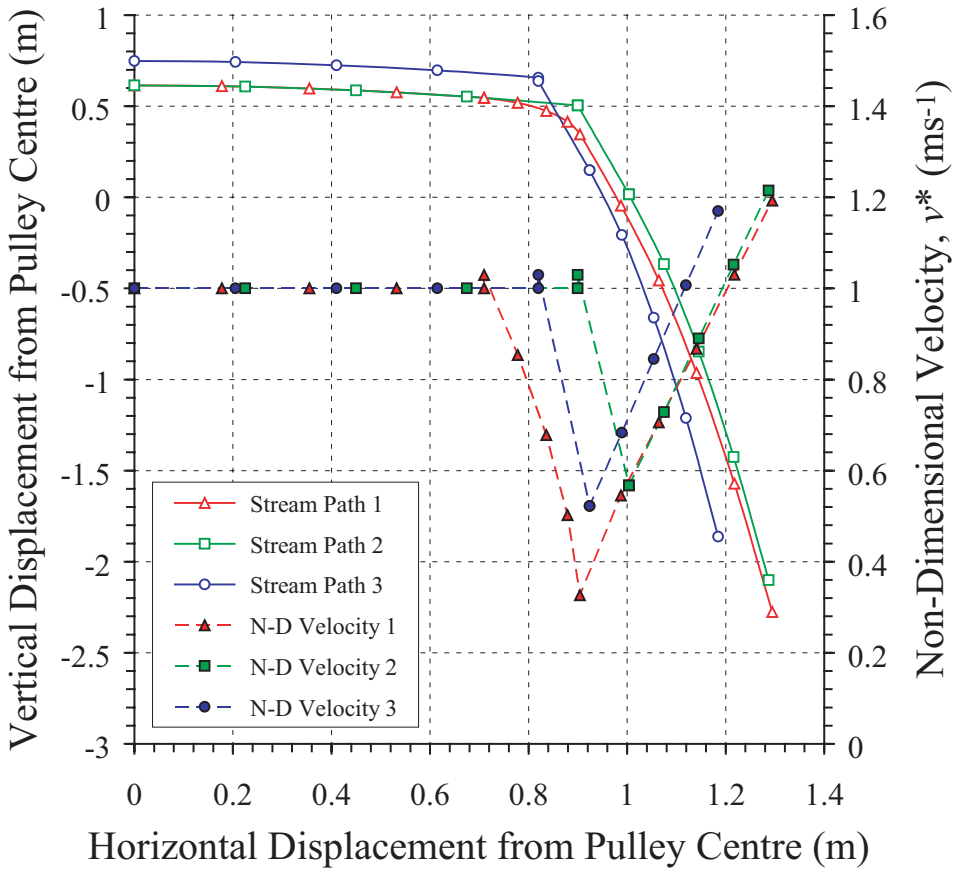

Figure 3.6 Analysis of material impact upon flat plate

In Figure 3.6 the material stream centre line paths for the Korzen cohesive and non-cohesive models follow approximately the same path, with the major differences being the existence of the flow-round zone in the cohesive model, and the reduced trajection of the cohesive model from the end of the impact plate due to the velocity at the flow-round zone exit being less than the equivalent term for the non-cohesive model.

The approximation given by Arnold & Hill for the non-cohesive model yields a centerline trajectory path that is higher than that given by Korzen in the section before it strikes the impact plate, and also seems to traject less than the Korzen cohesive and non-cohesive models. What must be considered though is that these differences are the result (for the most part) of the different height calculations used. This results in the Arnold & Hill non-cohesive approximation having a thicker flow of material than that of Korzen. For high material drops this could become significant depending on whether a floor 'rock box' type or load-out plate arrangement was used, or a 'Spoon' or U-form transfer chute was used. For the latter, the trajectory prediction is important for optimal placement.

The non-dimensional velocities all show similar trends in Figure 3.6. Generally there is a constant velocity until impact, where the velocity dramatically reduces (though there is a slight curvature to the cohesive model). It then linearly increases until the end of the impact plate where the velocity increases further during material free fall. It can be observed that the influence of friction in the sliding flow region does not greatly affect the velocity. The cohesive model experienced the greatest velocity loss during the impact process. Comparing the stream paths and non-dimensional velocities of the non-cohesive models of Korzen and Arnold & Hill reveals the Arnold & Hill approximation to give good results, and hence provide a quicker solution than the lengthy iterative technique of Korzen.

The experimental work conducted by Arnold & Hill (1991b) showed that the analytical work of Korzen (1988) regarding impact on flat plates gave close approximations for the exit velocities. If the material drop height is not too great, Arnold & Hill's method is more practical as its calculation time is quicker than Korzen's.

3.3.3 Comparisons for Impact upon a Curved Plate

A plot showing the comparison between the material stream paths and non-dimensional velocities produced by the Arnold & Hill (1991b) and Roberts (2001) methods for material impinging on a curved impact plate is shown in Figure 3.7. For the analysis of curved plate impacts 'Stream Path 1' and 'Non-Dimensional Velocity 1' corresponds to Arnold & Hill (1991b) without corrected angle of entry; 'Stream Path 2' and 'Non-Dimensional Velocity 2' corresponds to Arnold & Hill (1991b) with corrected angle of entry; and 'Stream Path 3' and 'Non-Dimensional Velocity 3' corresponds to Roberts (2001)

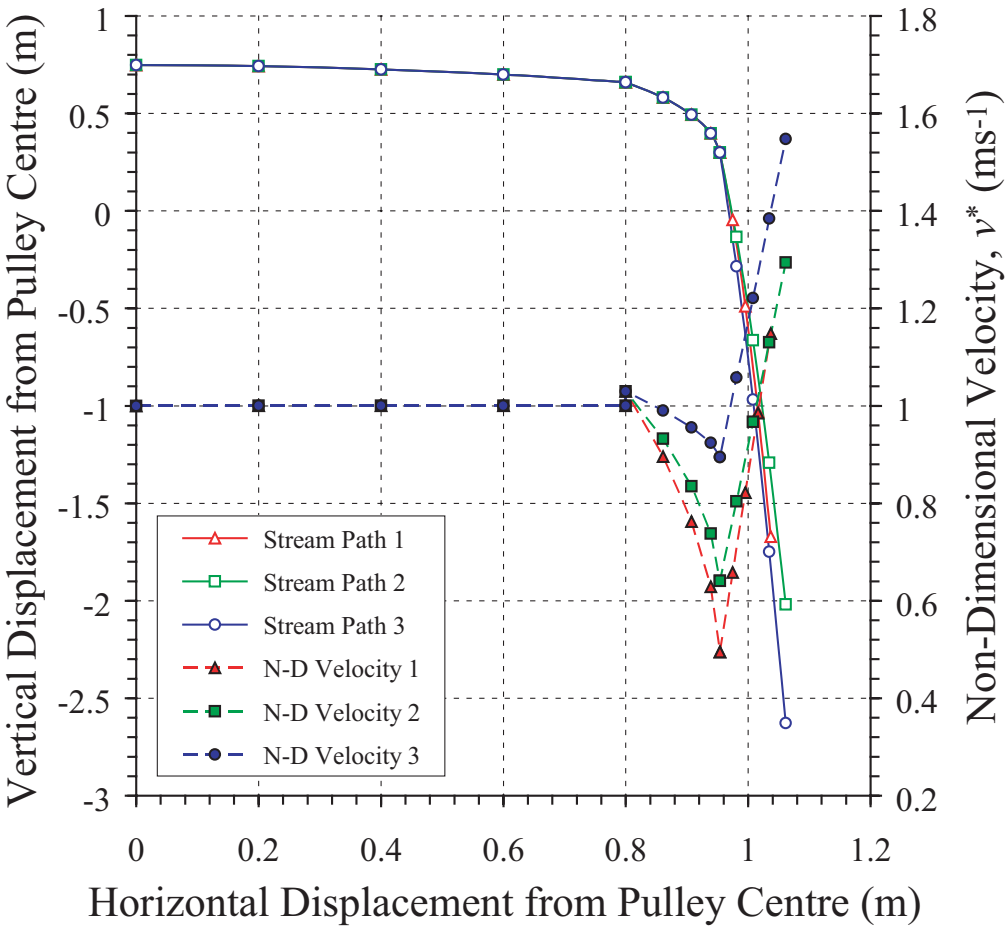

Figure 3.7 Analysis of material impact upon curved plate

In Figure 3.7 the first stream path (Arnold & Hill 1991b) was based on the material impacting upon the curved plate using the given impact angle. The second stream path (Arnold & Hill 1991b) used a corrected angle of entry, where the entry vector for the material stream was assumed to be tangential to the impact point. The final stream path (Roberts 2001) is identical to that of the first stream path until the end of the impact plate. Referring to the method of Arnold & Hill (1991b), the corrected angle of entry does not contribute to the stream path rather it influences the magnitude of the exit velocity of the material stream from the plate. Similarly, the stream path of Roberts (2001) utilises a different theory yet the stream path is assumed to be the same, however the velocity magnitude is greater than that of Arnold & Hill, which can be inferred from the non-dimensional velocity.

Referring to Figure 3.7 all the velocities follow a general pattern. There is a constant velocity until the impact with the curved plate where a slight jump occurs in the velocity magnitudes and then there is a gradual reduction in velocity until the end of the plate is reached, where there is a linear increase in velocity magnitude resulting from material free fall. This is in contrast to the situation for the flat plates, where the velocity increases as the material slides along the plate. It is noticeable that the method of Roberts (2001) experiences less deceleration and hence starts with the greatest plate exit velocity. The sudden jump in velocity at the point of impact arises from an equation inequality in the method of Arnold & Hill (1991b) where the velocity magnitude resulting from well known parabolic motion equations does not equal the velocity magnitude before impact given by Arnold & Hill. The magnitude of this velocity jump is minor however.

Figure 3.7 illustrates that the second technique of Arnold & Hill (1991b) which uses the corrected angle produces a trajectory that has greater velocity around the curved plate to that using the ordinary impact angle. Roberts (2001) technique produces an even higher velocity. Though the issue is not explored in the current work, the greater velocities indicate that the rate of abrasive wear on the curved plate will also increase.

The experimental work conducted by Arnold & Hill (1991b) revealed that the equations derived for the curved plates only gave an approximate value for the bulk material velocity after impact. This could possibly be due to the use of the Korzen (1988)

cohesive model being used as its basis. The radius of a curved deflector is larger than that of the flow-round zone found in cohesive impact upon a flat plate, and hence realistically the material should increase in velocity as it flows around the curved plate. This is especially critical when considering that Arnold & Hill identified that the use of curved impact plates allowed the bulk material's momentum to be maintained, resulting in less spread, degradation and dust emissions, making the use of curved impact plates more effective than flat plates in the same situation. Roberts' (2001) work was experimentally validated for U-form or gravity flow chutes, and is hence assumed to provide a closer approximation for predicting velocity profiles for the curved upper chute element.

3.3.4 Material Impact and Flow Summary – Upper Chute Element

The stream paths and velocities throughout the impact and flow process for flat and curved plates have just been described. The review indicates that models must be developed that examine the complex flow mechanisms occurring in during the material impact process, particularly for curved chutes. As the material flows through a transfer point, each element depends upon the one prior to provide a reasonable approximation. In this case, if the impact plate is not designed or installed correctly, all material flow operations in the transfer after it could suffer serious problems. Particular attention must be paid to stream impingement upon curved impact plates. The work performed by Benjamin (1999, 2001), Benjamin & Nemeth (2001) and Benjamin et al (1999a, 1999b) in their three-dimensional curved 'Hood-Spoon' arrangements and the on-site work of McBride (2000) described the advantages of using a curved plate however analytical processes were not detailed. In summary, the approximations for flat plates are best described by Korzen's (1988) work and for curved plates by Roberts' (2001) work.

3.4 Material Impact and Flow – Lower Chute Element

3.4.1 Material Impact Overview

Only two works in the literature were found that examined the outcomes generated by impact processes on the lower chute element: the work of Stuart-Dick & Royal (1991,

1992), and that of Roberts (2004). Figure 3.8 shows a family of curves of v_3^* / v_4^* for values of θ as a function of ϕ. The ratio v_3^* / v_4^* was obtained by dividing Equation (2.89) and Equation (2.90) in Chapter Two. Referring to this, Stuart-Dick & Royal have illustrated the advantage in terms of maintaining velocity of a stepped deflector over a single deflector. Extending this argument, they have shown that a curved deflector will slow down a material stream the least, and the larger the radius of curvature, the better the stream's velocity will be maintained. This illustrates the advantage of curved profile upper and lower chute elements. Note that Roberts equation for a single deflector type arrangement was considered using ε = 0 i.e. no rebound occurring. These analyses however do not examine the flow processes of an impacting stream of material, and it is clear that comprehensive analysis similar to that developed by Korzen (1988) for material impacting upon a flat plate is required.

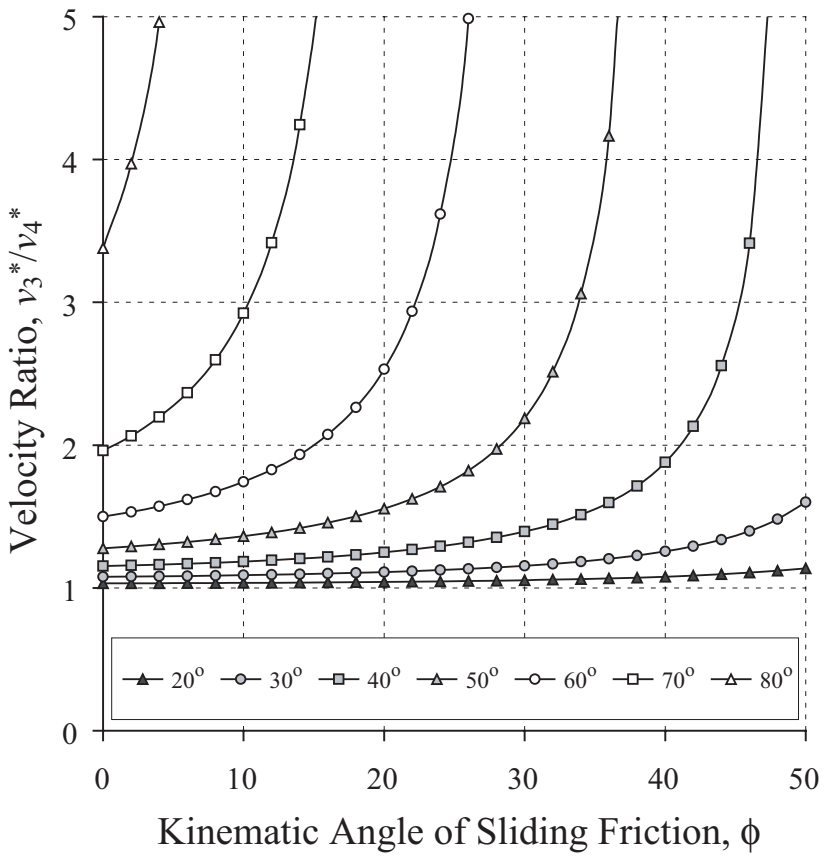

Figure 3.8 Ratio between particle velocity after impacting two half angles to particle velocity after one impact (adapted from Stuart-Dick & Royal 1991, 1992)

3.4.2 Gravity Flow Chute Comparisons

The two comprehensive analytical methods developed by Roberts (developed over time in the work of Parbery & Roberts 1986, Roberts 1967, 1969, 1998b, 2000, Roberts & Arnold 1971, Roberts & Scott 1981) and Korzen (1984a) for curved chutes with rectangular cross-section were firstly examined individually. The author attempted to mimic the results presented by each author in their respective papers, and found that all efforts to try and replicate results published by Roberts in his papers were met with success. This is in contrast however to the testing performed to try and match the results presented in the paper of Korzen (1984a) where the author was unsuccessful, due to the lack of parameter information, which will shortly be explained in detail. Despite not being able to reproduce Korzen's results, a number of parameter values were assumed and his method was compared to the work of Roberts to observe the scale of disparity in the results.

Roberts' work shall be used as the reference method, since it has been experimentally validated. Due to the lengthy equations and iterative procedure of Korzen, Microsoft® Excel was used to perform the calculations and plot the results. The chute and material for analysis is random and has the following characteristics: chute of constant radius (R): 3 m and width (B): 0.8 m, with a horizontal entry point (φ_0): 90° and vertical outlet point (φ_E): 0°; initial velocity of material vertically entering the chute (v_0): 6 ms^{-1}; material flow rate (Q_m): 4000 th^{-1}; material surcharge angle (λ): 20°; coefficient of wall friction (μ): 0.4; equivalent coefficient of friction (μ_E): 0.5; and density (ρ): 1000 kgm^{-3}.

Figure 3.9 illustrates the variation of velocity components along the chute for each method. The velocity profiles given by the methods of Roberts and Korzen show similar trends. The major difference occurred with the horizontal velocity component which in turn influenced the total velocity. The horizontal component given by Roberts decreased at a greater rate than that from Korzen's analysis near the end of the chute. Such differences and the possible causes will be explained below.

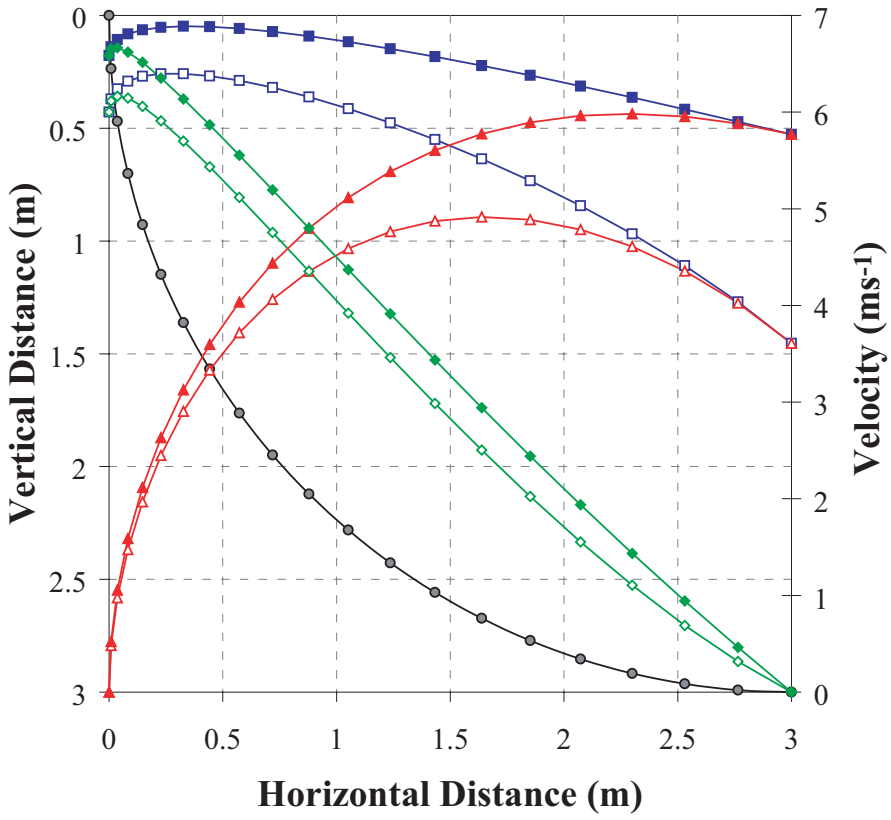

Figure 3.9 Variation of horizontal and vertical components of velocity and total velocity along the chute. The lines represent: the chute profile {—●—}; the total velocity as given by Roberts {—□—} and Korzen {—■—}; the horizontal component of velocity as given by Roberts {—△—} and Korzen {—▲—}; and the vertical component of velocity as given by Roberts {—◇—} and Korzen {—◆—}.

Figure 3.10 illustrates the cross-sectional area and stream thickness along the chute for each method. As mentioned in Chapter Two, for stable 'fast' flow conditions, it is most desirable that $H/H_0 < 1$ and that H/H_0 decreases as s increases. Figure 3.10 illustrates that for the hypothetical chute tested these conditions are not satisfied at all. With Roberts' material flow the ratio H/H_0 dramatically increases above the value 1 in the latter half of the chute. Korzen's material flow lies in the range $H/H_0 < 1$ until nearing the end of the chute, however during the majority of the material flow the ratio H/H_0 is increasing. The cross-sectional area has a similar trend to the ratio H/H_0 for both methods as the chute width is constant through the chute. It is clear that the specified

curved chute would not be suitable for maintaining fast flow conditions using either method; however this was not an existing or proposed example, rather an examination of the results given by the methods of Roberts and Korzen, and to see the fundamentals of each theory, which will now be described in greater detail.

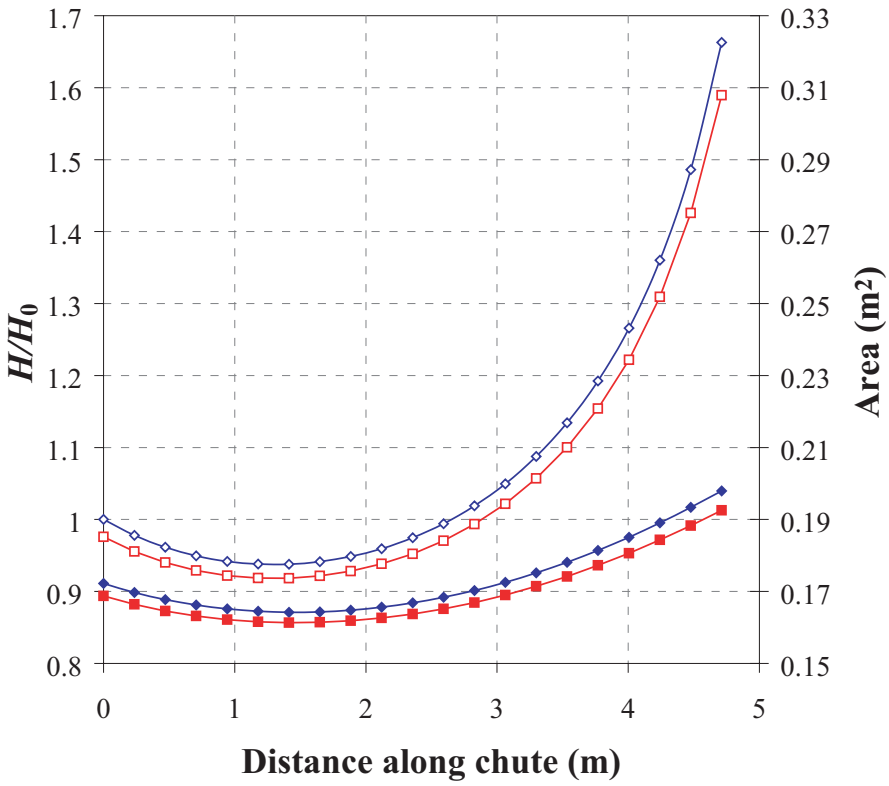

Figure 3.10 Variation of cross-sectional area and stream thickness ratio along the chute. The lines represent H/H_0 as given by Roberts {—◇—} and Korzen {—◆—}; and the cross-sectional area as given by Roberts {—□—} and Korzen {—■—}.

The assumptions used in the work of Roberts limit the chute theory to only free flowing materials with a relatively large radius of curvature (with respect to the material stream thickness). Potentially very cohesive materials such as limestone and iron ore fines for example could not be analysed with such theory. There are also aspects of the work of Roberts that require empirical results to obtain values, such as the inter-granular stress constant C for which very few values have been found in literature, particularly for

materials such as coal. Initial testing found that Roberts' approximation for calculating the height H_2 and area A_2 of material surcharge was very inaccurate, often giving a value larger than the height H_1 and cross-sectional area A_1 of the main rectangular portion of the stream. Therefore this calculation was omitted in the results shown. Korzen's model does not consider the height or areas resulting from the material surcharge. Nonetheless, for designing chutes that are transferring general coal with low moisture, Roberts' analysis may suffice. Korzen's work has these limitations also, and a number of further comments are warranted about his theory, as follows.

One of the main problems in Korzen's work is that a method for calculating the friction value of motion f_φ at any angle around the chute φ is not given, and therefore a constant value for f_φ was assumed in the analysis, equal to μ. Korzen's iterative procedure also produced anomalies when calculating the initial material stream thickness h_0 at the chute entry position. Using Eq. (2.122) an initial value was obtained, however after the iterative process, a different value was obtained. One possible reason for this is the assumption in the current work $\mu = f_\varphi$ at $\varphi = \pi/2$, however as mentioned, there was no indication given in the paper of Korzen to show how to calculate this value. Korzen also introduces a number of parameters in his theory that were not detailed in the main body of the text, nor in any nomenclature, and hence could not be used for the analysis.

Korzen's model was more lengthy to implement than that of Roberts', as the iterative procedure needs to be completed for the parameters h_φ, R_φ and v_φ every location φ around the chute that the user wishes to examine. For the current analysis, five approximation steps were used in Korzen's model, giving a tolerated relative deviation of $\xi = \sim 0.001\%$. As a side note, even after three approximations for the current work Korzen's iterative scheme gave a deviation of only ~ 0.258%, showing that its rate of convergence is quick.

3.4.3 Material Impact and Flow Summary – Lower Chute Element

The first section briefly examined impact upon the lower chute element, and it was found that there is a distinct advantage to utilizing curved profile upper and lower chute

elements. These methods do not comprehensively examine the flow processes of an impacting stream of material however.

Two different analytical methods for examining material flow through gravity flow chutes was presented. It was found that although Korzen's analysis was theory intensive, the results produced and the anomalies discovered deemed the method of Roberts to be superior. Additionally, Roberts' work has been validated for a number of free flowing bulk materials. The use of a number of parameters in Korzen's work needs to be explained, and until then it is suggested that such an analysis not be utilized for chute design theory, which is in contrast to the recommendations given to his works detailing discharge and trajectory aspects (Korzen 1989) and impact upon flat plates (Korzen 1988).

3.5 Overall Comments and Summary

The transfer point in a bulk solids handling system is an area that has not been examined in great detail and as a result is lacking detailed analytical literature. Many of the various models and design methods available to calculate or predict the relevant parameters were compared in this chapter.

Overall there is a great quantity of work however in general these analyses are not distributed evenly between the transfer components. Most of the literature is devoted to discharge and trajectory of the material off the head pulley. The reason for this is that in general, engineers in the mining industry attempt to model the path of the material accurately and then elect to design the shape of the impact plate using a general understanding of flow processes based on the material being transferred and trial and error rather than analytical means. The drawback to this is that in many cases, the chute design fails, often more than once, resulting in repeated capital outlay. Hence further analysis of impact plates that considers the relevance of bulk solids properties and flow characteristics in addition to the work of Korzen (1988) is required.

Leading on from the above point, another major problem is the lack of work to date that examines the whole system using a single analytical technique. Currently, implementing transfer chute design and analysis requires in certain cases the combination of the analytical Korzen (1989) and graphical Dunlop (1982) methods during the design procedure. A number of works use such techniques (Burnett 2000a, 2000b, Scott & Choules 1993a, 1993b) where separate methods for each transfer chute component are used. This works to an extent though integrating the two types of methods creates problems with the implementation of graphical output as theoretical input and vice-versa. Recent developments in the field have been published (Benjamin 1999, 2001, Benjamin & Nemeth 2001, Benjamin et al 1999a, 1999b) though these do not detail the processes or derivations used in their designs.

Another issue is that design literature falls at two extremes: the literature caters specifically for either academics, with lengthy analytical methods requiring iterative procedures; or an industry perspective utilizing simple theory with discussions based on empiricism, resulting in possibly inaccurate predictive techniques. A compromise is needed between these two extremes. The problem is that when certain methods are complex in their material interactions and utilise lengthy equations requiring iterative techniques (e.g. impact models detailed by Korzen (1988)), the time consumption required to implement them renders them unattractive for industry personnel.

The lack of investigations in certain problematic areas such as material impact warrants research to be conducted in transfer chute technology. An analysis is required that can cover all transfer chute design aspects and hence negate the need to refer to a range of literature. The topic of air entrainment is an area that requires consideration, however is of greater significance to the transfer of fine particles, and has little impact if the drop height between the conveyor belts is small. Further experimental work is also suggested in addition to that conducted by Arnold & Hill (1991b). The drawback of their work is that it does not provide sufficient data to plot trajectories and stream paths resulting from their experimental work. The recommendations and theory provided however were able to be used as a basis for quantifying other prediction methods for the current work.

There is a number of additional areas of interest in transfer chute design. From the volume of literature found, the most widely investigated of these is the concept of wear

in transfer chutes, which is directly related to the velocity of the material flowing over the chute surface. A close quantitative approximation of the velocity profiles through the system will allow a close approximation of the abrasive wear factor. The reader is referred to the work of Roberts (1988, 1990, 1991, 2001), Roberts & Ooms (1985), Roberts & Wiche (1993), Roberts et al. (1984, 1989, 1990, 1991), Rozentals (1983, 1991) and Sabina et al. (1984) for discussions on wear. The next chapter will begin describing the work undertaken to create a Distinct Element Method (DEM) code, and will detail the few investigations that have applied DEM to analyse flow of ore materials through chutes at transfer stations.

Chapter Four

DISTINCT ELEMENT METHOD (DEM)

4.1 Introduction

There are numerous problems in engineering dominated by discontinuous mechanical behaviour. Examples of such engineering problems are numerous, and can vary from stability of rock slopes comprised of rock mass elements, to the failure analysis of brittle materials such as ice and ceramics, to the flow of bulk solids in chutes and hoppers. Conventional continuum based procedure such as the Finite Difference Methods (FDM) or Finite Element Methods (FEM) cannot solve most problems relating to systems exhibiting such large scale discontinuous behaviour. The category of numerical modelling techniques known as *Distinct Element Methods* (DEM) is specifically designed for such problems. For further details and applications of Distinct Element Methods (or Discrete Element Methods as they are often called) the reader is referred to the proceedings of relevant conferences, such as Cook & Jensen (eds. 2002), Mustoe et al. (eds. 1989), and Williams & Mustoe (eds. 1993).

Formally, Distinct Element Modelling is one class out of eight main classes of numerical methods for discrete element modelling (Bardet 1998), the seven others being Modal methods, Discontinuous Deformation analysis (DDA), Momentum-Exchange methods, Multibody Dynamics methods (MDM), Structural Mechanics methods (SMM), Mean Field method, and Energy Minimisation method. Figure 4.1 summarises the attributes of the methods listed above. The performances of the methods are grouped in three categories, ranging from good to not applicable, illustrating the advantages and shortcomings of each method.

When selecting a numerical method from the eight classes, future directions for the current work were considered. Distinct element methods and modal methods were the short-listed classes, and have similar capabilities that were ideal for the proposed research. However the amount of literature available, including online computing resources, heavily favoured DEM, and hence was chosen.

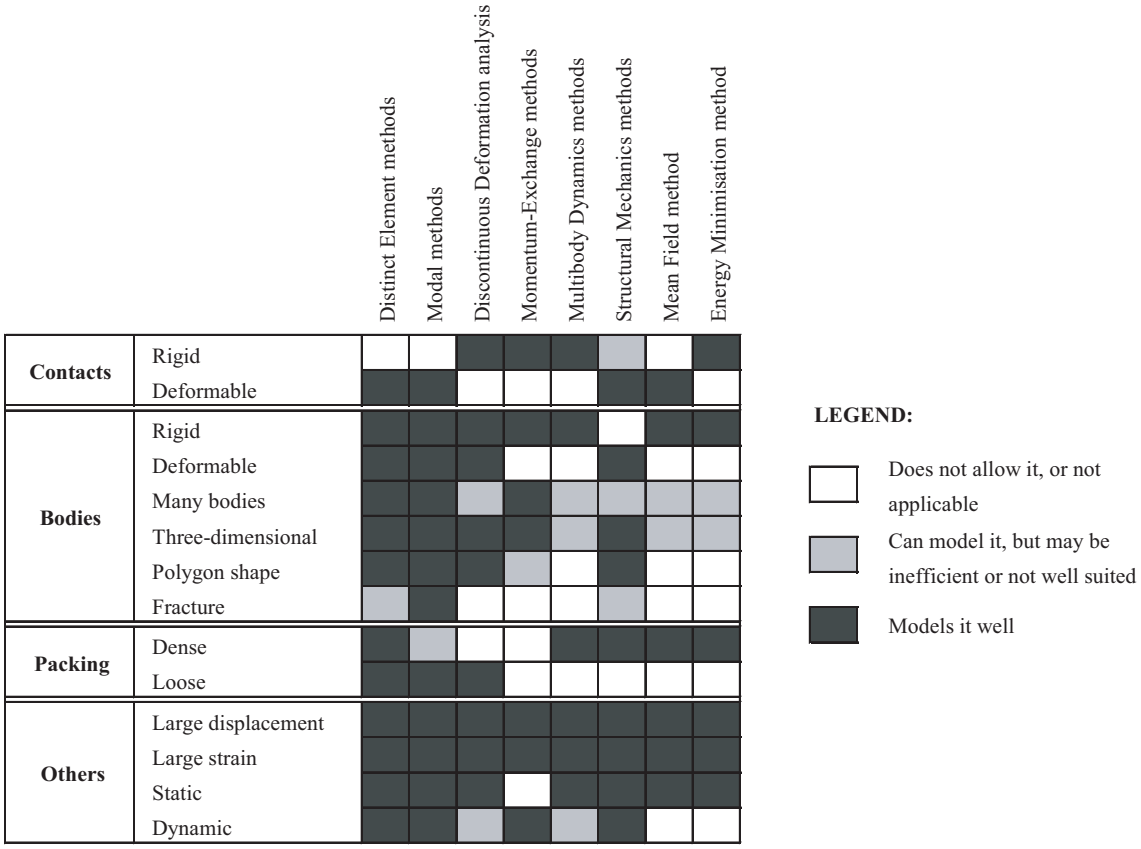

Figure 4.1 Attributes of the various classes of discrete element methods (Bardet 1998)

4.1.1 DEM Overview

Fundamentally, DEM is a modelling concept that uses Newtonian rigid-body mechanics to model the translational and rotational motion of each sphere in a model assembly. Overlapping contact is permitted between neighbouring particles where it is assumed that particle deformation is very small compared to the particles' displacements as rigid bodies. As a result of a particular stiffness and/or damping characteristic, contact forces are developed. These forces can be calculated with simple mechanical models such as a spring (simulates elasticity), a dashpot (damping) and a frictional slider (friction). All the forces and moments acting on each particle at every time step are tracked. The equations of motion are then integrated to obtain the new state of the system at the end of each time step. If boundaries experience fully kinematic motion then equations of motion are also solved for the boundary objects with which the particles interact. The technique is explicit, as it is assumed during each time step disturbances cannot

propagate from any particle further than its immediate neighbours. Therefore at any time increment the resultant forces and hence the accelerations on any particle are determined only by its interactions with the particle(s) or boundary with which it is in contact.

4.1.2 DEM Background

The distinct element method was developed by Cundall (1971) for the analysis of rock mechanics problems. Cundall & Strack (1979) pioneered the application of the original DEM concept to granular assemblies, and viewed the interaction of the particles in DEM as a transient problem with states of equilibrium developing whenever the internal forces balance. The original work has been extended and applied in several directions by others, including Walton & Braun (1986b). Review articles by Barker (1994), Campbell (1990), and Walton (1992) describe the DEM methodology further and many of the findings made about granular flows, including advanced areas of DEM research. Progress into utilising various particle shapes has occurred over the past few years, with DEM used to successfully simulate granular material by modelling the dynamic behaviour of circular disks (Cundall & Strack 1979, Sadd et al 1993, Walton & Braun 1986b), large assemblies of spheres and/or clusters of spheres (Jensen et al. 1999, Tsuji 1993, Walton 1993a, Walton & Braun 1986a, Xu 1997, Xu & Yu 1997, Zhang & Vu-Quoc 2000), 3-D ellipsoids (Lin & Ng 1997, Mustoe & Miyata 2001), blocks and other polygonal shapes (Walton 1982a, 1982b, Walton et al. 1991), superquadrics (Barr 1981, Mustoe & Miyata 2001, Mustoe et al. 2000), and other non-round shapes (Hogue 1998, Hogue & Newland 1994, Potapov & Campbell 1998). However, DEM is currently limited by the number, size range and shape of particles to be handled (Roberts 1998a), and this issue is further explored in the next section.

4.1.3 Merits and Drawbacks of DEM

The Distinct Element Method has number of attractive qualities. The ability to model interactions between particles has the potential to provide more realistic approximations of granular flows. The complex behaviour of a system can be analysed, altered and improved by correctly modelling its individual properties. For example, continuum mechanics has been used in transfer chute applications (McIlvenna & Mossad 2003,

Nordell 1994, Nordell & Van Heerden 1995), where the behaviour of the material is described by constitutive equations. Simulating with continuum-based numerical modelling techniques such as finite difference or finite element methods has significant drawbacks however. They rely on an assumed constitutive equation and often have global assumptions on the material such as steady-state behaviour or uniform constituency (Langston et al. 1995). The numerical method suffers as material parameters such as plasticity, compressibility and cohesiveness are not accounted for in the relevant equations. Another problematic issue with continuum mechanics for transfer chute analysis is that the stream path must be known prior to investigation. In DEM the parameters (many of which affect inter-particle contacts) can be determined from the properties of materials, such as Young's modulus, Poisson's ratio and the coefficient of restitution. This means that the DEM approach needs fewer assumptions than the continuum based approaches. For example, Tsuji et al. (1993) illustrated how the particle size and density distribution can be directly taken into account in a DEM simulation if necessary, due to the specification of characteristic properties of individual particles such as size and density.

There are however drawbacks in utilising the DEM numerical method. Experience has shown that complicated particle shapes increase the complexity of the algorithm for contact detection and add to the computation time. In fact, even utilising multiple sized spheres adds to program compilation time. The computation time is also extremely long when the number of particles is of the same order as in real flows of fine materials, and it is this aspect which is the limiting factor for DEM. Walsh (2004) has found that the computation time is roughly proportional to the square power of the number of particles in a typical algorithm. This inhibiting factor in carrying out very large multi-particle simulations can be overcome somewhat by breaking the simulation area into a number of smaller distinct particle systems. Here the computational time approaches a linear relationship to the number of particles.

4.2 Applications of Distinct Element Method

The distinct element method is a numerical technique that is capable of handling particles of almost any shape, and as a result has been utilised as a tool for analysing a great range of industrial applications. To cover the range of DEM applications is beyond the scope of the thesis, with the discussion here to focus on applications of DEM to transfer points. In general though, DEM has been applied to solve problems in numerous fields with the conference proceedings mentioned earlier containing various investigations. The extension to non-geological industrial applications such as mining and mineral processing applications has occurred over the past several years. These studies are dramatically on the rise as evidenced by the extensive literature published in recent years by an increasing number of individuals and research groups. Particular case study investigations include:

- Ball mill operation (Cleary 1998a, 2001, Cleary & Sawley 1999);
- Belt conveyor transfer points (Alspaugh et al. 2002, Dewicki 2003, Dewicki & Mustoe 2002, Hustrulid 1998, Hustrulid & Mustoe 1996, Kruse 2000, n.d., Nordell 2003, n.d., O'Donovan 2003, Qiu & Kruse 1997a, 1997b);
- DEM modelling of a ploughshare mixer (Cleary et al. 2002);
- DEM modelling of gas-solid flow in a bed (Xu 1997, Xu & Yu 1997, Xu et al. 2000, 2001);
- Discharge from a cylindrical hopper (Cleary & Sawley 1999);
- Dragline excavators (Cleary 1998a, 1998b, 2000);
- Flow in centrifugal mills (Cleary 1998a, 2000, Cleary & Hoyer 2000);
- Hicom nutating mill (Cleary & Sawley 1999);
- Mixing in tumblers (Cleary 1998a, 2000);
- Numerical simulations of flows of particles in rotating cylinders (Walton 1994, Walton & Braun 1993, Wightman et al. 1998);
- Numerical simulations of particles flowing down an inclined surface (Drake & Walton 1995, Hanes & Walton 2000, Vu-Quoc et al. 2000, Walton 1993a);
- Numerical simulations of the movement of particles under the influence of a constant body force (Walton 1993b);

- Simulation studies which focus on shearing flow in assemblies of particles (Walton 1990, Walton & Braun 1986a, 1986b);
- Size separation by a vibrating screen (Cleary & Sawley 1999); and
- Other selected industrial applications including: vibrational segregation by size and density, flows from slot hoppers, idler induced segregation, and cutter bias for commodity samplers (Cleary 1998a).

The need to explore numerical methods for investigation of transfer chutes has partly arisen due to the use in literature of separate design methods for each transfer chute component, which was described in Chapters Two and Three. DEM is advantageous in that it can be used to analyse the whole transfer of material while also obtaining the required information about flow through each particular component. DEM also allows the user to examine both quantitatively and qualitatively the micro-mechanics of inter-particle contacts.

4.2.1 DEM Applied to Transfer Chute Analysis

There are few DEM case studies however investigating belt conveyor transfer points. Relevant companies that have developed DEM code or are utilising existing DEM software were contacted to obtain technical papers or references, however most did not respond. A search of the literature has shown there to be only four technical papers (Hustrulid 1998, Hustrulid & Mustoe 1996, Qiu & Kruse 1997a, 1997b), six pseudo-technical papers (Dewicki 2003, Dewicki & Mustoe 2002, Kruse 2000, n.d., Nordell 2003, n.d.) and two commercially oriented works (Alspaugh et al. 2002, O'Donovan 2003) that examine DEM simulations depicting material flow through transfer chutes in mining applications. None of the available investigations detail aspects regarding comparison with and quantification of existing transfer chute design theories, such as material trajectory prediction, the impact process, or gravity chute flow issues. Significantly, the available studies also do not adequately detail the numerical processes or algorithms utilised, nor provide sufficient references to available literature. The use of on-site data has been implied by a number of papers (e.g. Nordell n.d.) however numerical figures have not been published.

It should be noted that there has been a number of studies to date that have examined flows of granular materials down straight inclined chutes, for example the work of Campbell & Brennen (1985), Vu-Quoc et al. (2000) and Zhang & Vu-Quoc (2000). Generally these works have developed analytical or computational means to simulate flows and then compare with quantitative experimental data. Obtaining, interpreting, and presenting data in these studies is more straightforward as these studies do not have to consider irregular flow stream aspects such as free falling material impacting on the chute surface or material flow around curved surfaces, rather they utilise periodic boundaries ensuring a constant stream of flowing material allowing analysis of one portion of the chute. Such chutes are rarely used in the mining industry where there is a relatively high-speed conveyor belt feeding the material, or when angled transfers are required.

The Colorado School of Mines was arguably the first institution to develop DEM code for application to transfer stations. Hustrulid & Mustoe (1996) presented a 3-D DEM study of a transfer point. Preliminary information such as the material flow regime as it passes through the transfer point, forces acting on the transfer chute structure, and forces acting on the lower conveyor belt at the load point region were presented. The deficiencies in the study with respect to the current work centre around the lack of comparisons to existing chute design theories. Material stream velocities as the material trajected off the belt were not presented, which are essential to providing an initial approximation to good chute design. The relative velocity of contacts between the DEM and transfer chute back plate were provided, however the orientation of axes was not adequately described. Again, a comparison to existing chute design theory was neglected. In this case the velocities produced by the DEM could have been compared to say those produced using Korzen's (1988) analytical work for impact plates. The relative velocity of contacts between the DEM and exiting belt was provided, however a clear interpretation of the graphs was not described.

Further work conducted by Hustrulid (1998) discusses several methods of presenting the data from 3-D discrete element simulations that are used to improve the performance of a transfer station, including wear profile, moment arm and lateral force diagrams. Graphical techniques such as animations colour coded for differing velocity ranges are illustrated; however with respect to the current work corroboration of

velocity profiles using existing theories is not presented. Animations can qualitatively describe the velocity regimes however quantitative data are essential to check the DEM against existing theories. The paper gives significant discussion on the transfer station setup, however there is little information regarding the numerical procedures used.

Dewicki (2003) and Dewicki & Mustoe (2002) presented an overview of belt conveyor transfer points and associated problems. They described the DEM software now utilised by Overland Conveyor Company Inc. for simulating material flow at a transfer point, titled Chute Analyst^{TM}. The typical process that an engineer performs to design a new transfer was described. A successful application of their DEM code to an industrial problem was presented, with captures of simulations showing particle velocity distributions through the transfer, however quantitative data were not presented. Dewicki & Mustoe (2002) mention how the DEM closely approximated the flows through the installed chute, which could be deemed one measure of quantification. However, a detailed analysis is required at the macroscopic level, which was implied, but not presented in their work.

Conveyor Dynamics Inc. also applied DEM to solving problems at transfer stations. Qiu & Kruse (1997a) presented a 3-D application of DEM to the analysis of ore flow in transfer chutes. Clusters of spheres of different sizes were employed to represent the particles of the bulk material and triangle discrete elements were used to model the surfaces of the chute. The effect of chute geometry on the characteristics of ore flow and the corresponding impact of particles on the receiving belt surface was investigated. Aspects such as pressure and wear damage on the belt were examined. An industrial application was presented where the performance of a rock box was compared to that of a curved chute. The research did not examine aspects relevant to this thesis, namely velocity distributions throughout the transfer. There was also no mention of prior quantification of the DEM against existing chute design theories.

Further work published by representatives of Conveyor Dynamics Inc. had commercial aspects in their work. Kruse (2000) presented various types of granular flow problems currently being solved using DEM, including transfer chute applications. The fundamentals of DEM were introduced as well as relevant design parameters. The results and potential benefits of the case problems were also discussed. Specific aspects

of transfer chutes that were examined included the impact and shearing work between particles leading to material degradation and also belt wear. Captures of animations where particles have been colour coded according to velocity have been provided however detailed quantitative velocity data such as exact data values from snapshots taken at particular times are not shown. Comparisons to existing theories are also absent.

Nordell (2003) presented a qualitative overview of the transfer chute designs developed from DEM, and examined aspects such as belt wear life, product degradation and dust generation, spillage, belt alignment, and lower chute element damage. Significantly, his work is the only investigation that compares DEM to an existing theory. In his work, a comparison is made between material trajectories produced by DEM simulations to those generated using theory from the popular C.E.M.A. (1997) manual. Nordell's work indicates that at the relatively higher speed of 6 ms^{-1}, the DEM simulations match the C.E.M.A. theory. However this does not agree with the experimental work performed by Arnold & Hill (1991b) and their other studies (Arnold & Hill 1990a, 1991a, Arnold 1993) which have shown the CEMA guide to predict greater material throw than what occurs in actuality. Nordell also presents captures of animations at various stages of the transfer of material through a chute where particles have been colour coded according to velocity. This is a useful tool for a general interpretation of the velocity profiles, however is not adequate to use for quantification against other sources as the colour gradients are not sufficiently defined.

Nordell (n.d.) presented various applications of DEM in the mining industry, including transfer chutes. The basic numerical structure, such as the dynamics of equilibrium were presented however sufficient detail is not given as to the DEM setup used for the simulations other than the particle and boundary constraints. Two industrial investigations are presented that compare a rock box against a curved chute with emphasis placed on wear issues and pressure intensities. There are no analyses of the velocity profiles at critical locations in the system. Comparisons between the DEM and existing theories have not been presented.

Kruse (n.d.) presented the fundamentals of DEM and examples of DEM applications in mining, including transfer chute design. Aspects such as material degradation, chute wear, belt wear, and pollution control were examined. The work does not qualitatively

or quantitatively describe DEM material stream velocity aspects. The comparisons of DEM to existing theory to check the material flow profile or trajectory through the system are not presented. This work, and also that of Nordell (n.d.) have commercial elements in their nature with both papers presenting the advantages of DEM, rather than wholly technical.

In addition to the research described, there have also been commercially oriented papers by representatives of Overland Conveyor Company Inc. which detailed successful applications of DEM based upon the work originally conducted at the Colorado School of Mines. Alspaugh et al. (2002) presented an overview online of the DEM process applied to conveyor transfers, including one practical application. The non-technical nature of the article alludes to the success of the DEM simulations however quantitative discussions were not present. Visual representations of the velocity regimes through the transfer were discussed though these discussions were commercial in nature and insufficient as a technical tool. Again no mention is made of comparing the DEM to existing theories so as to quantify the DEM results against certain transfer aspects such as trajectory and curved chute velocity profiles.

O'Donovan (2003) presented a similar review to that of Alspaugh et al (2002), including the DEM application to the same industry project. His discussion on the basic numerical procedure for DEM is quite vague however. The same deficiencies with regards to validation against existing non-DEM theories are also evident, however are to be expected given the commercial nature of the paper.

None of the works described above presented qualitative testing of their relevant DEM codes at the macroscopic level. Certain works such as that of Nordell (n.d.) described a procedure for validating the DEM model by comparing results against a laboratory shear tester, however any results he obtained or any possible areas of weakness in their model were not detailed.

4.2.2 Summary and Proposed Area of Investigation

The general theme of the existing published work describing the application of DEM to model particulate flow through transfer chutes is that velocity distributions throughout

the material flow can be qualitatively represented by colour coded animations and used for discussion. For conveying information rapidly or in an *ad hoc* fashion to an engineer or mine personnel onsite it would suffice, however for an in-depth technical analysis, further quantitative information is needed. The review of the literature available has revealed the severe lack of analyses in three critical areas: (a) qualitative testing of the DEM code; (b) quantitative examinations of DEM velocity regimes; and (c) quantification of these DEM velocity regimes to those presented by existing theory. The lack of published technical papers is due to the nature of problem solving in the industry. Chapter Two and Three described the lack of attention given to conveyor transfers, hence any advancements made in the area are usually not published to maintain competitiveness against rival companies. Literature was found published by Overland Conveyor Company Inc. however permission was required to refer to those papers. To examine transfer chute aspects quantitatively, this chapter and further chapters will now focus on the development of a DEM code and attempt to obtain the necessary results.

4.3 Mathematical Formulation for Distinct Element Method

Generally speaking, two colliding spheres will undergo deformation ranging between the extremes of perfectly plastic and perfectly elastic. Possible mechanisms for dissipation include plastic deformation, upon which the force-displacement model is based. However before resolving the forces, the particle-particle and particle-wall interactions need to be defined.

Before proceeding it should be noted that SI units have been used. It is desirable to work with non-dimensional units however they are not always practical. For example, non-linear force laws (as will be used in the current work) do not define a unique timescale (Schäfer et al. 1996).

4.3.1 Particle–Particle Definitions and Interactions

The current work is limited to spherical particles restricted to three degrees of freedom – two translational and one rotational. Figure 4.2 illustrates two spheres of radii R_i and R_j

in contact, with position vectors $\mathbf{r}_i^N$ and $\mathbf{r}_j^N$, velocities $\mathbf{v}_i^{N-1/2}$ $(=\dot{\mathbf{x}}_i^{N-1/2}+\dot{\mathbf{y}}_i^{N-1/2})$ and $\mathbf{v}_j^{N-1/2}$ $(=\dot{\mathbf{x}}_j^{N-1/2}+\dot{\mathbf{y}}_j^{N-1/2})$, and angular velocities $\omega_i^{N-1/2}$ and $\omega_j^{N-1/2}$. We let $\hat{\mathbf{k}}_{ij}^N$ be the current unit vector pointing from the centre of sphere *i* to the centre of sphere *j*:

$$\hat{\mathbf{k}}_{ij}^N = \frac{\mathbf{r}_j^N - \mathbf{r}_i^N}{\left\| \mathbf{r}_j^N - \mathbf{r}_i^N \right\|} \tag{4.1}$$

The vector $\hat{\mathbf{k}}_{ij}^N$ is also the unit normal at the contact point.

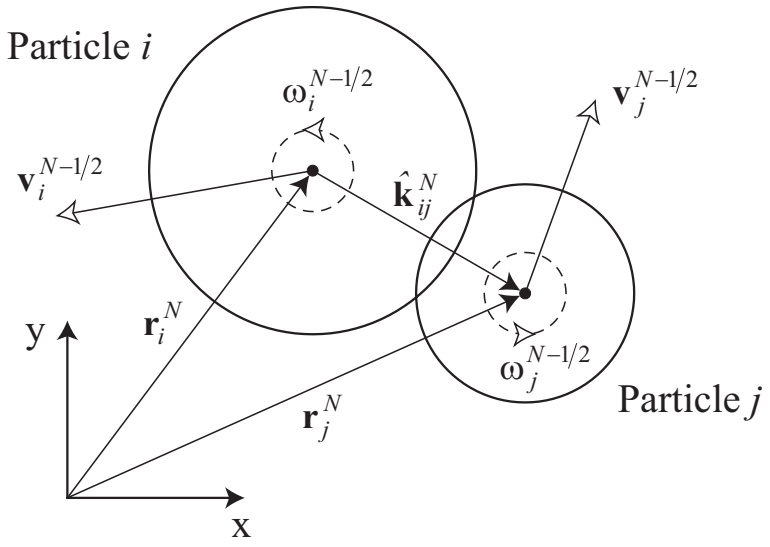

Figure 4.2 Definition of the quantities used for description of the impact

Consider the particle-particle collision of two particles illustrated in Figure 4.3. If we let dx^N be the horizontal displacement difference between particles and dy^N be the vertical displacement difference between particles then:

$$\left(dn^N\right)^2 = \left(dx^N\right)^2 + \left(dy^N\right)^2 \tag{4.2}$$

Let the sum of the sphere radii be given by:

$$d_{ij} = R_i + R_j \tag{4.3}$$

If $\left(dn^N\right)^2 < \left(d_{ij}\right)^2$ particle-particle interaction occurs and the force calculation routine must be executed. The virtual overlap of the particles is therefore given by:

$$\delta_n^N = max\left(0,\, R_i + R_j - \left\| \mathbf{r}_j^N - \mathbf{r}_i^N \right\|\right) \tag{4.4}$$

The force-displacement models relating to this overlap will be explored in Section 4.3.5.

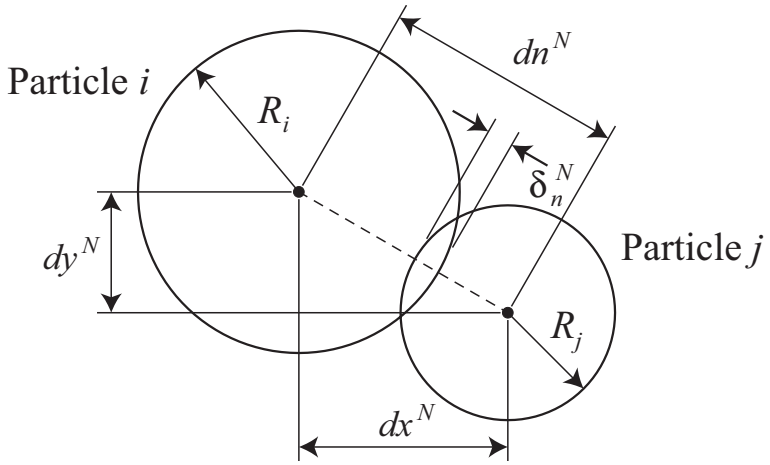

Figure 4.3 Overlap between colliding particles with radii R_i and R_j

To prevent conditions such as excessive overlap between particles, or particles passing through one another or wall elements, the overlap between particles or a particle and a surface must be constrained to a fraction of the radius of the smallest particle in the assembly. For the current work an average overlap typically in the range of 0.5%–1.5% of a particle diameter is desired.

Polydispersity is utilised in the current work, where a range of particle diameters can be input. In the coding, the spherical particles can be input as one of three types of particle size: mono-sized, binary-sized or multi-sized. The maximum and minimum particle diameters $\{D_{max}, D_{min}\}$ for each case is defined as follows. For mono-sized spheres D_{max}

= D_{min} = D_{mono} where D_{mono} is the particle diameter specified by the user. For binary-sized spheres, D_{max} and D_{min} are obviously already defined and the proportion of each can be nominated by the user. For multi-sized spheres:

$$D_{max} = D_{base} + nD_{var} \tag{4.5}$$

$$D_{min} = D_{base} - nD_{var} \tag{4.6}$$

where D_{base} is the base diameter, D_{var} is the variance between particle sizes, and the parameter n is a function of the total number of particles in the system ensuring the size distribution is user defined. For a system that incorporates multi-sized particles, the particle diameter sampling can also be selected from a random distribution.

Once the particle diameters have been defined, the mass of each particle must be determined, which in turn will allow the moment of inertia to also be calculated. For spheres the mass of a particle is given by $m_i = \left(4/3\,\pi R_i^3\right)\rho_i$ where R_i and ρ_i are the radius and density of a particle i. The moment of inertia of a sphere i is given by $I_i = 2/5\, m_i R_i^2$. For all particle size distributions the values for m_i and I_i are easily determined.

4.3.2 Particle-Boundary Definitions and Interactions

In the computer coding, a major subroutine called *READ_NEUTRAL* basically initialises and sets up the straight and curved physical boundaries within the calculation space. Firstly, the file is read, with coordinates for every line both straight and curved given in the form shown in Table 4.1. The definition of four coordinates for each of the x, y and z directions is due to the initial pre-processor defining boundary or line coordinates in such a way. This issue will be further explored and discussed in Chapter Five.

Table 4.1 Formation of coordinates in text file containing boundary data

Straight Line Point No.	Curved Line Point No.	*x*-coordinate	*y*-coordinate	*z*-coordinate
1 (Start)	1 (Start)	x_1	y_1	z_1
–	2	x_2	y_2	z_2
–	3	x_3	y_3	z_3
2 (End)	4 (End)	x_4	y_4	z_4

4.3.2.1 Straight Line Boundaries

For a straight line only the first and fourth coordinates in Table 4.1 are used for straight lines, with the second and third coordinates set equal to zero. The coordinates are then denoted as following:

$$x1_i^{\text{line}} = x_1,\ y1_i^{\text{line}} = y_1 \tag{4.7}$$

$$x2_i^{\text{line}} = x_4,\ y2_i^{\text{line}} = y_4 \tag{4.8}$$

with every i representing the line numbers. Note that z_1 and z_4 are set equal to zero in the current work as the calculation space is restricted to two dimensions. The definitions are illustrated in Figure 4.4. The line end point coordinates are checked to see if the line is vertical. If the following condition holds, then the line is vertical:

$$x1_i^{\text{line}} = x2_i^{\text{line}} \tag{4.9}$$

The straight line equation is of the form $y = Mx + C$ where M is the line gradient and C is the y-axis intercept. These values are calculated as follows:

$$m_i^{\text{line}} = \frac{y2_i^{\text{line}} - y1_i^{\text{line}}}{x2_i^{\text{line}} - x1_i^{\text{line}}} \tag{4.10}$$

$$c_i^{\text{line}} = y2_i^{\text{line}} - m_i^{\text{line}}\ x2_i^{\text{line}} \tag{4.11}$$

$$\phi_i^{\text{line}} = tan^{-1}\left(m_i^{\text{line}}\right) \tag{4.12}$$

Note that the line is checked to see if it is vertical explicitly due to the possibility of computation errors occurring if the denominator of Eq. (4.10) equals zero. The line will be horizontal if the numerator of Eq. (4.10) is equal to zero.

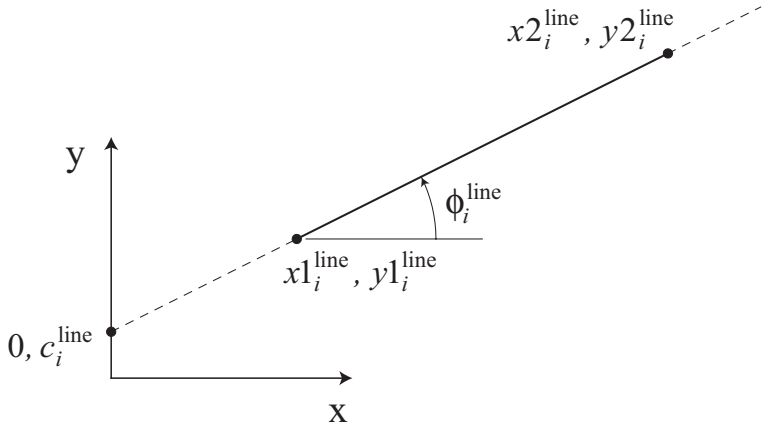

Figure 4.4 A representation of a straight line in the system

4.3.2.2 Curved Line Boundaries

Curved surfaces are not preferred in the manufacture of chutes, however if they are required, the author's industry experience has shown that on almost all occasions the curved surface is represented by an arc as they are simpler to manufacture than say a curve represented by a polyline or spline. For this reason, for a curved line the coordinates described in Table 4.1 are all used with the curve described as an arc passing through four coordinate points, which are then denoted as following:

$$x1_i^{\text{arc}} = x_1,\ y1_i^{\text{arc}} = y_1 \tag{4.13}$$

$$x2_i^{\text{arc}} = x_2,\ y2_i^{\text{arc}} = y_2 \tag{4.14}$$

$$x3_i^{\text{arc}} = x_3,\ y3_i^{\text{arc}} = y_3 \tag{4.15}$$

$$x4_i^{\text{arc}} = x_4,\ y4_i^{\text{arc}} = y_4 \tag{4.16}$$

with every i representing the arc numbers. Note that z_1, z_2, z_3 and z_4 are set equal to zero in the current work as the calculation space is restricted to two dimensions. The definitions are illustrated in Figure 4.5.

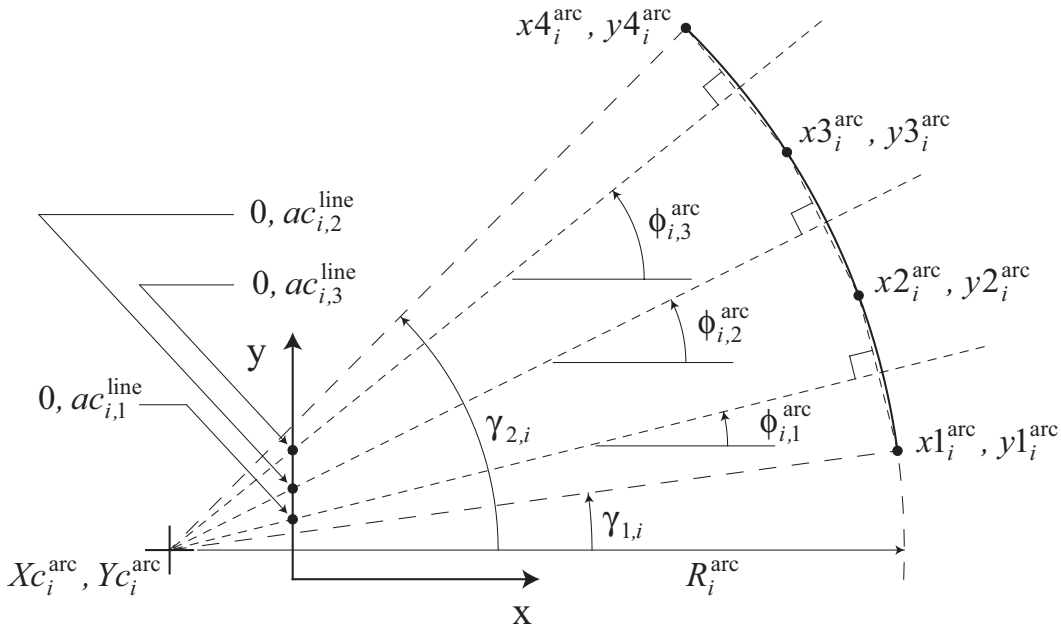

Figure 4.5 A representation of an arc in the system

The gradients, perpendiculars, and intercepts of each line between successive points are used to calculate the centre and radius of each arc in a curve, and these are described as follows:

$$am_{i,j}^{line} = -\left(\frac{x(j+1)_i^{arc} - x(j)_i^{arc}}{y(j+1)_i^{arc} - y(j)_i^{arc}}\right) \tag{4.17}$$

$$ac_{i,j}^{line} = \frac{y(j)_i^{arc} + y(j+1)_i^{arc}}{2} - am_{i,j}^{line}\left(\frac{x(j)_i^{arc} + x(j+1)_i^{arc}}{2}\right) \tag{4.18}$$

$$\phi_{i,j}^{arc} = tan^{-1}\left(am_{i,j}^{line}\right) \tag{4.19}$$

where $am_{i,j}^{\text{line}}$ is the gradient of the perpendicular to the chord between successive points on the arc, $ac_{i,j}^{\text{line}}$ is the y-axis intercept of the perpendicular, i represents arc numbers and j=1,2,3 are the three chord and perpendicular numbers for each arc. The line segments within the arc are also tested to see if any are approximately vertical, in other words, to see if the following holds true:

$$\frac{x(j+1)_i^{\text{arc}}}{x(j)_i^{\text{arc}}} = 1 \tag{4.20}$$

The centre and radius of each arc is calculated as follows:

$$Xc_i^{\text{arc}} = \frac{ac_{i,3}^{\text{line}} - ac_{i,1}^{\text{line}}}{am_{i,1}^{\text{line}} - am_{i,3}^{\text{line}}} \tag{4.21}$$

$$Yc_i^{\text{arc}} = am_{i,1}^{\text{line}}\ Xc_i^{\text{arc}} + ac_{i,1}^{\text{line}} \tag{4.22}$$

$$R_i^{\text{arc}} = \sqrt{\left(x1_i^{\text{arc}} - Xc_i^{\text{arc}}\right)^2 + \left(y1_i^{\text{arc}} - Yc_i^{\text{arc}}\right)^2} \tag{4.23}$$

The start ($\gamma_{1,i}$) and finish ($\gamma_{2,i}$) angle of each arc is calculated as from:

$$\gamma_{1,i} = cos^{-1}\left(1 - \frac{\left(x1_i^{\text{arc}} - Xc_i^{\text{arc}} - R_i^{\text{arc}}\right)^2 + \left(y1_i^{\text{arc}} - Yc_i^{\text{arc}}\right)^2}{2\left(R_i^{\text{arc}}\right)^2}\right) \tag{4.24}$$

$$\gamma_{2,i} = cos^{-1}\left(1 - \frac{\left(x4_i^{\text{arc}} - Xc_i^{\text{arc}} - R_i^{\text{arc}}\right)^2 + \left(y4_i^{\text{arc}} - Yc_i^{\text{arc}}\right)^2}{2\left(R_i^{\text{arc}}\right)^2}\right) \tag{4.25}$$

There are also conditions that govern the calculation of the angles, however these are minor (eg. addition and subtraction of π, 2π depending upon which quadrant of a circle the angle is located in) and shall not be discussed further.

4.3.2.3 Particle – Boundary Interactions

In the computations, all the boundaries are taken to be rigid. When a particle hits a boundary, it gets deformed without causing any deformation to the boundary. As both straight and curved surfaces are considered in the current work, they will be considered separately as the interaction processes are geometrically different.

Before we can test for the interaction between a particle and a straight wall, a few of the geometric quantities must be defined. The program considers interactions between either vertical boundaries or non-vertical boundaries. The particle centre is represented by $\{x_i,\ y_i\}$. The terms i and j denote particle numbers and boundary numbers respectively. Referring to Figure 4.6, for an interaction with a vertical boundary we automatically allocate the following identities:

$$x^{\text{line}} = x1_j^{\text{line}} \tag{4.26}$$

$$y^{\text{line}} = y_i \tag{4.27}$$

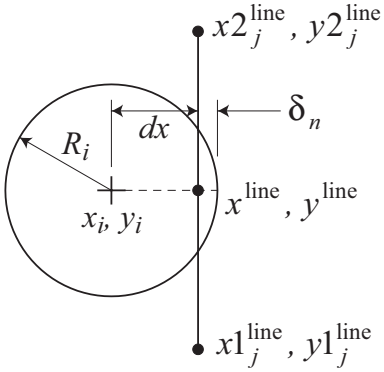

Figure 4.6 Overlap between a particle and a vertical line

However we check to see if the particle centre lies below the line, or $y_i < min\left(y1_j^{\text{line}}, y2_j^{\text{line}}\right)$, and if it is true then:

$$y^{\text{line}} = min\left(y1_j^{\text{line}}, y2_j^{\text{line}}\right) \tag{4.28}$$

We also check to see if the particle centre lies above the line, or $y_i > max\left(y1_j^{\text{line}}, y2_j^{\text{line}}\right)$, and if it is true then:

$$y^{\text{line}} = max\left(y1_j^{\text{line}}, y2_j^{\text{line}}\right) \tag{4.29}$$

Referring to Figure 4.7, for interaction with non-vertical boundaries the following identities are automatically allocated:

$$x^{\text{line}} = \frac{x_i + m_j^{\text{line}}\left(y_i - c_j^{\text{line}}\right)}{\left(m_j^{\text{line}}\right)^2 + 1} \tag{4.30}$$

$$y^{\text{line}} = m_j^{\text{line}}\, x^{\text{line}} + c_j^{\text{line}} \tag{4.31}$$

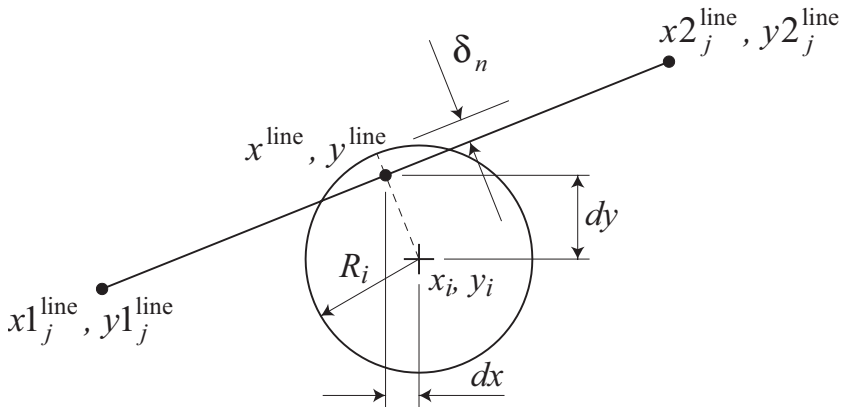

Figure 4.7 Overlap between a particle and a non-vertical line

We check to see if the approximate point of intersection lies to the left of the line, or $x^{\text{line}} < x1_j^{\text{line}}$, and if it is true then:

$$x^{\text{line}} = x1_j^{\text{line}} \tag{4.32}$$

We also check to see if the approximate point of intersection lies to the right of the line, or $x^{\text{line}} > x2_j^{\text{line}}$, and if it is true then:

$$x^{\text{line}} = x2_j^{\text{line}} \tag{4.33}$$

These inequalities are checked to ensure that the particles interacting with the line endpoints do not cause the program to react as if a sudden large overlap has occurred. Once these identities have been determined, we let:

$$dx = x^{\text{line}} - x_i \tag{4.34}$$

$$dy = y^{\text{line}} - y_i \tag{4.35}$$

For the general vertical wall case presented in Figure 4.6, *dy* is zero therefore we let:

$$(dn)^2 = (dx)^2 \tag{4.36}$$

$$d_{ij} = R_i \tag{4.37}$$

If $(dn)^2 < (d_{ij})^2$ particle-boundary interaction occurs and the force calculation routine must be executed. The virtual overlap of the particles is thus given by:

$$\delta_n = max(0,\, R_i - dn) \tag{4.38}$$

For the general case where a non-vertical wall is considered as presented in Figure 4.7, we let:

$$(dn)^2 = (dx)^2 + (dy)^2 \tag{4.39}$$

$$d_{ij} = R_i \tag{4.40}$$

If $(dn)^2 < (d_{ij})^2$ particle-boundary interaction occurs and the force calculation routine must be executed. The virtual overlap of the particles is thus given by:

$$\delta_n = max(0,\, R_i - dn) \tag{4.41}$$

As for the particle interaction with a straight boundary, a few geometric definitions must be described before examining possible interactions with curved boundaries. Referring to Figure 4.8, the angle of the particle with reference to the arc (Φ_{ij}) must be calculated:

$$\Phi_{ij} = cos^{-1}\left(1 - \frac{ASQ}{2\ RSQ}\right) \tag{4.42}$$

where:

$$RSQ = \left[x_i - Xc_j^{\text{arc}}\right]^2 + \left[y_i - Yc_j^{\text{arc}}\right]^2 \tag{4.43}$$

$$ASQ = \left[x_i - Xc_j^{\text{arc}} - (RSQ)^{1/2}\right]^2 + \left[y_i - Yc_j^{\text{arc}}\right]^2 \tag{4.44}$$

The particle in Figure 4.8 has its mass centre above the centre of the arc. There are conditions which govern other cases, for example where the centre of the arc has a greater y-position or the arc and particle interaction occurs in a different quadrant. These however are minor and can be solved with minimal algebraic addition or subtraction and hence will not be discussed further. Therefore limiting the explanation to the situation shown in Figure 4.8, the coordinates of the approximate intersection point can be found from:

$$x^{\text{arc}} = Xc_j^{\text{arc}} + R_j^{\text{arc}}\, cos\,\Phi \tag{4.45}$$

$$y^{\text{arc}} = Yc_j^{\text{arc}} + R_j^{\text{arc}}\, sin\,\Phi \tag{4.46}$$

We let:

$$dx = x^{\text{arc}} - x_i \tag{4.47}$$

$$dy = y^{\text{arc}} - y_i \tag{4.48}$$

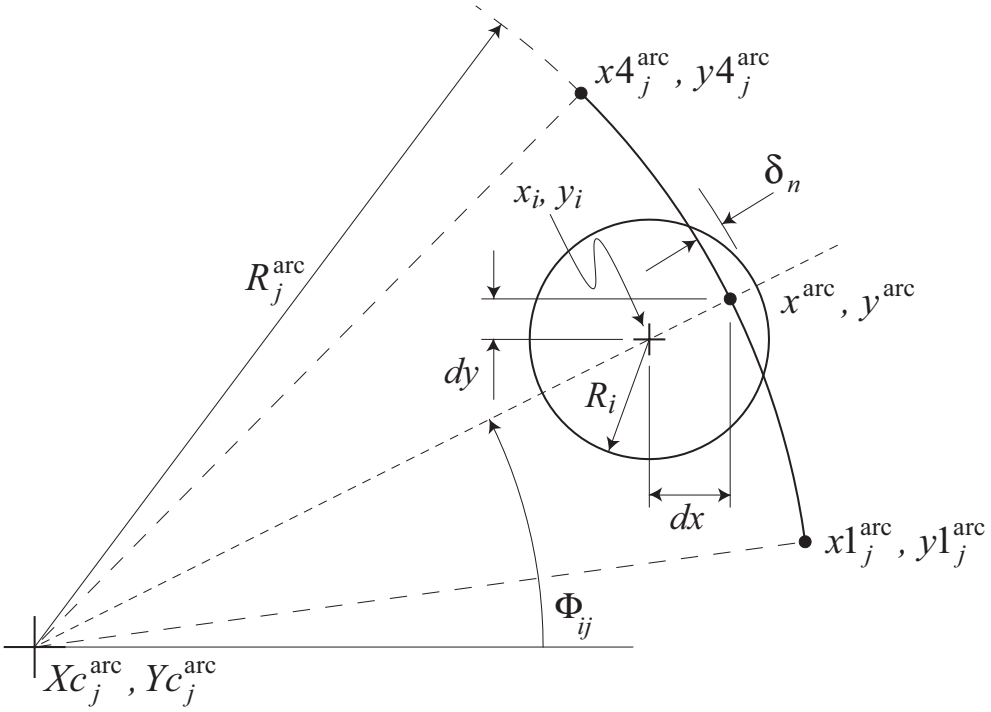

Figure 4.8 Overlap between a particle and an arc

Now the displacement difference *dn* and the perpendicular from the particle centre through the contact point to the particle radius d_{ij} can be given by:

$$(dn)^2 = (dx)^2 + (dy)^2 \tag{4.49}$$

$$d_{ij} = R_i \tag{4.50}$$

If $(dn)^2 < (d_{ij})^2$ particle-boundary interaction occurs and the force calculation routine must be executed. The virtual overlap of the particles is thus given by:

$$\delta_n = max(0, R_i - dn) \tag{4.51}$$

4.3.3 Further Boundary Aspects

4.3.3.1 Modelling Moving Boundaries

In the transfer of materials through a chute, the belt motion of the discharging and receiving conveyors is an important design consideration and hence must be modelled. The kinematics of such moving boundaries in the work is modelled using quasi-kinematic surface motion. This can be utilised as there is no change in the position of the surface with respect to the global reference frame. Basically, pre-defined contact point velocities are applied to the surface of the boundary up to a nominated perpendicular distance above the belt. The applied velocity vectors are collinear to the two-dimensional boundary surface. For the current work, the velocity profiles given to the material upon the simulated belt can range from simple uniform distributions to non-linear profiles of high order, and the specific profiles used will be detailed further in the simulation setups.

4.3.3.2 Periodic Boundaries

The computing capacity currently available limits the total number of particles that can be realistically used in a DEM simulation to be significantly less than the actual number of particles existing in the transfer of material through a chute system. Therefore to increase computing efficiency, *periodic boundaries* are utilised. The periodic boundaries allow a particle to pass out of a user specified section of the domain and automatically reappear at another section. For truly periodic conditions (Jensen et al. 1999), the inlet and outlet sections are opposing boundaries with particles exiting one side and reappearing at the other with the same y-coordinate (or similar geometric condition) and velocity with which it left. The control volume is hence constant. Truly periodic boundaries are very useful when examining particular sections of particle flow traveling in a constant direction, as for particulate flows down inclined chutes, as mentioned earlier. However, for examining systems where specifics of particulate motion against different shaped surfaces are required, a variation is necessary, where only certain portions of the boundaries allow particles to exit or re-enter. The specifics of the periodic boundaries utilised for the current work will be detailed in Chapter Seven.

To illustrate the concept, consider the case shown in Figure 4.9 (a) which is similar to the case illustrated by Jensen et al. (1999). Basically as particle *i* passes out the right-hand side boundary at vertical position y_1, another particle with identical translational and rotational motion is introduced at the left boundary with the same vertical position y_1. As particle *i* passes through the right-hand boundary, its position is (x_1, y_1) with total rotation θ_1. The new particle *i'* that is introduced on the left-hand boundary has position $(x_1 - L, y_1)$ and rotation θ_1 as shown in Figure 4.9 (b). Also during this period of time, the particles have exactly the same kinematics ($v_{x,i'} = v_{x,i}$, $v_{y,i'} = v_{y,i}$, $\omega_{i'} = \omega_i$). This is just one particular case, with the numbers and sizes of the periodic boundaries chosen at the user's discretion.

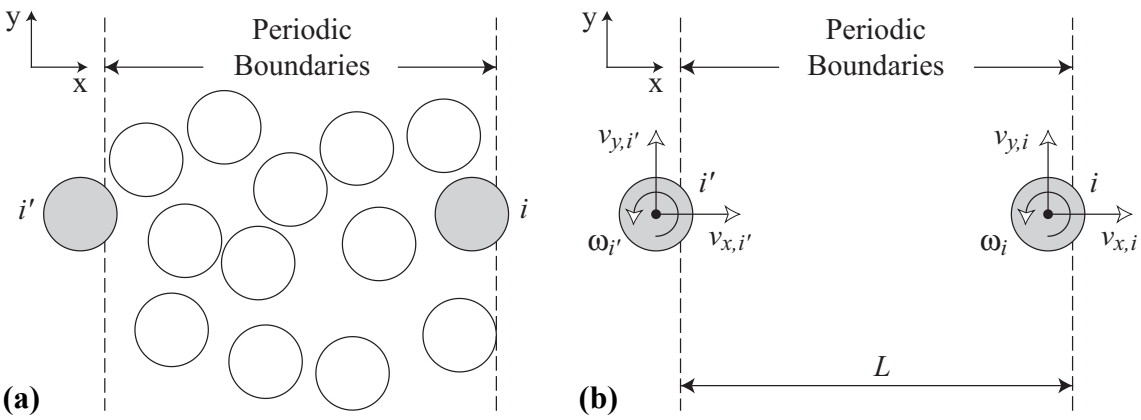

Figure 4.9 **(a)** An assembly of spherical particles with periodic boundaries at left and right hand sides; **(b)** Introduction of particle *i'* at left hand periodic boundary as particle *i* leaves right hand periodic boundary (adapted from Jensen et al. 1999).

4.3.4 Governing Equations

A particle in a large assembly of spheres can undergo two types of motion, translational and rotational, depending on the forces and torques acting on it, which may come from its interactions with neighbouring particles or with boundary elements. The distinct element method allows for unlimited translational and rotational movements of the solids. By applying Newton's second law of motion to the motion of each individual

particle at any time t, the governing equation for the translational motion of particle i can be written as:

$$m_i \frac{d\mathbf{v}_i}{dt} = m_i \mathbf{g} + \sum_{j=1}^{k_i} \left(\mathbf{F}_n + \mathbf{F}_t \right)_{ij} \tag{4.52}$$

where m_i is the mass of particle i given by $m_i = 4/3\,\pi R_i^3 \rho_i$ for a spherical particle, and $\mathbf{v}_i$ (= $\dot{\mathbf{x}}_i + \dot{\mathbf{y}}_i$) is the velocity of particle i. The forces involved are the gravitational force, $m_i\mathbf{g}$, and the inter-particle force (comprising the normal contact force $\mathbf{F}_n$ and tangential contact force $\mathbf{F}_t$) between particles i and j. This inter-particle force is summed over the k_i particles in contact with particle i.

The gravitational force acts on the mass centre of particle i, whilst the inter-particle force acts at the contact point between particles i and j. The inter-particle force will generate a torque $\mathbf{T}_{ij}$ causing particle i to rotate. For a spherical particle of radius R_i, $\mathbf{T}_{ij}$ is given by:

$$\mathbf{T}_{ij} = \mathbf{R}_i \times \mathbf{F}_t \tag{4.53}$$

Where $\mathbf{R}_i$ is a vector of magnitude R_i from the mass centre of the particle to the contact point and $\mathbf{F}_t$ is the tangential contact force. Thus the governing equation for the rotational motion of particle i is:

$$I_i \frac{d\omega_i}{dt} = \sum_{j=1}^{k_i} \mathbf{T}_{ij} \tag{4.54}$$

Where ω_i is the angular velocity, and I_i is the moment of inertia of particle i, given by $I_i = 2/5\, m_i R_i^2$ for a spherical particle.

The inter-particle forces involved in Eq. (4.52) are determined from their normal and tangential components, $\mathbf{F}_n$ and $\mathbf{F}_t$, which depend on the normal and tangential deformations δ_n and δ_t respectively. As the technique is explicit, each particle

communicates only with its nearest neighbours which results in sets of unconnected equations describing its motion. The next section details the models available to quantify the inter-particle forces.

4.3.5 Modelling of Contact Forces

The particles in the multi-body system interact with each other and boundaries at contact points only through normal and tangential forces. The influence of the tangential friction traction on the normal pressure and contact area during a collision is generally small and can be neglected (Johnson 1985), allowing the normal and tangential contact forces to be calculated separately. There are a number of models that have been proposed for the evaluation of the normal inter-particle contact forces. These can be broadly grouped into three categories (Xu 1997): the linear model, the non-linear model, and the hysteretic model. Similarly, in the tangential direction, linear, non-linear and hysteretic models have been developed and will be shown in Section 4.3.5.2. The tangential contact law for evaluation of tangential inter-particle contact forces is more complicated than that for normal forces, particularly when considering non-linear laws. This renders it is more difficult to derive than those for normal contacts as the current value of the tangential contact force may depend upon the history and amplitude of the normal contact force, and there is also the possibility of slip occurring in the contact area. A few of the normal and tangential inter-particle force models that have been commonly used for DEM shall now be presented, along with the contact force model utilised for the current work.

4.3.5.1 Normal Inter–Particle Contacts

The simplest of the models for evaluation of normal inter-particle forces is the normal linear contact model, which assumes that the relative displacement occurs only in the contact area, and the normal contact force between two discrete particles is directly proportional to their deformation. The original work of Cundall & Strack (1979) utilised this model.

However, modelling a force that leads to inelastic collisions requires at least a repulsion term and a term that allows some sort of dissipation. Usually the normal force model

just described is modified to include a damping term that irreversibly extracts energy from the motion of the particles. The simplest and most commonly used normal force model with these properties is the linear spring-dashpot:

$$F_n = -K_n\delta_n - \gamma_n\dot{\delta}_n \tag{4.55}$$

where γ_n is the damping constant, $\dot{\delta}_n$ is the rate of change of the distance between centres of the colliding particles, and K_n is related to the stiffness of a spring whose elongation or the normal overlap is δ_n. This model was utilised by Walton (1982b).

Further refinement of the normal force model can be achieved by omitting the velocity-dependent damping component and utilising deformation-dependent damping, such as the non-linear hysteretic contact law of Sadd et al. (1993, 2000). This approach is preferable because plasticity is a phenomenon related to displacements and not velocity (Di Renzo & Di Maio 2004). This type of law is among the most complicated force displacement models as the different loading and unloading behaviours are considered. Energy is automatically dampened during a cycle in proportion to the amount of deformation of each particle, simulating work hardening and plasticity effects. Sadd et al. (1993, 2000) considered a non-linear relationship between the normal contact force and relative displacement between two particles, and used a simplified relation that appears to match with the approximate solution of Johnson (1985). In their model, the normal force varied with 1.4 power of deformation. In other words, the overlap δ_n would be raised to the power of 1.4.

For the current work, a form of deformation-dependent damping will also be used in the normal direction. Walton & Braun (1986a, 1986b) used an empirical normal force model that approximates the behaviour observed in experiments and finite element calculations (described in (Walton 1992)) of an elastic-perfectly plastic sphere in contact with a rigid surface. The two-dimensional disk interaction was approximated with a partially latching-spring model, consisting of a bilinear spring model for the normal-direction force and a non-linear, hysteretic model for the tangential force, and is shown in Figure 4.10. This particular model (applied to spherical particles) is used for

the current work, with the normal force-displacement (NFD) relationship a function of the form (Walton & Braun 1986a, 1986b):

$$F_n = \begin{cases} K_{n1}\delta_n^a & \dot{\delta}_n \geq 0 \quad (loading) \\ K_{n2}(\delta_n - \delta_{n0})^a & \dot{\delta}_n < 0 \quad (unloading) \end{cases} \tag{4.56}$$

where F_n is the normal force, K_{n1} and K_{n2} are the normal stiffness coefficients for the loading and unloading stage respectively, δ_n is the normal overlap (relative displacement of the centres of the two spheres), δ_{n0} is the residual displacement after complete unloading (the value where the unloading curve goes to zero), and a is the index allowing for differing loading and unloading paths. Energy is automatically dampened during a cycle in proportion to the amount of deformation of each particle. The stiffness coefficients are chosen to be large enough to ensure that the overlap remains small compared to particle size. Note that $K_{n2} > K_{n1}$ and no negative (or tensile) values are allowed for F_n meaning $F_n \geq 0$ is always applicable.

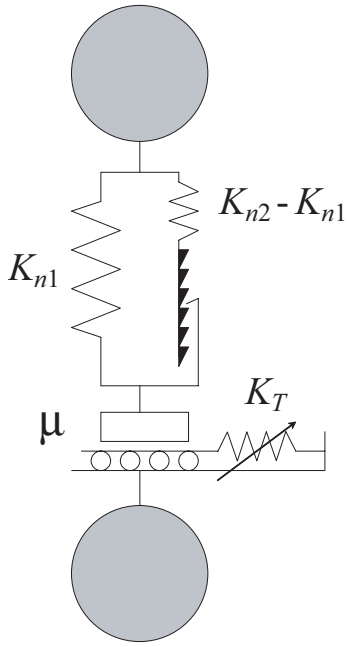

Figure 4.10 Schematic of partially-latching spring model (Walton & Braun 1986b)

In this model, for the index $a = 1$, the normal force has a linear loading curve (with a slope K_{n1}) and a steeper linear unloading curve (with slope K_{n2}). Many investigations (Drake & Walton 1995, Hanes & Walton 2000, Vemuri et al. 1998, Vu-Quoc et al. 2000, Walton 1992, Walton 1993a, Walton & Braun 1986a, 1986b, Wightman et al. 1998, Walton et al. 1991), have utilised $a = 1$ in this particular model. During the loading stage, only the spring with stiffness K_{n1} functions, since the latch device allows free sliding. During unloading the latch device locks, making both springs with stiffness K_{n1} and stiffness $(K_{n2} - K_{n1})$ work simultaneously, giving the resulting stiffness K_{n2}. Figure 4.11 depicts this particular normal force-displacement relationship. Initial loading is along the line from point *a* to point *b*, with slope K_{n1}. If unloading is initiated after reaching point *b* then it will be along the line from *b* to *c*. Reloading from point *c* follows the path *c*, *b*, *d* and subsequent unloading from point *d* follows the path *d*, *f*. This illustrates how the normal force model exhibits a position dependent hysteresis. The energy dissipated by the system is given by the area of the triangle *abc*, or *adf* if reloading occurred.

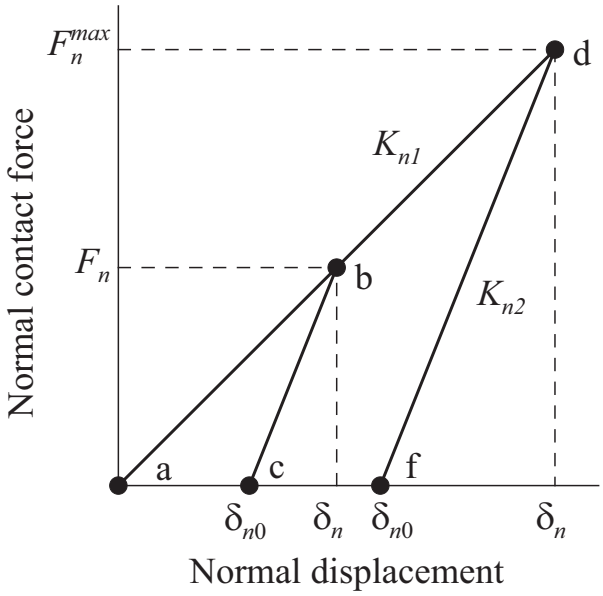

Figure 4.11 Schematic of force-displacement curve used to describe inelastic normal direction forces acting between two colliding spheres (adapted from Walton & Braun 1986b)

The slope of the unloading/reloading curve, K_{n2}, can be set to increase linearly with the maximum force reached during a contact, or it can be set to a constant value. If the unloading slope K_{n2} was independent of the past load history (hence a fixed value), then a constant coefficient of restitution results given by:

$$\varepsilon = \sqrt{K_{n1} / K_{n2}} \tag{4.57}$$

The coefficient of restitution ε is simply the fraction of energy that is returned at the end of a complete load-unload cycle and can be described by (Vu-Quoc et al. 2001):

$$\varepsilon = \sqrt{\frac{area\ under\ unloading\ curve}{area\ under\ loading\ curve}} \tag{4.58}$$

The coefficient of restitution allows the incorporation of collision inelasticity into the simulation. In general, the coefficient of restitution has a constant value for given particle properties. In the variable coefficient of restitution mode, the unloading slope, K_{n2}, is allowed to increase linearly with the magnitude of the maximum force ever experienced by the contact:

$$K_{n2} = K_{n1} + SF_n^{max} \tag{4.59}$$

In this model, the coefficient of restitution depends on the relative velocity of approach, v_0, as given by (Walton & Braun 1986b)

$$\varepsilon = \left[\omega_0 / \left(Sv_0 + \omega_0\right)\right]^{1/2} \tag{4.60}$$

where:

$$\omega_0 = \left(2K_{n1} / m_{ij}\right)^{1/2} \tag{4.61}$$

where S is an empirically determined model parameter and the effective mass of the particles acting in series is given by:

$$m_{ij} = \frac{m_i m_j}{m_i + m_j} \tag{4.62}$$

Experimental evidence for this model and finite element calculations that this model imitates are discussed in the work of Walton (1992). For the plastic impacts of a sphere, the coefficient of restitution is proportional to $\dot{\delta}_n^{-1/4}$ (Johnson 1985).

For a non-linear loading curve, $a \neq 1$ in Eq. (4.56). For the current work, a Hertzian type model was utilised, where the power a of the displacement terms in Eq. (4.56) was raised to 3/2, resulting in the initial loading being the same form as Hertz' elastic solution. Generally the coefficient of normal stiffness according to Hertz theory can be found from (Vu-Quoc & Zhang 1999a, 1999a):

$$K_{n1} = \frac{4}{3} E_{ij} \sqrt{R_{ij}} \tag{4.63}$$

with the relative contact curvature R_{ij} and equivalent elastic modulus E_{ij} respectively given by:

$$R_{ij} = \frac{R_i R_j}{R_i + R_j} \tag{4.64}$$

$$E_{ij} = \frac{E_i E_j}{E_i\left(1-\nu_j^2\right) + E_j\left(1-\nu_i^2\right)} \tag{4.65}$$

where R_i and R_j are the radii of the two spheres, ν_i and ν_j being the Poisson's ratios, and E_i and E_j the Young's moduli of the materials of the two spheres. For the collision of a sphere i with a wall j, the same relation applies for E_{ij}, whereas $R_{ij}=R_i$. For the current work however, the particulate material simulated in Chapter Seven (coal) did not have readily available material properties. Therefore the stiffness's were chosen based upon limiting particle overlap. The coefficient of restitution corresponding to the Hertzian type model is given by (Walton 1992):

$$\varepsilon = \sqrt[3]{\frac{K_{n1}}{K_{n2}}} \tag{4.66}$$

Thus with the normal loading stiffness K_{n1} and the coefficient of restitution ε given, the normal unloading stiffness K_{n2} can be calculated.

4.3.5.2 Tangential Inter–Particle Contacts

The simplest tangential contact model to implement just applies the Coulomb law (product of the normal force and the coefficient of friction) of dynamic friction, giving the shear force relation as:

$$F_t = -\mu \cdot \|F_n\| \cdot sign(v_t) \tag{4.67}$$

where μ is the coefficient of friction and v_t is the tangential velocity. This model has been used by Haff & Werner (1986). The problem with this model is that the shear force can only slow v_t down to zero and thus cannot provide reversal of tangential velocity. This force scheme also does not account for tangential elasticity.

Another straightforward tangential contact model to implement is the linear tangential contact law, which assumes the linear relationship between the tangential force and relative displacement, similar to the linear normal contact discussed in Section 4.3.5.1. The proportionality constant is given by tangential elasticity. The friction limit given by the Coulomb law is used to determine whether slip occurs between two particles or not when calculating the tangential force.

$$F_t = min(\|K_t \delta_t\|, \|\mu F_n\|) \cdot sign(\delta) \tag{4.68}$$

where K_t is some tangential stiffness and δ_t is the displacement in the tangential direction that has taken place since contact was first established. This particular model was introduced by Cundall & Strack (1979). Certain tangential contact models also utilised a damping term as a dissipative mechanism in addition to the linear relationship described by Eq. (4.68), such as that used by Xu (1997).

A number of non-linear tangential contact laws are derived from Mindlin's (1949) elastic frictional sphere contact force model. Mindlin expanded on the Hertz contact stress theory by also considering oblique forces. The theory shows that when a tangential force is applied, an annulus of micro-slip develops surrounding an inner region of sticking in the contact area. The annulus of micro-slip grows as the force increases until ultimately the whole contact area goes into a state of slip. A subsequent publication by Mindlin & Deresiewicz (1953) showed that the stress state and the annulus of slip in the contact area is dependent not only upon the initial state of loading but upon the entire past history of loading and the instantaneous relative rates of change of the normal and tangential forces.

Modelling of the full Mindlin-Deresiewicz theory in a multi-body simulation is impractical (Els 2003), and therefore models have been developed that provide good approximations, such as the Walton & Braun (1986b) model, and its corrected and improved editions by Lesburg et al. (1997), Vu-Quoc (2000), Vu-Quoc & Zhang (1999a, 1999b) and Vu-Quoc et al. (2004). Walton & Braun (1986b) proposed a one-dimensional approximation to Mindlin's (1949) and Mindlin & Deresiewicz's (1953) contact mechanics theory where the effective tangential stiffness of a contact decreases with tangential displacement until it is zero when full sliding occurs.

Walton (1993a) extended this one-dimensional approximation into a two-dimensional (surface) model, where the tangential displacement parallel to the current friction force $\Delta\delta_{t,||}$ and the displacement perpendicular to the existing friction force $\Delta\delta_{t,\perp}$ are considered separately. The tangential friction force F_t is set equal to the vector sum of $F_{t,\perp}$ and $F_{t,||}$, and checked to ensure it does not exceed the total friction force limit given by the Coulomb law. After contact occurs between particles, tangential forces build up non-linearly resulting in displacements in the tangent plane of contact.

As the current work is in two dimensions, the one-dimensional tangential force-displacement model (TFD) approximated by Walton & Braun (1986b) is used. For future work purposes, the implementation theory of the two-dimensional (surface) TFD model of Walton (1993a) is derived in Appendix II. The derivation is readily useable in

the current work by letting the perpendicular tangential displacement component equal zero.

In the tangential direction, let F_t^N and F_t^{N+1} be the tangential force magnitude at time t^N and time t^{N+1} respectively. The relationship between F_t^N and F_t^{N+1} is given by the following incremental formula (Drake & Walton 1995, Vemuri et al. 1998, Vu-Quoc et al. 2000, Walton 1993a, Walton & Braun 1986b):

$$F_t^{N+1} = F_t^N + K_t^N \, \Delta\delta_t^N \tag{4.69}$$

where K_t^N is the tangential stiffness coefficient at time t^N and $\Delta\delta_t^N$ is the incremental tangential displacement at time t^N. The term $\Delta\delta_t^N$ will be calculated in Section 4.3.5.3. The effective tangential stiffness K_t^N in the direction parallel to the existing friction force is a function of the normal force F_n^N, the tangential force F_t^N, and F_t^*, which is the value of the tangential force F_t at the last turning point, as follows (Hanes & Walton 2000, Vemuri et al. 1998, Vu-Quoc et al. 2000, Walton 1993a, Walton & Braun 1986b, Walton et al. 1991):

$$K_t^N = \begin{cases} K_t^0 \left(1 - \dfrac{F_t^N - F_t^*}{\mu F_n^N - F_t^*}\right)^b & \left(for\ F_t\ increasing\right), \\ K_t^0 \left(1 - \dfrac{F_t^* - F_t^N}{\mu F_n^N + F_t^*}\right)^b & \left(for\ F_t\ decreasing\right), \end{cases} \tag{4.70}$$

where K_t^0 is the initial tangential stiffness and μ is the coefficient of friction. The value of F_t^* starts as zero (initial loading) and is subsequently set to the value of the tangential force F_t, whenever the magnitude changes from increasing to decreasing, or vice versa. The model assumes that in each time step, the normal force changes only by a small amount that will not significantly influence tangential force. For the thesis, the fixed parameter *b* is set to 1/3 to agree with Mindlin's frictional sphere theory detailed in his works (Mindlin 1949, Mindlin & Deresiewicz 1953).

The TFD curve for the current work is shown in Figure 4.12. The force-displacement state ❶ corresponds to the case with F_n constant and F_t decreasing. As the tangential force F_t decreases to zero, the tangential displacement δ_t decreases to a non-zero value δ_r, which is the residual tangential displacement. This residual displacement is a result of the energy loss that occurs due to the presence of friction on the contact area (Vu-Quoc et al. 2001). The area inside the hysteresis loop is equal to the energy dissipation in one cycle of the tangential force (Vu-Quoc et al. 2004).

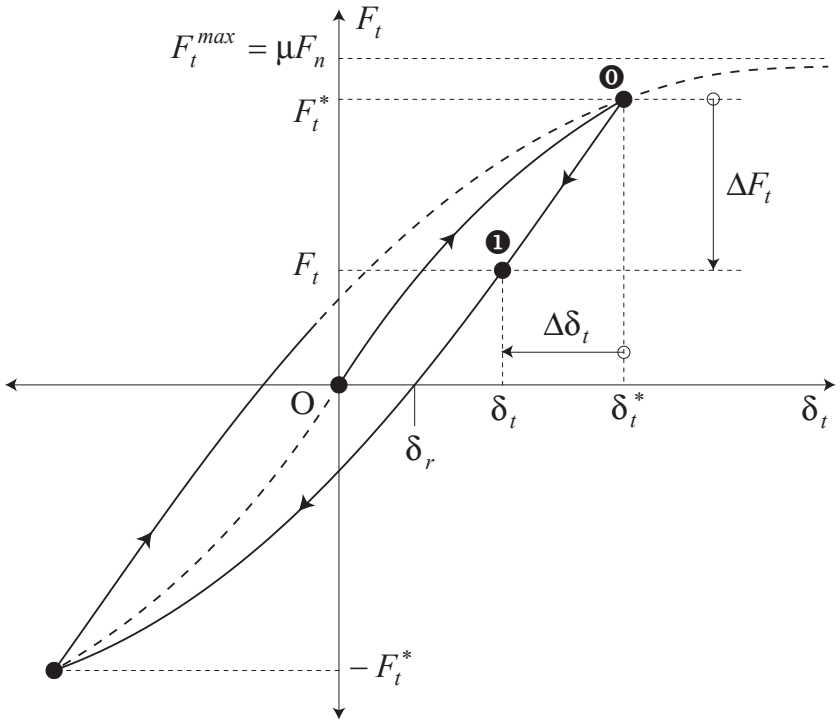

Figure 4.12 Elastic-frictional contact: TFD curve for constant F_n and varying F_t showing hysteresis loop and residual displacement (adapted from Vu-Quoc et al. 2004)

If the properties of the material are known, the initial tangential stiffness constant K_t^0 is a function of the equivalent shear modulus G_{ij} and radius R_{ij} and of the actual normal displacement δ_n (Vu-Quoc & Zhang 1999a, 1999b):

$$K_t^0 = 8G_{ij}\sqrt{R_{ij} \cdot \delta_n} \tag{4.71}$$

where:

$$G_{ij} = \frac{G_i G_j}{G_i\left(2-\nu_j\right)+G_j\left(2-\nu_i\right)} \tag{4.72}$$

is the shear modulus of particles *i* and *j* respectively. For the collision of a sphere *i* with a wall *j* the same relation applies for G_{ij}. However as mentioned for the NFD model employed in the current work, certain quantitative properties could not be obtained in the literature, and therefore the initial tangential stiffness constant was set equal to the normal stiffness unless otherwise specified.

4.3.5.3 Implementing Tangential Force-Displacement Model

The implementation of the frictional TFD model outlined in Section 4.3.5.2 into the DEM simulation code involves some algebraic and vector manipulations. This is because the direction of the surface normal at contact changes continuously during a typical contact (Walton 1993a). The time step size in the simulations will be small hence the displacements from one time step to the next are relatively small. The vector quantities are difficult to apply however in the computer code directly. Therefore the necessary working to manipulate the equations into a more useable form is also shown here. For the following work, the basic equations for implementation were taken from relevant sources, and these are both referenced and marked by (♦). The superscripts *N*-1, *N*, and *N*+1 refer to time t^{N-1}, t^N, and t^{N+1} respectively.

Before proceeding the unit vector $\hat{\mathbf{k}}_{ij}^N$ defined in Section 4.3.1 will be manipulated to give a form that is simpler to implement. Let:

$$\mathbf{r}_i^N = x_i^N \mathbf{i} + y_i^N \mathbf{j} \tag{4.73}$$

$$\mathbf{r}_j^N = x_j^N \mathbf{i} + y_i^N \mathbf{j} \tag{4.74}$$

where $\{x_i^N, y_i^N\}$ and $\{x_j^N, y_j^N\}$ are the horizontal and vertical components for the position vector for particles *i* and *j* respectively. From Eq. (4.73) and (4.74) the following algebraic expression can be created:

$$\mathbf{r}_j^N - \mathbf{r}_i^N = \left(x_j^N - x_i^N\right)\mathbf{i} + \left(y_j^N - y_i^N\right)\mathbf{j} \tag{4.75}$$

Also let:

$$dx^N = x_j^N - x_i^N \tag{4.76}$$

$$dy^N = y_j^N - y_i^N \tag{4.77}$$

then substituting Eq. (4.76) and (4.77) into Eq. (4.75) gives:

$$\mathbf{r}_j^N - \mathbf{r}_i^N = dx^N\mathbf{i} + dy^N\mathbf{j} \tag{4.78}$$

Substituting Eq. (4.78) into Eq. (4.1) gives:

$$\hat{\mathbf{k}}_{ij}^N = \frac{dx^N\mathbf{i} + dy^N\mathbf{j}}{\left\|dx^N\mathbf{i} + dy^N\mathbf{j}\right\|} \quad \Rightarrow \quad \hat{\mathbf{k}}_{ij}^N = \frac{dx^N\mathbf{i} + dy^N\mathbf{j}}{\sqrt{\left(dx^N\right)^2 + \left(dy^N\right)^2}} \tag{4.79}$$

Let:

$$\left(dn^N\right)^2 = \left(dx^N\right)^2 + \left(dy^N\right)^2 \tag{4.80}$$

Substituting Eq. (4.79) into Eq. (4.80) and simplifying gives:

$$\hat{\mathbf{k}}_{ij}^N = \left(\frac{dx^N}{dn^N}\right)\mathbf{i} + \left(\frac{dy^N}{dn^N}\right)\mathbf{j} \quad \Rightarrow \quad \hat{\mathbf{k}}_{ij}^N = cn^N\mathbf{i} + sn^N\mathbf{j} \tag{4.81}$$

where:

$$cn^N = \left(dx^N / dn^N\right) \tag{4.82}$$

$$sn^N = \left(dy^N / dn^N\right) \tag{4.83}$$

This form of the unit vector $\hat{\mathbf{k}}_{ij}^N$ is simpler to implement in the DEM computer code. Now in general, the direction of the normal at contact changes continuously, therefore the tangential force vector at time t^N has to be adjusted as follows. Let $\mathbf{F}_{t,old}^N$ be the tangential force vector at the end of the previous time step. Referring to Figure 4.13, the current tangential force vector $\mathbf{F}_t^N$ at time t^N is computed by projecting the vector $\mathbf{F}_{t,old}^N$ onto the current tangent plane to sphere *i* having normal $\hat{\mathbf{k}}_{ij}^N$ (Walton 1993a):

$$\mathbf{F}_{t,0}^N = \hat{\mathbf{k}}_{ij}^N \times \mathbf{F}_{t,old}^N \times \hat{\mathbf{k}}_{ij}^N \quad \Rightarrow \quad \mathbf{F}_{t,0}^N = \mathbf{F}_{t,old}^N - \hat{\mathbf{k}}_{ij}^N \left(\hat{\mathbf{k}}_{ij}^N \cdot \mathbf{F}_{t,old}^N\right) \tag{4.84♦}$$

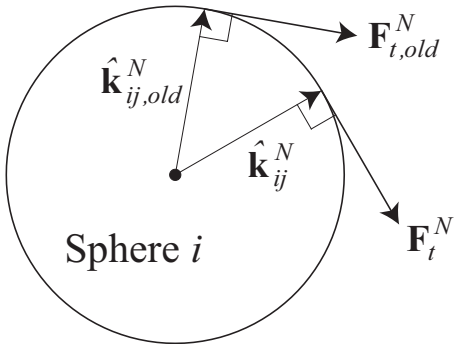

Figure 4.13 Direction change of tangential force (adapted from Vu-Quoc et al. 2000)

Separating $\mathbf{F}_{t,old}^N$ into horizontal and vertical components:

$$\mathbf{F}_{t,old}^N = F\_x_{t,old}^N \mathbf{i} + F\_y_{t,old}^N \mathbf{j} \tag{4.85}$$

and then by substituting Eq. (4.81) and (4.85) into Eq. (4.84) we get:

$$\begin{aligned}\mathbf{F}_{t,0}^{N} &= F\_x_{t,old}^{N}\mathbf{i} + F\_y_{t,old}^{N}\mathbf{j} \\ &\quad - \left(cn^{N}\mathbf{i} + sn^{N}\mathbf{j}\right)\left[\left(cn^{N}\mathbf{i} + sn^{N}\mathbf{j}\right)\cdot\left(F\_x_{t,old}^{N}\mathbf{i} + F\_y_{t,old}^{N}\mathbf{j}\right)\right]\end{aligned} \tag{4.86}$$

Rearranging Eq. (4.86) gives:

$$\mathbf{F}_{t,0}^{N} = F\_x_{t,old}^{N}\mathbf{i} + F\_y_{t,old}^{N}\mathbf{j} - \left(cn^{N}\mathbf{i} + sn^{N}\mathbf{j}\right)\left[cn^{N}F\_x_{t,old}^{N} + sn^{N}F\_y_{t,old}^{N}\right] \tag{4.87}$$

If we let:

$$F_{t,const}^{N} = cn^{N}F\_x_{t,old}^{N} + sn^{N}F\_y_{t,old}^{N} \tag{4.88}$$

then substituting Eq. (4.87) into Eq. (4.88) and simplifying gives:

$$\mathbf{F}_{t,0}^{N} = \left(F\_x_{t,old}^{N} - cn^{N}F_{t,const}^{N}\right)\mathbf{i} + \left(F\_y_{t,old}^{N} - sn^{N}F_{t,const}^{N}\right)\mathbf{j} \tag{4.89}$$

Simplifying further:

$$\mathbf{F}_{t,0}^{N} = F\_x_{t,0}^{N}\mathbf{i} + F\_y_{t,0}^{N}\mathbf{j} \tag{4.90}$$

where:

$$F\_x_{t,0}^{N} = F\_x_{t,old}^{N} - cn^{N}F_{t,const}^{N} \tag{4.91}$$

$$F\_y_{t,0}^{N} = F\_y_{t,old}^{N} - sn^{N}F_{t,const}^{N} \tag{4.92}$$

The following two identities are required for the next step in the process:

$$F\_mag_{t,old}^{N} = \left\| \mathbf{F}_{t,old}^{N} \right\| = \sqrt{\left(F\_x_{t,old}^{N}\right)^{2} + \left(F\_y_{t,old}^{N}\right)^{2}} \tag{4.93}$$

$$F\_mag_{t,0}^{N} = \left\| \mathbf{F}_{t,0}^{N} \right\| = \sqrt{\left(F\_x_{t,0}^{N}\right)^{2} + \left(F\_y_{t,0}^{N}\right)^{2}} \tag{4.94}$$

which are the magnitudes of $\mathbf{F}_{t,old}^{N}$ and $\mathbf{F}_{t,0}^{N}$ respectively. The projected friction force $\mathbf{F}_{t,0}^{N}$ is normalised to the old (previous) magnitude, so that $\left\| \mathbf{F}_{t}^{N} \right\| = \left\| \mathbf{F}_{t,old}^{N} \right\|$, to obtain a new virgin loading for the friction force $\mathbf{F}_{t}^{N}$ (Walton 1993a):

$$\mathbf{F}_{t}^{N} = \left\| \mathbf{F}_{t,old}^{N} \middle/ \mathbf{F}_{t,0}^{N} \right\| \mathbf{F}_{t,0}^{N} \qquad (4.95\blacklozenge)$$

Substituting Eq. (4.93) and (4.94) into Eq. (4.95) gives:

$$\mathbf{F}_{t}^{N} = \left(\frac{F\_mag_{t,old}^{N}}{F\_mag_{t,0}^{N}} \right) \left(F\_x_{t,0}^{N}\mathbf{i} + F\_y_{t,0}^{N}\mathbf{j} \right) \qquad (4.96)$$

Simplifying further:

$$\mathbf{F}_{t}^{N} = F\_x_{t}^{N}\mathbf{i} + F\_y_{t}^{N}\mathbf{j} \qquad (4.97)$$

where:

$$F\_x_{t}^{N} = \left(F\_mag_{t,old}^{N} \; F\_x_{t,0}^{N} \right) \middle/ F\_mag_{t,0}^{N} \qquad (4.98)$$

$$F\_y_{t}^{N} = \left(F\_mag_{t,old}^{N} \; F\_y_{t,0}^{N} \right) \middle/ F\_mag_{t,0}^{N} \qquad (4.99)$$

By letting:

$$F\_mag_{t}^{N} = \left\| \mathbf{F}_{t}^{N} \right\| = \sqrt{\left(F\_x_{t}^{N} \right)^2 + \left(F\_y_{t}^{N} \right)^2} \qquad (4.100)$$

we can manipulate the unit vector in the direction of the virgin loading $\hat{\mathbf{t}}_{ij}^{N} = \mathbf{F}_{t}^{N} \middle/ \left\| \mathbf{F}_{t}^{N} \right\|$ to a more useable form:

$$\hat{\mathbf{t}}_{ij}^{N} = F\_x_{t,u}^{N}\mathbf{i} + F\_y_{t,u}^{N}\mathbf{j} \qquad (4.101)$$

where:

$$F\_x_{t,u}^{N} = F\_x_{t}^{N} \big/ F\_mag_{t}^{N} \tag{4.102}$$

$$F\_y_{t,u}^{N} = F\_y_{t}^{N} \big/ F\_mag_{t}^{N} \tag{4.103}$$

Observing Eq. (4.84) and (4.95) it can be seen that the magnitude of $\mathbf{F}_t^N$ is the same as that of $\mathbf{F}_{t,old}^N$, whereas the direction of $\mathbf{F}_t^N$ is that of the projection of $\mathbf{F}_{t,old}^N$ into the tangent plane with normal $\hat{\mathbf{k}}_{ij}^N$.

The relative surface displacement vector $\Delta\boldsymbol{\delta}_t^N$ at time t^N is given by (Walton 1993a):

$$\begin{aligned}\Delta\boldsymbol{\delta}_t^N = &\left[\hat{\mathbf{k}}_{ij}^N \times \left(\mathbf{v}_j^{N-1/2} - \mathbf{v}_i^{N-1/2}\right) \times \hat{\mathbf{k}}_{ij}^N \right. \\ &\left. + R_i \left(\boldsymbol{\omega}_i^{N-1/2} \times \hat{\mathbf{k}}_{ij}^N\right) + R_j \left(\boldsymbol{\omega}_j^{N-1/2} \times \hat{\mathbf{k}}_{ij}^N\right)\right] \Delta t\end{aligned} \tag{4.104♦}$$

where $\{\mathbf{v}_i^{N-1/2}, \mathbf{v}_j^{N-1/2}\}$ are the velocity vectors and $\{\boldsymbol{\omega}_i^{N-1/2}, \boldsymbol{\omega}_j^{N-1/2}\}$ are the angular velocity vectors of spheres *i* and *j* respectively, all at time $t^{N-1/2}$ and Δt the time step size. The following approximation is made (Vu-Quoc et al. 2000):

$$\left(\mathbf{v}_j^{N-1/2} - \mathbf{v}_i^{N-1/2}\right)\Delta t \approx \Delta\mathbf{r}_{ij}^N = \mathbf{r}_{ij}^N - \mathbf{r}_{ij}^{N-1} \tag{4.105♦}$$

in Eq. (4.104) for $\Delta\boldsymbol{\delta}_t^N$ in the implementation for the TFD model. The term $\Delta\mathbf{r}_{ij}^N$ is the change in the relative position vector during the last time step, and is resolved into horizontal and vertical components for simpler algebraic manipulation:

$$\Delta\mathbf{r}_{ij}^N = \Delta r\_x^N \mathbf{i} + \Delta r\_y^N \mathbf{j} \tag{4.106}$$

where:

$$\Delta r\_x^N = dx^N - dx^{N-1} \tag{4.107}$$

$$\Delta r\_y^N = dy^N - dy^{N-1} \tag{4.108}$$

Now substituting Eq. (4.81) and (4.106) into Eq. (4.104) gives:

$$\begin{aligned}\Delta\boldsymbol{\delta}_t^N &= \left(\Delta r\_x^N\mathbf{i} + \Delta r\_y^N\mathbf{j}\right)\\ &\quad - \left(cn^N\mathbf{i} + sn^N\mathbf{j}\right)\left[\left(cn^N\mathbf{i} + sn^N\mathbf{j}\right)\cdot\left(\Delta r\_x^N\mathbf{i} + \Delta r\_y^N\mathbf{j}\right)\right]\\ &\quad + \left[R_i\left(\omega_i^{N-1/2}\mathbf{k}\times\left(cn^N\mathbf{i} + sn^N\mathbf{j}\right)\right)\right.\\ &\quad \left. + R_j\left(\omega_j^{N-1/2}\mathbf{k}\times\left(cn^N\mathbf{i} + sn^N\mathbf{j}\right)\right)\right]\Delta t\end{aligned} \tag{4.109}$$

Resolving dot products and cross products:

$$\begin{aligned}\Delta\boldsymbol{\delta}_t^N &= \left(\Delta r\_x^N\mathbf{i} + \Delta r\_y^N\mathbf{j}\right)\\ &\quad - \left(cn^N\mathbf{i} + sn^N\mathbf{j}\right)\left(cn^N\Delta r\_x^N + sn^N\Delta r\_y^N\right)\\ &\quad + \left[R_i\omega_i^{N-1/2}\left(cn^N\mathbf{j} - sn^N\mathbf{i}\right) + R_j\omega_j^{N-1/2}\left(cn^N\mathbf{j} - sn^N\mathbf{i}\right)\right]\Delta t\end{aligned} \tag{4.110}$$

Performing some factorisation:

$$\begin{aligned}\Delta\boldsymbol{\delta}_t^N &= \left[\Delta r\_x^N - \Delta r\_x^N\left(cn^N\right)^2 - \Delta r\_y^N cn^N sn^N\right]\mathbf{i}\\ &\quad + \left[\Delta r\_y^N - \Delta r\_y^N\left(sn^N\right)^2 - \Delta r\_x^N cn^N sn^N\right]\mathbf{j}\\ &\quad + \left(cn^N\mathbf{j} - sn^N\mathbf{i}\right)\left[R_i\omega_i^{N-1/2} + R_j\omega_j^{N-1/2}\right]\Delta t\end{aligned} \tag{4.111}$$

Grouping horizontal and vertical terms together and simplifying yields:

$$\Delta\boldsymbol{\delta}_t^N = \Delta\delta x_t^N\mathbf{i} + \Delta\delta y_t^N\mathbf{j} \tag{4.112}$$

where:

$$\begin{aligned}\Delta\delta x_t^N &= \left[\Delta r\_x^N - \Delta r\_x^N\left(cn^N\right)^2\right.\\ &\quad \left. - \Delta r\_y^N cn^N sn^N - sn^N\left(R_i\omega_i^{N-1/2} + R_j\omega_j^{N-1/2}\right)\Delta t\right]\end{aligned} \tag{4.113}$$

$$\begin{aligned}\Delta\delta y_t^N = \Big[& \Delta r\_y^N - \Delta r\_y^N \left(sn^N\right)^2 \\ & - \Delta r\_x^N cn^N sn^N + cn^N \left(R_i \omega_i^{N-1/2} + R_j \omega_j^{N-1/2}\right)\Delta t\Big]\end{aligned} \tag{4.114}$$

Now recall that $\hat{\mathbf{t}}_{ij}^N$ (Eq. (4.101)) is the direction of the projection of $\mathbf{F}_{t,old}^N$ on the tangent plane having normal $\hat{\mathbf{k}}_{ij}^N$ (Eq. (4.81)). The direction $\hat{\mathbf{t}}_{ij}^N$ is considered as the direction of continuing application of the tangential force $\mathbf{F}_t^N$. Therefore the loading history in the TFD model is to be applied in this direction. The displacement in the previous time step is (Walton 1993a):

$$\Delta\boldsymbol{\delta}_t^N = \left(\Delta\boldsymbol{\delta}_t^N \cdot \hat{\mathbf{t}}_{ij}^N\right)\hat{\mathbf{t}}_{ij}^N \tag{4.115♦}$$

Substituting Eq. (4.101) and (4.112) into Eq. (4.115) gives:

$$\Delta\boldsymbol{\delta}_t^N = \left[\left(\Delta\delta x_t^N \mathbf{i} + \Delta\delta y_t^N \mathbf{j}\right)\cdot\left(F\_x_{t,u}^N \mathbf{i} + F\_y_{t,u}^N \mathbf{j}\right)\right]\left(F\_x_{t,u}^N \mathbf{i} + F\_y_{t,u}^N \mathbf{j}\right) \tag{4.116}$$

Resolving the dot product gives:

$$\Delta\boldsymbol{\delta}_t^N = \left[\Delta\delta x_t^N F\_x_{t,u}^N + \Delta\delta y_t^N F\_y_{t,u}^N\right]\left(F\_x_{t,u}^N \mathbf{i} + F\_y_{t,u}^N \mathbf{j}\right) \tag{4.117}$$

Simplifying gives:

$$\Delta\boldsymbol{\delta}_t^N = \Delta\delta p_{const}^N \left(F\_x_{t,u}^N \mathbf{i} + F\_y_{t,u}^N \mathbf{j}\right) \tag{4.118}$$

where:

$$\Delta\delta p_{const}^N = \Delta\delta x_t^N F\_x_{t,u}^N + \Delta\delta y_t^N F\_y_{t,u}^N \tag{4.119}$$

Simplifying further we finally get:

$$\Delta\boldsymbol{\delta}_t^N = \Delta\delta p\_x^N \mathbf{i} + \Delta\delta p\_y^N \mathbf{j} \tag{4.120}$$

where:

$$\Delta\delta p\_x^N = \Delta\delta p_{const}^N F\_x_{t,u}^N \tag{4.121}$$

$$\Delta\delta p\_y^N = \Delta\delta p_{const}^N F\_y_{t,u}^N \tag{4.122}$$

If the value of the normal force $\mathbf{F}_n^N$ changes from one time step to the next, then the value of $\mathbf{F}_t^*$ in Eq. (4.70) is scaled in proportion to the change in normal force (Walton 1993a):

$$F_t^* = F_t^* \frac{\left\| \mathbf{F}_n^{N+1} \right\|}{\left\| \mathbf{F}_n^N \right\|} \tag{4.123♦}$$

The effective incremental tangential stiffness K_T^N is determined from Eq. (4.70) with the new scaled value for F_t^* in Eq. (4.123) above substituted in for the old F_t^*. The component of the tangential force along the direction $\hat{\mathbf{t}}_{ij}^N$ is incremented from the projected tangential force $\mathbf{F}_t^N$ in the same direction as Eq. (4.95) (Vu-Quoc et al. 2000):

$$\mathbf{F}_t^{N+1} = \mathbf{F}_t^N + K_T^N \ \Delta\boldsymbol{\delta}_t^N \tag{4.124♦}$$

Substituting Eq. (4.97) and (4.120) into Eq. (4.124) gives:

$$\mathbf{F}_t^{N+1} = \left(F\_x_t^N \mathbf{i} + F\_y_t^N \mathbf{j}\right) + K_T^N \left(\Delta\delta p\_x^N \mathbf{i} + \Delta\delta p\_y^N \mathbf{j}\right) \tag{4.125}$$

Grouping horizontal and vertical components together:

$$\mathbf{F}_t^{N+1} = \left(F\_x_t^N + K_T^N \ \Delta\delta p\_x^N\right)\mathbf{i} + \left(F\_y_t^N + K_T^N \ \Delta\delta p\_y^N\right)\mathbf{j} \tag{4.126}$$

Walton (1993a) describes the following. If both of the conditions $\Delta\boldsymbol{\delta}_t^N \cdot \hat{\mathbf{t}}_{ij}^N < 0$ and $F_t^N + \left(\Delta\boldsymbol{\delta}_t^N \cdot \hat{\mathbf{t}}_{ij}^N\right) K_T^N < 0$ are simultaneously true then, in effect, the direction of $\mathbf{F}_t^N$

has reversed, and in the model the sign of the effective 'remembered' turning point F_t^* is changed (i.e. F_t^* is replaced by - F_t^*) for the next time step. The value given by Eq. (4.126) is checked to ensure it does not exceed the friction limit, i.e.:

$$\left\| \mathbf{F}_t^{N+1} \right\| \leq \mu \left\| \mathbf{F}_n^{N+1} \right\| \tag{4.127}$$

and if it does it is scaled back so its magnitude equals that limit. In other words, the final updated tangential force at time t^{N+1} is set to be (Vu-Quoc et al. 2000):

$$\mathbf{F}_t^{N+1} = min\left(\left\| \mathbf{F}_t^{N+1} \right\|, \left\| \mu \, \mathbf{F}_n^{N+1} \right\| \right) \frac{\mathbf{F}_t^{N+1}}{\left\| \mathbf{F}_t^{N+1} \right\|} \tag{4.128♦}$$

4.4 Summary

The chapter introduced the background and methodology of the distinct element method, and the merits and drawbacks of this numerical technique. Industrial applications of DEM were presented, with a detailed review of DEM applied to transfer chute design in the mining industry. Any areas that were lacking with respect to the current work were identified. The mathematical formulation for DEM was developed in the chapter, with particle-particle and particle-boundary definitions and interactions described. Governing equations were presented, along with a review of normal and tangential contact force models available in literature. The general force-displacement relations used for the current work and implementation of the hysteretic tangential force-displacement model was shown. Chapter Five will now detail the numerical processes and computational aspects required for the current research.

Chapter Five

NUMERICAL METHODS AND COMPUTATION ASPECTS

5.1 Introduction

This chapter will begin with a brief overview of numerical methods available to solve the ordinary differential equations prevalent in DEM. These equations were defined in Chapter Four and govern the translational and rotational motions of a system of particles. Solving the equations will allow the particle positions, velocities and accelerations to be obtained at the next time level from those known at the current time level. The numerical algorithm chosen for the current work shall be described. An outline of contact detection schemes utilised in the literature will be briefly detailed, with the scheme to be used for the current work formulated, and the issue of critical time step selection will be explored. The chapter will end by briefly outlining the graphical techniques used for the visualizations that will be produced (to be shown in Chapters Six and Seven), and also some comments regarding the separate program to facilitate parameter inputs.

5.2 Numerical Methods

5.2.1 Background

Numerical methods based on time integration principles are widely used for solving time dependent problems in a variety of engineering disciplines, such as structural dynamics, fluid dynamics, and molecular dynamics (Xu 1997). The literature search has shown that these numerical methods originated from the field of structural dynamics, in which the branch of discrete element modelling known as Finite Element Methods (FEM) has been applied to solve problems relating to dynamic structural analysis. The majority of developments that have taken place over the years with regards to time integration methods have been in this field of study. The primary aim has been to try

and develop an efficient computational method for the time integration of the differential equations of structural dynamics.

The host of numerical methods developed for integration of structural dynamics' equations will not be presented here, however the reader is referred to the works of Belytschko et al. (1979), Goudreau & Taylor (1972), Hilber & Hughes (1978), Hilber et al. (1977), Hughes & Liu (1978), Hulbert (1992) and Miranda et al. (1989) for reviews and comparisons between methods, and also further background in the topic area. The area of molecular dynamics has also seen numerous developments to ascertain the most suitable time integration method, such as the work of Gear (1971), Swope et al (1982), and Toxvaerd (1982). The following discussion is limited to an overview of the advantages/disadvantages and characteristics of each method. These numerical methods can be readily applied to DEM systems.

The translational and rotational equations of motion in DEM are classified as ordinary differential equations, and are solved using a finite difference method. This numerical technique transforms a calculus problem into an algebra problem by (Hoffman 1992):

1. Discretising the continuous physical domain;
2. Approximating the exact derivatives in the ordinary differential equation by algebraic finite difference approximations;
3. Substituting the finite difference approximations into the ordinary differential equation to obtain an algebraic finite difference equation.

Hence the equations are solved on a step by step basis with the general procedure as follows: given the particle positions and velocities at time t^N, the positions and velocities are obtained at the next time t^{N+1} ($= t^N + \Delta t$), with the degree of accuracy determined by the choice of algorithm.

5.2.2 Implicit, Explicit, and Implicit-Explicit Methods

Broadly speaking, the numerical methods involved in the time integration of the equations of motion can be classified as implicit or explicit methods. The classification basically depends on the time level at which the value of the dependent variables is

evaluated. Extensive finite difference definitions are further explored by Hoffman (1992).

Implicit methods are sometimes adopted in finite element methods (Seville et al. 1997). In this an iteration is undertaken between t^N and t^{N+1} to satisfy the assembly matrix differential equations at t^{N+1}. The requirement of a solution of a coupled set of algebraic equations to obtain the values at the next time level (Xu 1997) results in a more accurate method which can tolerate a larger timestep, but the analysis is more complex and requires more computer memory (Seville et al. 1997). On the other hand there is a great numerical advantage in explicit methods over implicit methods as the positions at t^{N+1} are obtained directly from the acceleration at t^N, meaning explicit methods do not require the solution of a coupled set of algebraic equations for advancing time from the current time level to the next.

Explicit methods are conditionally stable however, while implicit methods have the advantage of being unconditionally stable. As a consequence, to ensure numerical stability when using an explicit method, small time steps must be employed, which results in the scheme being computationally expensive. Hoffman (1992) provides a comprehensive review of implicit and explicit numerical methods. An evaluation of the earlier implicit and explicit methods upon which current advancements are based can be found in the work of Goudreau & Taylor (1972) and Hilber & Hughes (1978).

There are engineering problems for which explicit methods are very efficient and others for which implicit methods are very efficient (Xu 1997). In certain cases however neither method is efficient by itself and a compromise is made called an implicit-explicit method which seeks to maintain the advantages of both implicit and explicit methods while removing the disadvantages of both methods. Xu (1997) gives an extensive analysis of implicit-explicit methods.

5.2.3 Implementation of Numerical Method

For the current work, a central difference scheme known as the ‘leap-frog’ method is used to explicitly integrate the equations of motion and thus dynamically update particle velocities and positions throughout the DEM simulation duration. The algorithm is

algebraically equivalent to the Verlet (1967) scheme and is described in detail by Allen & Tildesley (1987) and illustrated in Figure 5.1.

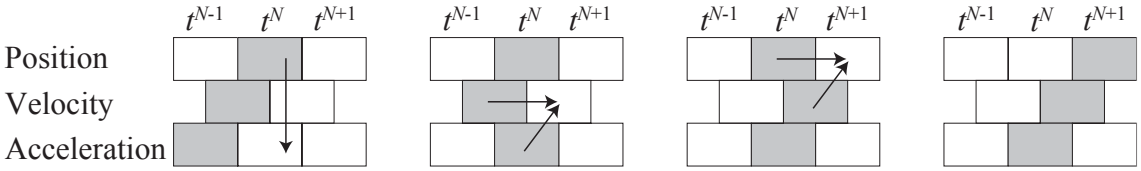

Figure 5.1 Successive steps in the implementation of the leap-frog algorithm. The stored variables are in grey boxes (adapted from Allen & Tildesley 1987)

For the motion of one spherical particle in the x and y directions and rotation about its z-axis, the finite difference equations for translation and rotational positions and translation and rotational velocities can be written as follows:

$$x^{N+1} = x^N + \Delta t \dot{x}^{N+1} \tag{5.1}$$

$$y^{N+1} = y^N + \Delta t \dot{y}^{N+1} \tag{5.2}$$

$$\theta^{N+1} = \theta^N + \Delta t \dot{\theta}^{N+1} \tag{5.3}$$

$$\dot{x}^{N+1/2} = \dot{x}^{N-1/2} + \Delta t \ddot{x}^N \tag{5.4}$$

$$\dot{y}^{N+1/2} = \dot{y}^{N-1/2} + \Delta t \ddot{y}^N \tag{5.5}$$

$$\dot{\theta}^{N+1/2} = \dot{\theta}^{N-1/2} + \Delta t \ddot{\theta}^N \tag{5.6}$$

The current positions x^N, y^N and θ^N and accelerations $\ddot{x}^N$, $\ddot{y}^N$ and $\ddot{\theta}^N$ are stored together with the velocities $\dot{x}^{N-1/2}$, $\dot{y}^{N-1/2}$ and $\dot{\theta}^{N-1/2}$ at the mid time step. The accelerations can be determined from the sum of all contact forces acting on the sphere, including any gravitational components. The equations for velocity (Eq. (5.4), (5.5) and (5.6)) are implemented first, and the velocities 'leap' over the current time coordinates to give the next mid step values $\dot{x}^{N+1/2}$, $\dot{y}^{N+1/2}$ and $\dot{\theta}^{N+1/2}$. The current velocities are calculated during this step:

$$\dot{x}^N = \frac{1}{2}\left(\dot{x}^{N+1/2} + \dot{x}^{N-1/2}\right) \tag{5.7}$$

$$\dot{y}^N = \frac{1}{2}\left(\dot{y}^{N+1/2} + \dot{y}^{N-1/2}\right) \tag{5.8}$$

$$\dot{\theta}^N = \frac{1}{2}\left(\dot{\theta}^{N+1/2} + \dot{\theta}^{N-1/2}\right) \tag{5.9}$$

This is necessary so that any quantities that require positions and velocities at time t^N can be calculated. Eq. (5.1), (5.2) and (5.3) are then used to drive the positions once more ahead of the velocities. The new accelerations can then be evaluated ready for the next step. The numerical benefits for this scheme derive from the fact that the difference of two large quantities is never taken to obtain a small quantity, minimising loss of precision in the computations (Allen & Tildesley 1987).

5.3 Contact Detection Scheme

An important computational issue is the detection of contacts between neighbouring particles, and contacts between particles and boundaries. In order to calculate the interparticle forces, it is necessary to know which particles and boundaries are in contact at the current time step, and which particle pairs and/or particle–boundary pairs will lose contacts or form contacts during the next time step.

5.3.1 Particle – Particle Contacts

The simplest way to determine if a contact occurs between particles is to check every particle in the system against every other, however it is well known that simulation of N interacting particles with DEM involves an $N(N\text{-}1)/2$-pair of contacts search problem. Clearly, if there are tens of thousands of particles involved, this technique is prohibitive. Several methods have been developed and are available in the literature to design an efficient contact detection algorithm and thus save substantial computation time. Most adopt the idea of a neighbour list where contact searches are focused in many small regions. This tends to allow the computation time required to compile a simulation to increase linearly with the number of particles N rather than quadratically (Xu 1997).

Two widely used approaches exist for determining the near neighbours (Asmar et al. 2002): (1) a neighbourhood list approach, which is a body based cell algorithm; and (2) a zoning or boxing algorithm, which is a basic grid subdivision method. Both of these methods are exhaustive spatial sorting schemes, meaning that they make no *a priori* assumptions about the problem evolution and reason based only on the present state of the geometry (Williams & O'Connor 1995). Advanced contact detection schemes suitable for particular applications and particle shapes are also increasingly being developed and are briefly described in Section 5.3.1.3.

5.3.1.1 Neighbourhood List Approach

The neighbour list concept originated from the area of molecular dynamics (Xu, 1997). The term *neighbour* refers to a molecule whose interaction with a reference molecule is not negligible. There are many types of long distance interactions between molecules, such as the popular Lennard-Jones potential, which disappear when the molecules are separated by a distance greater than the potential cutoff. Therefore to track the motion of a particular molecule, a neighbour list is constructed, which allows the program to check only those molecules appearing on the neighbour list rather than checking all the remainders. The search time and hence memory requirements of the CPU is greatly reduced.

Verlet (1967) presented one of the earliest neighbour lists of this kind, depicted in Figure 5.2, where two concentric spheres of radius r_1 and r_2 are associated to each molecule. A list is made of the neighbours of each molecule out to the radius r_2, whose magnitude influences the algorithm efficiency. The effect of this radius and an optimum choice for its value was discussed by Thompson (1983). This particular neighbour list has been further explored, with Fincham & Ralston (1981) and Thompson (1983) describing an algorithm that allows the program to automatically update the neighbour lists. Rapaport (1980) developed algorithms for the scheduling of events such as molecular collisions. Streett et al. (1978a, 1978b) proposed a method where effectively two time steps are used: one for the primary forces that come from close neighbours and another for the secondary forces from remote neighbours. The time spent in evaluating forces within the cutoff range was reduced leading to increases in computing speed.

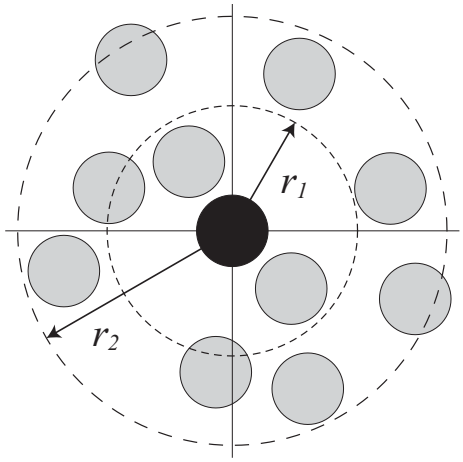

Figure 5.2 Diagram illustrating the conventions chosen for the Verlet method

Naturally, the logical testing of every pair in a system of molecules is inefficient. If the system involves a large number of molecules then the conventional neighbour list discussed above becomes quite large and can create memory concerns. Such neighbour lists require the computation of squares which are CPU time intensive (Hoomans et al. 1996). Also, unlike situations in molecular dynamics, the interactions between discontinua such as lumps of coal occur only at immediate neighbours. Neighbour lists have been utilised in distinct element simulations recently, for example see Wightman et al. (1998), who used a Verlet type neighbour list in the simulation of particles in a rotating cylindrical vessel. Langston et al. (1994) also utilised neighbour lists in their analysis of hoppers, however noted that there were inefficiencies with regards to recompiling the neighbours lists. Advancements of their work (Langston et al. 1995, 1996) utilised a boxing algorithm. This approach allows a more efficient method of tracking neighbours for large systems of particles, and shall now be described.

5.3.1.2 Zoning / Boxing Algorithm

The zoning or boxing algorithm has been used in the area of molecular dynamics. Quentrec & Brot (1973) introduced a scheme in which the system is divided into many small non-overlapping zones and molecules are sorted into these zones at the beginning of the simulation. Each molecule is considered in turn, with all other molecules in the same zone and immediately surrounding zones considered as potential interaction

partners. The zone size was chosen so that its dimension is greater than the cutoff distance for the long distance forces.

Zone structured neighbour lists are used widely in distinct element simulations where a spherical particle is sorted into the square zones according to its mass centre. Some examples include the work of Langston et al. (1995) and Hoomans et al. (1996), where potential interactions among particles are found by scanning through the zones. The particle diameters and maximum particle velocities expected in the simulation are considered when determining the size of the zones, with a large zone size generally required when the particle velocities are high. This is illustrated by Hoomans et al. (1996) who used a zone length of 5 times the particle diameter in the simulation of a gas fluidised bed while Langston et al. (1995, 1996) used zone lengths of 1.86 and 2 times the particle diameter respectively in the simulation of hopper flow. Zhang et al. (1993) on the other hand used a cell size dimension to be twice the diameter of a disk in their simulations of hydraulic flow problems, and Taylor & Preece (1989) chose a box size based on the largest sphere in the system in their investigation of modelling the rock motion associated with conventional blasting. Rajamani et al. (2000) also utilised cell size equal to maximum diameter of the disk in their analysis of tumbling mills. Kremmer & Favier (2001a) developed a method for representing three-dimensional boundaries of arbitrary geometry and for modelling the interaction between moving boundary objects and particles. They too utilised equal-sized cubic cells where cell size is based on the largest particle diameter in the system. The combination of a relatively small zone size with very high particle velocities could result in flawed particulate motion patterns due to contacts possibly being omitted from the calculations.

There is no general rule that governs the choice of a small or large zone size. Basically if the zone size is small there are less neighbour particles in the list. Contact detections for each particle can thus be completed quickly but requires more frequent updates of the neighbour list (Xu 1997). Contrary to this, if the zone size is large there are a greater number of neighbour particles in the list. This means that more contact detections are required per particle at each time step, but fewer updates of the neighbour list are required (Xu 1997).

5.3.1.3 Recent Advances in Contact Detection

For systems involving circular particles numbering in the order of 10^5 or more, advanced contact detection schemes have been developed, such as the NBS (No Binary Search) contact detection algorithm by Munjiza & Andrews (1998). As identified in Chapter Four, there has also been an increasing use of non-circular or non-spherical shapes in DEM simulations. This has the major drawback of being highly computational resource intensive. To reduce computation times there have been investigations that have focused on providing contact detection schemes that are more advanced than the grid subdivision or body based cell approaches outlined above. For example contact detection algorithms have been developed for elliptical particles (Rothenburg & Bathurst 1991, Wang & Liang 1997) and ellipsoidal particles (Lin & Ng 1995, Ouadfel & Rothenburg 1999, Vemuri et al. 1998, Wang et al. 1999). Contact detection schemes for particles of arbitrary geometry have been developed by Hogue (1998) and Perkins & Williams (2001) who present a new search algorithm: Double-Ended Spatial Sorting (DESS). For the current work, and most systems utilising disks or spherical shaped particles, the original exhaustive spatial sorting schemes should suffice.

5.3.2 Particle – Wall Contacts

Very little work could be found in the literature describing the contact detection schemes used for particle-wall interactions. As the current project considers a pseudo three-dimensional system, the ratio of boundaries to particles will in most cases remain low. Therefore the contact detection scheme employed is simply to check every particle against every boundary, and is not computationally expensive. The straight boundaries are firstly checked, followed by curved boundaries. Note that checking for particle-boundary interactions occurs after the first particle-particle contact scheme cycle has been completed. The next section describes the contact detection algorithm developed for the present work. The algorithm is based upon the zone structured method.

5.3.3 Implementation of Particle – Particle Contact Detection

For the current work, the grid subdivision method and body based cell approach with rectilinear surrounding cells is combined, allowing for a spatial sorting scheme that s

more robust. The contact detection for particle-particle interactions is implemented as follows. At the beginning of each simulation, the calculation domain is discretised into many small non-overlapping square cells by placing grid lines both horizontally and vertically across the domain. As the particles may have different physical properties such as size and density in the simulations, the size of these cells, and hence the number of cells, is based upon three parameters: the diameter of the largest particle in the system D_{max}, the diameter of the smallest particle D_{min}, and a user defined term N_{grid} that specifies the maximum number of particles to be allowed in one cell. D_{max} and D_{min} were defined in Chapter Four.

Also, the size of each cell is within an upper and lower cell size limit so that if desired, a compromise between the combination of zone size and contact detections per time step can be found to give minimum compilation time for the DEM program. The maximum number of boxes in the horizontal and vertical directions can be found from:

$$Max\_boxes\_x = \text{Integer}\left(\frac{xlen}{D_{max}}\right) \tag{5.10}$$

$$Max\_boxes\_y = \text{Integer}\left(\frac{ylen}{D_{max}}\right) \tag{5.11}$$

The minimum number of boxes in the horizontal and vertical directions can be found from:

$$Min\_boxes\_x = \text{Integer}\left(\frac{xlen}{\text{Real}\left(\text{Integer}\left(\text{Real}\left(Ngrid\right)\right)^{1/2}\right)D_{min}}\right) \tag{5.12}$$

$$Min\_boxes\_y = \text{Integer}\left(\frac{ylen}{\text{Real}\left(\text{Integer}\left(\text{Real}\left(Ngrid\right)\right)^{1/2}\right)D_{min}}\right) \tag{5.13}$$

The terms ‘Integer’ and ‘Real’ in Eq. (5.10) to (5.13) denote the parameter convention types used in the computer code. If the number of particles within a specific cell is greater than N_{grid}, the program stops compiling and a warning is presented on screen to the user. At the same time as the domain is discretised, each particle in the system is sequentially given an identification number so that each particle is unique. Consider the

example shown in Figure 5.3 (a) where eleven particles appear in a calculation domain that is divided into sixteen square cells.

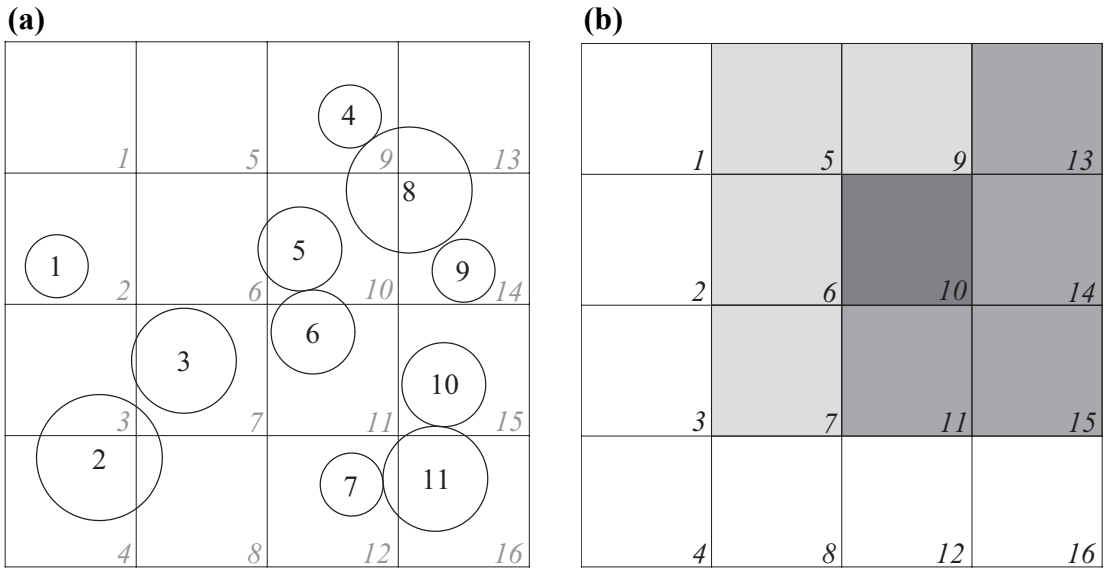

Figure 5.3 Schematics of: **(a)** cell structure with arbitrary particle configurations, and **(b)** cell structure with coloured cells showing target cells to be searched

After specifying the identification number for each particle and constructing the cells within the calculation domain, the next step is for each particle in the system to be sorted into a cell according to the coordinates of its centre of mass, similar to the technique used by Xu (1997). Two arrays that are associated with each cell are established. The number of particles inside each cell is recorded by the array *NO_PARTICLES*, while the particles recorded are identified by the second array *PARTICLE*. At the beginning of each sorting process the values of both arrays are initialised to zero. When a particle is sorted into a cell, the value of array *NO_PARTICLES* increases by an integer 1, and at the same time the array *PARTICLE* records the identification number of this particle. Hence enough information about the particle locations is stored with the assistance of the two arrays. The array *NO_PARTICLES* will help the program skip any cells that do not contain particles. For the cell structure and particle configurations shown in Figure 5.3 (a), the sorting results are summarised in Table 5.1.

Table 5.1 Sorting results for cell structure and particle configurations as shown in Figure 5.3 (a)

Cell Number	**1**	**2**	**3**	**4**	**5**	**6**	**7**	**8**	**9**	**10**	**11**	**12**	**13**	**14**	**15**	**16**
NO_PARTICLES	0	1	0	1	0	0	1	0	1	1	1	1	0	2	1	1
PARTICLE	0	1	0	2	0	0	3	0	4	5	6	7	0	8,9	10	11

After the completion of the sorting process, the contact detection check is performed only within those cells that contain particles, the neighbouring cells, rather than checking through every cell in the domain. When using a conventional approach, the neighbours of a particle are found by searching through the cell where its centre of mass is located and also all surrounding cells (Xu 1997). For example, the neighbours of any particle in cell 10 are to be found in the nine cells 5, 6, 7, 9, 10, 11, 13, 14 and 15 as shown in Figure 5.3 (a). Similarly the neighbours of a particle in cell 11 are the nine cells 6, 7, 8, 10, 11, 12, 14, 15 and 16. It is clear that certain neighbour cells are not exclusive and hence double counting can occur if using this approach (Xu 1997), which could result in unrealistic multiple addition of contact forces. The particles in cells 10 and 11 are mutually acting as neighbours.

The algorithm designed by Walsh (2004) will be utilised to avoid this problem and is as follows. The neighbour list of particles in this cell was constructed using a search through cell 10 (coloured by ■ in Figure 5.3 (b)) and only its four nearby cells of greater index, 11, 13, 14 and 15 (coloured by ■ in Figure 5.3 (b)). The information about its four nearby cells of lesser index 5, 6, 7 and 9 (coloured by ■ in Figure 5.3 (b)) is known through Newton's third law of motion during the previous contact detection until reaching this cell. Using this method, if the contact detection starts along the increasing direction of the cell index all potential contacts among particles will be established without double counting. Hence substantial program compiling time is saved.

During this step by step process of neighbour determination, once a particle does appear on the list of a host particle, the theory outlined in Chapter Four will be used. The separation distance between the centres of mass of the two particles will be determined. As described in Chapter Four, contact occurs when the separation distance between the two particles is less than the sum of their radii. If this is the case, then the inter-particle forces are calculated and the results applied to both contacting particles.

5.3.4 Implementation of Particle – Boundary Contact Detection

As specified in Chapter Four, all boundaries have been given an identification number when line parameters were initially read into the program, so this step does not repeat here. Also, the original numbers given to particles are used. In other words, the number given sequentially to each particle as each is created at the start of the program is used. This number is different to that assigned to each particle for the particle-particle contact detection scheme in the previous section. To further explain, consider the following scenario using the particle locations in Figure 5.3 (a) as a template. During the initialisation stage of the simulation, the particles may have been assigned numbers such that the calculation space looked like Figure 5.4 (a).

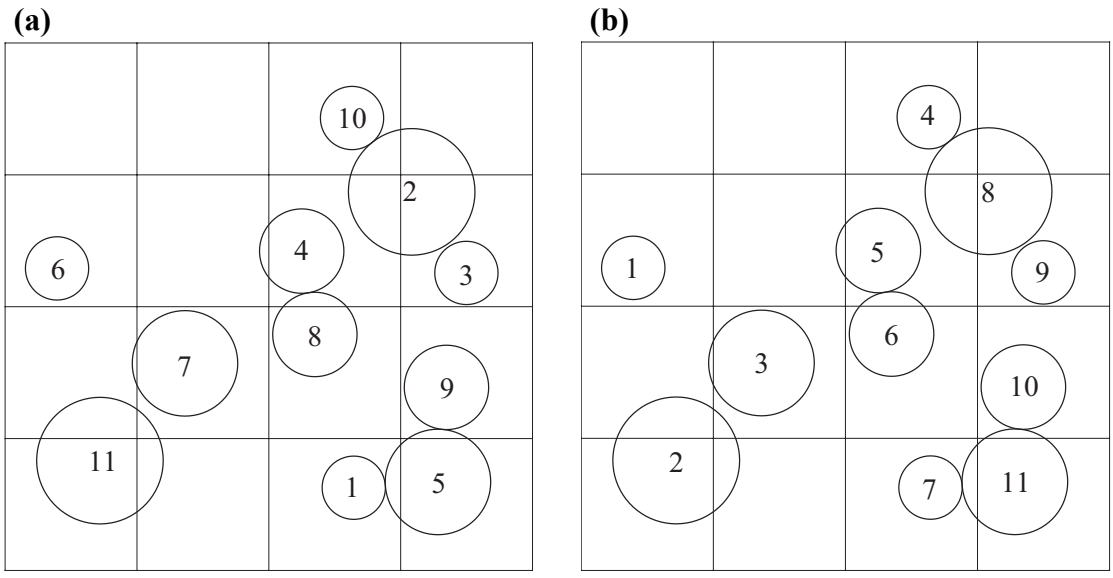

Figure 5.4 **(a)** particle numbering at start of program **(b)** particle numbering during contact detection subroutine

But after specifying an identification number when implementing the contact detection, the numbering for that process will be that shown in Figure 5.4 (b), which is identical numbering to that shown in Figure 5.3 (a). For detection of particle-boundary contacts, the numbering follows that process used in Figure 5.4 (a) due to the ease of coding the program.

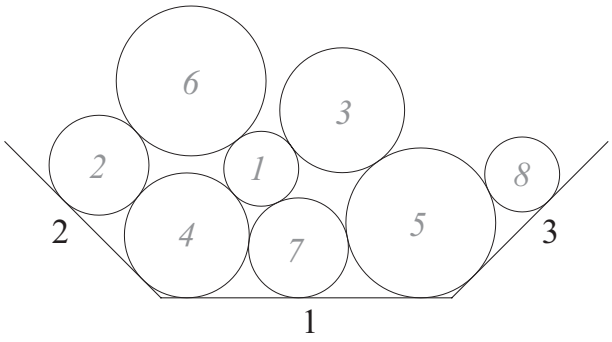

Figure 5.5 Searching through boundary contacts

Consider Figure 5.5, where there are eight particles and three boundaries. The particles and boundaries will be checked for contact between each other using a basic *YES/NO* routine as shown in Table 5.2. Note that every boundary is checked against one particle, and then proceeds to the next particle, and so on.

Table 5.2 Sorting results for boundary configurations as shown in Figure 5.5

Particle Number		***1***	***2***	***3***	***4***	***5***	***6***	***7***	***8***
Boundary Number	1	No	No	No	Yes	Yes	No	Yes	No
	2	No	Yes	No	Yes	No	No	No	No
	3	No	No	No	No	Yes	No	No	Yes

If the boundaries of the cell and calculation domain coincide, then additional contact detections are performed, similar to the case of contact with a straight boundary. Note

that boundaries are assumed to have infinite mass. Once it has been established that contacts do occur, the theory outlined in Chapter Four will be used. A particle is defined as being in contact with a boundary if the distance from the centre of mass of the particle to the closest point on the boundary is less than the radius of the particle. If this is the case, then the NFD and TFD models are used to calculate the particle forces and the results applied to the contacting particle.

5.4 Selection of Critical Time Step

The important parameters involved in solving Distinct Element Modelling equations need to be specified before computations can proceed. Arguably the most important of these simulation parameters is the computational time step, which has often been determined with a large degree of empiricism in literature (Xu 1997). The calculation scheme of the DEM is cyclic based and the length of the time step is critical, as it will determine the numerical stability and the computation time. The smaller the timestep, the more stable the calculation, but the computation time is significantly increased. The timestep should be as large as possible to save computation time yet keep the calculations stable.

5.4.1 Time Step Selection in Literature

To ensure the numerical scheme is both stable and accurate during the time integration it is imperative that the magnitude of the time step is chosen so that it is less than a critical value. If the time step is not small enough, then anomalies in the simulation will result, with particles overlapping excessively, or particles ‘passing through’ one another or wall elements rather than contacting and rebounding. The time step needs to be chosen so as to allow a particle to travel a small enough distance in one step so that contacts can be evaluated. The initial criterion is thus for the time step to be significantly smaller than the time taken for the particle to travel its own length. The length scale of the particle is equal to the smallest particle diameter in the system. Also, if the time step in the computations is chosen sufficiently small, then it can be assumed

that during a single time step disturbances do not propagate from any particles further than its immediate neighbours (Tsuji et al. 1992).

The critical time step should be determined from the two constraining factors in Distinct Element Modelling (Xu 1997): (1) conservation of energy and momentum for each particle during interactions with neighbour contacting particles, and (2) maintaining the stability of the numerical scheme due to the explicit nature of the method used. The first constraint, conservation of energy and momentum, will be utilised in the current work to determine the time step as it ensures a strict environment within which all interactions take place. Governing physical laws will be adhered to, unlike the potentially unrealistic outcomes that may occur if a time step (and other parameters) are chosen to ensure numerical stability rather than realism. The complexity of the problem necessitates that the critical time step be determined empirically (Xu 1997).

Evidenced from its use in literature, one of the most widely used methods to estimate the critical time step is based on the natural period of oscillation of the one-dimensional vibration system shown in Figure 5.6, consisting of a mass connected to ground by a linear spring.

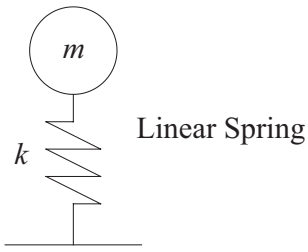

Figure 5.6 One-dimensional vibration system

A criterion can be established so that the critical time step limits the particle movement during the collision process within the possible interaction ranges (Xu 1997). Based on this criterion, the critical time step used is of the form:

$$\Delta t_c \propto \sqrt{\frac{m_{min}}{k_{max}}} \tag{5.14}$$

where m_{min} is the mass of the smallest particle and k_{max} is the largest interparticle spring stiffness. Xu (1997) used π as a representative proportional constant so that one half of the natural period represents the contact duration during a collision. Several other values for the proportional constant are suggested in literature for varying DEM applications. Vu-Quoc & Zhang (1999a, 1999b) used $\pi/40$, Jensen et al. (1999) used 0.1, Tsuji et al (1993) used $\pi/5$, and Cundall & Strack (1979) and Rajamani et al. (2000) used 2. An equation for calculating the critical time step that considers velocity and restitution coefficient directly was given by Cleary (1998a, 1998b) as:

$$\Delta t_c = min\left(\frac{\pi}{25}\sqrt{\frac{K_n}{m_{ij}\left(1-\gamma^2\right)}}, \frac{1}{10}\frac{D_{min}}{n_s U_{max}} \right) \tag{5.15}$$

where U_{max} is the maximum particle velocity, D_{min} is the smallest particle diameter, n_s is the number of time steps between searches, and K_n is the spring constant in the normal direction. The terms γ and m_{ij} are given by (Cleary 2000, Cleary & Hoyer 2000, Cleary 2001):

$$\gamma = -\frac{ln\,\varepsilon}{\sqrt{\pi^2 + ln^2\,\varepsilon}} \tag{5.16}$$

$$m_{ij} = \frac{m_i m_j}{m_i + m_j} \tag{5.17}$$

respectively where m_{ij} is the reduced mass of particles i and j with masses m_i and m_j respectively, and ε is the coefficient of restitution which is the ratio of the post-collision to pre-collision normal component of the relative velocity. For systems involving many particles of different properties, the critical time step is obviously chosen to be the minimum value calculated for all particles so that stability of the numerical scheme is achieved.

A second criterion used in classical engineering modelling (Langston et al. 1995) is to estimate the critical time step based on Rayleigh waves travelling along the surface of the solid spherical particles. A criterion can be established so that the critical timestep should be less than the time for which a wave can traverse the particle of smallest size in a particle assembly. Based on this criterion, the critical timestep is given by:

$$\Delta t_c = \frac{\pi R_{min}}{\Phi}\sqrt{\frac{\rho}{G}} \tag{5.18}$$

where R_{min} is the radius of smallest sized particle in the system, ρ is the density of particle material, G is the rigidity modulus of particle material, and Φ is a Poisson ratio (ν) dependent parameter $\{0.90 < \Phi < 0.95\}$ (Johnson 1985). Equation (5.18) however does not consider the velocity of the particles or wall surface elements and may give a time step which is still too large to satisfy Hertzian contact principles (Kremmer & Favier 2001b). Note that for this criterion it is assumed the properties of all materials in the assembly are the same. Similarly to the previous method of time step estimation, for systems involving many particles of different properties, the critical timestep is chosen to be the minimum value calculated for all particles.

It is clear from the two criteria defined in Eq. (5.14) and (5.18) that the critical time step is dependent on material properties, which presents a conundrum for Distinct Element Model development, described best by Xu (1997): Does one now choose to use *hard particle* modelling system, where a very hard particle is to be used with a small realistic overlap level but cover only a small portion of the time in an event? Or does one choose to use a *soft particle* modelling system, where a very soft particle is to be used with a large artificial overlap level but cover a large portion of time in an event? The author will use a compromise, so as to have an overlap in particle-particle and particle-boundary collisions that is small enough to be able to correctly calculate forces arising, depending upon the particulate simulation at hand.

Langston et al. (1995) suggest that the critical time step based on Rayleigh wave speed is more appropriate if the dynamics on the asperity level were being followed, whilst if the dynamics on the particle diameter level is considered the critical time step based on

the natural period of an oscillator is more appropriate. Note that in practice the actual time step used in the computations is only a fraction of the conservative estimates given by Eq. (5.14) and (5.18) (Langston et al. 1995). There are however instances where the method determining critical time step has allowed the maximum value of a series of time steps to be chosen as the critical time step in the simulation. See Tsuji et al. (1992, 1993) for details. The particles chosen for these simulations are very soft however. A number of papers (Xu 1997, Xu & Yu 1997, Xu et al. 2000) determine the time step from a series of tests where a particle is dropped from a fixed height to a flat wall. The maximum time step that allows the particle to bounce back to its initial dropping height is used as the time step. This technique was used originally for the current work and shall now be described, along with the method eventually used.

5.4.2 Selection of Critical Time Step for Current Work

The original critical time step selection procedure is identical to and described further in the work of Xu (1997), Xu & Yu (1997), and Xu et al. (2000). Consider a particle initially at rest at a fixed height above a wall. The time step is determined by dropping the particle and allowing it to rebound off the wall without any form of dissipation ($\varepsilon = 1$). The DEM mathematical and numerical methods outlined earlier in this chapter and the previous chapter are utilised to solve the motion of this particle using different time steps with a first approximation estimated from Eq. (5.14). Energy and momentum conservation is met if the particle can bounce back to its initial drop height, and the maximum time step giving such results can be determined after a series of tests. The collision mechanism between particle-particle interactions and particle-wall interaction is essentially the same; hence the time step determined above is applicable to colliding particle pairs.

With the various types of simulations performed (differing particle sizes, particle densities, boundary conditions, single particle tests, multiple particle tests) however, it was found that the process needed to be replicated repeatedly for each different condition. Ultimately the critical time step was calculated using Eq. (5.14) with a proportional constant that was selected based upon the type of simulation performed. The time step used was between 5% – 10% of this critical time step where applicable.

5.5 Computation Aspects

This section briefly outlines the general computational method for the DEM and the techniques used to facilitate animations and other graphical output. The general process of DEM is basically as follows:

1. Create text input file or manually input relevant parameters;
2. Perform DEM computations;
3. Generate text output to be graphically processed via graphs or animations.

For the current work, a pre-processor and a post-processor have been developed to facilitate steps one and three above, with an easy to use graphical interface used for each of these stages. The pre-processor facilitates parameter inputs and the relevant parameters needed to run the simulations are divided into two groups: the particle physical properties and other specified model data, and the geometric data for the relevant boundaries used. These are located in external files and are called by the main program during the simulation. The post-processor is used for visualising the simulation. The external files created that incorporate the particle positions, velocities, and other relevant data are used so that animations can be created and manipulated. These data files can also be called by commercial spreadsheet software such as Microsoft® Excel to convey information using graphs.

The computer code has been tested on both a 1.26 GHz Pentium III Processor with 512 MB of RAM and also a 2.0 GHz Pentium IV Processor with 1024 MB of RAM, both utilising the Microsoft® Windows XP Operating System. Compatibility wasn't a problem when tested on Windows versions 98 SE and 2000.

5.5.1 Pre – Processing Module

The first stage of the simulation process requires the creation of a number of input data files. Rather than manually create text files, a Microsoft® Windows Graphical User Interface (GUI) was developed using Microsoft® Visual Basic 6.0 for input of

calculation parameters and particle physical properties. All parameters required to execute the simulation can be easily input and changed using this interface. A flow-chart of the current pre-processing module is detailed in Figure 5.7.

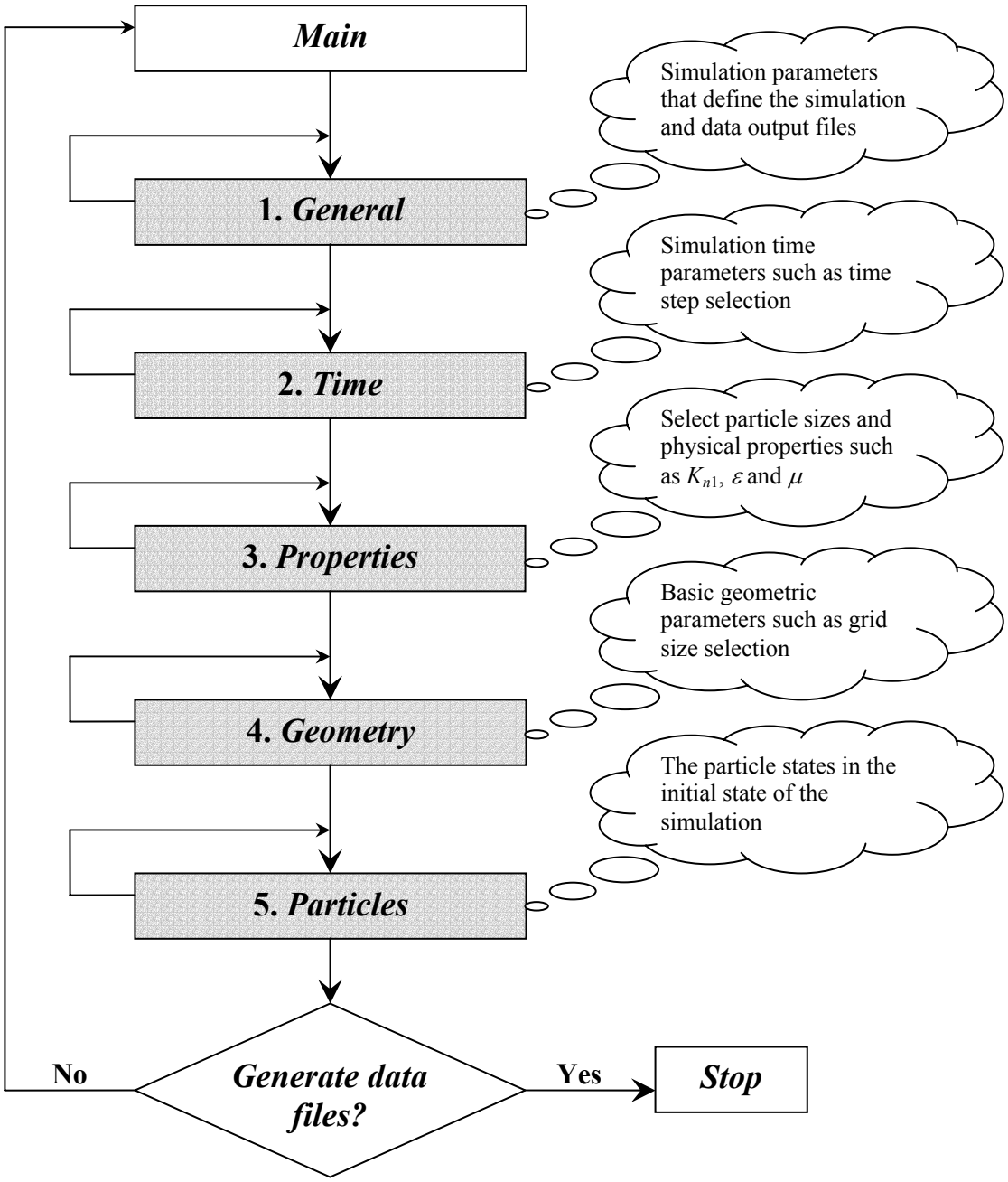

Figure 5.7 Flowchart of pre-processing module used to create input data files

A major window called the *MAIN* contents window contains buttons that lead to dialogue boxes. When the user is satisfied with the current dialogue box input, he or she must click '*OK*' and the *MAIN* window returns. The information is stored in memory until the end of the process. Once all the fields have been completed external data files are created. The return arrows in Figure 5.7 indicate that the user returns to the MAIN window by clicking '*Cancel*' if he or she is unsatisfied with the input.

The boundaries in the current work were originally generated from a graphical pre-processor. The Display III™ module (*User's Manual for Display III™* 1995) for the NISA Finite Element Analysis Software was used to facilitate a graphical means where the author can observe and correct irregularities or potential stability errors while creating boundaries. The concept originated from concurrent research conducted at the university (Walsh, M. A. 2001, pers. comm., 23 October). The software produced a text file containing sets of coordinates in the formation shown in Table 5.3.

Table 5.3 Layout of text file produced by Display III™ module

Column 1	Column 2	Column 3	Column 4	Column 5
x_1	y_1	z_1	x_2	y_2
z_2	x_3	y_3	z_3	x_4
y_4	z_4			

In the software, straight lines are represented by two points and curves by four points, and this was used as the basis for defining the boundaries detailed in Chapter Four. As the research progressed however, the author found the use of a Microsoft® Excel spreadsheet to be more productive, and ultimately all coordinate generation was created using a spreadsheet, though still producing the coordinate layout presented in Table 5.3. Graphical data are saved in text format for subsequent input into the calculation module. Examples of the input files created by the pre-processor are presented in Appendix III.

5.5.2 DEM Calculation Module

The DEM Calculation Module applies the theory outlined in this chapter and Chapter Four and uses the data files created in the pre-processing module as input data. The program was coded using Compaq Visual Fortran 6.6.0. The three key steps for the DEM calculations in this module are: (1) Initialisation of the boundaries, particle positions and velocities, and material properties; (2) Check for contacts using contact detection scheme, utilise force-displacement methods, and the numerical time integration of the resulting equations of motion; and (3) System flow characteristics such as particle positions and velocities, and any further quantities specified by the user are saved over the duration of the calculation, and this data is output in a nominated format for post processing. The basic flow-chart is detailed in Figure 5.8.

The DEM calculation module includes a restart capability in case simulations are stopped at any point and need to be restarted again from the same point. This has the potential to save a significant amount of time.

5.5.3 Post – Processing Module

The final module utilises well known graphical techniques to produce animations. The decision concerning which language to be used for the development of a DEM application is interrelated with the selection of the computer graphics library for animating the simulation. A selection of a computer graphics library for the animating part of the simulation in the same programming language used for the DEM computation part of the application offers significant advantages (Komodromos & Williams 2002).

The sheer amount of information available on the web suggests OpenGL is the most extensively documented 3D graphics API available. As the DEM code was written in Fortran, it was preferred that the animation coding be written in the same language, and fortunately Fortran bindings for OpenGL were available. Therefore the module for the current work was coded in Compaq Digital Visual Fortran 6.6.0 and used the OpenGL

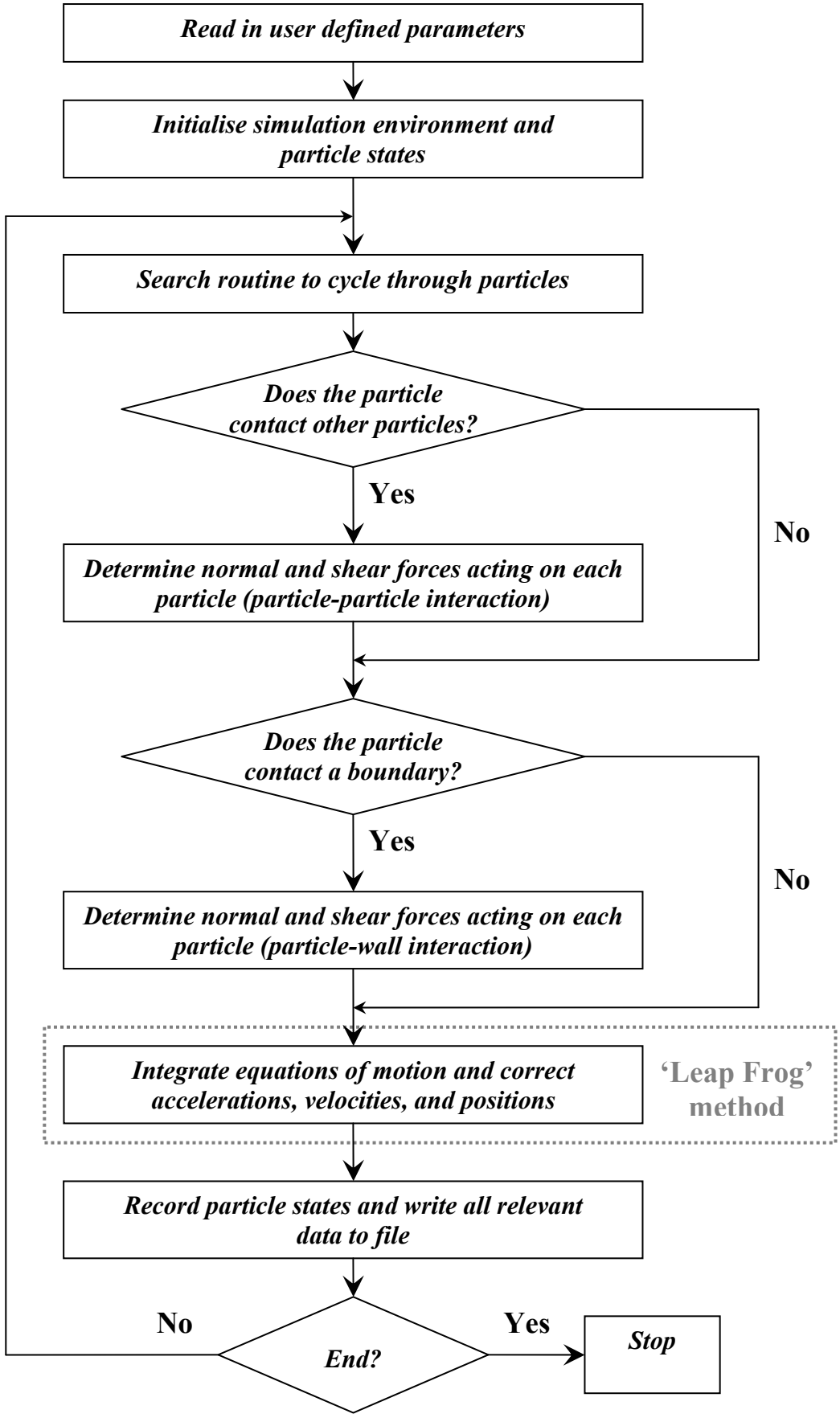

Figure 5.8 Flowchart for DEM calculation module

graphics library under the Microsoft® Windows operating system. OpenGL's Utility Toolkit 3.7.1 (GLUT) is a library that was used extensively as it contains a number of functions that simplify the writing of OpenGL programs considerably.

The post-processing module uses the data files generated in the DEM calculation module to animate particle flow. The module incorporates the following features to allow qualitative analysis of particulate flows:

- Zooming (both real-time zoom and window zoom functions are incorporated);
- Panning (real-time panning is incorporated);
- Particle recolouring (based upon either particle sizes or numerical data ranges such as velocity distributions);
- Simulation fast-forward, slow-down, and stopping capability.

All software features may be used whilst the animation is executing. Data such as particle positions may be displayed using this module whilst particles positions are simultaneously being calculated using the calculation module in the background. A basic flow-chart of the module is illustrated in Figure 5.9. With each successive loop, the data at the next time step are read and the simulation moved forward in time. The simulation stops at either the end of the data files, or if the user cancels the simulation.

5.6 Summary

This chapter provided an overview of the numerical algorithm chosen for the current work to solve the ordinary differential equations defined in Chapter Four. An outline of contact detection schemes utilised in the literature was briefly described with the scheme to be used for the current work formulated. The selection and determination of the critical time step selection was explored. The chapter concluded by briefly outlining a few of the computational aspects, including the graphical techniques enabling animations of the simulations, and some comments regarding the separate computer code developed to facilitate parameter inputs.

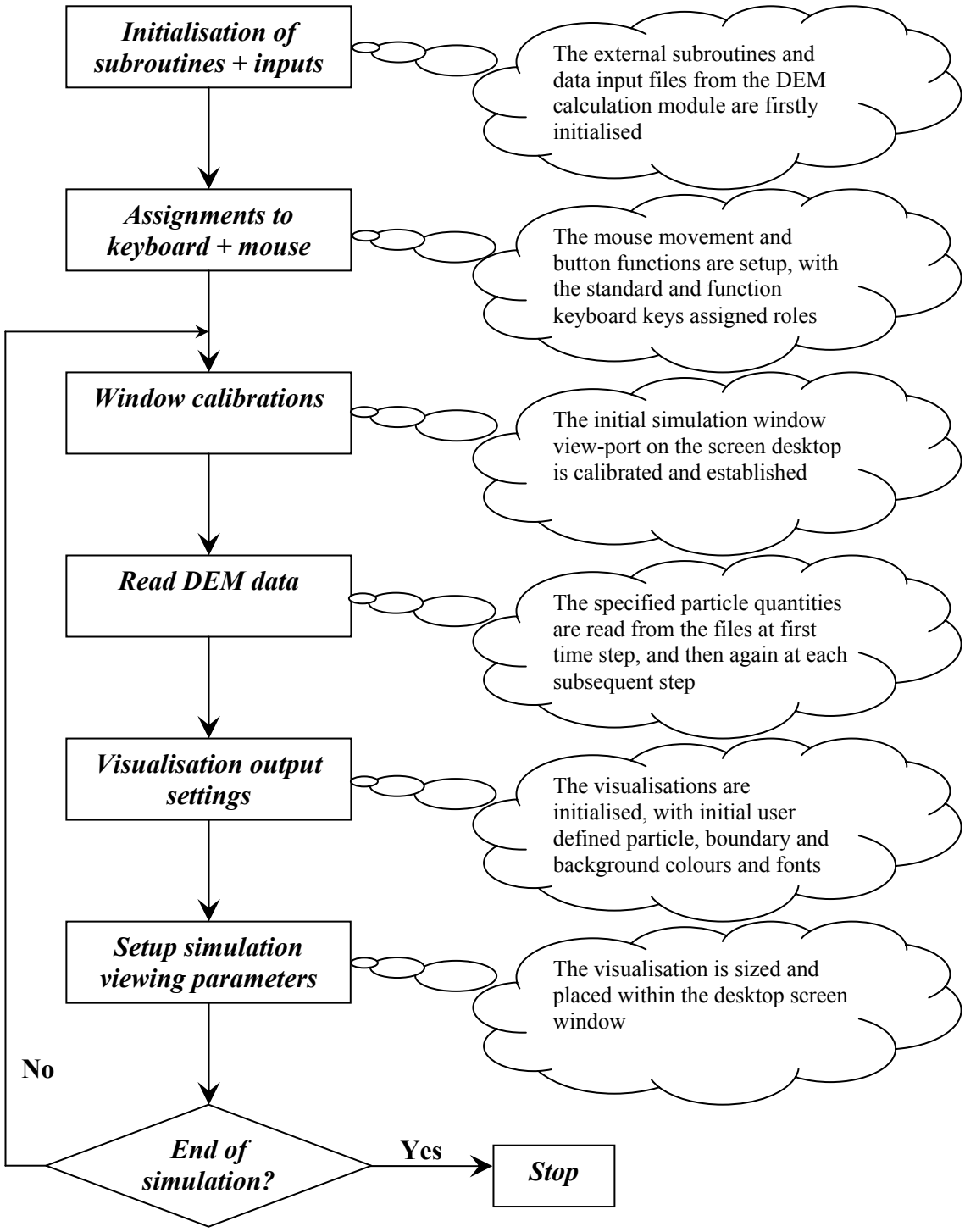

Figure 5.9 Flowchart of post-processing module that creates the visualisations

Chapter Six

QUALITATIVE TESTING OF DEM COMPUTER CODE

6.1 Introduction

Before proceeding to simulate the flow of material through a transfer chute, the DEM code developed in Chapters Four and Five must be qualitatively tested at the macroscopic level to ensure its correctness. The first part of the chapter will examine the contact-force models in the normal and tangential directions for single contact situations i.e. a particle contacting a particle, and a particle interacting with a wall. The second section of the chapter will describe a multiple contact situation where the influence of parameters such as normal and tangential stiffness coefficients, restitution coefficient, and friction coefficient will be examined along with the performance of the boundaries. The third and final part of the chapter describes a simple procedure where the dissipation of energy is checked to verify the numerical stability of the system.

6.2 Single Contact Tests

The validation tests for single contacts are modelled on the work presented by Asmar et al (2002), however with modifications due to the differing contact force models used and differing geometric conditions – Asmar et al. (2002) conducted further geometric tests not detailed here as they used a three-dimensional system, while the current work performs simulations in two dimensions. The following tests are performed:

1. Normal contact between particles (see Figure 6.1 (a));
2. Normal contact between particle and wall (see Figure 6.1 (b));
3. Normal contact with rotation, particle – particle (see Figure 6.2 (a));
4. Normal contact with rotation, particle – wall (see Figure 6.2 (b)).

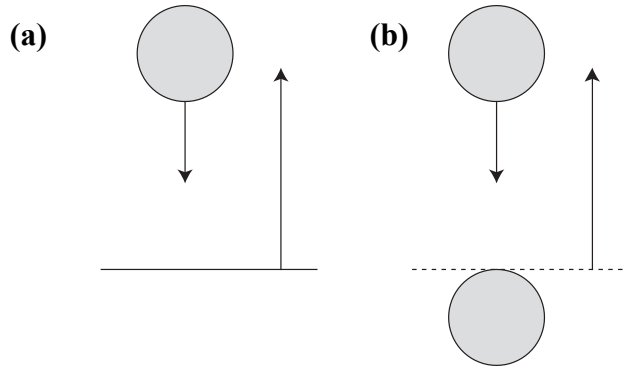

Figure 6.1 Normal contact between: **(a)** particle and wall; **(b)** particle and particle

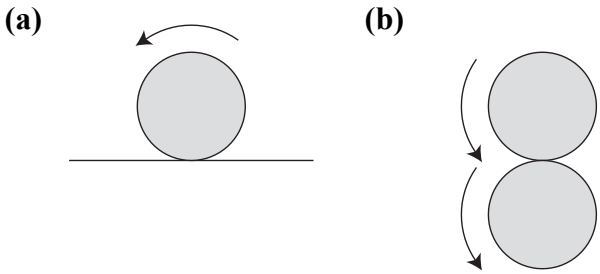

Figure 6.2 Normal contact with rotation between: **(a)** particle and wall; **(b)** particle and particle

Each case tests the implementation of the force-displacement algorithms used in the theory in isolated, single contacts. A summary of each test case is presented below. The computer code was modified for certain cases and shall be described further in each relevant section. The basic parameters used are listed in Table 6.1. In the table PP and PW refer to particle-particle and particle-wall respectively. The percentage overlap or overlap ratio ξ is defined as one minus the ratio of the distance between the mass centres of two contacting particles *dn* to the sum of their radii d_{ij} (Xu 1997), or:

$$\xi = 1 - \frac{dn}{d_{ij}} \tag{6.1}$$

The overlap ratio will be referred to in tests numbers 3 and 4 where particle rotational aspects are examined.

Table 6.1 Common parameters used for the single contact tests

Particle diameter	D_{base}	0.020	m
Particle density	ρ_p	1000	kg m^{-3}
Normal stiffness constant {PP / PW}	K_{n1}	1×10^7 / 1×10^7	N m^{-1}
Initial tangential stiffness {PP / PW}	K_t^0	1×10^7 / 1×10^7	N m^{-1}

6.2.1 Normal contact between particles

For the normal contact between two particles, the test simulates an initially stationary, free falling particle under gravity hitting a fixed particle, as illustrated in Figure 6.1 (b). Initial rotation was set to zero. A time step of $\Delta t = 1\times10^{-4}$s and coefficient of friction $\mu = 0.5$ were used. Two different coefficients of restitution were tested, $\varepsilon = 0.3$ and $\varepsilon = 0.6$.

Figures 6.3 (a) and 6.3 (b) show the vertical position and normal force respectively. For both $\varepsilon = 0.3$ and $\varepsilon = 0.6$ it can be seen that when the particle rebounds it fails to reach its original height and its height decays due to the dissipation of energy. The decline in the normal force at consecutive contacts can be seen. There was no movement in the horizontal direction and no rotation. As expected, the decay is more rapid for the lower restitution coefficient. The first normal force peak for $\varepsilon = 0.3$ isn't visible as it is coincident with the peak for $\varepsilon = 0.6$ in Figure 6.3 (b).

6.2.2 Normal contact between particle and wall

For the normal contact between a particle and a wall, the test is identical to that for the particle-particle case except that the falling particle hits a horizontal wall instead of a stationary particle, as illustrated in Figure 6.1 (a). The particle was dropped from the same height for both tests. A time step of $\Delta t = 1\times10^{-4}$s and coefficient of friction $\mu = 0.5$ was used. As for the particle-particle case, two different coefficients of restitution were tested, $\varepsilon = 0.3$ and $\varepsilon = 0.6$.

Figures 6.4 (a) and 6.4 (b) show the vertical position and normal force respectively. Since the particle is dropped from the same height as for the particle-particle contact case, the result for both cases is identical. Again as expected, the decay is more rapid for the lower restitution coefficient. Also, the first normal force peak for $\varepsilon = 0.3$ isn't visible as it is coincident with the peak for $\varepsilon = 0.6$ in Figure 6.4 (b).

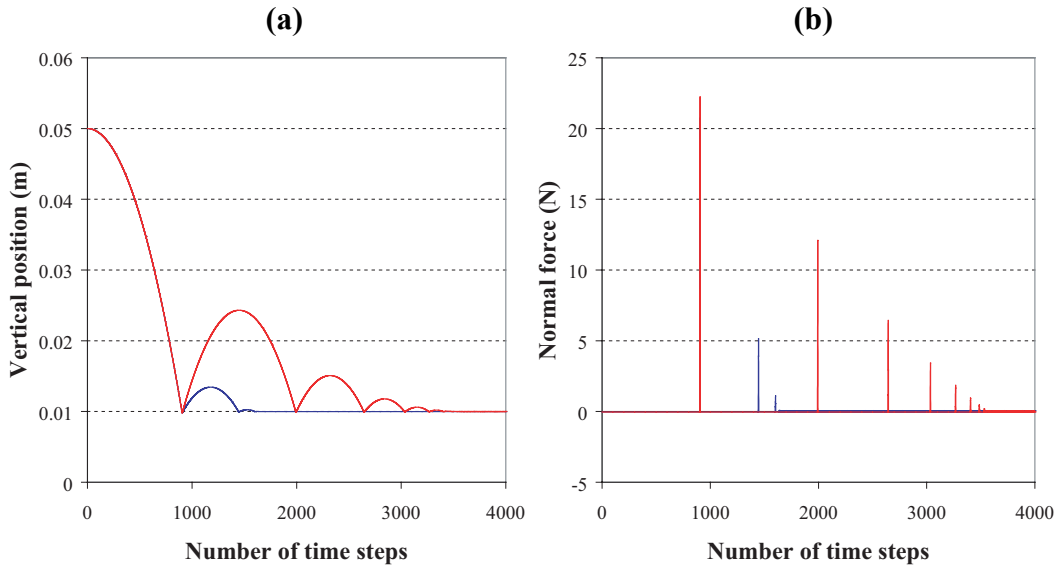

Figure 6.3 Vertical position **(a)** and normal force **(b)** for particle-particle contact with $\varepsilon = 0.3$ {—} and $\varepsilon = 0.6$ {—}

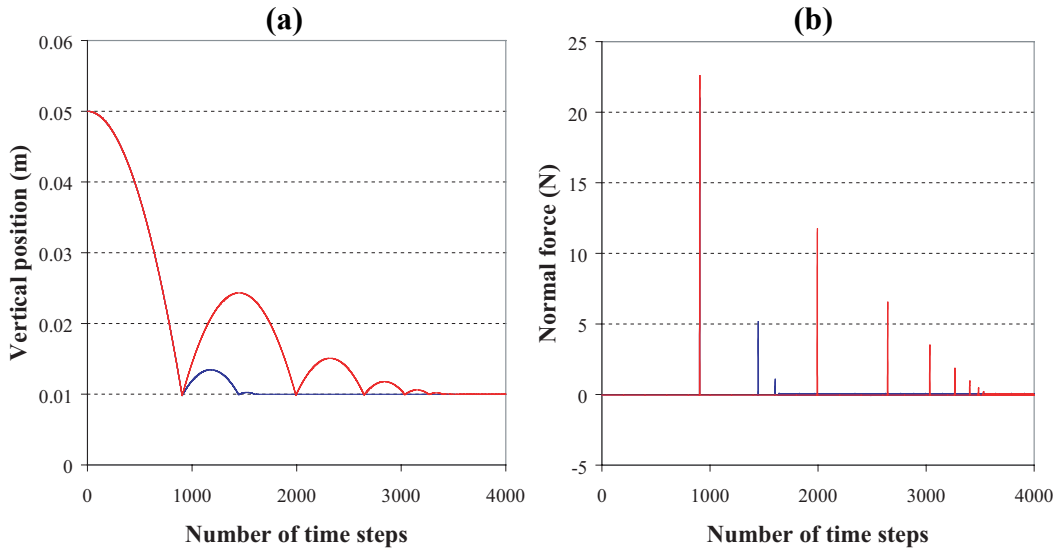

Figure 6.4 Vertical position **(a)** and normal force **(b)** for particle-wall contact with $\varepsilon = 0.3$ {—} and $\varepsilon = 0.6$ {—}

6.2.3 Normal contact with rotation, particle – particle

For this test, two particles are simulated, with fixed overlap and with no linear position update, and with gravitational force set to zero, as depicted in Figure 6.2 (b). An initial angular velocity of equal magnitude (40 $rads^{-1}$) is given to each particle. A time step of $\Delta t = 1\times10^{-7}$s and coefficient of restitution $\varepsilon = 0.5$ were used. Two different coefficients of friction were used, $\mu = 0.5$ and $\mu = 0.9$. The testing was conducted using particle-particle overlap ratios of $\xi = 0.1\%$, $\xi = 1.0\%$, and $\xi = 10.0\%$.

Figures 6.5 (a) and 6.5 (b) and Figure 6.6 (a) and 6.6 (b) illustrate the angular position and angular velocity respectively for $\mu = 0.5$ and $\mu = 0.9$. It can be clearly seen that for the highest overlap ratio used ($\xi = 10$ %) the angular position and angular velocity change in a harmonic manner that is analogous in manner to a linear spring where the particle rotates around itself and returns to the same position. The friction force shown in Figure 6.7 (a) and 6.7 (b) also oscillates. For the next overlap ratio ($\xi = 1$ %), a slight attenuation of the angular position and angular velocity can be observed, which is also evident in the friction force shown in Figure 6.7 (a) and 6.7 (b). For the smallest overlap ratio used ($\xi = 0.1$ %) the particles move into the gross sliding region as shown by the shift in the zero points in the angular position and angular velocity, after which attenuation can be seen. The corresponding force plateau can be observed in Figure 6.7 (a) and 6.7 (b), and this information illustrates the dissipation of energy. The general trends between the plots of $\mu = 0.5$ and $\mu = 0.9$ are similar, with the particles' time in the gross sliding region of greater length with the lower coefficient of friction.

6.2.4 Normal contact with rotation, particle – wall

For the case of particle-wall contact, the same test is conducted as for the particle-particle case, but with one particle and a static wall, as depicted in Figure 6.2 (a). A time step of $\Delta t = 1\times10^{-7}$s and coefficient of restitution $\varepsilon = 0.5$ were used. As for the particle-particle case, two different coefficients of friction were used, $\mu = 0.5$ and $\mu = 0.9$, and the testing was conducted using particle-wall overlap ratios of $\xi = 0.1\%$, $\xi = 1.0\%$, and $\xi = 10.0\%$.

Figures 6.8 (a), 6.8 (b), 6.9 (a), 6.9 (b), 6.10 (a) and 6.10 (b) illustrate the angular position, angular velocity and friction force respectively for $\mu = 0.5$ and $\mu = 0.9$. Since particle one starts from relatively the same position as for the particle-particle case, the results of both cases are similar. Again the longer period of time in the gross sliding region is for the lower coefficient of friction.

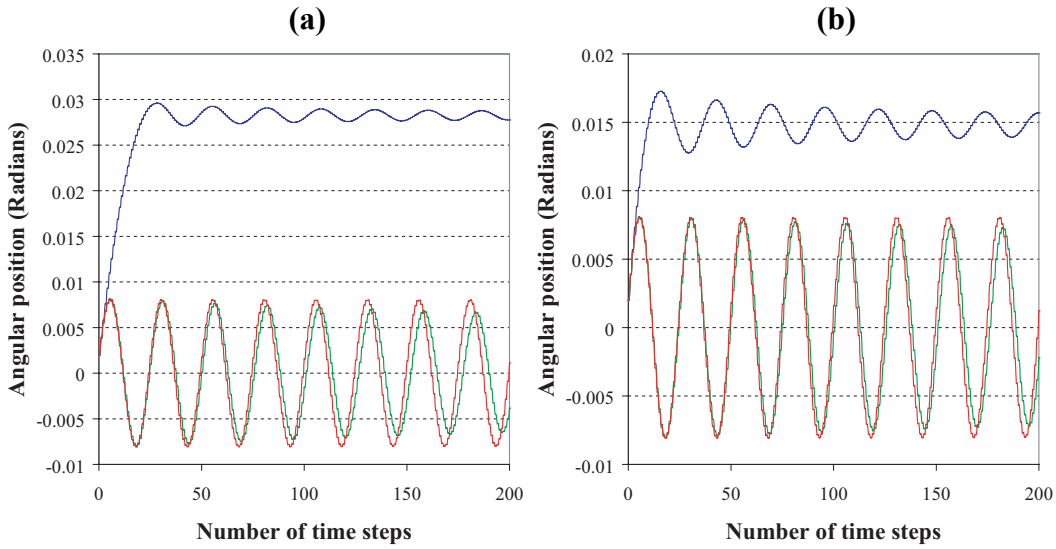

Figure 6.5 Angular position for particle-particle contact with **(a)** $\mu = 0.5$ and **(b)** $\mu = 0.9$, and overlap ratio $\xi = 0.1$ % {—}, $\xi = 1.0$ % {—}, and $\xi = 10.0$ % {—}

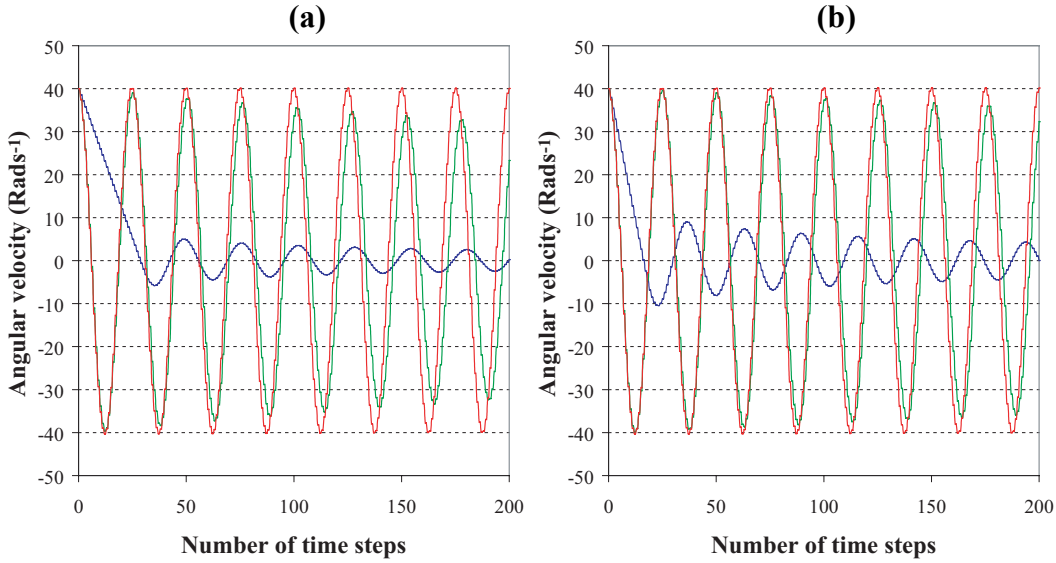

Figure 6.6 Angular velocity for particle-particle contact with **(a)** $\mu = 0.5$ and **(b)** $\mu = 0.9$, and overlap ratio $\xi = 0.1$ % {—}, $\xi = 1.0$ % {—}, and $\xi = 10.0$ % {—}

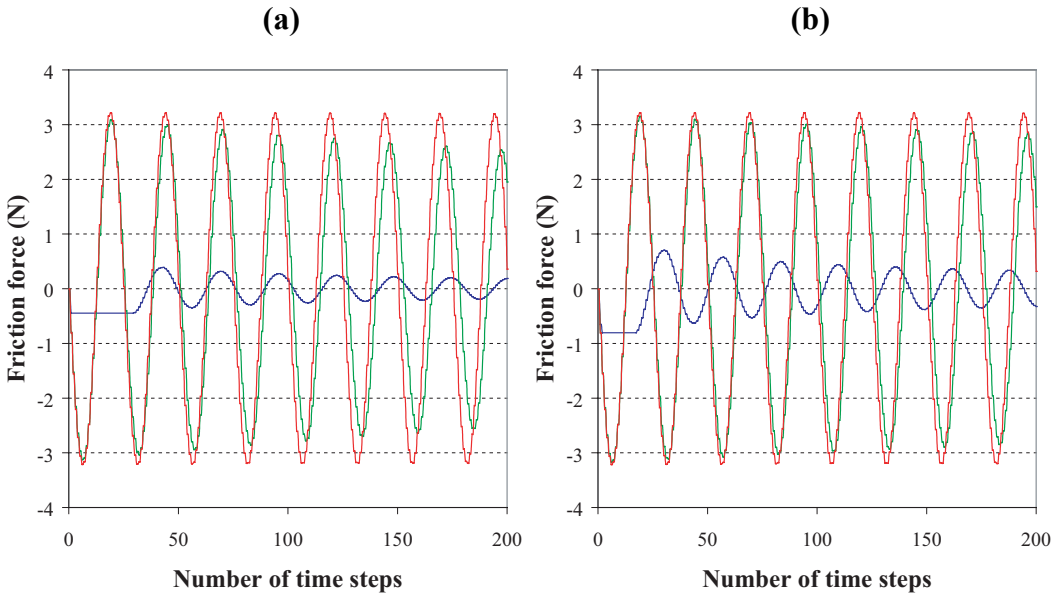

Figure 6.7 Friction force for particle-particle contact with **(a)** $\mu = 0.5$ and **(b)** $\mu = 0.9$, and overlap ratio $\xi = 0.1$ % {—}, $\xi = 1.0$ % {—}, and $\xi = 10.0$ % {—}

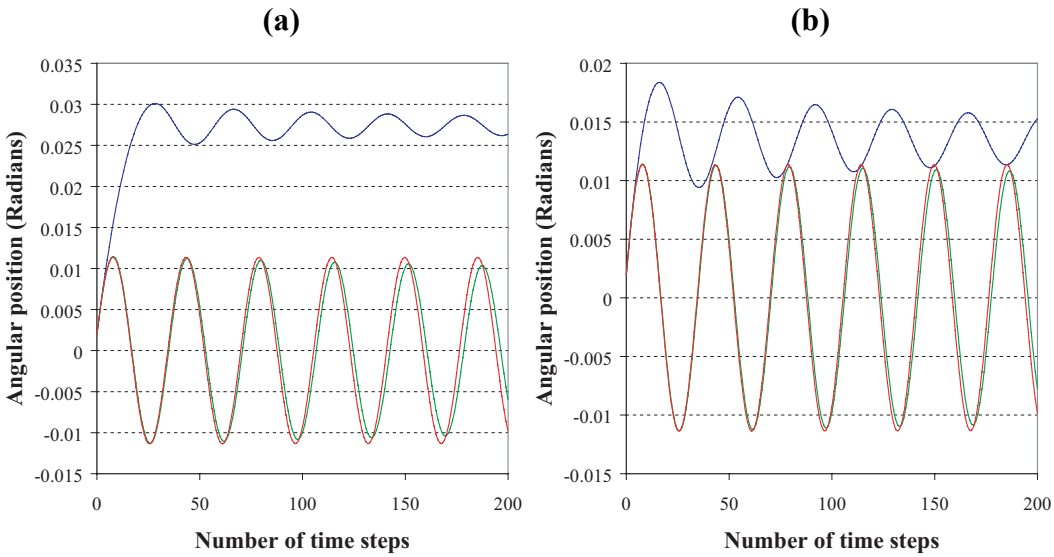

Figure 6.8 Angular position for particle-wall contact with **(a)** $\mu = 0.5$ and **(b)** $\mu = 0.9$, and overlap ratio $\xi = 0.1$ % {—}, $\xi = 1.0$ % {—}, and $\xi = 10.0$ % {—}

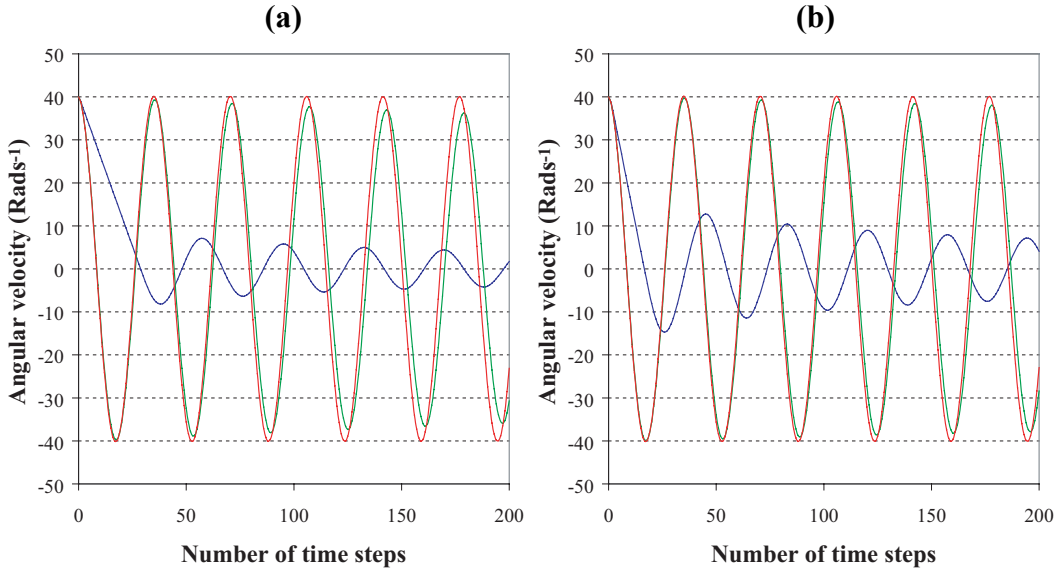

Figure 6.9 Angular velocity for particle-wall contact with **(a)** $\mu = 0.5$ and **(b)** $\mu = 0.9$, and overlap ratio $\xi = 0.1$ % {—}, $\xi = 1.0$ % {—}, and $\xi = 10.0$ % {—}

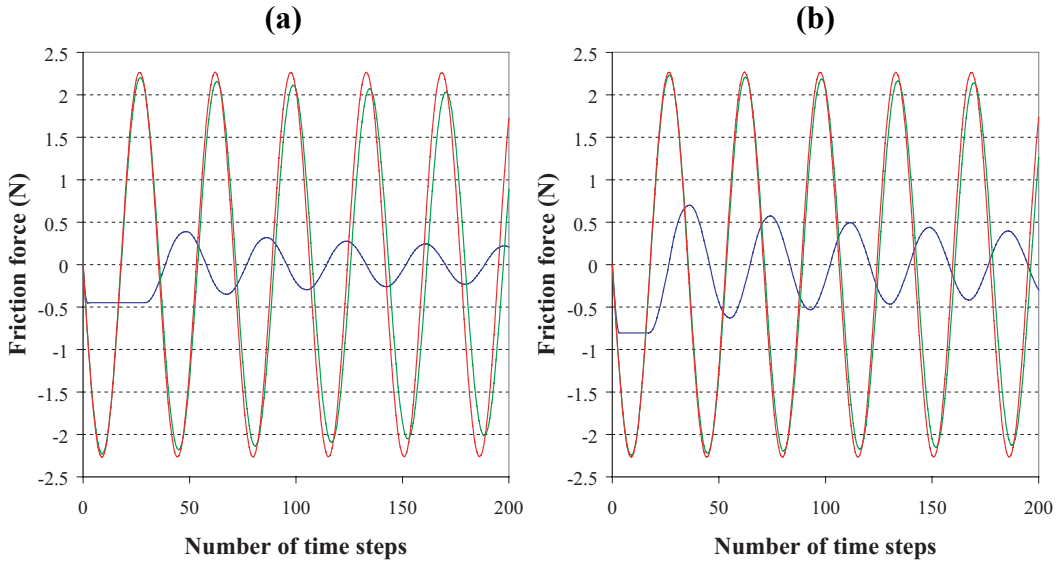

Figure 6.10 Friction force for particle-wall contact with **(a)** $\mu = 0.5$ and **(b)** $\mu = 0.9$, and overlap ratio $\xi = 0.1$ % {—}, $\xi = 1.0$ % {—}, and $\xi = 10.0$ % {—}

6.3 Multiple Contact Tests

For this test, an 'hour-glass' type arrangement will be utilised and the particle flow will be observed to ensure that general physical principles are followed in the model. The motion of the particles upon the boundaries will also be observed to gauge the performance of the particle and boundary definitions and contact force models. The hour-glass is set up in the initial configuration illustrated in Figures 6.11 (a), 6.12 (a), 6.13 (a), and 6.14 (a). The particles are set up in the hexagonal group as shown with a dilation factor of 1.2 and allowed to fall under the influence of gravity. The dilation factor is given by dn/d_{ij} where dn and d_{ij} are defined by Eq. (4.2) and (4.3) respectively in Chapter Four.

The general parameters used for the tests are listed in Table 6.2. The test allows for observations of particle interactions against one another, particle interactions against straight and curved boundaries, dissipation of energy as the particles lose momentum, and frictional effects among others. In the table PP and PW refer to particle-particle and particle-wall respectively.

Table 6.2 General parameters used for the multiple contact tests

Number of particles	N	100	
Time step	Δt	5×10^{-7}	s
Calculation space (x – direction)	X_{len}	0.8	m
Calculation space (y – direction)	Y_{len}	1.2	m
Base diameter	D_{base}	0.020	m
Diameter variance	D_{var}	0.005	m
Particle density	ρ_p	5000	kg m^{-3}
Coefficient of friction {PP / PW}	μ	0.3 / 0.3	
Normal stiffness constant {PP / PW}	K_{n1}	1×10^7 / 1×10^7	N m^{-1}
Initial tangential stiffness {PP / PW}	K_t^0	1×10^7 / 1×10^7	N m^{-1}
Coefficient of restitution {PP / PW}	ε	0.2 / 0.2	

The test will be separated into two streams. The first will examine the influence of normal and tangential stiffness values on the particulate flow, and the second will look at the influence of restitution and friction coefficients. Though the particles are spherical they have been animated using (in this case) partial disk objects and have been coloured differently in each quadrant to allow rotational motion to be examined.

6.3.1 Influence of Normal and Tangential Stiffness

The general parameters used for this test are presented in Table 6.2. However, in this test the normal and tangential stiffness's are varied, with the initial tangential stiffness set equal to the normal particle stiffness for each case. The first simulation used $K_{n1} = K_t^0 = 1 \times 10^5$ Nm^{-1} and the second used $K_{n1} = K_t^0 = 1 \times 10^7$ Nm^{-1}. The higher normal stiffness coefficient values were chosen to ensure the particle overlap was quite small, approximately 1.5 % of the smallest particle diameter, and hence one of the aims was to see if the excessive overlap given by the lower values for stiffness affected the flow in any way. Screen captures at selected intervals for each simulation are shown in Figure 6.11 (a) to 6.11 (f) for $K_{n1} = K_t^0 = 1 \times 10^5$ Nm^{-1} and Figures 6.12 (a) to 6.12 (f) $K_{n1} = K_t^0 = 1 \times 10^7$ Nm^{-1}.

The screen captures show similar particulate motion for both sets of stiffness parameters, indicating that K_{n1} and K_t^0 do not greatly influence the particulate flow motion depicted in the hour-glass arrangement. The lower value for stiffness and associated greater overlap between particles and boundaries did not cause the motion of flow to differ greatly. The use of a lower value for K_{n1} is therefore feasible. However the danger when using such low values of K_{n1}, particularly for smaller particles, is that there is always a chance of a particle passing through a boundary. This usually occurs when applied body forces are great.

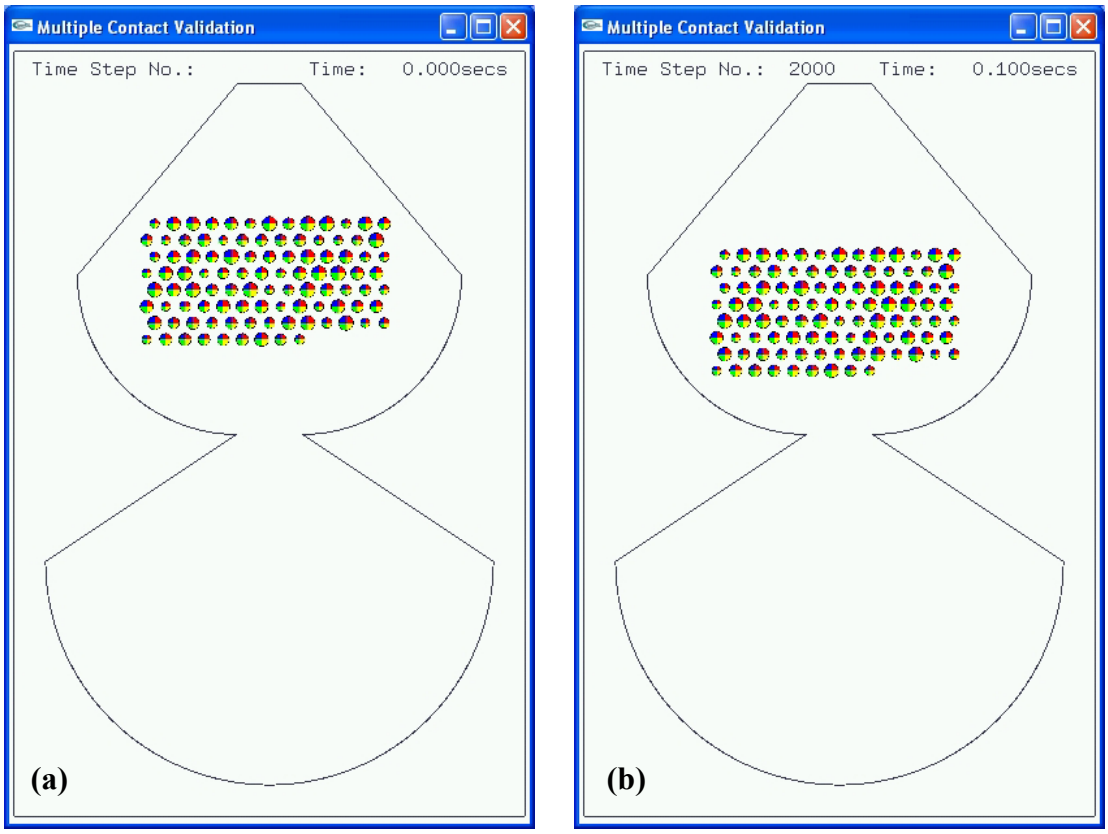

Figure 6.11 Hour-glass with $K_{n1} = K_t^0 = 1 \times 10^5$ Nm^{-1} at **(a)** $t = 0.00$ s; **(b)** $t = 0.10$ s

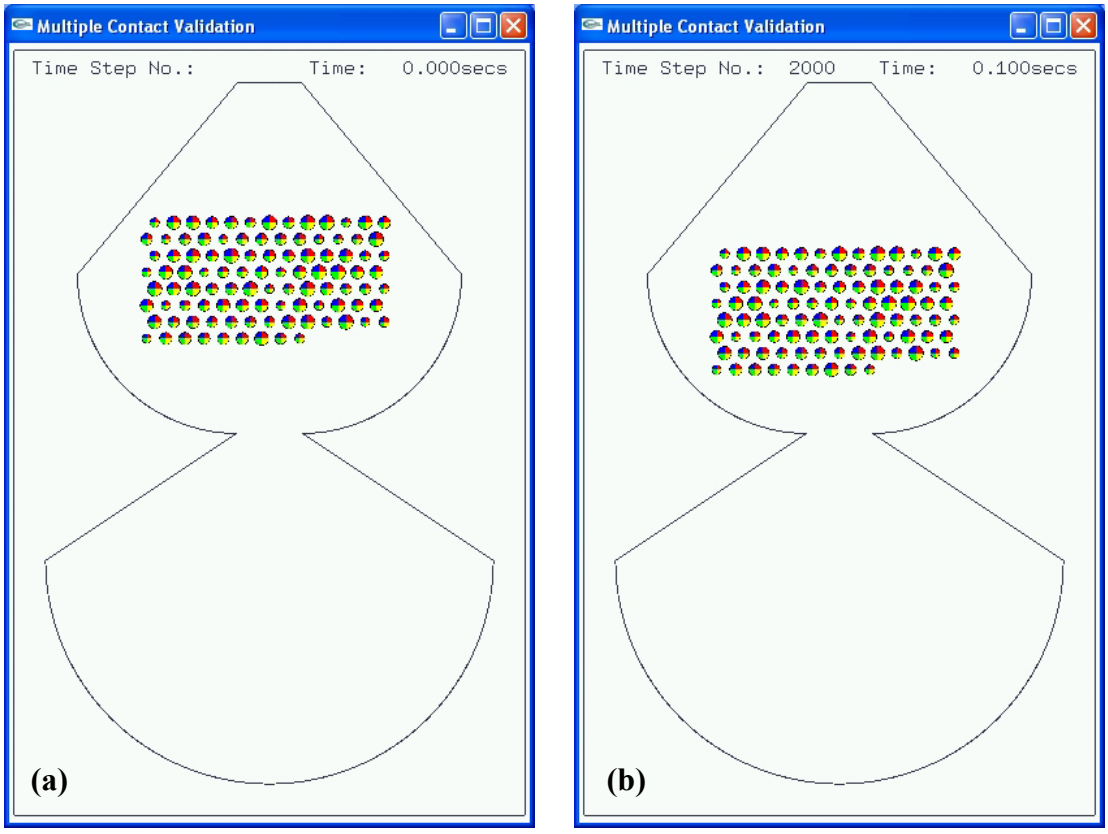

Figure 6.12 Hour-glass with $K_{n1} = K_t^0 = 1 \times 10^7$ Nm^{-1} at **(a)** $t = 0.00$ s; **(b)** $t = 0.10$ s

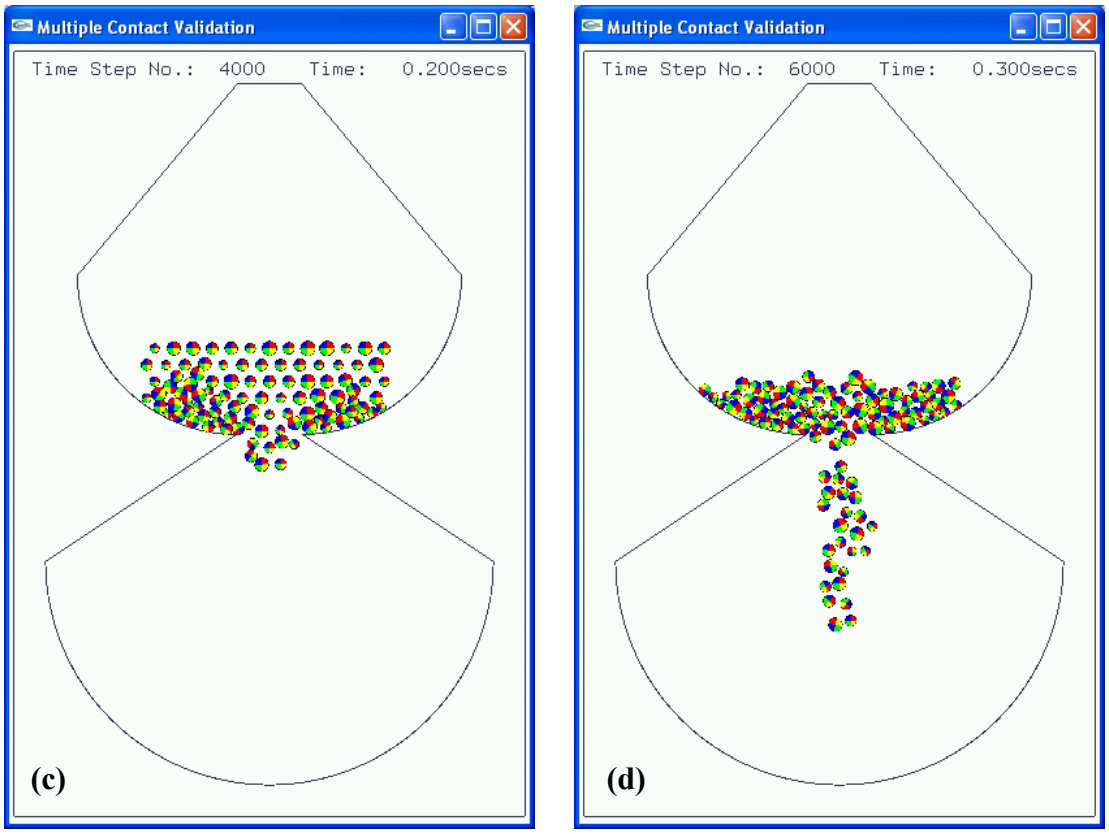

Figure 6.11 Hour-glass with $K_{n1} = K_t^0 = 1 \times 10^5$ Nm^{-1} at **(c)** $t = 0.20$ s; **(d)** $t = 0.30$ s

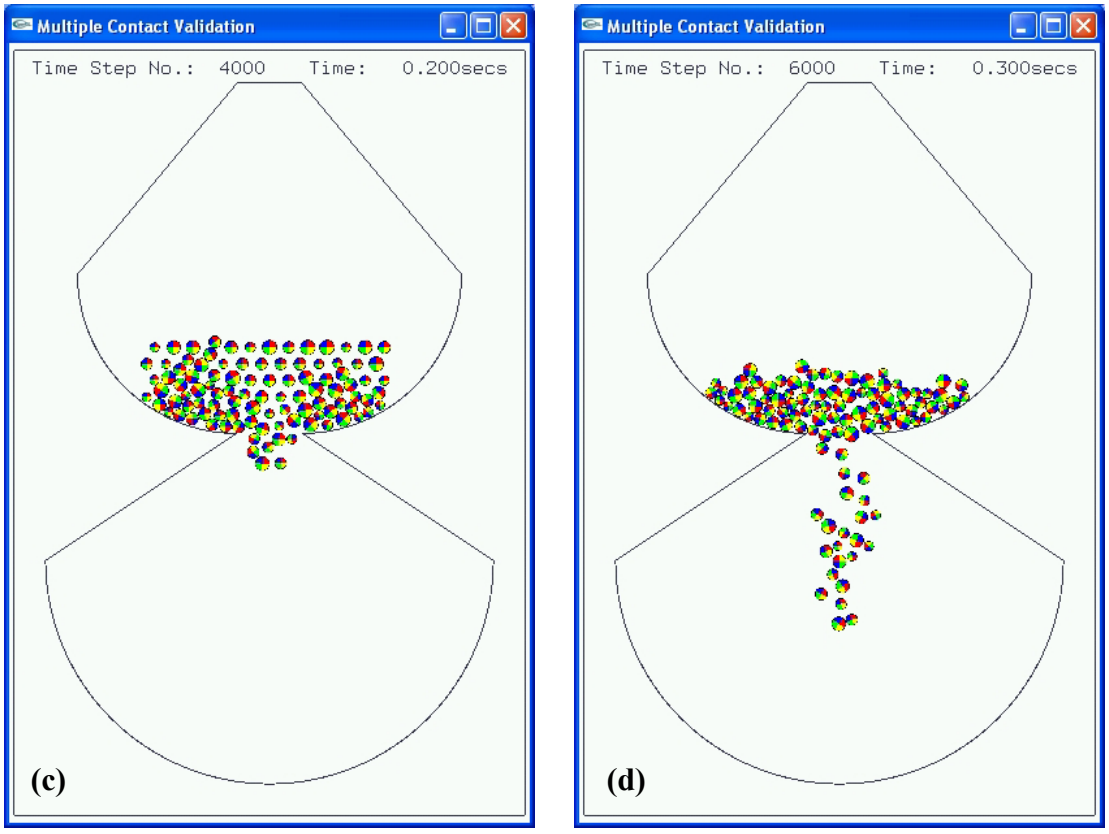

Figure 6.12 Hour-glass with $K_{n1} = K_t^0 = 1 \times 10^7$ Nm^{-1} at **(c)** $t = 0.20$ s; **(d)** $t = 0.30$ s

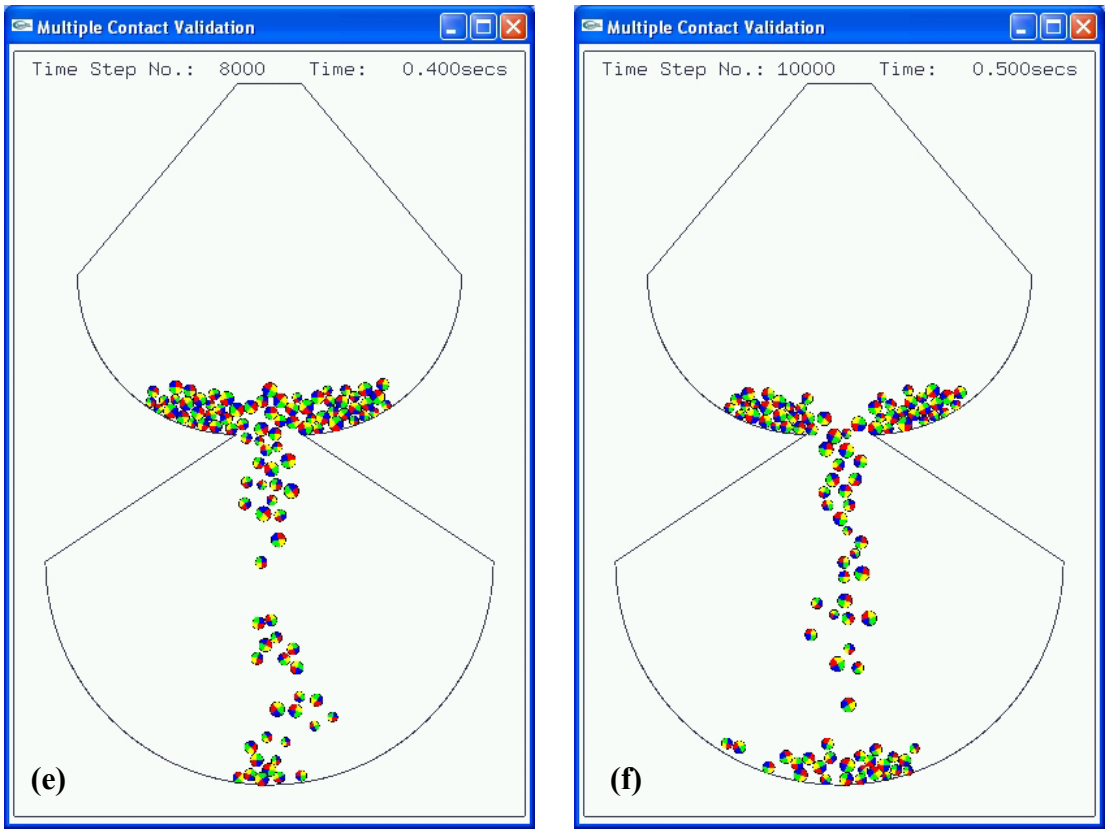

Figure 6.11 Hour-glass with $K_{n1} = K_t^0 = 1 \times 10^5$ Nm^{-1} at **(e)** $t = 0.40$ s; **(f)** $t = 0.50$ s

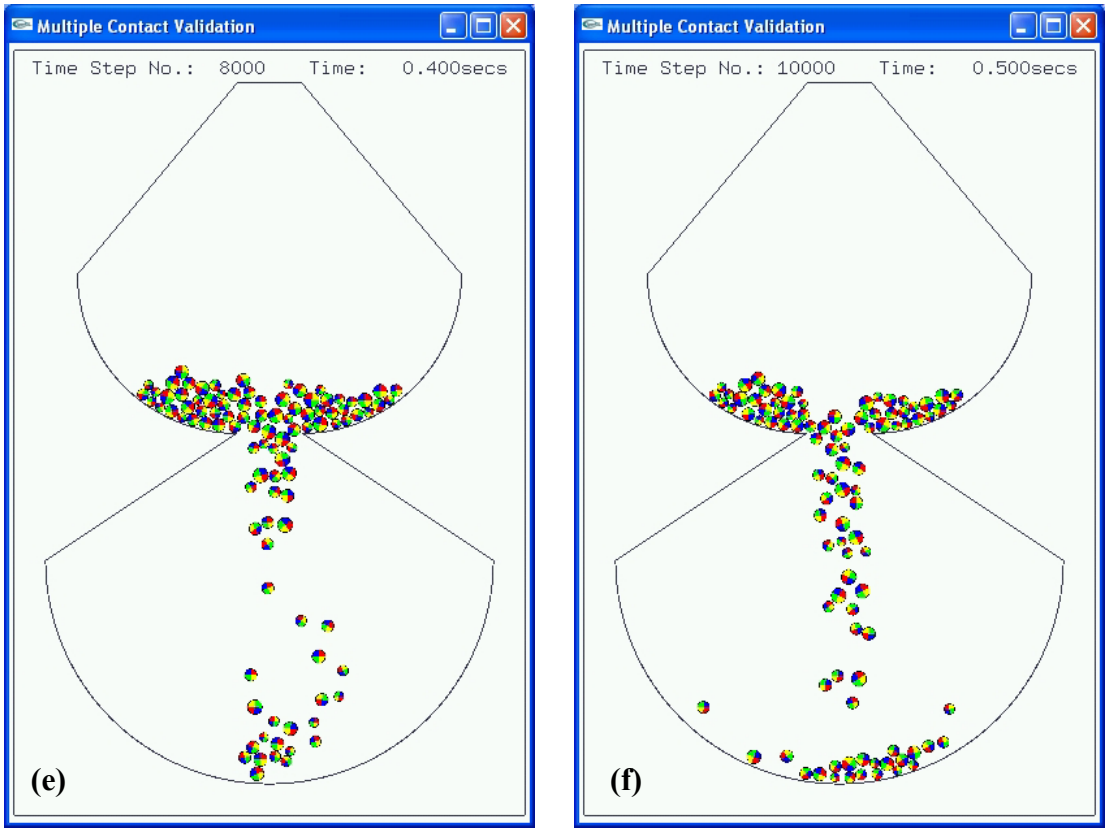

Figure 6.12 Hour-glass with $K_{n1} = K_t^0 = 1 \times 10^7$ Nm^{-1} at **(e)** $t = 0.40$ s; **(f)** $t = 0.50$ s

6.3.2 Influence of Coefficient of Restitution and Friction

The general parameters used for this test are presented in Table 6.2, however with the first simulation using $\varepsilon = 0.9$ and $\mu = 0.1$ and the second using $\varepsilon = 0.1$ and $\mu = 0.9$. Screen captures at selected intervals for each simulation are shown in Figures 6.13 (a) to 6.13 (f) for $\mu = 0.1$ and $\varepsilon = 0.9$ and Figures 6.14 (a) to 6.14 (f) for $\mu = 0.9$ and $\varepsilon = 0.1$.

The screen captures clearly show that μ and ε influence the particulate flow considerably. Figure 6.13 (d) shows the rebound and wild motion of the particles as the particle group drops onto the two upper curved surfaces flanking the aperture, which is in contrast to the motion shown in Figure 6.14 (d). A similar difference in particle motion states can be seen between Figure 6.13 (f) and Figure 6.14 (f), as the particles drop through the aperture and contact the lower curved surface of the hour-glass.

In summation, particle agitation and rebound are evident for $\mu = 0.1$ and $\varepsilon = 0.9$, while the particulate flow for $\mu = 0.9$ and $\varepsilon = 0.1$ is more restrained with less rebound. Energy is dissipated at the greater rate in the simulation using the higher friction coefficient and lower restitution coefficient. The choice of friction and restitution coefficients is important, not only for obtaining a close approximation to a bulk material, but also stability. For example, too great a value for ε could render a particle to rebound out of the calculation space. The boundaries also performed as desired, with particle impacts and rolling motion upon the curved surfaces qualitatively looking good. Similarly the inter-particle motion performed well.

6.4 System Stability Check

The numerical stability of the DEM system shall be verified by energy checking. The total energy E_T of a particle i at any given time can be found from the summation of its translational kinetic energy, rotational kinetic energy, gravitational potential energy, and elastic potential energy, which can be expressed by the following well known relation:

$$E_T = KE_{Translational} + KE_{Rotational} + PE_{Gravitational} + PE_{Elastic} \tag{6.2}$$

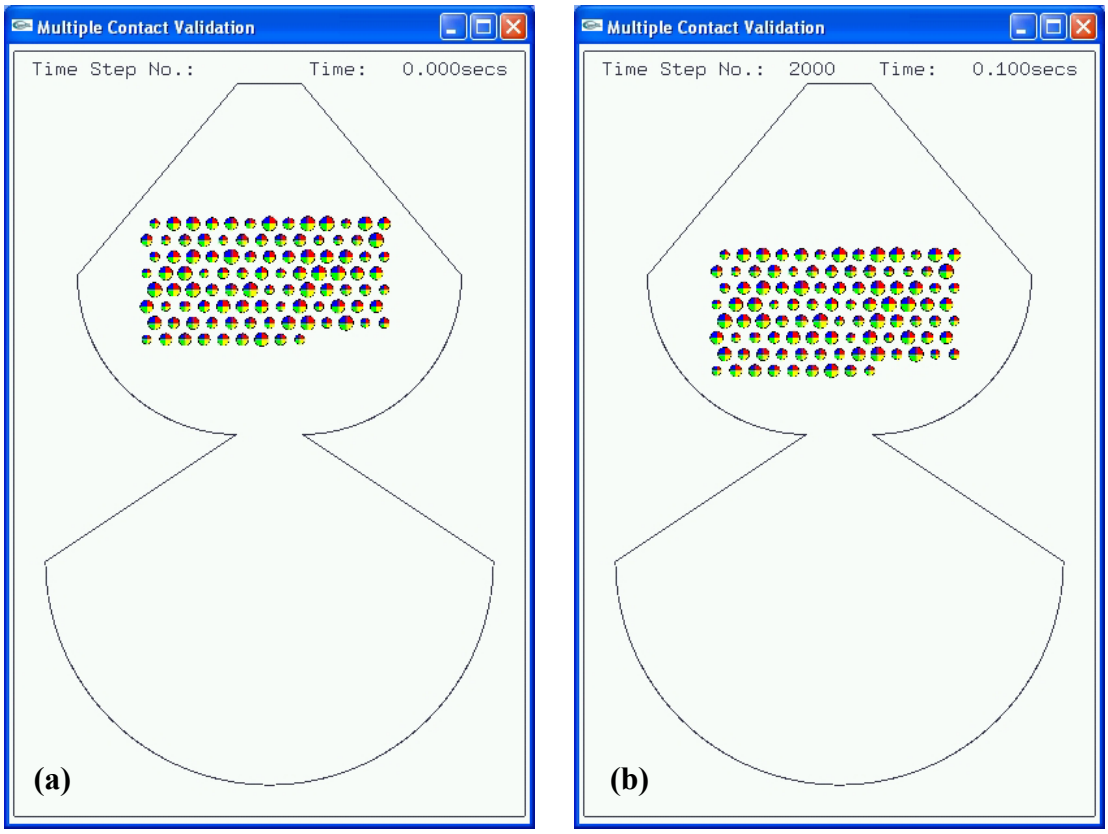

Figure 6.13 Hour-glass with $\varepsilon = 0.9$ and $\mu = 0.1$ at **(a)** $t = 0.00$ s; **(b)** $t = 0.10$ s

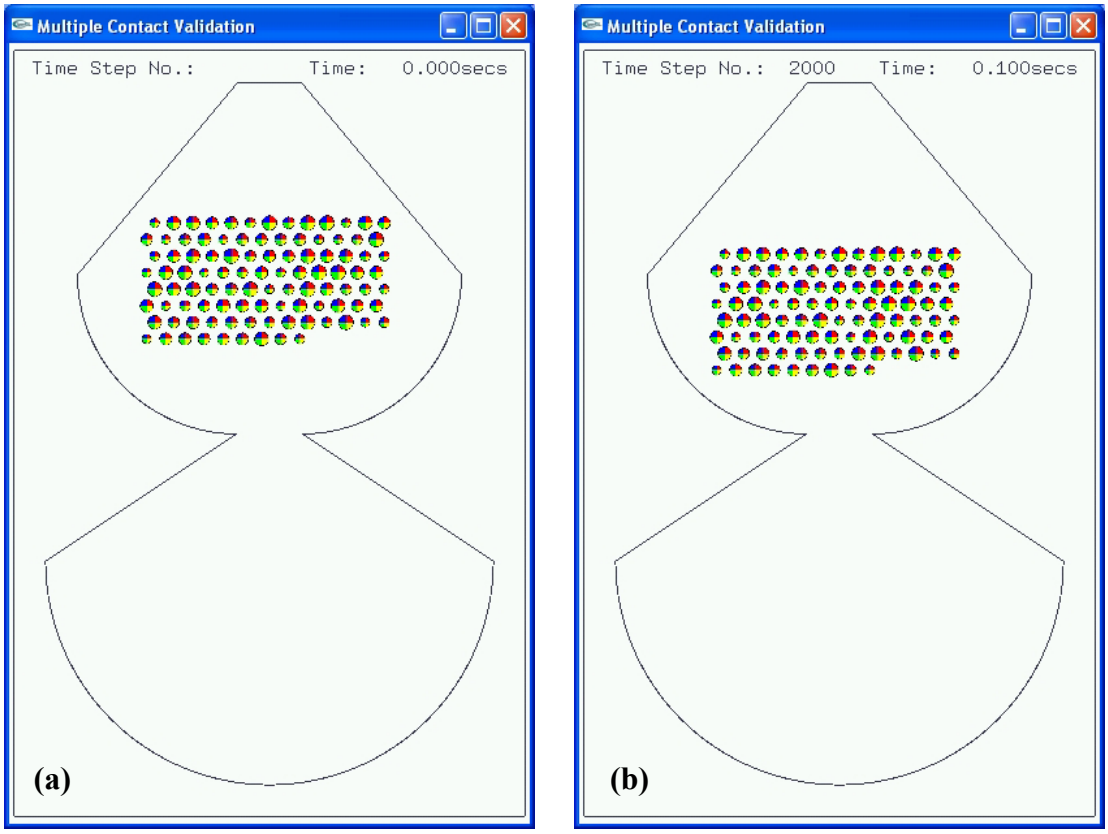

Figure 6.14 Hour-glass with $\varepsilon = 0.1$ and $\mu = 0.9$ at **(a)** $t = 0.00$ s; **(b)** $t = 0.10$ s

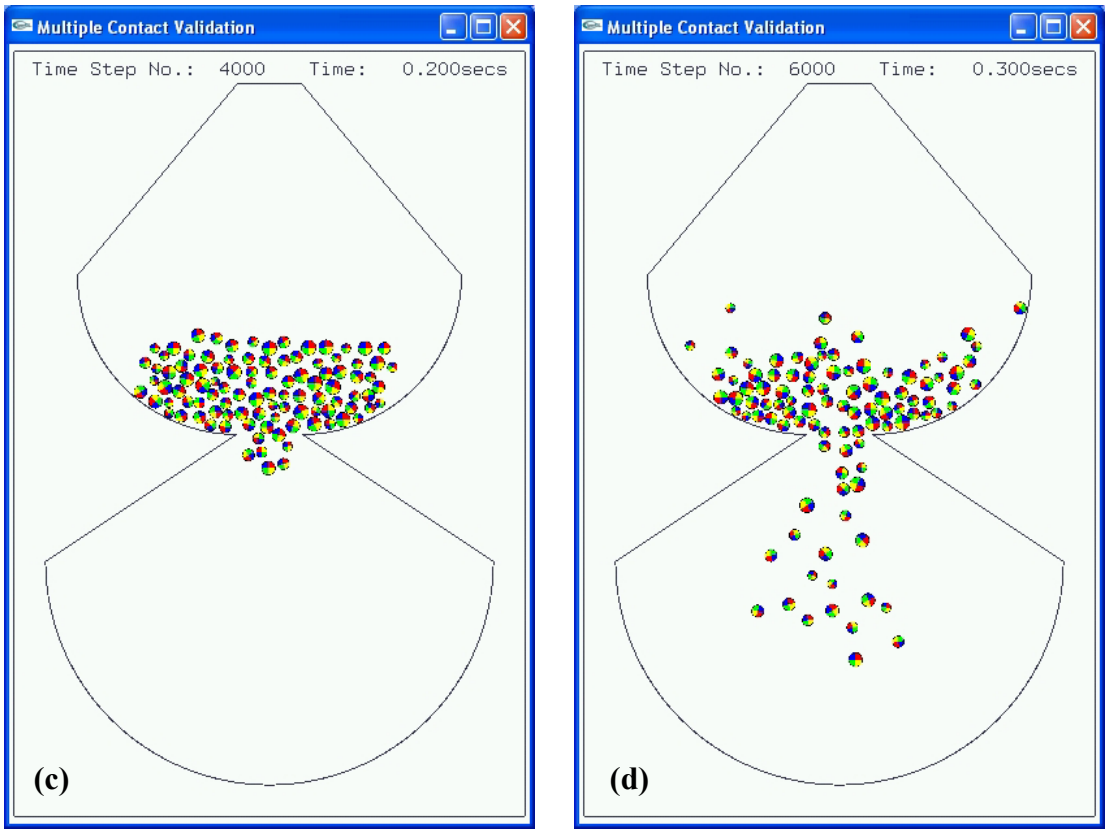

Figure 6.13 Hour-glass with $\varepsilon = 0.9$ and $\mu = 0.1$ at **(c)** $t = 0.20$ s; **(d)** $t = 0.30$ s

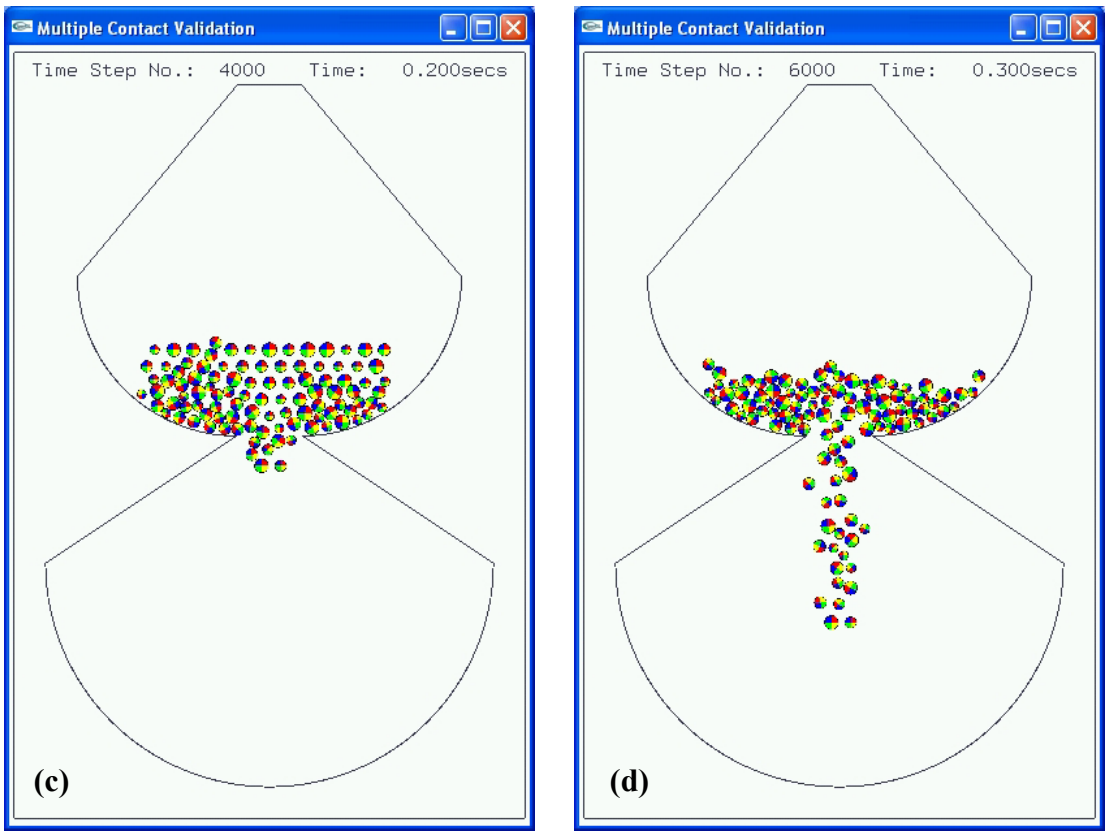

Figure 6.14 Hour-glass with $\varepsilon = 0.1$ and $\mu = 0.9$ at **(c)** $t = 0.20$ s; **(d)** $t = 0.30$ s

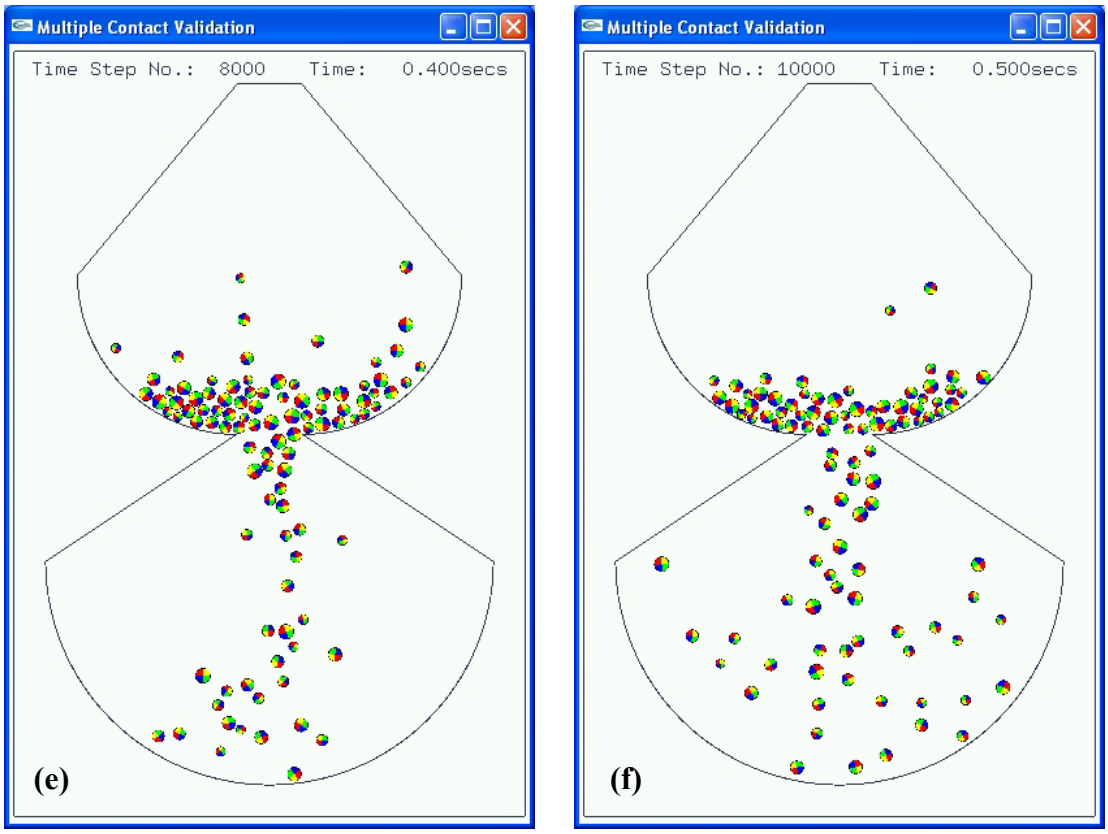

Figure 6.13 Hour-glass with $\varepsilon = 0.9$ and $\mu = 0.1$ at **(e)** $t = 0.40$ s; **(f)** $t = 0.50$ s

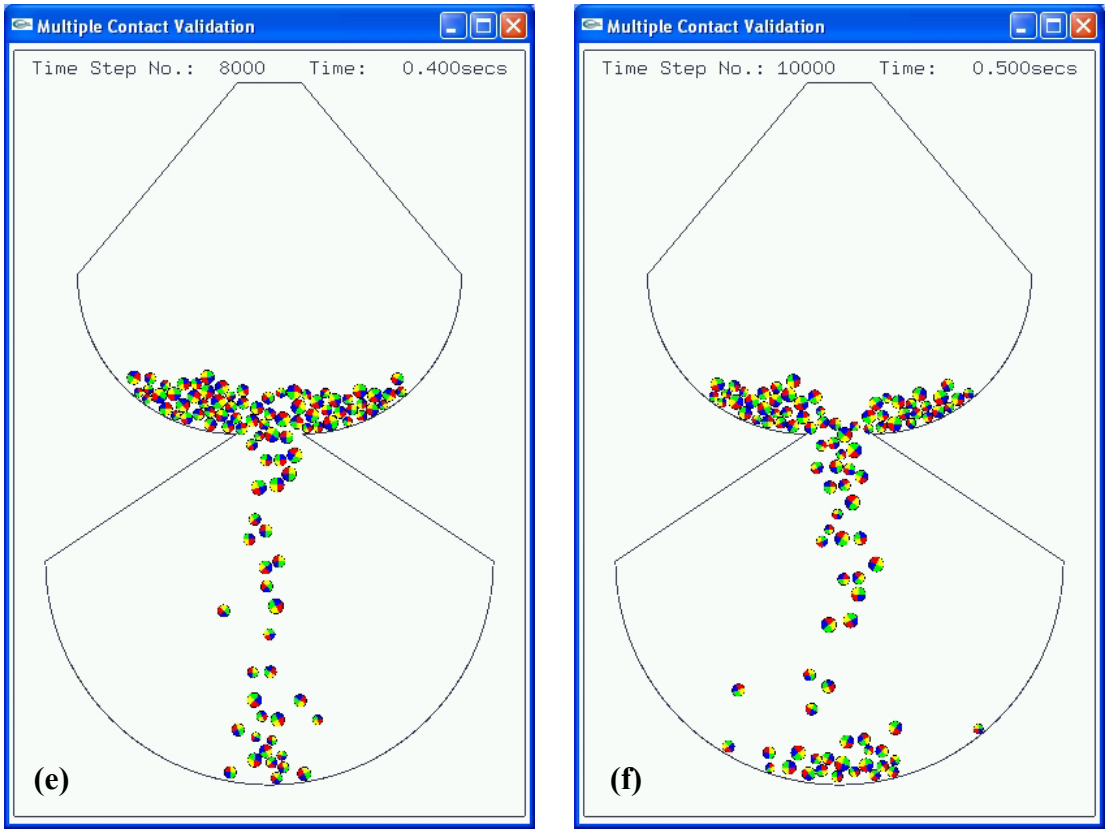

Figure 6.14 Hour-glass with $\varepsilon = 0.1$ and $\mu = 0.9$ at **(e)** $t = 0.40$ s; **(f)** $t = 0.50$ s

where:

$$KE_{Translational} = \frac{1}{2} m_i \left(\dot{x}_i^2 + \dot{y}_i^2 \right) \tag{6.3}$$

$$KE_{Rotational} = \frac{1}{2} I_i \dot{\theta}_i^2 \tag{6.4}$$

$$PE_{Gravitational} = m_i g h_i \tag{6.5}$$

$$PE_{Elastic} = \frac{1}{2} K_{1n} \delta_{n,i}^2 \tag{6.6}$$

where m_i is the mass and $\dot{x}_i$ and $\dot{y}_i$ are the translational velocities of particle i, I_i and $\dot{\theta}_i$ are the moment of inertia and angular velocity of particle i, g is gravity, h_i is the height of particle i above the surface nominated as a datum, and K_{1n} and $\delta_{n,i}$ are the stiffness and overlap respectively of particle i.

A simple test system will be used consisting of a rectangular shaped box with 40 identical spherical particles, distributed in the calculation space as shown in Figure 6.15 (a). All the particles are of radius R_i = 0.05 m and density ρ_p = 1000 kgm^{-3}. For both particle-particle and particle-wall interactions the coefficient of friction μ used was 0.2, the normal and initial tangential stiffness's were $K_{n1} = K_t^0 = 1 \times 10^7$ Nm^{-1}, and a relatively high coefficient of restitution $\varepsilon = 0.9$ was used. A time step of $\Delta t = 5 \times 10^{-6}$ s was used, and the simulation was ended after 1×10^6 time steps.

The particles were allowed to fall from rest under the influence of the gravity until they settled on the lower boundary surface. Basically, if the total kinetic energy of the system is zero after settlement, the system is stable. Further screen captures of the DEM simulation at nominated times are shown in Figures 6.15 (a) to 6.15 (f).

Figure 6.16 presents the four components of energy as time progresses. The translational kinetic energy starts at a value of zero and rises to peak at approximately 4.5 s, which corresponds to the time just before impact. The impact process and settling of particles can be observed in Figures 6.15 (b), 6.15 (c) and 6.15 (d). After impact the energy rapidly decreases after which any minor increases are due to the slight shift in

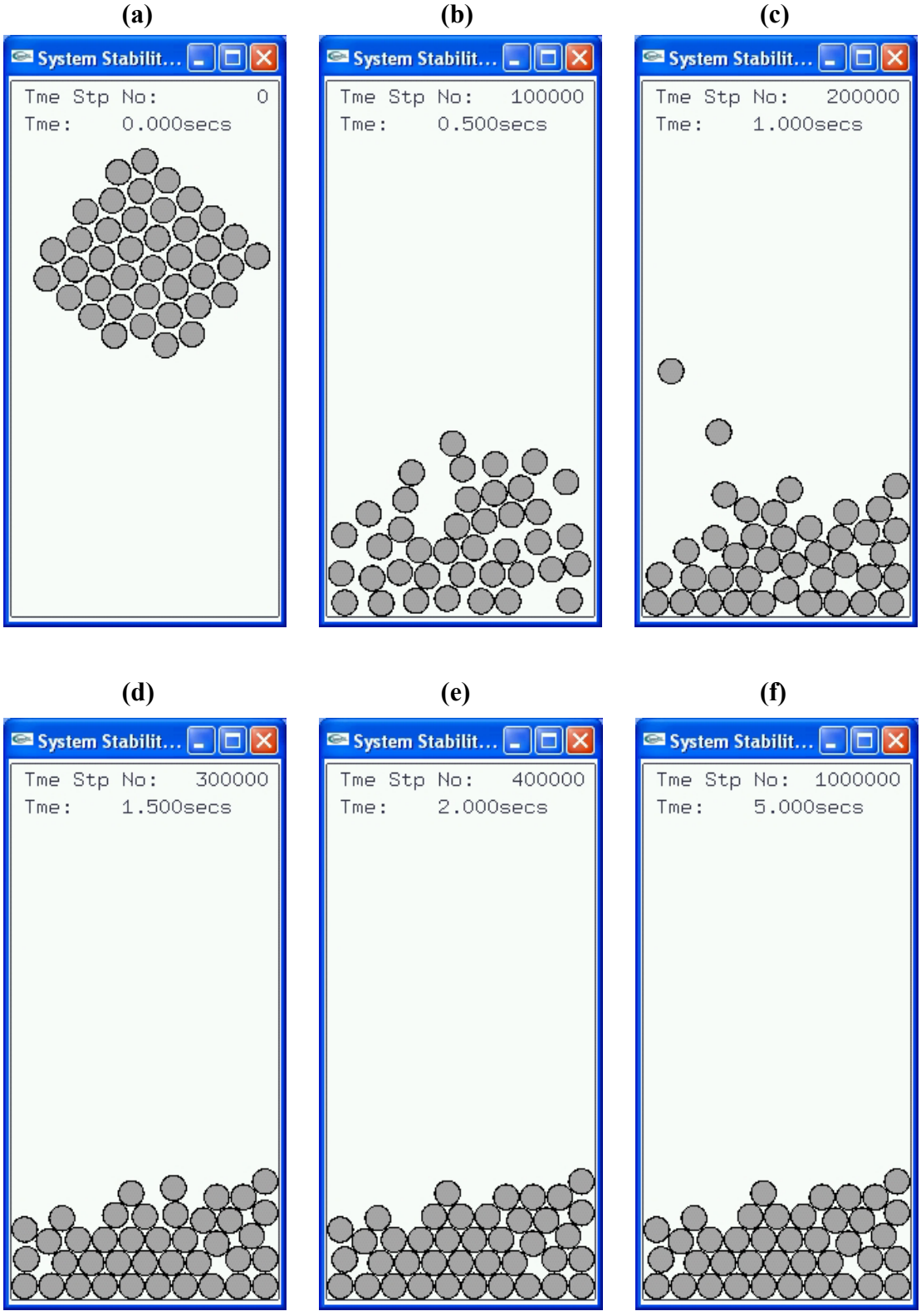

Figure 6.15 Distribution of particles within rectangular shaped boundary for numerical stability checking at times **(a)** $t = 0.0$ s **(b)** $t = 0.5$ s **(c)** $t = 1.0$ s **(d)** $t = 1.5$ s **(e)** $t = 2.0$ s **(f)** $t = 5.0$ s

particle positions during the settling process. Eventually this energy component reduces to zero once the particles are stationary, as can be seen in Figures 6.15 (e) and 6.15 (f). The rotational component of kinetic energy contributes very little, and can be seen to rise briefly at the point of impact in Figure 6.16 (a), however reduces back to zero as the particles settle.

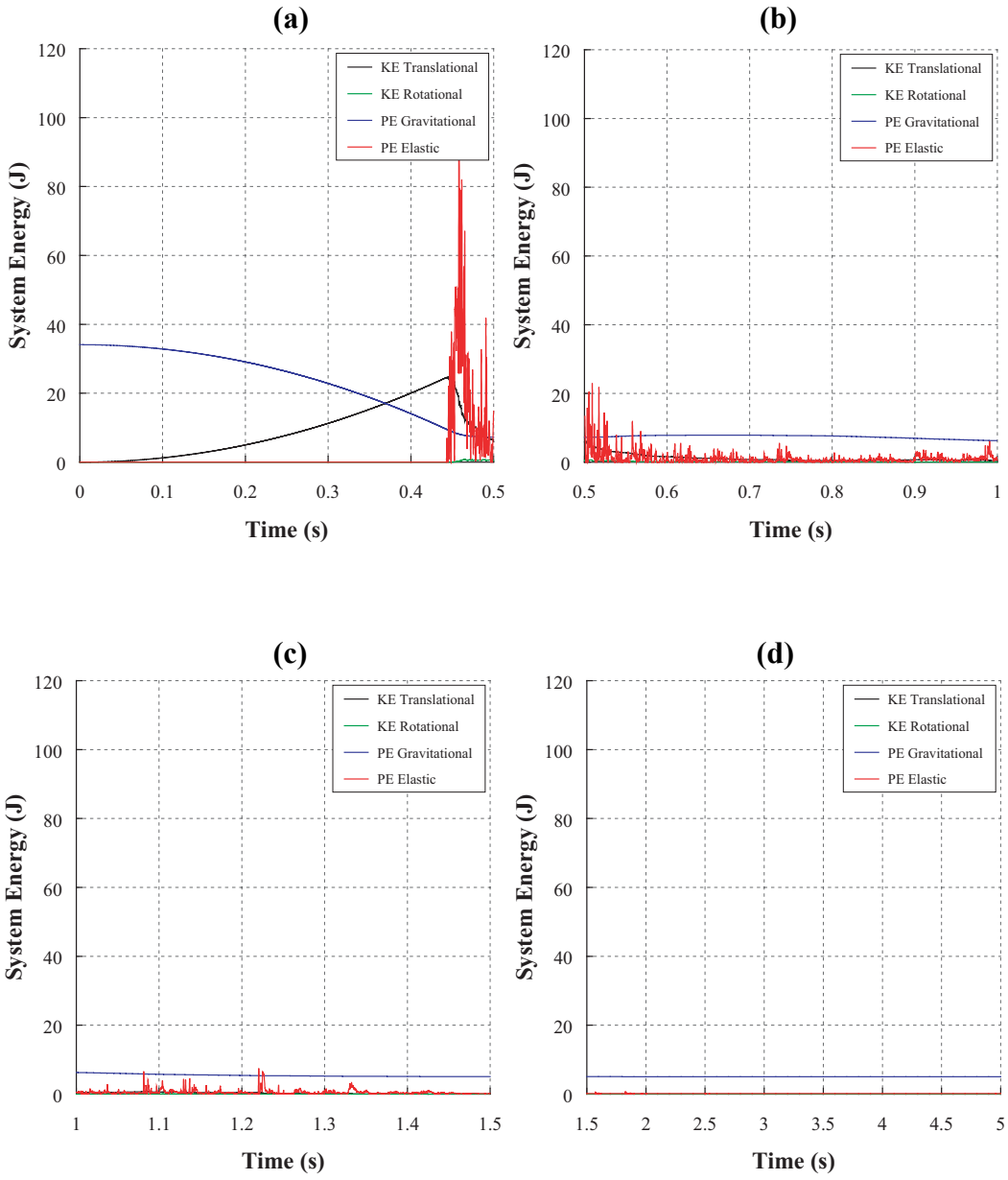

Figure 6.16 Progressive readings of each of the four system energy components at each time step at time intervals of: **(a)** t = 0.0 s – 0.5 s; **(b)** t = 0.5 s – 1.0 s; **(c)** t = 1.0 s – 1.5 s; **(d)** t = 1.5 s – 5.0 s.

The gravitational potential energy starts at its peak at the initial particle group position shown in Figure 6.15 (a), but gradually reduces as the particles fall. This component of energy can be seen to have a constant value when the particles are stationary, representing the gravitational potential energy in the system resulting from the particle mass centres above the datum point, which is the lower horizontal boundary.

The elastic potential energy has a 'noisy' appearance which is due to this energy component being calculated only after particulate overlaps occur. The highest peaks of the elastic energy representation in the plots arise quite suddenly and can be seen in Figures 6.16 (a) and 6.16 (b). This corresponds to the times when the particle group first impacts upon the lower boundary. Gradually the peaks lessen in height, and disappear completely after 1.5 s. The low upward shifts of elastic energy between approximately 0.7 s and 1.5 s in Figures 6.16 (b) and 6.16 (c) represent the gradual settling of the particles till they are stationary.

The total energy of the system i.e. summation of the four energy components is plotted in Figure 6.17. The total system energy is constant until impact occurs, where clearly the elastic potential energy obtains the greatest maxima and thus dominates the energy total. It is evident that eventually with both the translational and rotational kinetic energies equal to zero when the particles are stationary, the total energy is equal to the constant gravitational potential energy. Further tests with lower stiffness's were performed (not shown) and were found to reduce the maxima points slightly. One issue with plotting the total energy is that in the DEM calculations the kinetic energy is half a time step out of phase with the potential energy due to the explicit time integration scheme used (positions evaluated at every step, velocities evaluated at every half step). Such a summation thus renders the result slightly inaccurate, however qualitatively the trends in Figure 6.17 would not differ markedly. This inaccuracy could be reduced by utilising a smaller time step however computation times would obviously increase. The minimal improvement (theoretically) in results does not warrant such small time steps.

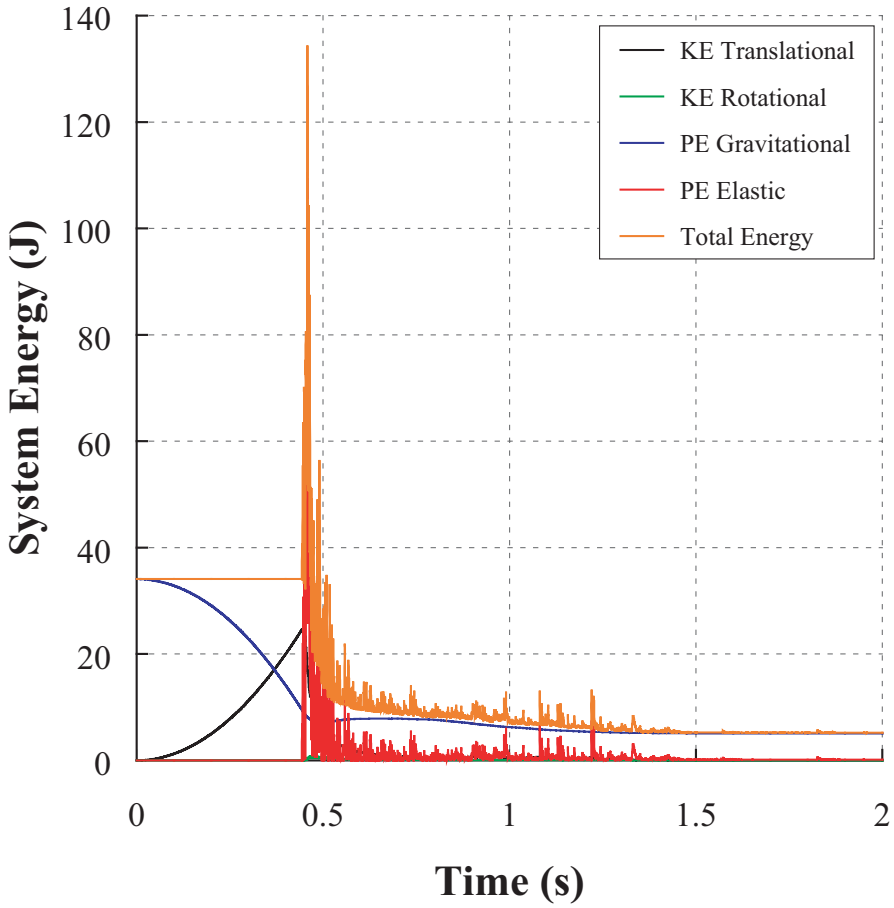

Figure 6.17 Total energy of the system plus each individual energy component from t = 0.0 s to t = 2.0 s

6.5 Summary

Single contact and multiple contact tests were conducted to qualitatively validate the distinct element model while the numerical stability was verified by energy checking. The trends observed in the particle's vertical position, normal force, angular position angular velocity, and friction force over time during the single contact tests were qualitatively very similar to the results published by Asmar et al (2002) and hence show the code to perform sufficiently for single contact situations.

The multiple contact model illustrated that friction and coefficient of restitution influenced the particulate flow significantly, more so than changing stiffness parameters. The motion characteristics and interactions of the particles with the boundaries were qualitatively very good, and the computer code did not show any errors during

compilation. This suggests the DEM methodology and applied numerical procedures for contact detection and simulating particle-particle and particle-wall contacts are working correctly.

The stability checking portion of the validation illustrated that kinetic energy reduced to zero once the particles had come to rest. For the test performed, the elastic potential energy reached high peaks briefly during the period of greatest contact, however dwindled soon after, which was expected as in that time interval the greatest particulate overlaps occurred. The constant amplitude of the gravitational energy component after dissipating the kinetic energy was also evident.

The next two chapters will now describe the utilisation of DEM code to model belt conveyor transfer applications, including one major aim of quantitatively comparing the results to those given by the analytical methods presented and analysed in Chapters Two and Three.

Chapter Seven

INTRODUCTION TO INDUSTRY CHUTE SYSTEMS

7.1 Introduction

In this chapter two separate chute systems designed by Gulf will be introduced. All preliminary work pertaining to utilising the Distinct Element Method described in Chapters Four and Five to model the particulate flow through the chute systems will be described. Any approximations to facilitate the three-dimensional transfers in a two-dimensional DEM environment will be explained. The animation coding outlined in Chapter Five will also be used to visualise the particulate flow, and particular areas of concern regarding memory concerns and coding the relevant animation aspects will be highlighted. Chapters Two and Three detailed and identified the most accurate analytical chute design methods, and these will be applied to the two chute systems as a means of comparison against the DEM results. This chapter specifies the particular design techniques used, while the results will be described in Chapter Eight.

7.2 Selection and Overview of Chute Systems

The current work utilises spherical particles that are constrained to move within a x-y coordinate structure, resulting in what is essentially a two-dimensional system. Potential transfer chute systems were selected based upon which system limited pertinent factors that could affect flow motion (and hence require a three-dimensional analysis to investigate further). Drop heights between chutes were required to be minimal to ensure the ‘footprint’ or cross-section of the material exiting the hood was relatively similar to that entering the spoon. Air entrainment factors can affect the cross-section for large drop heights hence this requirement. Another requirement was that the vertices of the rear and side walls at the lowest point of the hood were to coincide with the vertices of the side and rear walls at the highest point of the spoon for any right-angled transfers.

This ensured that the breadth of the material footprint exiting the hood could be assumed to be equal to the width of the material footprint entering the spoon and thus allow the transfer chute to be examined in two dimensions. The spoon would be (virtually) rotated around 90 degrees. The chute system chosen must transfer free-flowing or non-cohesive materials as neither the analytical methods nor the developed DEM code catered for 'sticky' materials.

Taking the above requirements into consideration, the two chutes chosen for analysis were a hood-spoon system with trapezoidal footprint to transfer material 90 degrees, and a hood with rectangular footprint transferring material onto a stockpile. Both chutes were designed by Gulf for a client whose colliery is located in Lithgow, Australia, and have been commissioned and are currently in use. The transfer chutes were designed using Gulf's EasyFlow™ technology, and to date the transfer performance has exceeded colliery expectations. This patented design tool has been overhauled by the author to include many of the analytical design techniques described in Chapters Two and Three, hence the comparison with DEM. Figures 7.1, 7.2, 7.3 and 7.4 show SolidWorks™ representations of the chutes. Detailed AutoCAD® assembly drawings and further three-dimensional SolidWorks™ images for each chute are located in Appendix IV. It can be observed from Figures 7.1 and 7.2 that for the hood-spoon chute system chosen, the lower portion of the hood is actually inside the upper section of the spoon but only marginally, therefore the lowest point of the hood and the highest point of the spoon are assumed to be coincident with each other.

7.3 System Setup

7.3.1 DEM processes

The first step in analysing the transfer system using DEM was to model the loading of the discharging belt. Hustrulid (1998) outlines a number of methods for loading the discharging belt. He utilised a particle 'generation box', which has the advantage of using a minimal amount of particles and the desired mass flow rate can be controlled (in

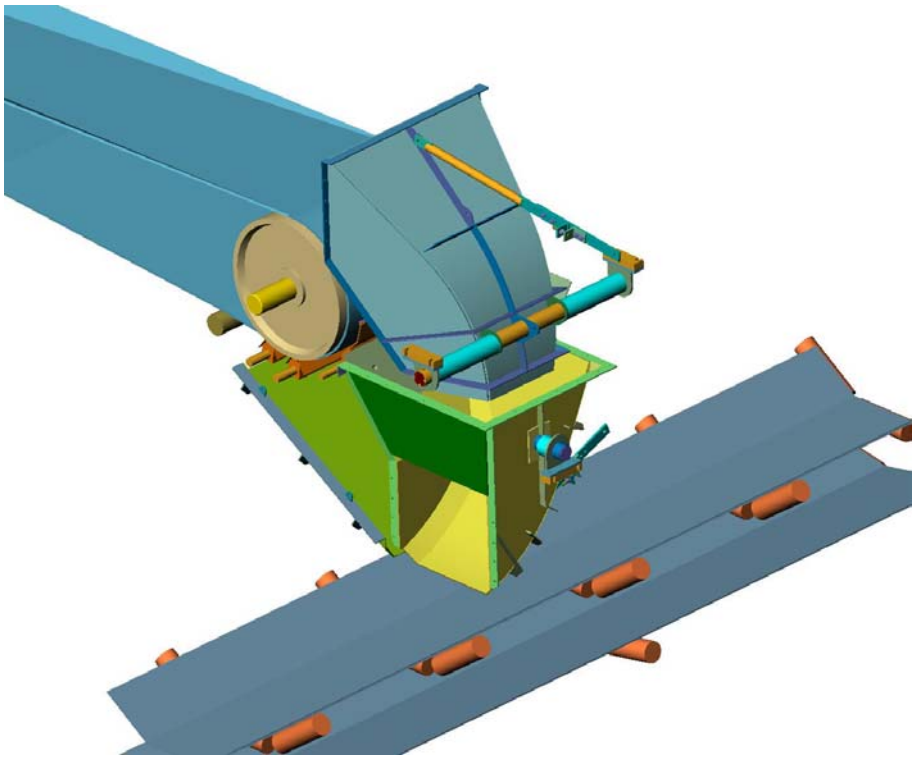

Figure 7.1 Image depicting hood-spoon transfer chute system – view one

Figure 7.2 Image depicting hood-spoon transfer chute system – view two

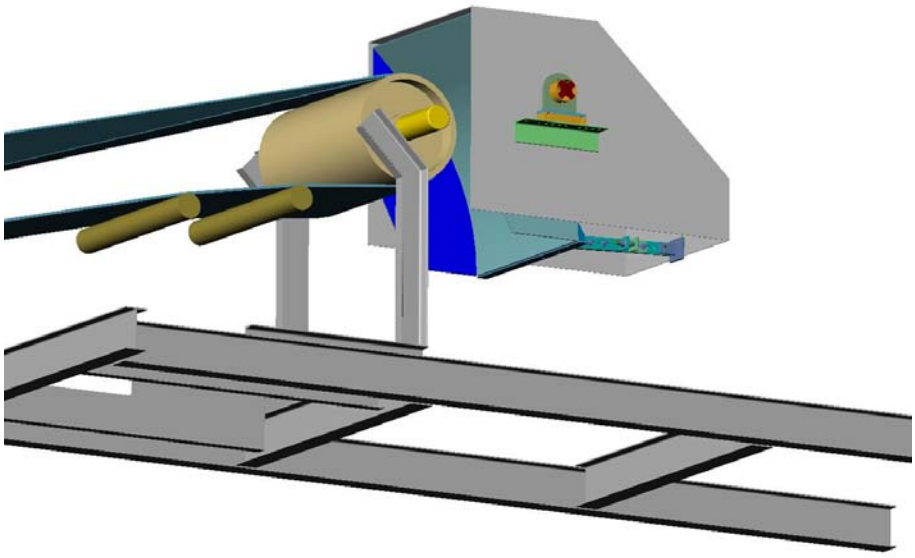

Figure 7.3 Image depicting single hood transfer chute system – view one

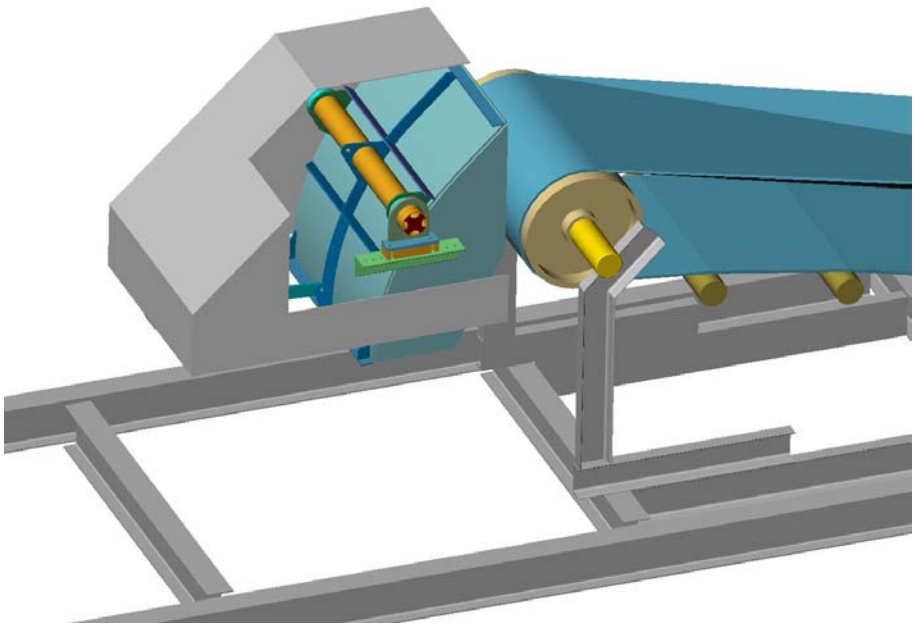

Figure 7.4 Image depicting single hood transfer chute system – view two

three-dimensional systems). The disadvantage however is that data within the files containing positions, velocities, and other relevant data are difficult to utilise in an application such as Microsoft® Excel without significant time allocated to shifting around or manipulation of data. Also, with such enormous data file sizes, the efficient transfer of data is essential. This was particularly critical for the current work, where large segments of data were required for importing into a spreadsheet application as instantaneous captures or snapshots of the system information, for comparison with data produced from analytical methods.

The quantitative data that is of use can only be obtained once the whole system has reached a steady state condition, so the key is to ensure that there are enough particles flowing in the simulations to allow such a situation to be reached. However to ensure a smaller compilation time the number of particles must also be minimised. Periodic boundaries were therefore used as they have the advantage of allowing a cyclic particulate flow motion. As mentioned in Chapter Four, periodic boundaries obviously work best for those systems that have a symmetrical calculation space and no boundaries, and with a relatively constant rate of particles exiting and re-entering the system. However, they are also useful for non symmetrical systems, such as for the current work, and enables the number of particles to remain both constant and manageable in quantity.

A number of further methods are available of loading the belt. One way is to load the incoming belt by simulating a fully loaded feeder that discharges material onto the belt. On its own this method necessitates the need for a greater number of particles to be modelled at the beginning of the simulation, which increases program compilation time. However, coupled with the periodic boundaries this achieves an ideal system set up, as the number of particles remains constant, and the data can be exported and imported efficiently.

Figures 7.5 and 7.6 show the feeder and periodic boundary set ups for the DEM simulations. The exit and entry points for the periodic boundaries are as follows for each chute system. For the hood-spoon system, particles can exit the calculation space at the end of the receiving conveyor, and re-enter at the top of the feeder, as illustrated

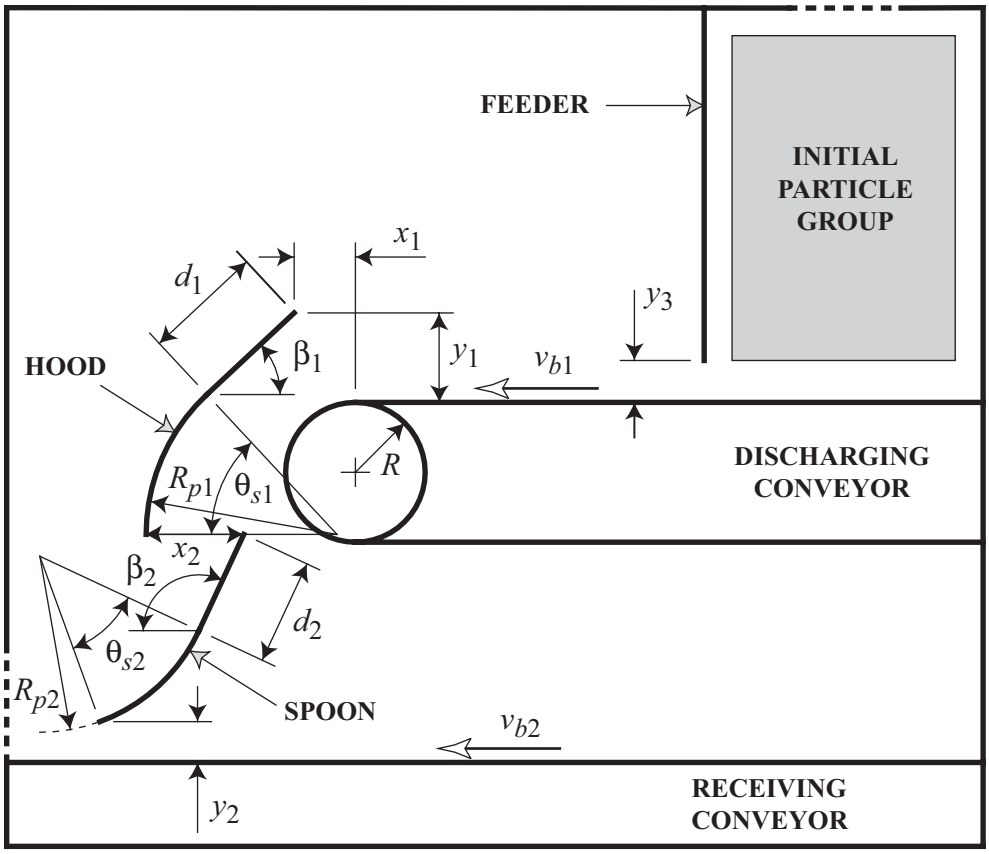

Figure 7.5 A schematic of the first transfer to be examined, comprising a hood-spoon chute system. The heavy dotted lines represent the periodic boundaries.

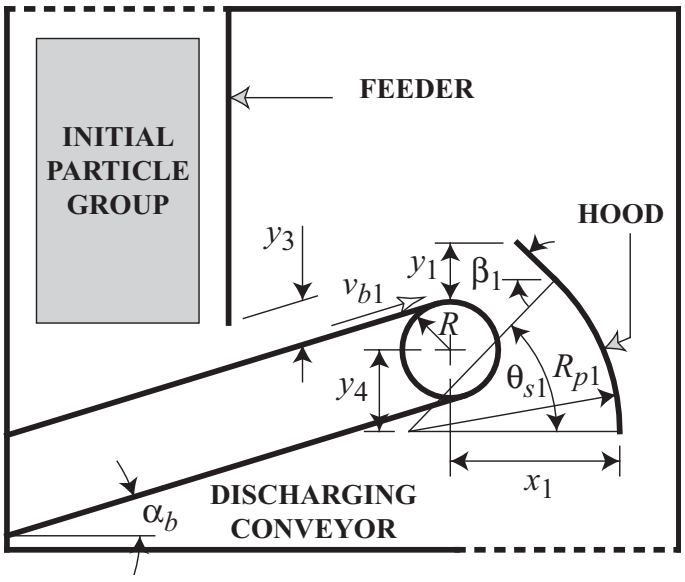

Figure 7.6 The second transfer to be examined is composed of a single hood to redirect material flow. The heavy dotted lines represent the periodic boundaries.

in Figure 7.5. Early chute simulations were performed using a periodic boundary location that allowed particles to re-enter at the right hand end of the screen upon the discharging conveyor, but this was abandoned as true cyclic motion for all particles was never reached – certain particles were stuck within a small triangular zone of material located within the feeder above the particles flowing on the belt. For the single hood chute system, the particles exit at a pre-defined location below the hood, and re-enter at the top of the feeder as shown in Figure 7.6.

The DEM calculation space for the first transfer is 7 m × 6 m and for the second is 4 m × 4 m within which all the boundaries are located and particle interactions occur. The first chute system is composed of a feeder bin, discharging and receiving conveyors, and a hood-spoon style transfer chute between the conveyors. The second chute system is composed of a feeder bin, a discharging conveyor and a chute system comprising only a hood element. Initially the spherical particles are randomly ordered in a group within the feeder and allowed to drop onto the moving conveyor under the influence of gravity. The particles travel through the aperture in the feeder and move along the belt until they traject off the belt at the head pulley. In the first transfer the particles flow through the hood and spoon elements and onto the receiving conveyor belt. In the second transfer the particles flow through the hood section and downwards. Table 7.1 details the relevant dimensions indicated in Figures 7.5 and 7.6. In the table 'Transfer A' designates the hood-spoon style chute and 'Transfer B' the single hood chute. The dimensions are identical to those contained within the assembly drawings in Appendix IV, with of course the major modification of having an inline transfer rather than an angled transfer.

One of the drawbacks in simulating particulate flow upon a conveyor in two-dimensions is that the height of material burden upon the belt prior to discharge must be manually determined. For the current work the height of the material as it passes over the head pulley is governed by the gap of the feeder aperture, therefore this is set equal to the material height determined from Eq. (2.13) and further work outlined in Chapter Two. As the conveyor attributes differ between each transfer chute system, the aperture heights differ accordingly. The aperture heights are indicated by y_3 in Figures 7.5 and 7.6.

Table 7.1 Values used for the dimensions indicated in Figures 7.5 and 7.6

	Transfer A	**Transfer B**			**Transfer A**	**Transfer B**	
d_1	0.856	–	m	y_1	0.64	0.397	m
d_2	0.76	–	m	y_2	0.292	–	m
R	0.5	0.325	m	y_3	0.132	0.123	m
R_{p1}	1.368	1.427	m	y_4	–	0.552	m
R_{p2}	1.259	–	m	α_b	–	17	°
v_{b1}	4.5	3.4	m s^{-1}	β_1	43	44	°
v_{b2}	4.5	–	m s^{-1}	β_2	115	–	°
x_1	0.439	1.147	m	θ_{s1}	47	46	°
x_2	0.7	–	m	θ_{s2}	45	–	°

7.3.2 Analytical processes

The material stream velocity characteristics produced by the DEM simulations will be quantitatively compared to the predictions given by the accurate (and for the most part experimentally validated) analytical methods described in Chapters Two and Three. Each component of the design phase will now be described further. Figure 7.7 and 7.8 show the areas of consideration for each transfer. The numbering in the schematics are sequential, meaning it is that order indicated which must be followed to design the chute.

Part ❶ refers to the discharge process of the material off the belt, and for this the Hybrid technique outlined in Section 3.2.2 of Chapter Three will be used. The reader will recall that using this method the material height prior to discharge is calculated using both material properties and conveyor geometry. The discharge conveyors for each transfer satisfy the high speed conditions presented as Eq. (2.1) in Chapter Two. The Hybrid technique will also be used to calculate the trajectory path of the material, shown by the number ❷. Air resistance or drag forces were not considered in the calculation of trajectory paths in either the analytical methods or the DEM, as it was established in Chapter Two that air drag has little effect if the majority of particles are

over 1 gram in mass. Therefore at any point throughout the systems where particles experience free fall, they follow well known parabolic motion and fall under the influence of gravity.

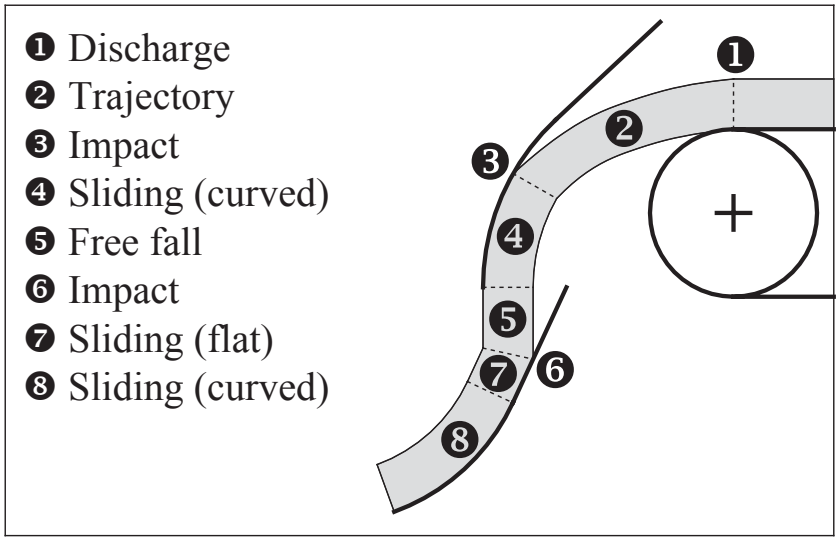

Figure 7.7 Schematic showing the numbering of design areas for hood-spoon system

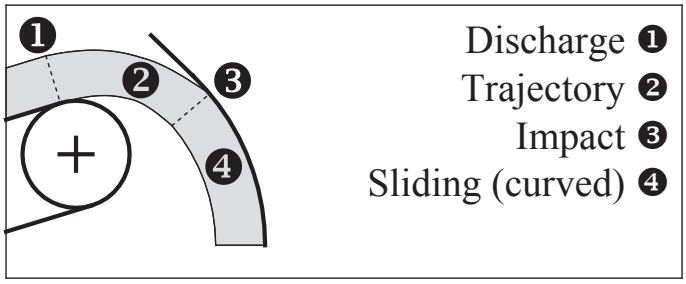

Figure 7.8 Schematic showing the numbering of design areas for single hood system

At the point of impact with the hood element, indicated by ❸, a change in velocity occurs, and for this Korzen's impact model will be used, detailed in Section 2.5.3 in Chapter Two. Although Korzen's model does not apply to curved impact plates, the instantaneous change in velocity has been calculated using the angle of tangency at the point of impact as the plate inclination. Burnett (2000a, 2000b) also applied Korzen's

flat plate model to curved elements. The flow of material around the curved portion of the hood is shown by the number ❹, and the relevant flow characteristics will be determined using Roberts' inverted chute flow model, outlined in Section 2.5.5 in Chapter Two. Part ❺ refers to the free fall of material and well known motion equations will be used to calculate positions and velocities. Since there is minimal drop height, air entrainment aspects are assumed to have little effect.

The number ❻ denotes the impact of the material stream with the straight portion of the spoon element, and the change in velocity will be calculated using the method provided by Stuart-Dick & Royal (1991, 1992) which was described in Section 2.7.1 in Chapter Two. The sliding flow along the straight portion of the spoon is represented by ❼ and the flow aspects will be calculated using the method of Arnold & Hill (1991b). Part ❽ shows the flow around the curved portion of the spoon, and the relevant values will be determined using Roberts' gravity flow chute model outlined in Section 2.7.3 in Chapter Two and has been the most extensively researched area of chute design. All the relevant parameters used in these calculations are described in the next section.

7.4 Parameter Selection

As mentioned both transfers in question satisfied the conditions for high-speed conveying outlined in Chapter Two, and therefore the initial material trajectories trajected at the point of tangency between the belt and head pulley. The discharge and receiving belts for the first transfer were both horizontal, while the discharging belt for the second transfer was inclined at 17° to the horizontal.

The parameters used for calculating particulate flow aspects using the analytical theories outlined in Chapters Two and Three are listed in Table 7.2 for each chute system, with 'Transfer A' again representing the hood-spoon style chute and 'Transfer B' the single hood chute. Many of these values were taken from the Gulf Client Data Sheet (CDS), which due to confidentiality clauses cannot be reproduced in the Appendices. The CDS is basically a document that is given to clients to obtain all relevant conveying, material, and site specific geometric parameters.

Table 7.2 Material properties and conveying conditions for each transfer

		Transfer A	**Transfer B**	
Conveyor belt speed (discharging)	v_b	4.5	3.4	m s^{-1}
Conveyor belt speed (receiving)	v_b	4.5	–	m s^{-1}
Conveyor inclination (discharging)	α_b	0	17	°
Angle of material discharge	α_d	0	17	°
Head pulley radius (discharging)	R	0.500	0.325	m
Conveyor belt width (discharging)	b	1.200	1.020	m
Conveyor belt thickness (discharging)	b_t	0.020	0.016	m
Troughing idler angles (discharging)	β_i	35	35	°
Surcharge angle (discharging)	θ	20	24	°
Horizontal distance to first impact	D	1.281405	0.962282	m
Radius of upper chute curve	R_p	1.368	1.427	m
Radius of lower chute curve	R_p	1.259	–	m
Angle of upper curve-end tangent	λ_{bottom}	0	0	°
Lower chute element width	B	0.84	–	m
Material type		Sized coal	Sized coal	
Particle size range	D_{max}	-50	-50	mm
Bulk density	ρ	850	850	kg m^{-3}
Proportionality constant	K	1.25	1.25	
Coefficient of wall friction	μ	0.2	0.2	
Equivalent coefficient of friction	μ_E	0.4	0.4	

Additional parameters and physical properties required for simulating the particulate flow using DEM are listed in Table 7.3 for each chute system. The term ‘PP’ refers to particle-particle contact and ‘PW’ to particle-wall contact. The values used here for the coefficient of friction μ between particles and particle-wall interactions for coal were obtained from and detailed in the work of Hustrulid & Mustoe (1996), as was the coefficient of restitution ε. The fixed parameter b was set equal to 0.3333 to agree with Mindlin’s frictional sphere theory. The dilation factor of the particles within the initial

group was set at 1.1 to ensure a reasonable gap between particles. General constants used were the acceleration due to gravity $g = 9.81$ ms^{-2} and $\pi = 3.14159265358979$.

Table 7.3 Initial DEM parameters used for simulating each transfer system

		Transfer A	**Transfer B**	
Number of particles	N	1500	900	
Time step	Δt	5×10^{-6}	5×10^{-6}	s
Calculation space (x – direction)	X_{len}	7	4	m
Calculation space (y – direction)	Y_{len}	6	4	m
Base diameter	D_{base}	0.031	0.031	m
Diameter variance	D_{var}	0.019	0.019	m
Coefficient of friction {PP / PW}	μ	0.3 / 0.2	0.3 / 0.2	
Normal stiffness constant {PP / PW}	K_{n1}	1×10^7 / 1×10^7	1×10^7 / 1×10^7	N m^{-1}
Initial tangential stiffness {PP / PW}	K_t^0	1×10^7 / 1×10^7	1×10^7 / 1×10^7	N m^{-1}
Coefficient of restitution {PP / PW}	ε	0.2 / 0.2	0.2 / 0.2	

The size distribution is accomplished by a random number generator that places non-overlapping spheres in a dilated rectangular array in the desired location shown in Figures 7.5 and 7.6. The particle sizes in the actual transfers ranged from fines to a maximum diameter of 50×10^{-3} m but the simulations for each chute were conducted with spherical particles of median diameter $D_{base} = 31 \times 10^{-3}$ m and variance $D_{var} = 19 \times 10^{-3}$, giving diameters in the range $12 \times 10^{-3} \leq D \leq 50 \times 10^{-3}$ m. A lower median diameter and greater variance would allow even smaller particles to be incorporated to simulate fines, however problems related to excessive particle overlaps would potentially have been a problem, particularly for very small particles contacting boundaries. The randomly selected particle size distribution for each transfer is shown in Figure 7.9.

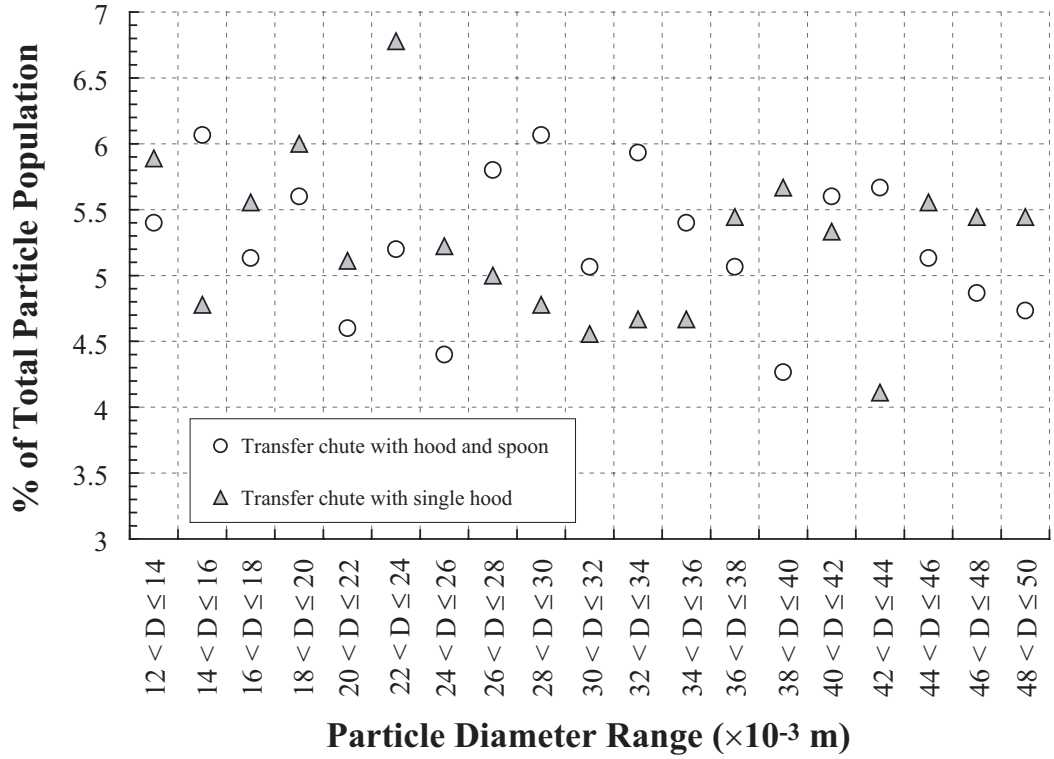

Figure 7.9 Particle size distributions for hood-spoon transfer chute and single hood transfer chute

7.5 Animating the Particulate Flow

7.5.1 Software Set-Up

The particulate flow was animated using the same programming language (FORTRAN) as that for the general DEM calculations, with the specifics outlined in Chapter Five. As the area of concern was primarily the flow of material through the chute, the animation screen captures focused on that particular region. The particle and boundary definitions were already defined to obtain the quantitative data, therefore the animation software was set up to basically read the relevant data files, and limit the view-port area to the chute location. For animations of the entire calculation space, including the feeder, select screen captures colour coded according to velocity magnitude are presented in Appendix V for each transfer chute. The layout in those animation screen captures is almost identical to the schematics, with only minor deviations in feeder width and

location from the head pulley, however this issue is not as important as the area of concern was the material flow through the chute. As mentioned previously, the specific dimensions and further details about the chutes can be found in the drawings in Appendix IV.

7.5.2 Problems Encountered and Solutions

In general, the boundaries of the animation were very close to those depicted in the schematics (Figures 7.5 and 7.6), which were to scale, however a few preliminary observations were made during the testing phase. It was found that the sheer size of most of the text files containing data was approaching many hundreds of megabytes, with certain files exceeding one gigabyte, and when coupled with the speed of the computer, problems in the visualisation software surfaced. Due to these memory issues, the OpenGL animation image would not compile correctly, and its size had to be limited. A number of options were considered to facilitate this. The first was to increase the time step size and thus reduce file size. This however inevitably creates an unstable DEM system, so this was promptly rejected. Another option was to reduce the number of particles and therefore change the geometry of the system and consequently also the periodic boundary positions.

Ultimately a new component was introduced into the DEM portion of the software that allowed files to be reread from any point at which the simulation stopped, named a *RESTART* subroutine. This component was developed by Walsh (2004) in his research. In essence, a number of separate files were created, with each file starting at the finishing point of the previous. Thus, the animation software read a sequence of smaller files, rather than one large file. As all particulate motions, forces and other relevant data were carried over between one file to the next, essentially there was no difference between simulating one large file or a number of smaller files.

In Chapter Eight the particles have been colour coded according to velocity or other nominated parameter, allowing the general particulars and trends of the material flow to be observed. All the animations will illustrate a coloured bar on the side representing either particulate velocities or other parameter, depending upon the discussion at hand. One limit of the bar indicates the maximum value for that parameter in that particular

animation. Testing runs of each simulation were conducted and on occasion it was found that the actual maximum value was much higher than the expected maximum value, and was the result of a stray particle(s) gaining abnormal motion characteristics. Therefore prior to 'properly' simulating the transfers, the quantitative data were examined at selected time steps and the expected maximum value was used as an upper limit in the coloured bar, and all other values above are coloured identical to this. Statistical techniques could be used if greater numbers of particles exhibited irregular qualities, but it was found that at most only a handful of particles showed these traits, always less than one percent of the total number, and usually in the order of a small fraction of a percent.

7.6 Preliminary Observations and Comments

A number of initial tests was performed to examine the characteristics and sensitivity of the simulated chute flows. Some observations were made which were not intuitively obvious before performing the simulations, and a number of changes had to be made to the proposed set up described above which are described in detail below.

7.6.1 Boundary Set-up

For the DEM simulation boundary development for the first transfer, the spoon was initially offset by an amount equal to the breadth of the hood rear wall at its lowest point, as described above in Section 7.2. However it was found that this produced a material stream that impacted on the spoon at a lower than expected point, rather than near the upper region of the straight inclined portion of the spoon as is the case with the actual chute in operation. A number of preliminary simulations were therefore conducted to gauge the optimal horizontal distance (x_2 in Table 7.1) between the lowest point of hood and the highest point on the spoon, to give a material stream that impacted near the upper region of the spoon. It was found that x_2 = 0.2 m gave an impact point that satisfied the initial objective. Figure 7.10 (a) shows the initial configuration and Figure 7.10 (b) shows the final boundary layout.

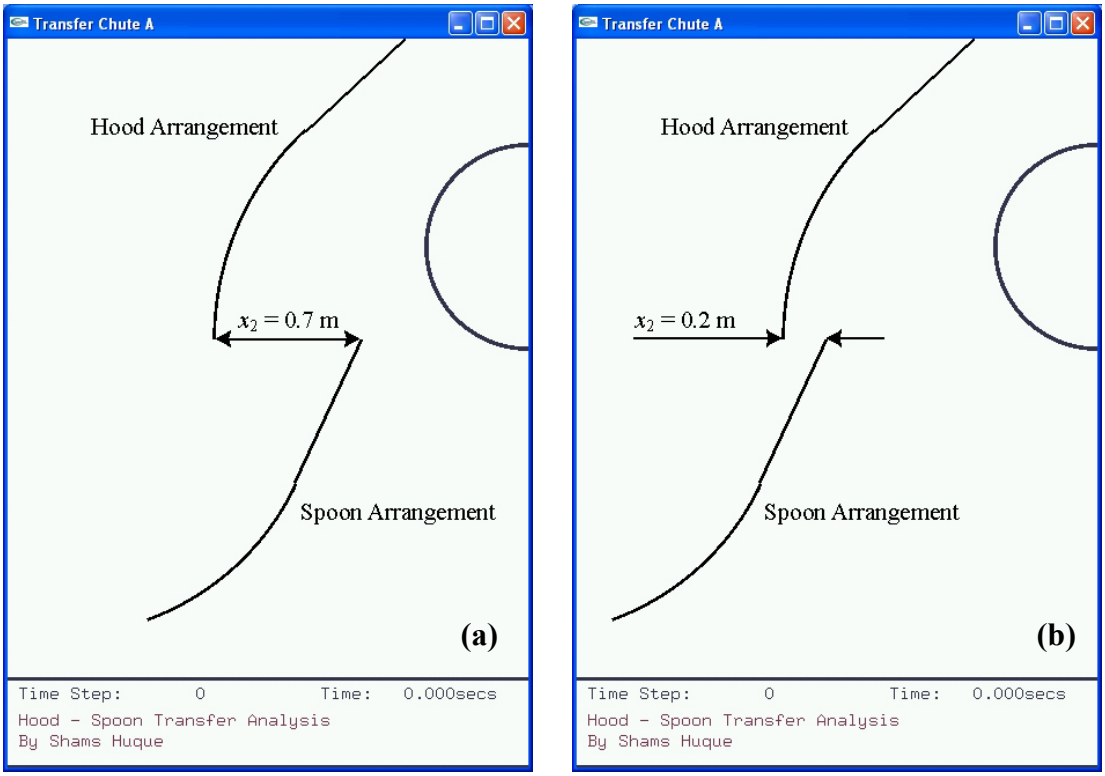

Figure 7.10 **(a)** Initial spoon location and **(b)** Final spoon location

7.6.2 Sensitivity to System and Material Parameters

The kinematics of the simulated material flow as the particles exited the feeder upon the belt was observed to be somewhat sensitive to the value of the coefficient of restitution between colliding particle-particle and particle-boundary pairs. Although a value of $\varepsilon = 0.2$ was used for the final simulations, values of $\varepsilon = 0.5$, $\varepsilon = 0.6$, $\varepsilon = 0.7$ and $\varepsilon = 0.8$ were tested to observe motion patterns. The flows were observed to be more energetic with greater elasticity in the particle interactions, particularly for $\varepsilon \geq 0.6$ where errors occurred during compilation due to particles moving out of the calculation space. These errors however could be partly attributed to the modified periodic boundary used: as particles re-entered the calculation space near the top of the feeder, they acquired motions that propelled them out of the calculation space. This was caused by the larger restitution coefficient coupled with the often large inter-particle overlaps.

Figures 7.11 and 7.12 show the average velocity components in the x and y directions for the hood-spoon and single hood transfers respectively, for $\varepsilon = 0.2$ and $\varepsilon = 0.5$, and illustrate the effect of higher elasticity. In Figure 7.11, the difference between the average horizontal velocities for $\varepsilon = 0.2$ and $\varepsilon = 0.5$ increases at approximately t = 0.65 s, and the difference remains near or below that level until t = 1.7 s, where greater differences appear. The difference between the average vertical velocities increases at t = 1.3 s and fluctuates as time progresses. Both of these differences can be attributed to the effect of the periodic boundary, as Figure 7.12 shows the average velocity component differences for the second transfer to be markedly less. The average horizontal and vertical velocities differ noticeably from around t = 0.6 s, however these differences are not as great as that observed in Figure 7.11 for the first transfer. The time step used was $\Delta t = 5 \times 10^{-6}$ s, and a smaller time step could allow simulations with greater elasticity to be compiled without errors, however the computation times would be exorbitant. Particle agitation was evident for $\varepsilon \geq 0.6$, particularly in the higher-speed domain of the hood-spoon transfer.

During the simulations, some of the particles were forced through the aperture between the belt and the feeder outlet upper wall resulting in large particulate/boundary overlaps, rather than flow through smoothly with minimal overlapping. These particles were in an agitated state and additionally the conveyor speed used reduced the opportunity for the particles to settle upon the belt. The abnormally large and unrealistic overlaps exacerbated any minor deviations from the particles' natural motion. Interestingly this problem was more evident in the hood-spoon transfer system than the single hood system, most probably due to the greater number of particles used and higher belt speed. To ensure the drawdown of material within the feeder would not affect the particulate material flow exiting the aperture, modifications were made to the computer code to ensure that all material lying within the forced velocity zone adjacent to the belt were affected by that velocity only and not influenced by any of the surrounding particles. This therefore negates the large compressive forces upon the lower lying particles from the remaining particles within the feeder and thus almost completely eliminates erroneous particle motions upon the belt.

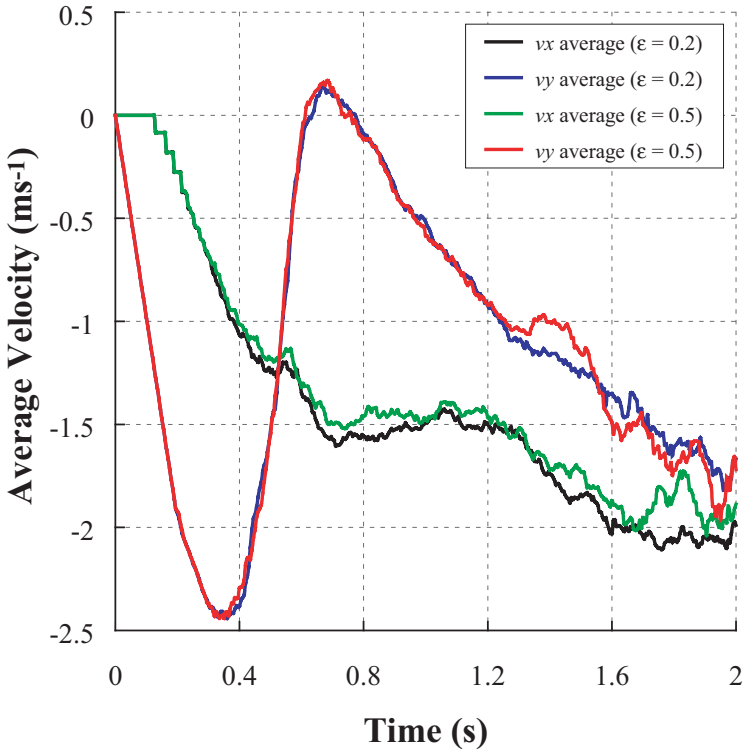

Figure 7.11 Average velocity components in x and y directions for first transfer with $\varepsilon = 0.2$ and $\varepsilon = 0.5$

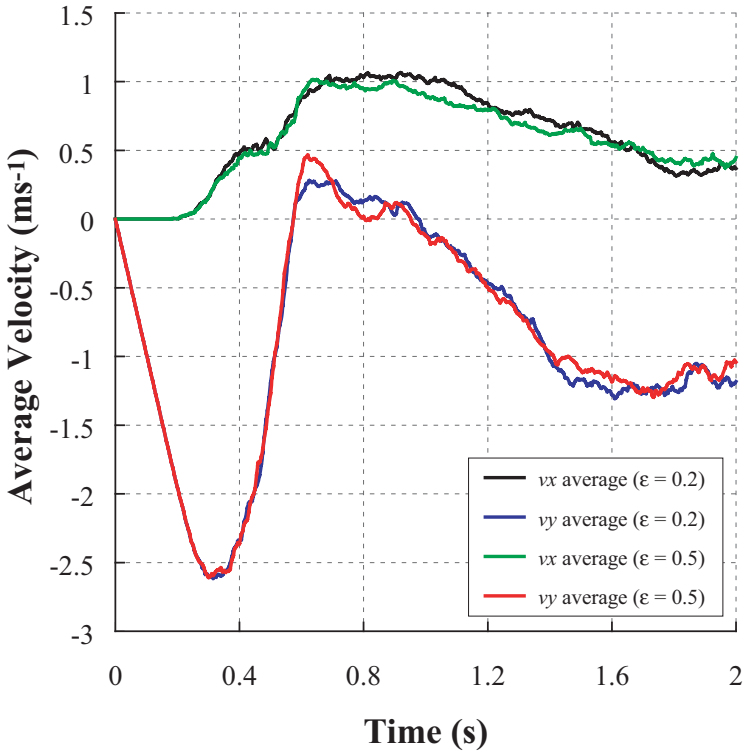

Figure 7.12 Average velocity components in x and y directions for second transfer with $\varepsilon = 0.2$ and $\varepsilon = 0.5$

As opposed to the influence of coefficient of restitution, it was observed that the flows were somewhat less sensitive to changes in the coefficient of friction. Also the simulated flow of the particles within the feeder and upon the belt was generally not sensitive to the inter-particle normal stiffness constant, as long as virtual overlaps in energised collisions remained very small (in the order of ~1.0 % – 1.5 % of the smallest particle diameter). This finding parallels the results observed in the hour-glass simulations performed for the DEM code testing in Chapter Six, where the influence of stiffness constants was seen to have relatively little influence on the particulate flow.

The time step to be used was initially $\Delta t = 5 \times 10^{-6}$ seconds and resulted in computation times of almost 45 hours to simulate five seconds of particulate motion for the hood-spoon transfer. As the simulations needed to be repeated to obtain different sets of quantitative data, the program compilation became a time consuming issue. However it was found that increasing the size of the step by a factor of 10 up to 5×10^{-5} seconds had little effect upon the particulate flow and Figures 7.13 and 7.14 provide a comparison of average velocities using both the larger and smaller time steps. It is clear that the differences are not great, and any flow motion differences were not discernable in the animations, therefore this increased time step value was utilised saving approximately 40 hours of compilation time for every simulation.

7.6.3 Velocity Profile Set-up

The paths the DEM particles follow are governed by events occurring upon the belt, the major influences being the interactions of particles with one another and with the simulated conveyor belt. As mentioned above, the normal stiffness constant ($K_{n1} = 1 \times 10^7$ Nm^{-1}) and initial shear stiffness constant ($K_t^0 = 1 \times 10^7$ Nm^{-1}) have been chosen large enough so that particle overlap remains small. The coefficient of restitution ($\varepsilon =$ 0.2 {PP}; $\varepsilon = 0.2$ {PW}) is also a relatively small value so the elastic rebound achieved is not great. Initially, a simple velocity profile was used to simulate the moving conveyor belt for the first transfer. This created a local environment where the particles with centres up to no more than half the maximum particle diameter above the horizontal belt were assigned the belt velocity and affected the remaining particles. This

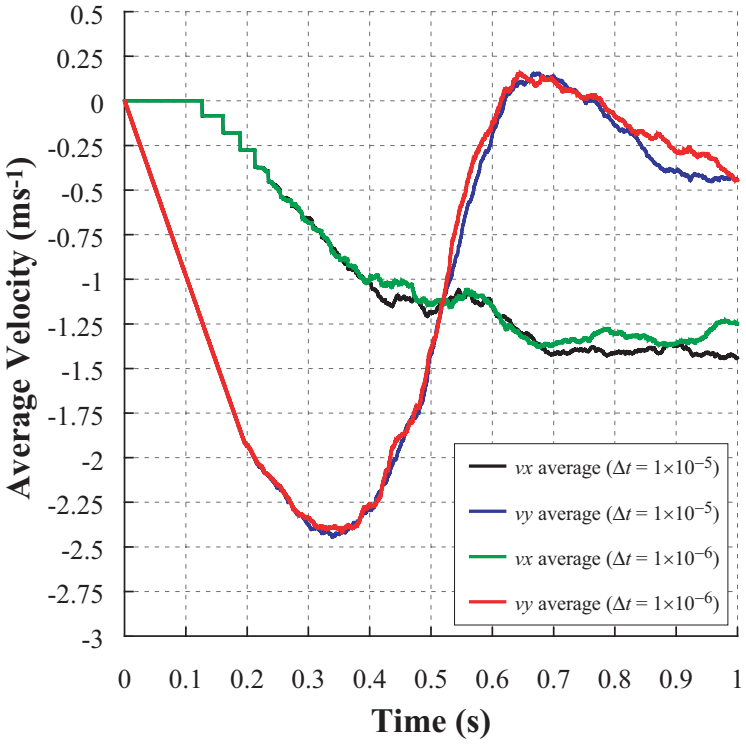

Figure 7.13 Average velocities in the x and y directions for $\Delta t = 1\times10^{-5}$ s and $\Delta t = 1\times10^{-6}$ s for the first transfer chute system comprising a hood and spoon

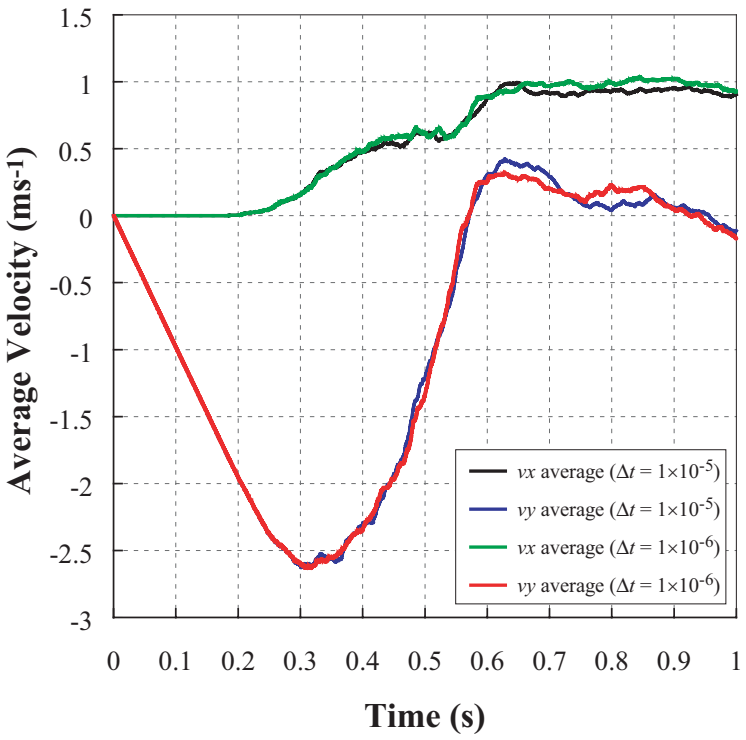

Figure 7.14 Average velocities in the x and y directions for $\Delta t = 1\times10^{-5}$ s and $\Delta t = 1\times10^{-6}$ s for the first transfer chute system comprising a single hood

meant that generally the lowest band of particles upon the belt was assigned the belt velocity and carried the others above. However if compressed sufficiently, as for the feeder situation described above, the contained energy in a particle would cause anomalies in its projected path, a great deal more so for the hood-spoon transfer.

Therefore to overcome such problems the velocity profile used for the first transfer is defined as follows. Every particle centre lying in the region above the belt up to a height equal to the feeder aperture was given a horizontal velocity of -4.5 ms^{-1} (in other words 4.5 ms^{-1} right to left on the screen) and the computer code ensured that this condition overrode any excessive overlaps. Though not realistic at the exit to the feeder, the material flow behaved as required at the point of trajection upon the head pulley as needed.

The velocity profile for the second transfer was complicated, due to the inclination of the conveyor belt. A series of *IF* statements was coded so that when the particle centres entered a specified region vertically they were given a horizontal and vertical velocity component whose total vector magnitude equalled 3.4 ms^{-1}. The conditions given were of the following form:

```
If {x(i) > velocity zone LHS x-coordinate} .and. {x(i) <
velocity zone RHS x-coordinate} then
   If {y(i) > belt inclination × x(i) + bottom LHS velocity
   zone y-coordinate} .and. {y(i) < belt inclination × x(i)
   + bottom LHS velocity zone y-coordinate + maximum
   particle ∅ } then
        vx(i) = horizontal velocity component
        vy(i) = vertical velocity component
   End If
End If
```

where *i* refers to the particle number. The drawback to this method was that a constant thick stream of material could not be trajected off the head pulley as for the first transfer case, rather the material height was specified by the contact mechanics of the particles

at the feeder aperture. The resulting particulate flow was not detrimental to the simulations however. If a thick velocity band was applied as for the first transfer with zero inclination, the particles would simply flow above the belt in the highest region of the velocity zone, rather than flow adjacent to the belt, due to the nature of the *IF* statement.

7.6.4 Time to Reach Steady-State Condition

The simulations were carried out over 5.0 seconds to assess the approximate time at which the flow could be described as being in a steady-state condition. The average velocity of the flow at an instant of time was calculated using the velocities of all the particles. The average velocities obtained from the hood-spoon and single hood simulation results are shown in Figures 7.15 (a) and 7.15 (b) and Figures 7.16 (a) and 7.16 (b) respectively for a series of time intervals. At the start of the simulation the average velocity of the flow fluctuates, as can be seen in Figures 7.15 (a) and 7.16 (a). After a certain period of time the flow settled down to steady state conditions, where the average velocities reached an asymptotic value, as seen in Figures 7.15 (b) and 7.16 (b). The component *vx* has the direction horizontally and the component *vy* has the direction vertically. For both transfers an approximate steady state flow regime is reached after 2.0 s, as shown in Figures 7.15 (b) and 7.16 (b). For confirmation, the kinetic energy in the systems was also compared.

The average kinetic energy in each transfer system is illustrated in Figure 7.17, and was found from the sum of the translational and rotational energies for all particles at each time step, and the total then divided by the number of particles. For the hood-spoon transfer system, the energies are shown for both the earlier and final periodic boundary systems. The noisy appearance of the energy for the current system starting at around 2.0 s in the first transfer can be attributed to the nature of the periodic boundaries – when the particles re-enter the calculation space they often have large overlaps that create great elastic forces. The resulting accelerations propel the particles in a multitude of directions at great speed. The peaks in this region represent a greater number of particles re-entering the calculation space, while the troughs correspond to a lesser number of re-entering particles. It can also be observed that the energy at this point

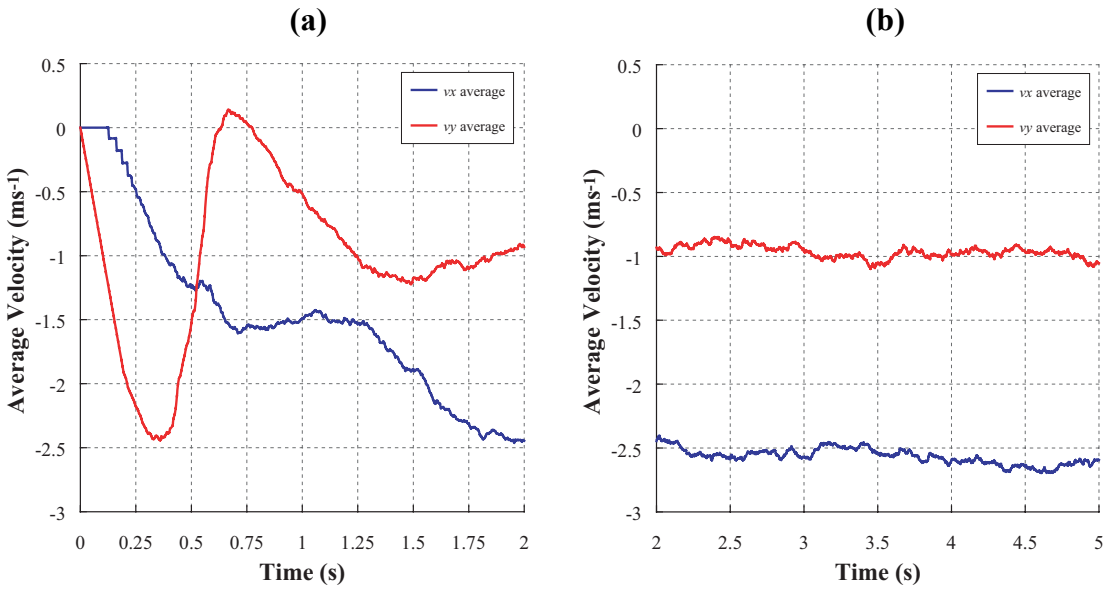

Figure 7.15 Average velocities of all particles for transfer chute simulation comprising hood and spoon, from **(a)** t = 0.00 s to t = 2.00 s **(b)** t = 2.00 s to t = 5.00 s

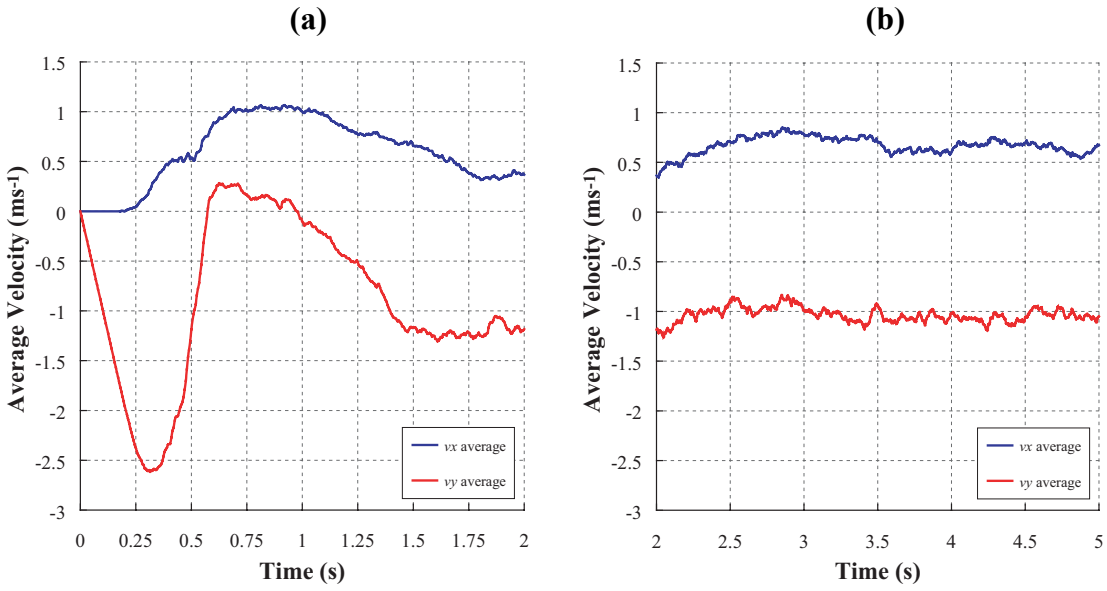

Figure 7.16 Average velocities of all particles for transfer chute simulation comprising single hood, from **(a)** t = 0.00 s to t = 2.00 s **(b)** t = 2.00 s to t = 5.00 s

fluctuates around a rough asymptotic region. If we observe the average kinetic energy for the first transfer using the earlier version of the periodic boundaries, it is clear that a steady value is reached after 2.0 s. Although the re-entry of particles into the feeder creates such large fluctuations of total system kinetic energy, the time step is small enough to ensure that particles do not 'pass through' the feeder boundaries. The reader must also remember that the velocity profile upon the belt overrides any of the possible erroneous motions possible from large overlaps, as described earlier in Section 7.6.2. The kinetic energy of the particles in the second transfer reaches a more clearly defined asymptotic value before 2.0 s. Therefore in effect the kinetic energy in the system is roughly stable after t = 2.0 s and based upon this and also the average velocity of the particles, the simulation data of relevance was captured on or after 2.0 s.

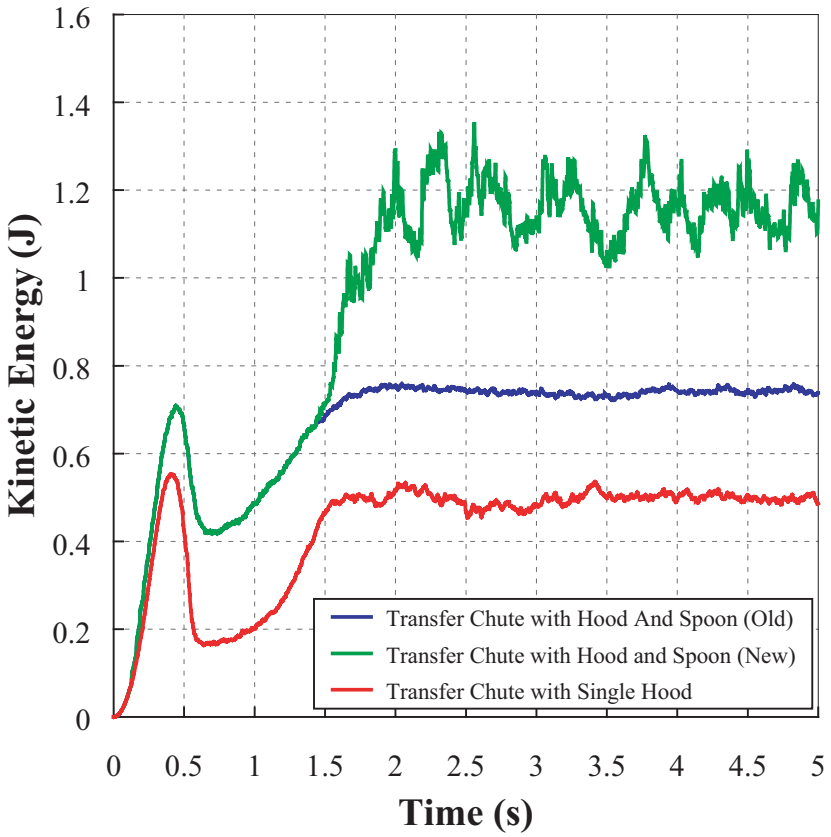

Figure 7.17 Kinetic energy in each transfer chute system from t = 0.0 to t = 5.0 s. The terms 'old' and 'new' in the legend refer to the earlier or latter periodic boundary locations used respectively for the first transfer system

7.6.5 Influence of Particle Size Distribution

As a point of interest, to examine the influence of particle sizes upon the general flow regimes, the simulations for each chute were conducted firstly with uniformly sized spherical particles of $D_{uniform} = 50 \times 10^{-3}$ m, and secondly with a median diameter $D_{base} = 31 \times 10^{-3}$ m and variance $D_{var} = 19 \times 10^{-3}$, giving diameters in the range $12 \times 10^{-3} \leq D \leq 50 \times 10^{-3}$ m. It was found that there was little observable difference between the generated material streams when using mono or varied particle sizes within the range specified. However this is most probably a consequence of simulating in two-dimensions. Material segregation and other effects have been observed in three-dimensional studies (Wright, B. 2004, pers. comm., 8 July). Screen captures at selected times are presented in Figures 7.18 (a) to 7.18 (d) and Figures 7.19 (a) to 7.19 (d) for the hood-spoon transfer and single hood transfer respectively.

Figure 7.18 shows that as the particles traject off the belt, the size distribution is random, with no evident segregation. The flow of material around the hood and spoon surfaces also suggests that particle mixing is evident with no defined regions of similar sized particles. This aspect can partly be attributed to the uniform velocity profile applied upon the belt, which does not allow regular particle interactions to take place. Similar observations were made for the second transfer shown in Figure 7.19.

7.6.6 General Comments Regarding Analytical Set-Up

It was found that approximately 12 hours was spent generating the results using the analytical techniques for the hood-spoon transfer chute system. Although many of the processes were very similar, another 6 hours was also spent applying the analytical processes to the single hood transfer chute. Spreadsheets had been developed for calculating relevant parameters for Chapters Two and Three, however there were many nuances that needed consideration. For example calculating the relevant impact point coordinates ultimately lead to complicated quadratic equations, which required iterative processes to solve.

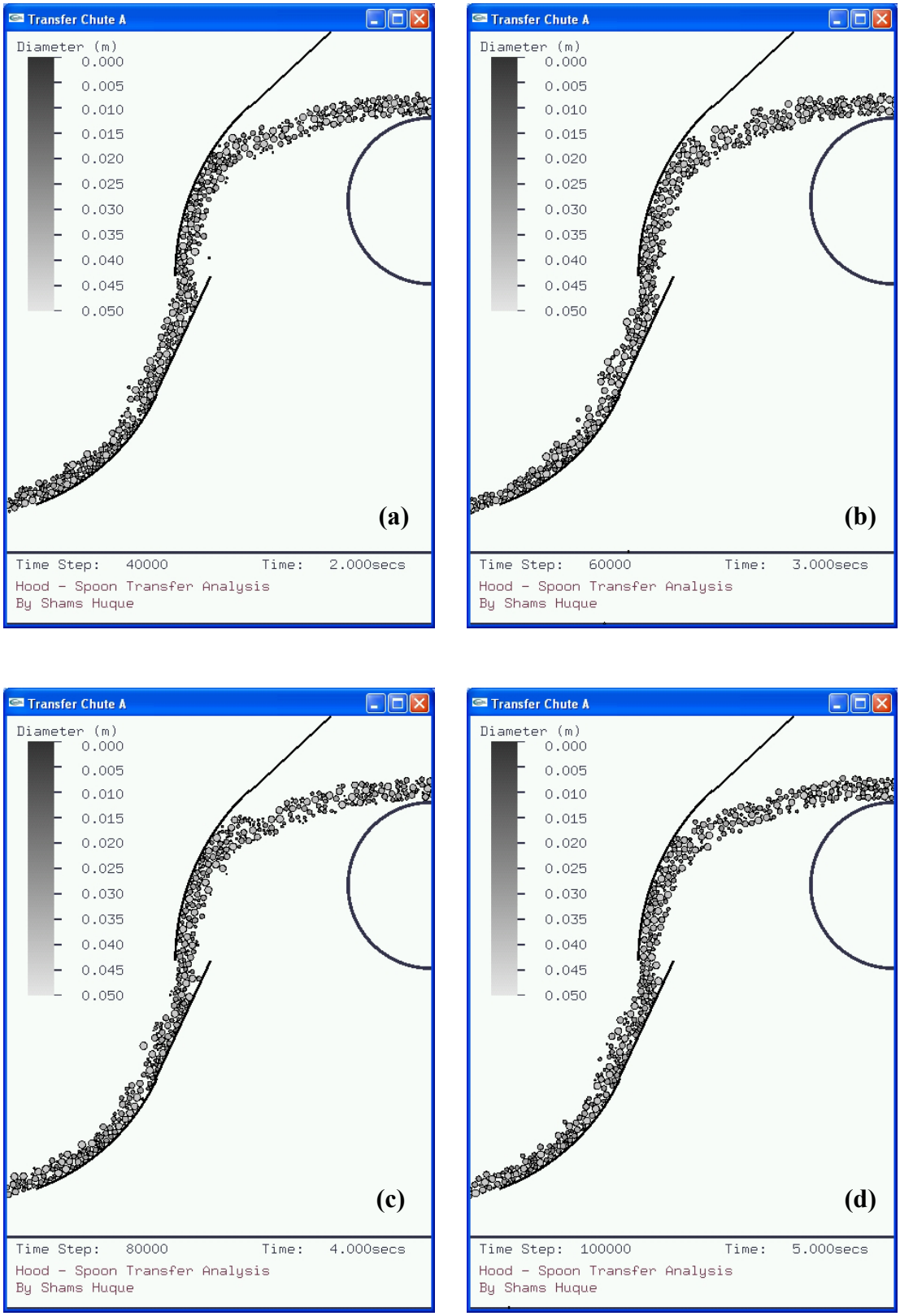

Figure 7.18 Screen captures at **(a)** $t = 2.0$ s, **(b)** $t = 3.0$ s, **(c)** $t = 4.0$ s, and **(d)** $t = 5.0$ s illustrating the particle size distribution for the first transfer

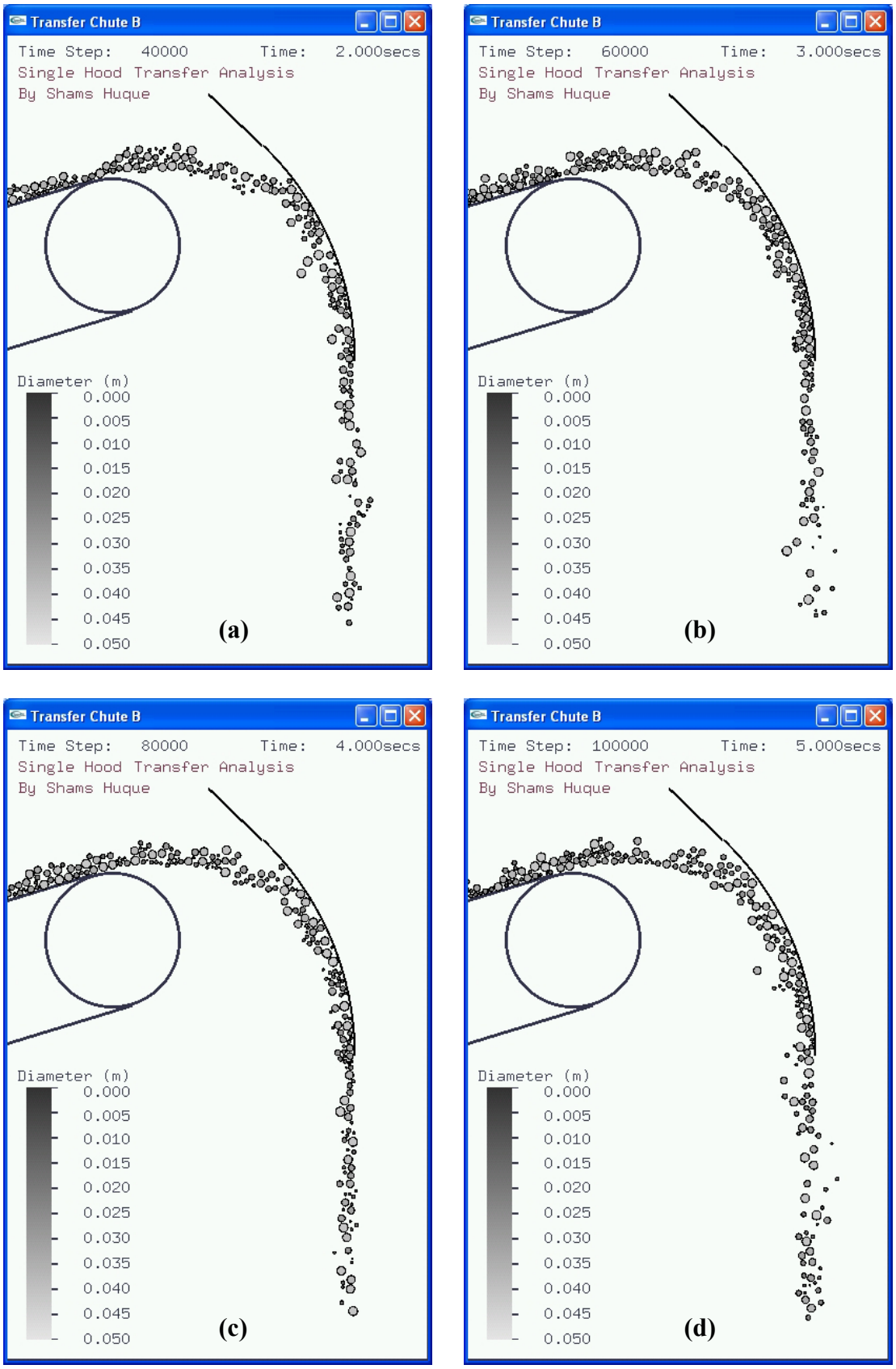

Figure 7.19 Screen captures at **(a)** $t = 2.0$ s, **(b)** $t = 3.0$ s, **(c)** $t = 4.0$ s, and **(d)** $t = 5.0$ s illustrating the particle size distribution for the second transfer

7.7 Summary

The chapter introduced the two chutes for analysis, and described the preliminary work required before starting a full DEM analysis of the particular material transfers in question. These aspects were not found in any of the literature detailing DEM transfer chute studies. Detailed preliminary work such as examination of kinetic energy and average velocities were conducted to establish the time domain of steady-state flow, and further observations regarding the initial DEM simulation start up were documented. Any pertinent observations that allowed adjustments to be made to allow the (essentially) two-dimensional DEM model to approximate the particulate flow were also described.

Each of the analytical methods required to calculate the velocity of the flowing stream off the discharging conveyor and through the chute system components was also described in the chapter. To the author's knowledge this work represents the first instance in literature to apply these design techniques to analyse a complete hood-spoon style transfer. One major problem identified with the analytical methods is that significant care must be taken during the design process, with every component requiring calculation in order and without error. For example, if the trajectory calculations are incorrect, these in turn will affect the subsequent results, meaning the entire design process needs repeating, which is unaffordable in industry.

The particulars and problems associated with animating particulate flow were also described, and this along with the work presented in Chapter Five, present one of the few backgrounds into visualisation, with most DEM literature not detailing animation aspects. The next chapter will analyse quantitatively and qualitatively the velocity distributions predicted using the DEM, and also compare the results of the DEM to that proposed by the analytical methods.

Chapter Eight

ANALYSIS OF INDUSTRY CHUTE SYSTEMS

8.1 Introduction

In Chapter Seven the two transfers to be examined were introduced, and the set-up and environment for the DEM simulations and analytical design methods were described. This chapter qualitatively and quantitatively examines in detail the velocity distributions through the chutes in question and also the micro dynamics of individual particles in the systems. Further aspects such as the inter-particle force distributions and associated torques are also introduced. The analytical methods detailed and identified in Chapters Two and Three as providing accurate design procedures are used as a means of comparison with the results produced using the DEM. The aim of this chapter is to gauge the effectiveness of the DEM simulations for modelling transfer systems. The general trends and intricacies of the particulate flow are highlighted, and some areas of interest for future examination are commented on for further explanation in Chapter Nine. It was found in Chapter Seven that for each simulation the particulate systems exhibited steady-state behaviour after 2.0 seconds. Therefore all information or screen captures presented in this chapter are taken at times of 2.0 s, 3.0 s, 4.0 s, and 5.0 s for each transfer.

8.2 Analysis of Velocity Distributions using Contours

The velocities of the particles are of primary importance, particularly those particles adjacent to chute surfaces due to the direct relationship between velocity and wear. It has been well established (Kruse 2000, n.d.) that the curved hood and spoon system and also the single hood maintain material velocity through the transfer very well (e.g. reduced stagnation points) when compared to a simple impact plate or rock box system. This results in less impact damage to the chute surface, however the potential for greater

abrasive wear is higher. However those research works do not analyse in detail the flow regimes, rather they have provided only a broad qualitative conclusion. The following results are primarily focused on analysing the velocity distributions throughout the flow by examining screen captures of the system animations similar to the way Dewicki & Mustoe (2002) and Hustrulid (1998) presented results. A coloured bar with linear data progression is used and represents the speeds and velocities.

8.2.1 Hood-Spoon Transfer Chute

Figures 8.1 (a) to 8.1 (d) illustrate the particle speeds at t = 2.0 s, t = 3.0 s, t = 4.0 s, and t = 5.0 s respectively for the hood-spoon transfer. The conveyor belt speeds are v_b = 4.5 ms^{-1} each. It can be clearly seen in each figure that the general trend of the material stream is to maintain the speed at the point of trajection through the transfer, with reductions in speed at the points of impact on the upper and lower chute sections, and an increase in speed as the material free falls and flows around the curved spoon section. The reductions in speed can be seen with the particles coloured yellow, orange, and red, while increasing speed can be seen in those particles coloured aqua or blue.

To gain a greater insight into the behaviour of the particulate stream the horizontal and vertical velocity contours are shown in Figures 8.2 and 8.3 respectively, at times (a) t = 2.0 s, (b) t = 3.0 s, (c) t = 4.0 s, and (d) t = 5.0 s. The horizontal velocity components of the particles remain constantly negative (positive direction is to the right) after trajection until the hood is impacted, where there is a rapid reduction of velocity to zero (colour change of orange to bright green), and a few particles even experiencing rebound as shown by the aqua coloured particles in a region of predominantly green and yellow coloured particles. As the material impacts and slides around the spoon, the velocity increases in the negative direction (colour change from bright green to orange). The vertical velocity components are zero at the point of trajection (green colour), but increase in the negative direction under the influence of gravity during free fall and after impact, reaching an approximate maximum prior to impacting the spoon (red colour). The particles' vertical velocity components then decrease gradually as the particles move around the system (colour change from red to light green). In general, the velocity distributions are as expected, with logical areas of velocity reduction at impact points upon the hood and spoon.

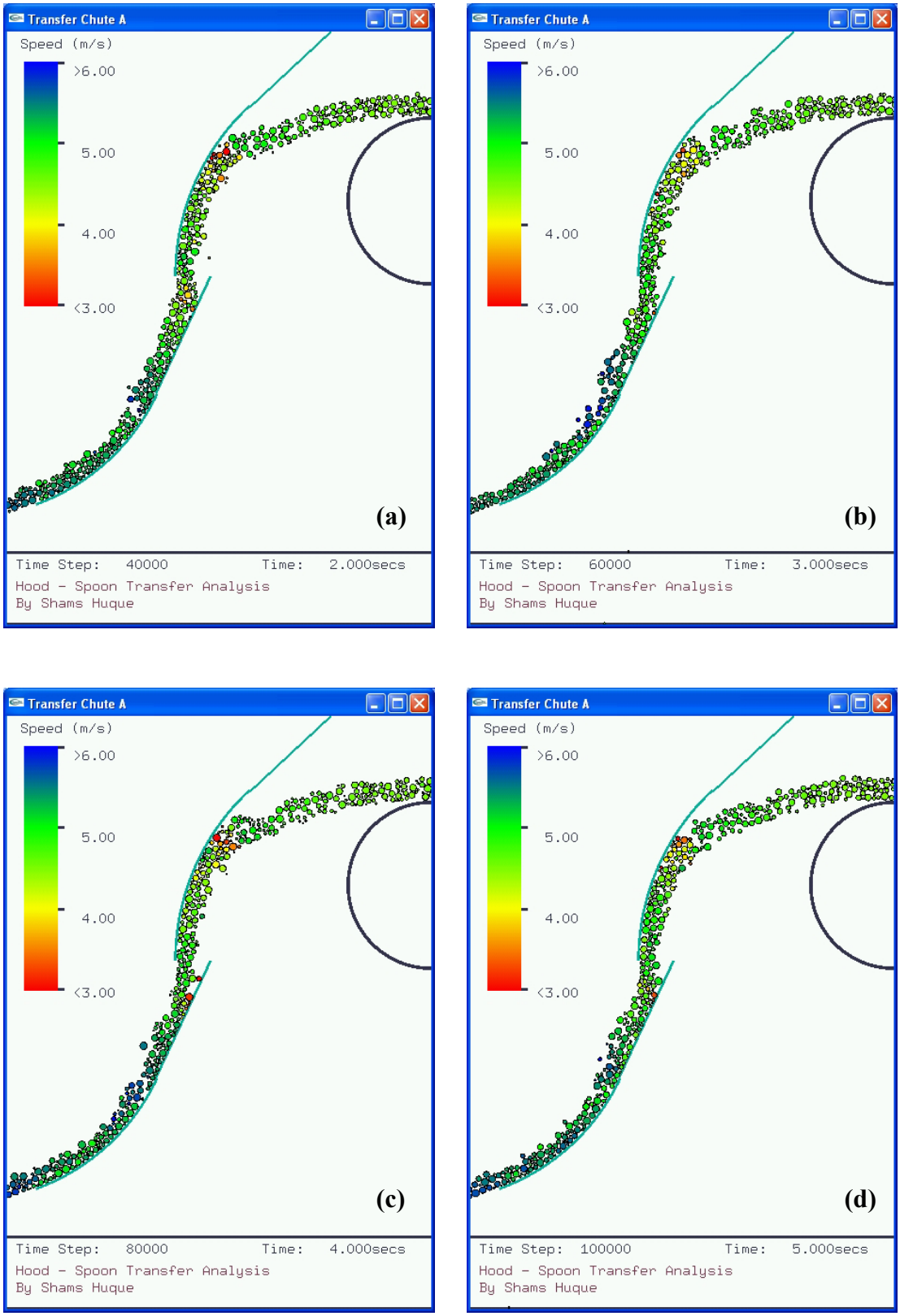

Figure 8.1 Screen captures that show the particulate speed distribution for the first transfer system at times of **(a)** $t = 2.0$ s, **(b)** $t = 3.0$ s, **(c)** $t = 4.0$ s, and **(d)** $t = 5.0$ s.

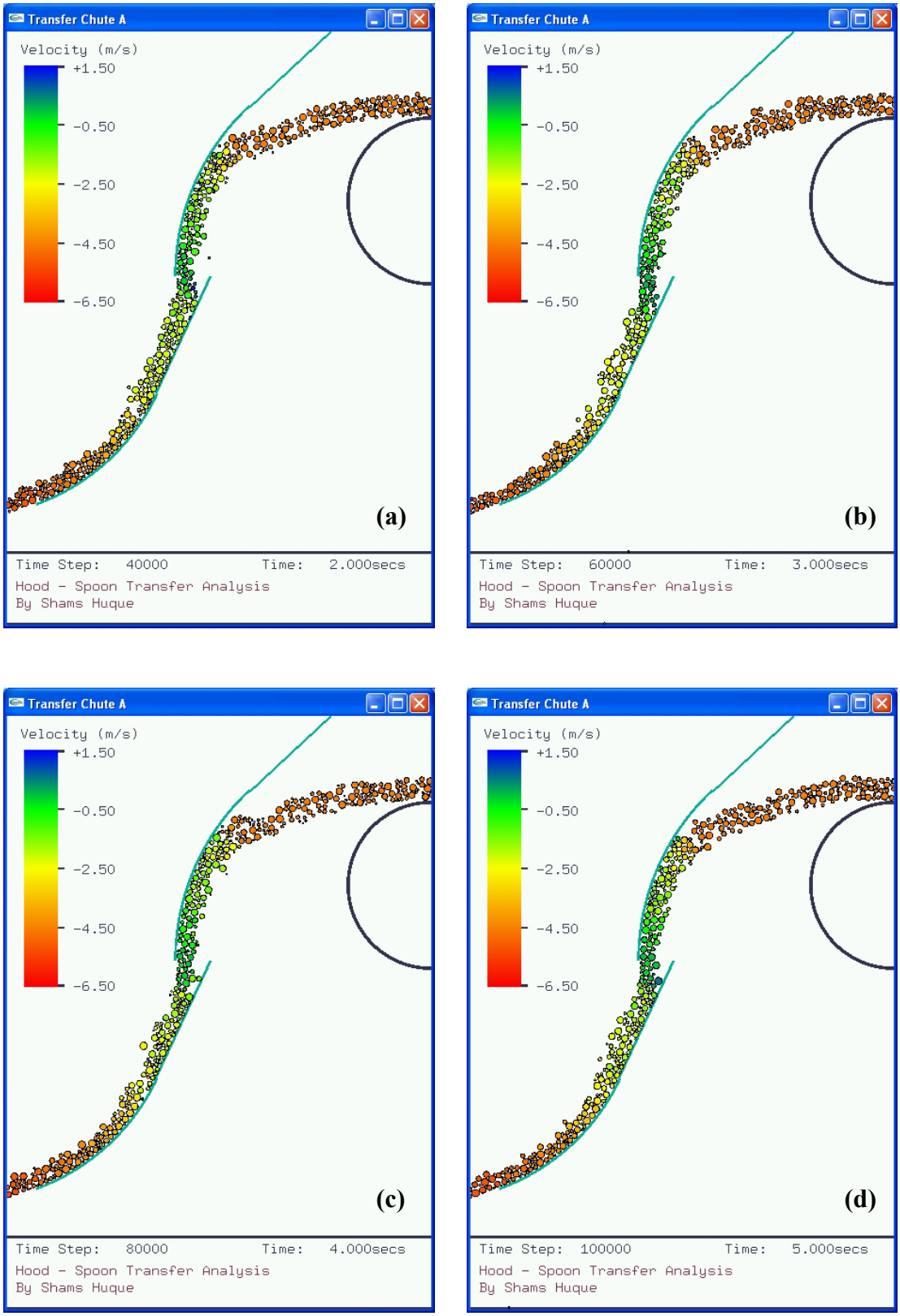

Figure 8.2 Snapshots of the hood-spoon transfer system showing horizontal velocity components at times of **(a)** $t = 2.0$ s, **(b)** $t = 3.0$ s, **(c)** $t = 4.0$ s, and **(d)** $t = 5.0$ s.

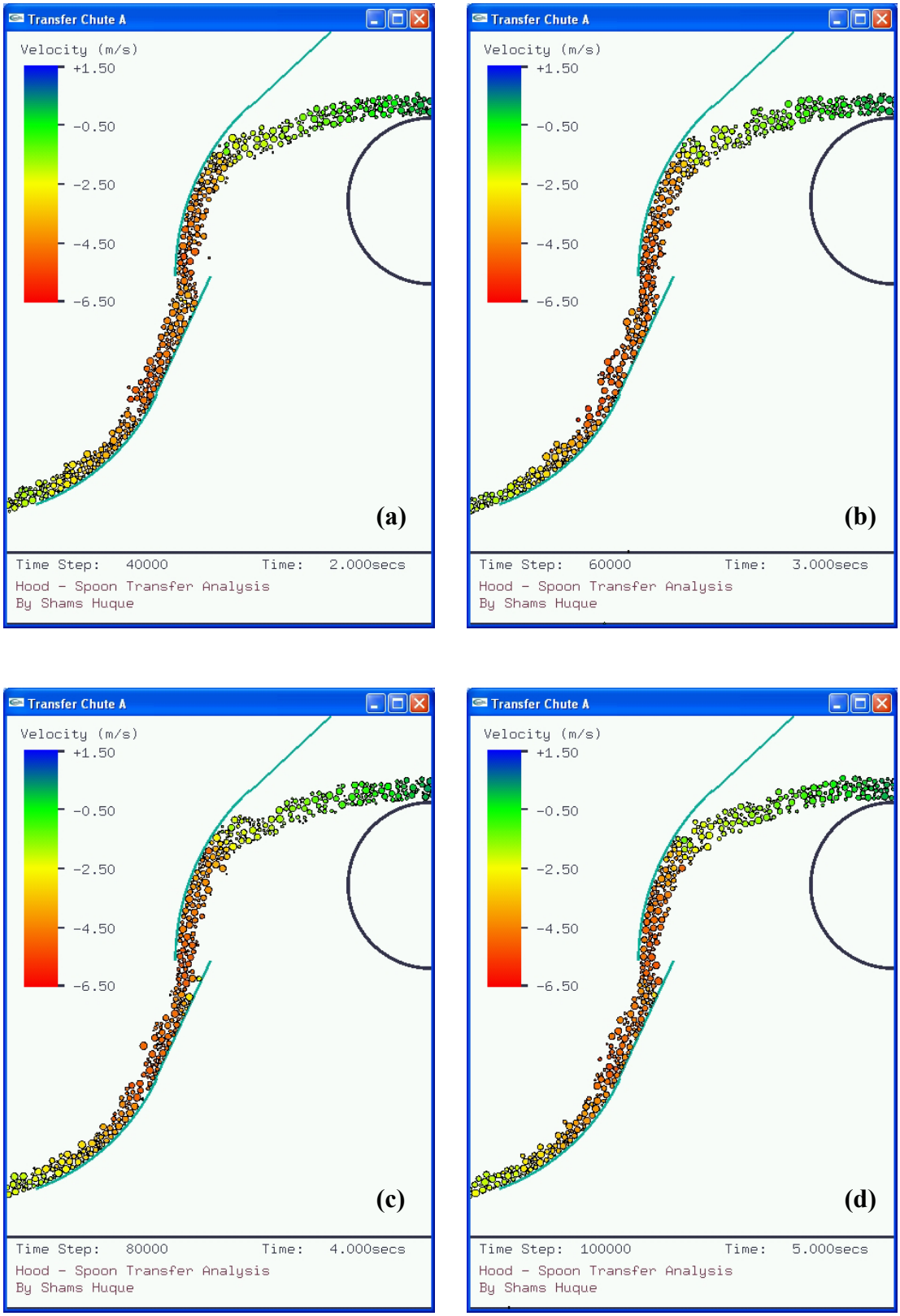

Figure 8.3 Snapshots of the hood-spoon transfer system showing vertical velocity components at times of **(a)** $t = 2.0$ s, **(b)** $t = 3.0$ s, **(c)** $t = 4.0$ s, and **(d)** $t = 5.0$ s.

8.2.2 Single Hood Transfer Chute

Figures 8.4 (a) to 8.4 (d) illustrate the particle speeds at t = 2.0 s, t = 3.0 s, t = 4.0 s, and t = 5.0 s respectively for the single hood transfer. The conveyor belt speed is v_b = 3.4 ms^{-1}. It can seen in each figure that the general trend of the material stream is to maintain the speed at the point of trajection through the transfer, with a slight decrease of speed at the impact point evidenced by the bright red particles. During free fall, the speeds increase as expected, shown by the colour transition from green to blue.

To gain a greater insight into the behaviour of the particulate stream the horizontal and vertical velocity contours are shown in Figures 8.5 and 8.6 respectively, at times (a) t = 2.0 s, (b) t = 3.0 s, (c) t = 4.0 s, and (d) t = 5.0 s. The horizontal velocity components of the particles remain constantly positive after trajection until impacting the hood, where the horizontal velocity reduces to and hovers around zero (colour change from dark blue to bright green). A few particles experience rebound as shown by the aqua coloured particles in a region of predominantly green particles. The vertical velocity components begin positively at the point of trajection as a result of the positively inclined conveyor (bright green colour), but then reduce to zero, and increase negatively during free fall, and impact and sliding around the hood (colour change from bright green to light orange). The particles gain negative velocity after free falling from the end of the hood, as expected (colour change from light orange to red). In general, the velocity distributions are as expected, with a logical area of velocity reduction at the impact point upon the hood.

8.3 Detailed Quantitative Analysis of Velocity Distributions

The colour coded speed and velocity distributions shown in Figures 8.1 to 8.6 are similar to the type of results shown by the authors mentioned earlier, and are useful for a broad quantitative examination of what is occurring with the particles as they flow through the transfers. However to scrutinise in detail some of the more subtle particulate behaviours and to also compare the DEM results to those produced using the analytical

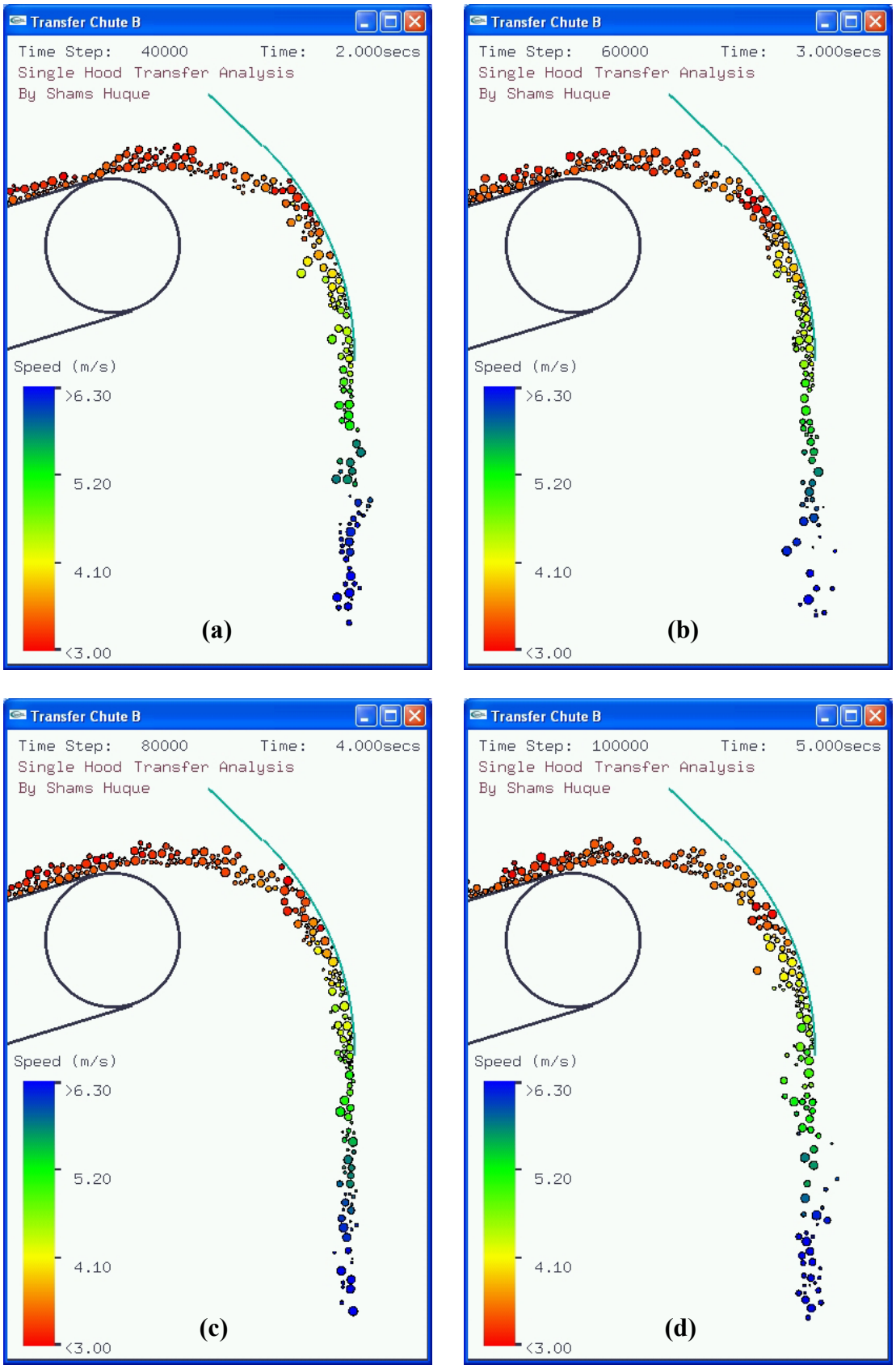

Figure 8.4 Screen captures that show the particulate speed distribution for the second transfer system at times of **(a)** $t = 2.0$ s, **(b)** $t = 3.0$ s, **(c)** $t = 4.0$ s, and **(d)** $t = 5.0$ s.

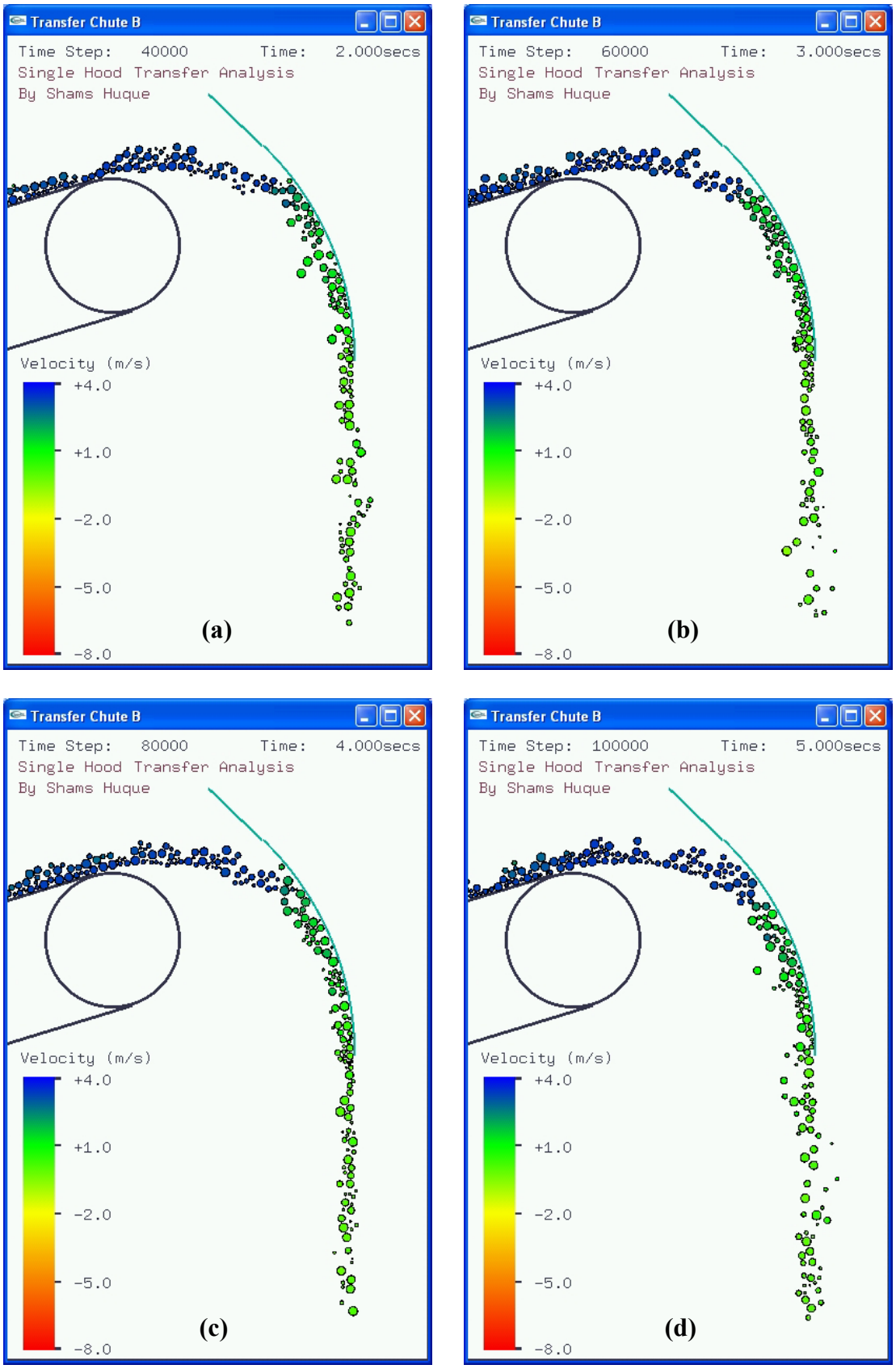

Figure 8.5 Snapshots of the single hood transfer system showing horizontal velocity components at times of **(a)** $t = 2.0$ s, **(b)** $t = 3.0$ s, **(c)** $t = 4.0$ s, and **(d)** $t = 5.0$ s.

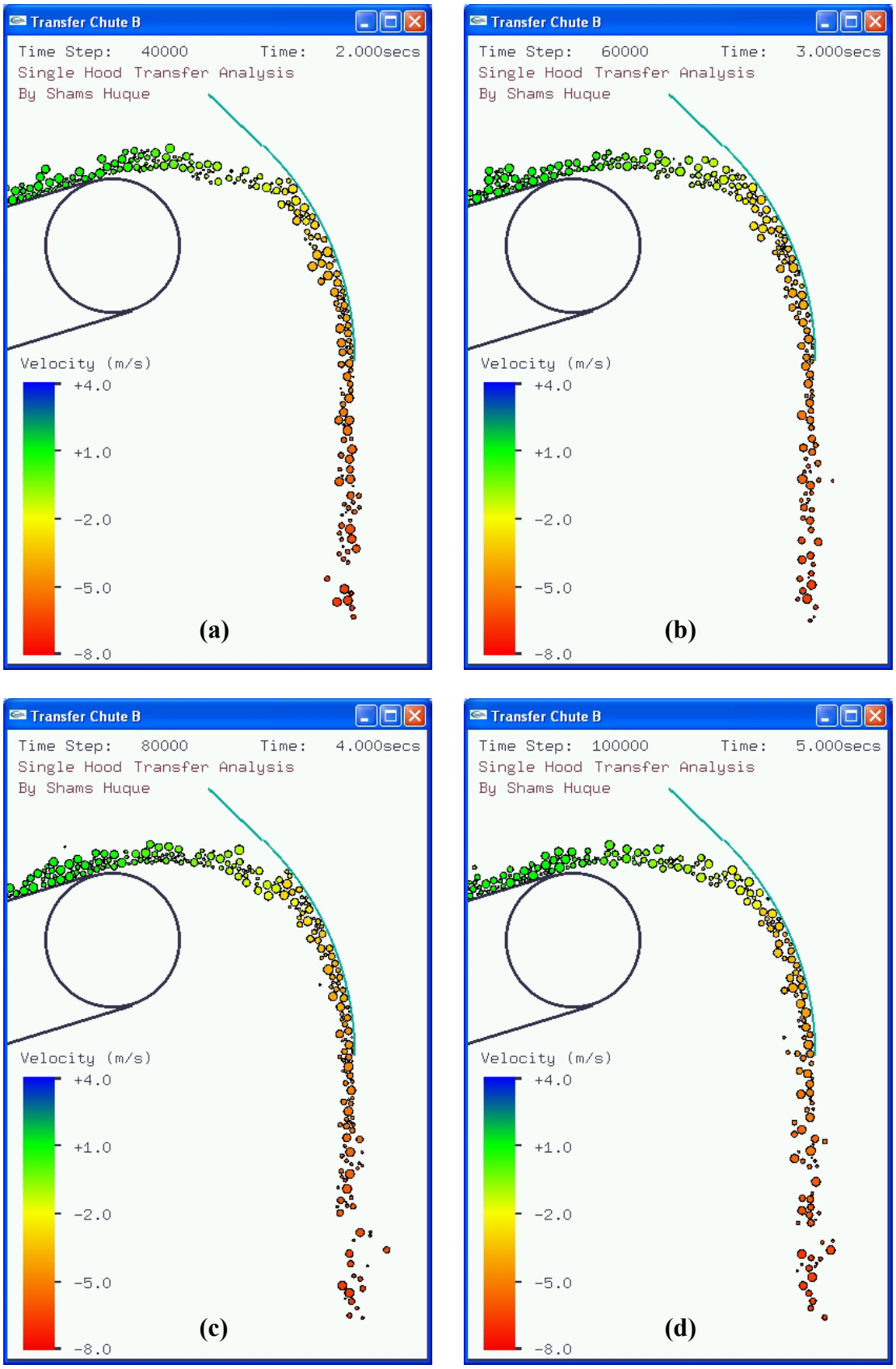

Figure 8.6 Snapshots of the single hood transfer system showing vertical velocity components at times of **(a)** $t = 2.0$ s, **(b)** $t = 3.0$ s, **(c)** $t = 4.0$ s, and **(d)** $t = 5.0$ s.

methods, quantitative data are needed, and for the current work, snapshots of the positional and velocity data will be taken once again at t = 2.0 s, t = 3.0 s, t = 4.0 s, and t = 5.0 s, and the data presented in conventional plots.

8.3.1 Hood-Spoon Transfer Chute

The first transfer chute to be examined comprises the hood-spoon system. Figure 8.7 shows the position, and horizontal and vertical velocity components of the material stream as calculated using the analytical methods. Note that the position indicated is that of the approximate centroid of the material stream.

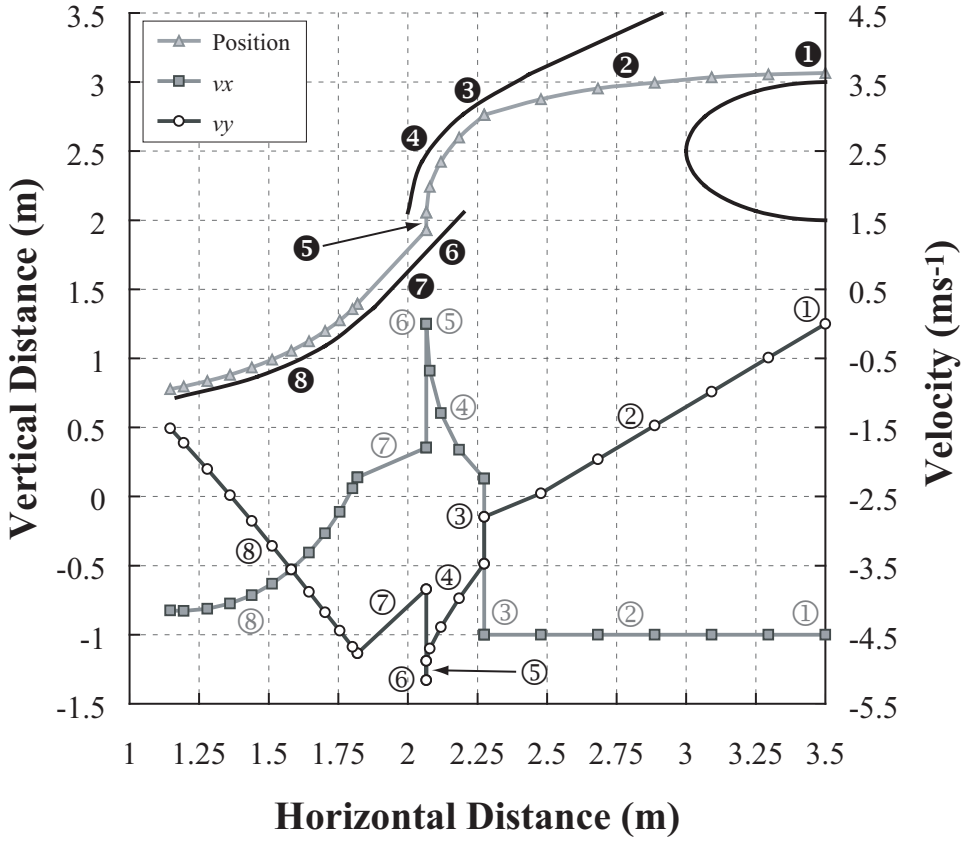

Figure 8.7 Particle position and horizontal & vertical components of velocity calculated using the analytical methods described in Section 7.3.2 for hood-spoon transfer chute. The numbers correspond to those shown in Figure 7.7.

The numbering was described in detail in Chapter Seven, however is briefly redescribed here with the differing shades representing particle positions, vertical velocity components, and horizontal velocity components respectively. The numbers ❶①① correspond to the discharge point of the material; the numbers ❷②② correspond to the trajectory of the material; numbers ❸③③ mark the impact point with the hood; numbers ❹④④ denote the sliding flow around the hood; the numbers ❺⑤⑤ represent the free fall of the particle stream; numbers ❻⑥⑥ mark the impact of the material with the spoon; numbers ❼⑦⑦ mark the sliding flow of the material along the straight portion of the spoon; and finally numbers ❽⑧⑧ denote the sliding flow of the material along the curved portion of the spoon.

Figures 8.8 (a) to 8.8 (d) are single snapshots of the simulated flow at times t = 2.0, 3.0, 4.0 and 5.0 s. Due to these times lying within the steady-state region of flow, there is very little difference between the data values in each plot. The chute surfaces and pulley are represented by solid black lines. The data values are as expected, that is there are no erroneous data points, illustrating steady and stable particulate flow.

Comparing the results from the analytical methods shown in Figure 8.7 to the four DEM snapshots shown in Figure 8.8 (a) to 8.8 (d) shows very good quantitative agreement. Examining the analytical results, the horizontal velocity component vx is initially constant at -4.5 ms^{-1} (①) until impact occurs (③) where vx reduces to a little less than -2.5 ms^{-1}. As the particles flow around the upper curve (④), the horizontal velocity component reduces to zero, however Figures 8.8 (a) to 8.8 (d) show a number of DEM particles with small positive horizontal velocity components in the region 2.0 m < x < 2.15 m, indicating rebound off the chute surface. Referring back to the analytical results, the material stream then free falls (⑤) until it hits the straight portion of the lower chute element (⑥) where the impact process gives a negative horizontal velocity component. This period of motion (free fall then impact) is not so well defined in the DEM snapshots, as any horizontal components of velocity attained after hitting the hood are constant until impact is made with the spoon. In the analytical results, after impact the material flows down the inclined straight surface (⑦), linearly gaining velocity until it reaches the curved portion of the spoon. At this point there is an initial rapid acceleration which gradually slows (⑧), and the material exits the spoon with a

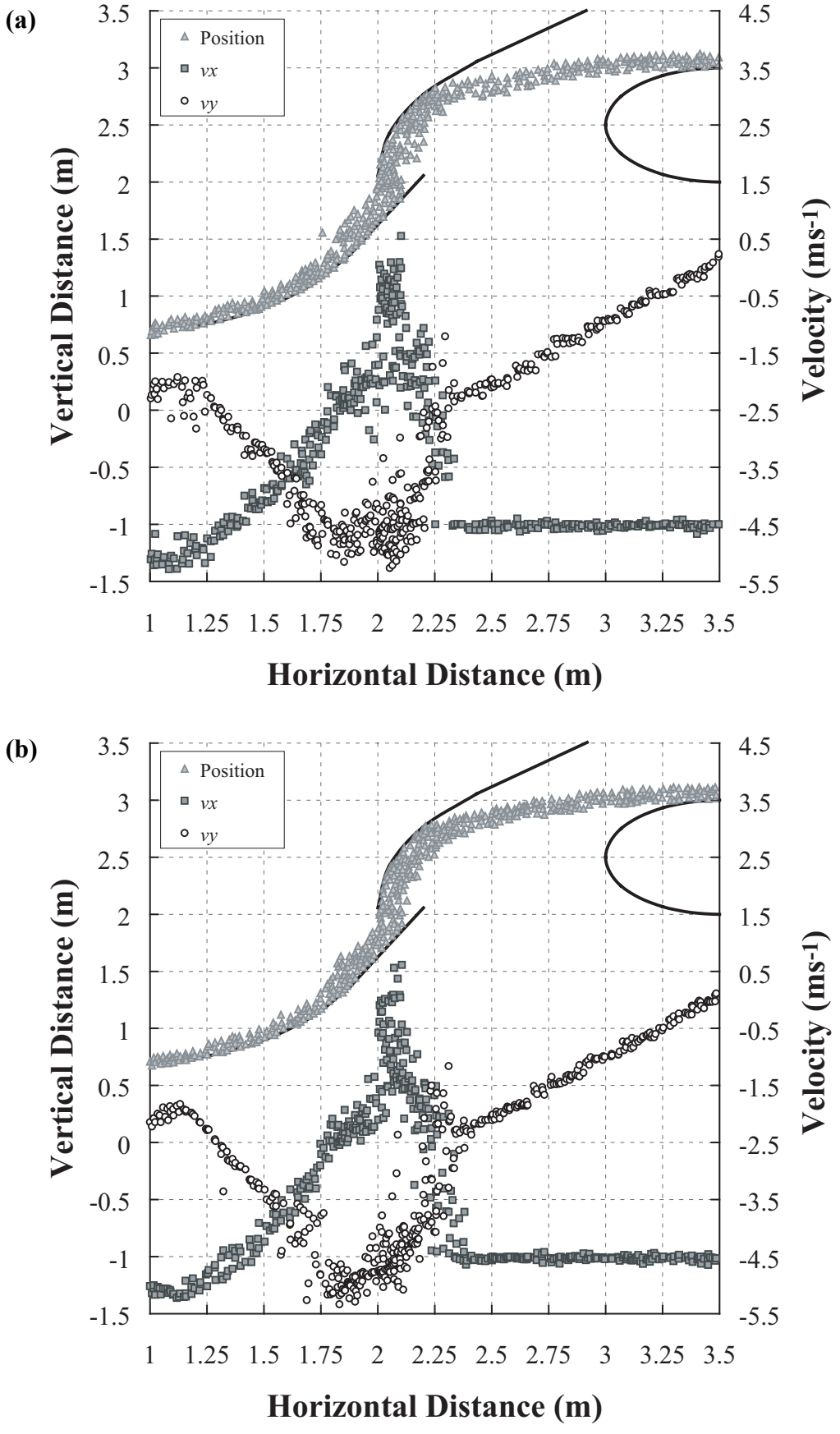

Figure 8.8 Snapshot of particle position, and horizontal and vertical components of velocity at **(a)** t = 2.00 s and **(b)** t = 3.00 s for hood-spoon transfer chute

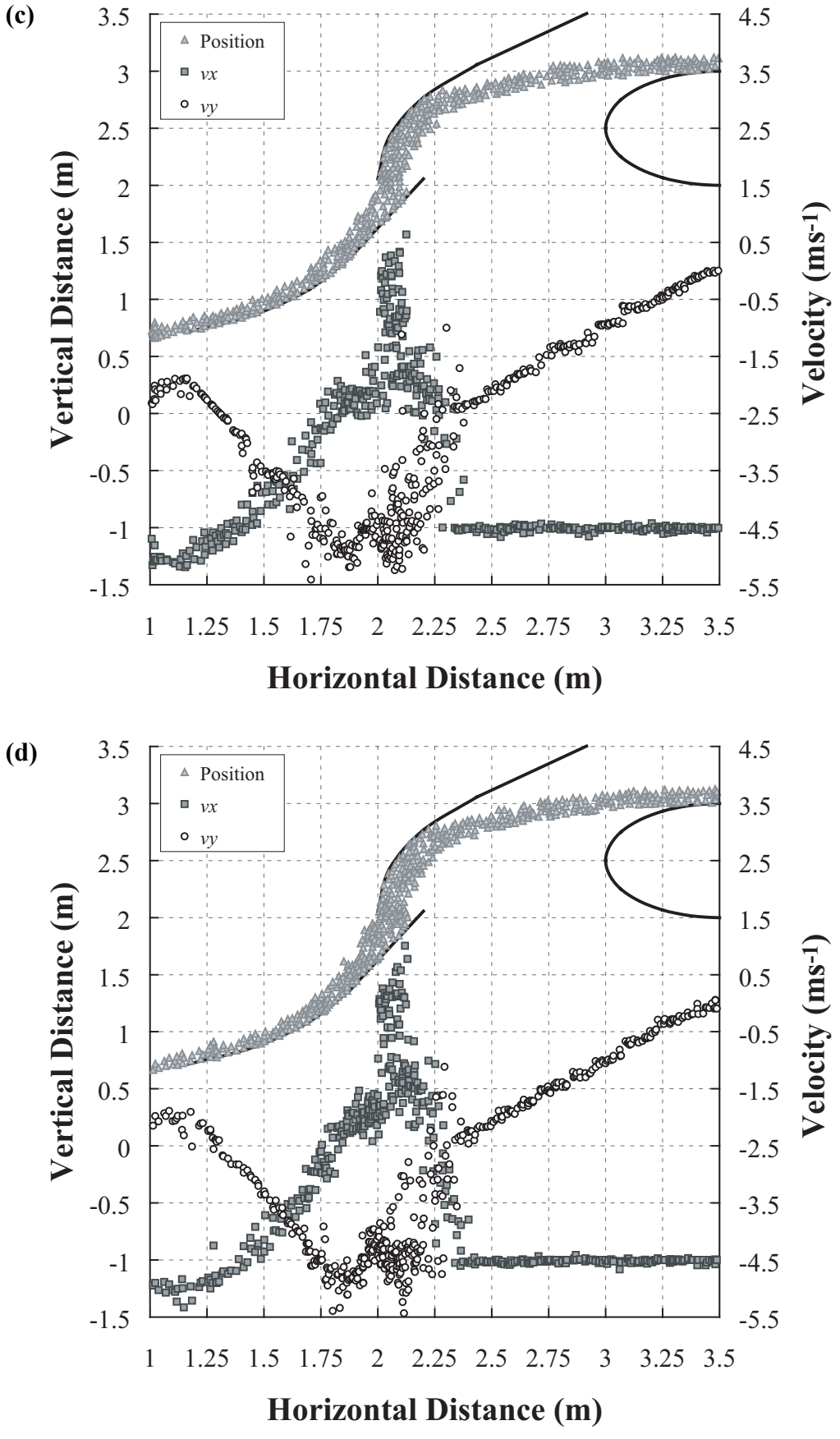

Figure 8.8 Snapshot of particle position, and horizontal and vertical components of velocity at **(c)** t = 4.00 s and **(d)** t = 5.00 s for hood-spoon transfer chute

horizontal velocity component of approximately -4.1 ms^{-1}, which is below the receiving conveyor velocity of -4.5 ms^{-1}. This process is also represented in the DEM snapshots, though the sudden acceleration as the particles start to flow around the curve is not so pronounced in the region 1.5 m < x < 1.8 m. This difference is as a result of using a constant equivalent friction coefficient μ_E in the analytical theory for the current work and therefore not accounting for inter-particle stress mechanisms. The snapshots also reveal that the particles attain a horizontal velocity component in the vicinity of -5.0ms^{-1}, which is greater than the receiving conveyor belt velocity. As a point of interest, the author enquired about the actual horizontal velocity component of the material stream resulting from the chute in operation. Unfortunately this information could not be obtained, however considering the chute performance was rated as very good, it can be assumed that the actual horizontal velocity component is close to the belt speed.

If we now examine the vertical velocity component in the analytical results, *vy* starts at zero at the point of trajection (①) and increases due to gravitational acceleration to approximately -2.7 ms^{-1} prior to impact (③). During the impact process with the hood, *vy* increases to approximately -3.5 ms^{-1} and accelerates as it flows around the curve (④) to reach approximately -4.9 ms^{-1}. The DEM snapshots reveal that a number of particles have lower than expected vertical velocity components, which are due to these particles lying in minor zones of stagnation. These small pockets owe their presence to the particulate flow 'holding up' certain particles as they impact and flow around the hood. This is similar to the 'flow round' zone phenomenon described by Korzen (1988), though to a lesser extent. Referring back to the analytical results, after free fall (⑤) the vertical velocity component reaches an approximate maximum of -5.1 ms^{-1} prior to impacting upon the lower chute element (⑥). During the impact process *vy* reduces in magnitude, however linearly gains velocity as it flows along the straight portion of the spoon (⑦). The DEM snapshots illustrated the complicated mechanisms at the point of contact and flow upon the lower chute. The data are not so well defined, and at first glance is rather of a stochastic nature. A closer inspection reveals however a definite trend in the DEM data to decrease then increase as impact and then flow occurs in the approximate region 1.75 m < x < 2.1 m. The vertical velocity component in the analytical results then linearly decreases (⑧) to -1.5 ms^{-1} at the exit of the spoon. The DEM data show a slight increase in the vertical velocity component of the particles, which is expected as at this point there is a brief drop onto the receiving conveyor belt.

8.3.2 Single Hood Transfer Chute

The second transfer chute to be examined comprises the single hood system. Figure 8.9 shows the position, and horizontal and vertical velocity components of the material stream as calculated using the analytical methods. Note that the position indicated is that of the approximate centroid of the material stream. The numbering was described in detail in Chapter Seven, however is briefly redescribed here with the differing shades representing particle positions, vertical velocity components and horizontal velocity components. The numbers ❶①① correspond to the discharge point of the material; the numbers ❷②② correspond to the trajectory of the material; numbers ❸③③ mark the impact point with the hood; and numbers ❹④④ denote the sliding flow around the hood.

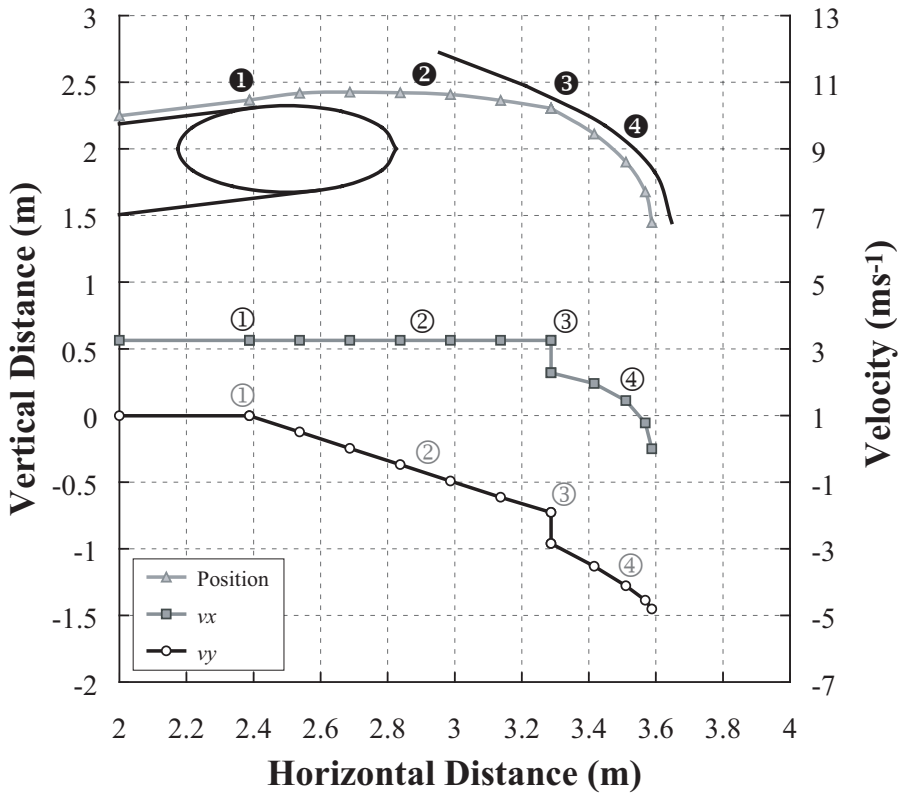

Figure 8.9 Particle position and horizontal & vertical components of velocity calculated using the analytical methods described in Section 7.3.2 for single hood transfer chute. The numbers correspond to those in Figure 7.8.

Figures 8.10 (a) to 8.10 (d) are single snapshots of the simulated flow at times t = 2.0, 3.0, 4.0 and 5.0 s. Due to these times lying within the steady-state region of flow, there is very little difference between the data values in each plot. The chute surfaces and pulley are represented by solid black lines. As for the first transfer the nature of the data shown indicates steady and stable particulate flow.

Comparing the results from the analytical methods shown in Figure 8.9 to the four DEM snapshots shown in Figures 8.10 (a) to 8.10 (d) again shows very good quantitative agreement. Examining the analytical results, the horizontal velocity component *vx* is constant at a little over 3.0 ms^{-1} (①) until impact is made with the hood element (③), where there is a drop in velocity. As the material travels around the curve (④), there is deceleration until at the exit of the spoon there is zero velocity horizontally. This is replicated to good effect in the DEM snapshots though the deceleration of *vx* around the curve is not as marked and is more linear in nature. This difference is probably due to the varying contact mechanisms that are present, such as sliding flow, particle rebound, and internal shear.

Referring back to the analytical results, the vertical velocity component *vy* is constant at 1.0 ms^{-1} until the point of trajection (①) at which point it decreases to zero as the material stream reaches its highest point, and then increases once again to approximately -1.9 ms^{-1} prior to impact. The impact process (③) increases *vy* to -3.0 ms^{-1} and it increases further as the material flows around the curve (④) to -4.9 ms^{-1} at the exit point of the hood. The DEM snapshots quantitatively agree very well, although the velocity increase at the point of impact at approximately x = 3.28 m is not clearly defined in the DEM data, which is due to the presence of data from particles flowing just before or after the impact point. After exiting the hood, the DEM particles increase their vertical velocity component in the negative direction, as expected.

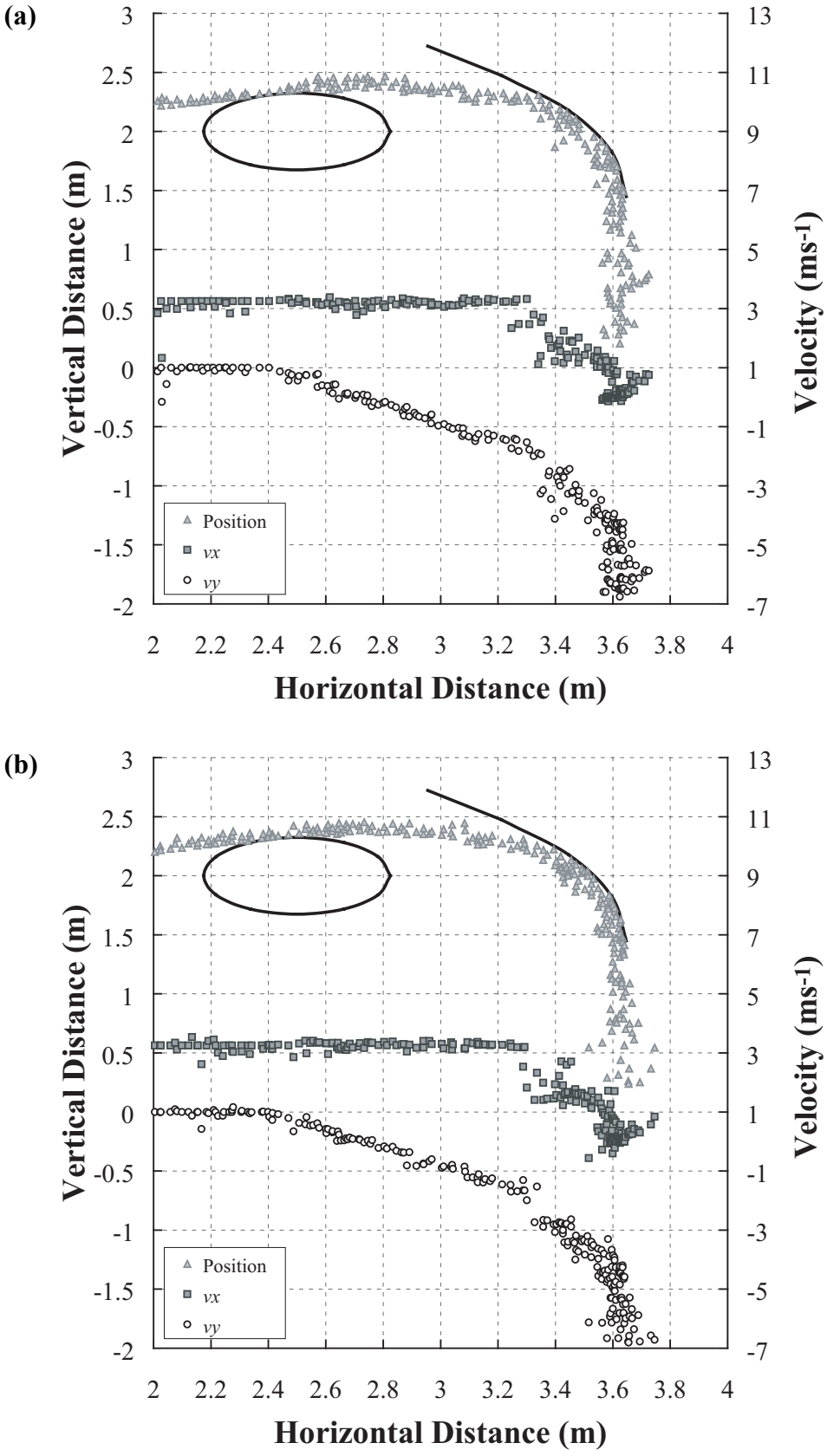

Figure 8.10 Snapshot of particle position, and horizontal and vertical components of velocity at **(a)** t = 2.00 s and **(b)** t = 3.00 s for single hood transfer chute

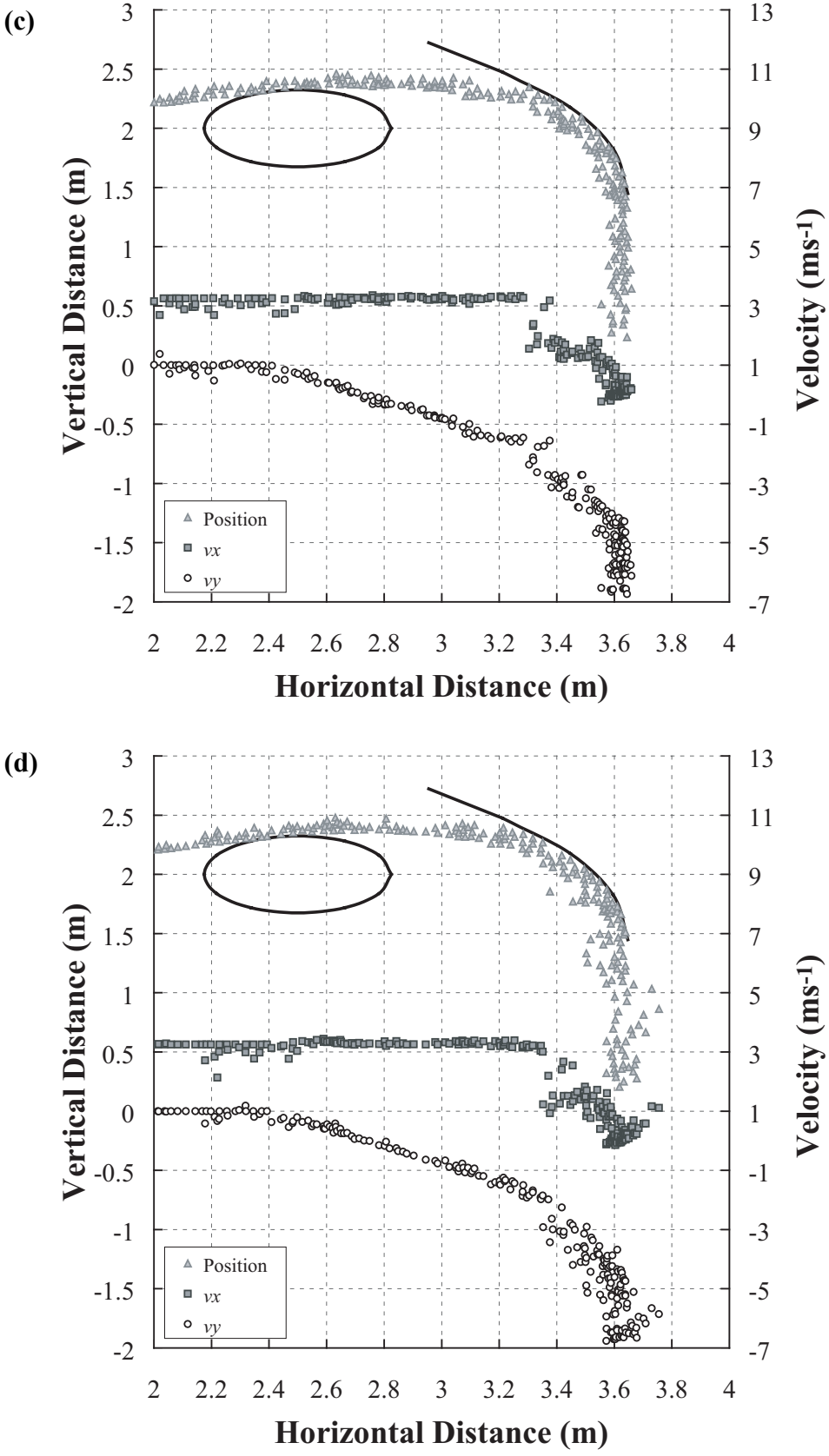

Figure 8.10 Snapshot of particle position, and horizontal and vertical components of velocity at **(c)** t = 4.00 s and **(d)** t = 5.00 s for single hood transfer chute

8.4 Micro Dynamics of Discrete Particles

The movement of an individual particle through the chute system can provide information on the dynamics experienced by that particle in a specific region of the material flow and help scrutinise a few of the less defined flow aspects from the DEM snapshots. For example, intuitively the author believes that the motion of a particle flowing with neighbouring particles will be different to that when the particle flows adjacent to a chute wall. The literature search showed that such transfer studies into the flow at the singular particle level have not been carried out, and therefore in this section we will examine the micro dynamics of a discrete particle. The term refers to the dynamics of an individual particle including its interactions with neighbouring particles, boundary elements and the effect of gravity. In addition to qualitatively analysing the motion, the positions, and horizontal and vertical velocity components of each particle are also compared to those resulting from the analytical processes detailed in Chapter Two and presented in Figures 8.7 and 8.9.

The particles selected for the evaluation of micro dynamic behaviour are as follows. For the hood-spoon transfer the selected particle numbers were randomly chosen from the 1500 particles simulated and are i = 26 and i = 1116. For the single hood transfer the selected particle numbers were randomly chosen from the 900 particles simulated and are i = 377 and i = 801. The positions of the particles in the initial group within each feeder are shown in Figures 8.11 (a) and 8.11 (b). The selected particles are coloured black with their identification numbers and positions indicated in the figures. Figures 8.12 and 8.13 show the paths, and horizontal and vertical velocity components of each selected particle for the hood-spoon system and single hood system respectively. During the simulation time of 5.0 s for the first transfer, both particles managed to flow through the system twice, and the numbers in parentheses in the plots represent the first or second run. During the simulation time of 5.0 s for the second transfer, both particles managed to flow through the system only once as opposed to the particles considered for the first transfer.

The main areas where the motion characteristics were not so well defined in the DEM snapshots for the first transfer analysed in Section 8.3 were the horizontal and vertical

velocity components during free fall and then impact upon the spoon, and also the flow around the spoon. For the second transfer, the main areas where the motion characteristics were not so well defined in the DEM snapshots analysed in Section 8.3 were the horizontal and vertical velocity components during impact and flow around the hood. The micro dynamic investigations will focus on these regions.

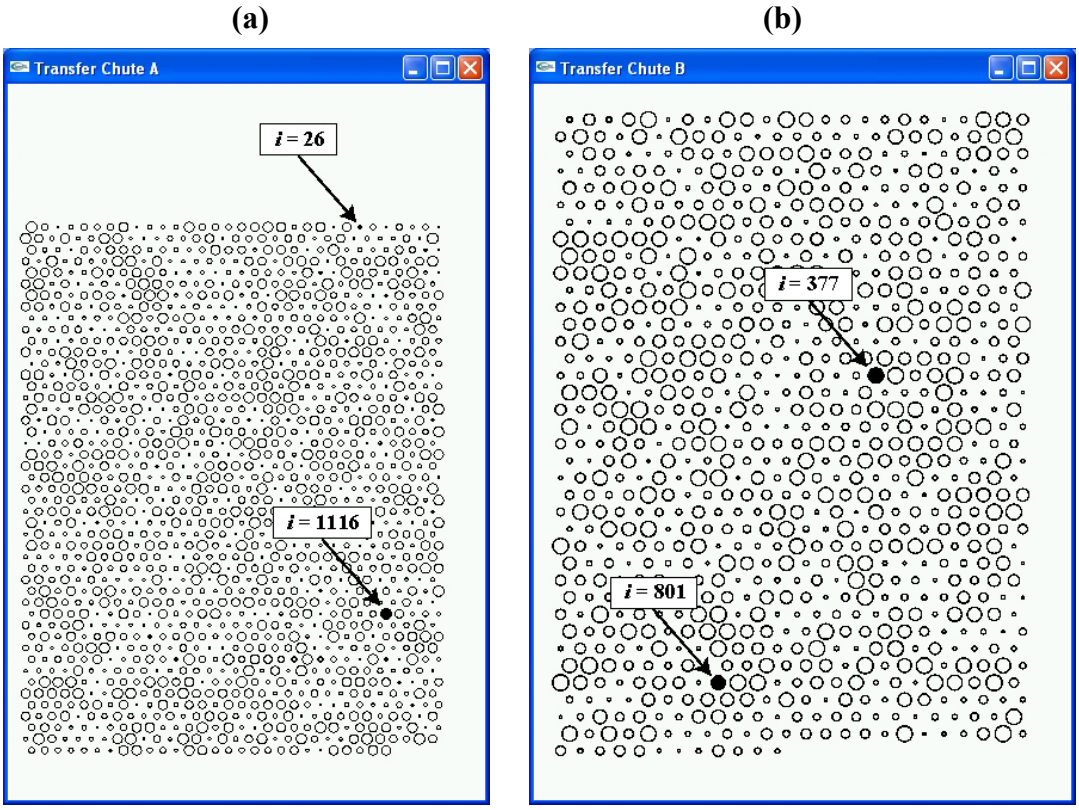

Figure 8.11 Initial positions of selected particles in feeder for **(a)** hood-spoon transfer and **(b)** single hood transfer

8.4.1 Hood-Spoon Transfer Chute

Examining Figures 8.12 (a) and 8.12 (b), it is clear that many of the trends exhibited by the single particles are similar to the analytical methods whose calculations are primarily based on the kinematics of a single element of mass. However, there are a few differences in velocity component magnitudes and trends, and these can be attributed to the contact mechanisms experienced by each single particle in their specific location in

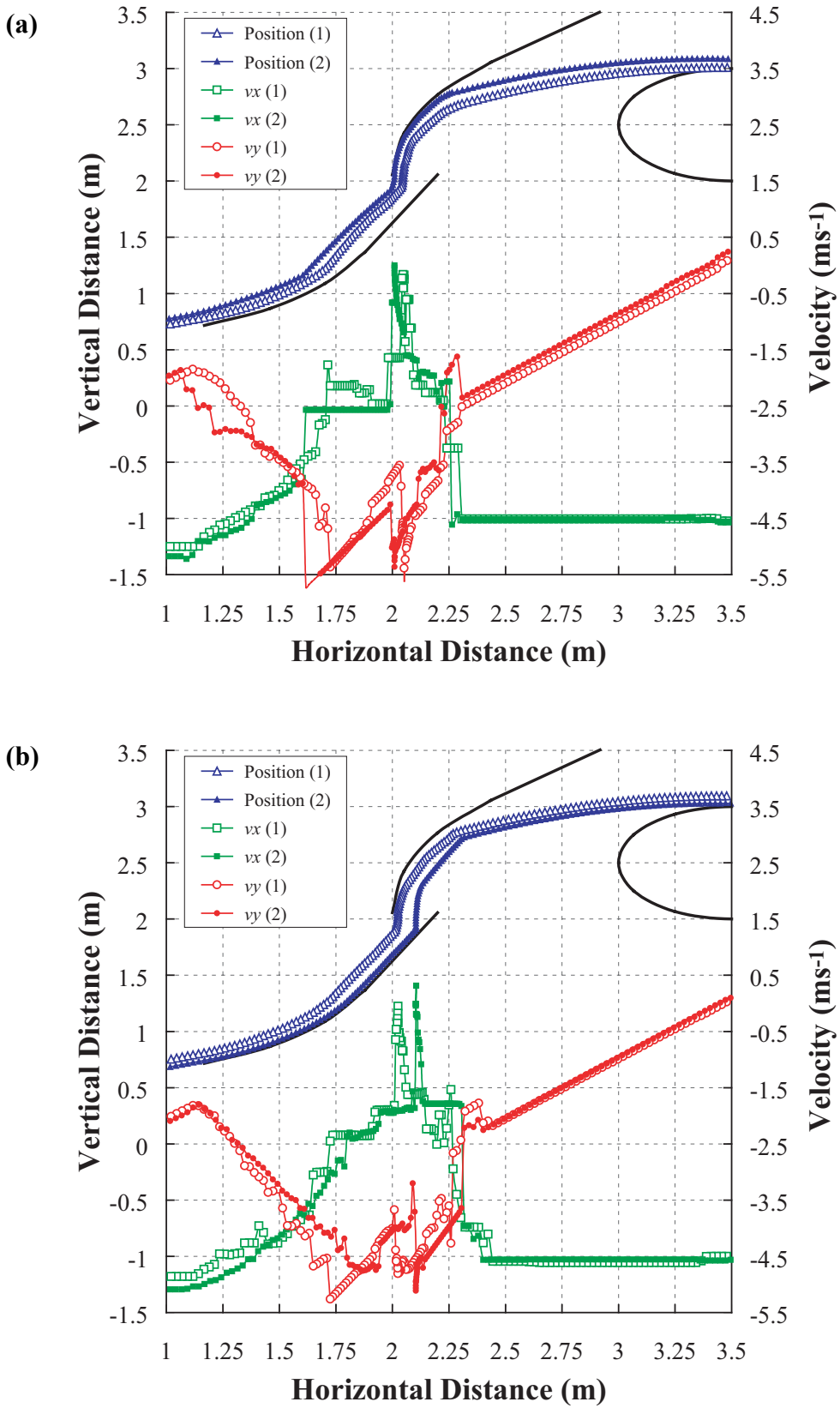

Figure 8.12 Two randomly selected particles from the hood-spoon DEM simulation with positions, and horizontal and vertical velocity components. The particle numbers examined are **(a)** $i = 26$ and **(b)** $i = 1116$

the material stream. For example, in Figure 8.12 (a) the single particle does not contact the hood or the spoon in its first run, suggesting that it was lying somewhere within the body of the particle stream, while in its second run the single particle lies in the upper portion of the stream and hence contacts the hood but does not contact the spoon. In Figure 8.12 (b) the particle only makes brief contact with the lowest portion of the hood, and does not contact the spoon in its first run, while in its second run the particle is in the lower portion of the stream, and continuously keeps contact with the spoon as it flows around.

The velocity components generally exhibit similar behaviour to those produced using the analytical methods, though are jagged in appearance due to the specific contact mechanisms experienced at each time step. Figures 8.12 (a) and 8.12 (b) provide information on velocity component aspects of individual particles in the upper and lower portions of the stream. The second run of the particle in Figure 8.12 (a) shows that at the hood impact point (x = 2.0 m) vx reduces to zero, however the second run of the particle in Figure 8.12 (b) shows vx to gain a finite positive value (at x = 2.11 m), illustrating that particles in the upper portion of the stream cannot experience rebound due to the stream of particles acting upon it from behind, while particles in the lower portion of the stream can do so as they have no constraints to their motion. During the sliding flow upon the spoon the situation is reversed, with the surrounding particles acting upon the lower lying particle adjacent to the spoon surface in Figure 8.12 (b) giving a motion similar to that shown by the analytical method in Figure 8.7. Meanwhile vx in Figure 8.12 (a) is constant for a region in the particle's second run which is inconsistent with Figure 8.7. Figure 8.12 (a) shows how there is a stepwise decrease in vx during its first run for 1.7 m < x < 1.9 m as opposed to the constant value achieved during its second run, meaning the transition from straight to curved surface flow for particles within the stream is not as smooth as observed for the particles on the flowing stream surface.

The vertical component of velocity vy also shows differences arising from the location of individual particles within the stream path. If we consider the second run of the particle shown in Figure 8.12 (a), it can be seen that during the flow around the hood, the particle's vertical velocity component increases non-linearly (for 2.0 m < x < 2.21 m) , and during flow along the straight and upper curved portion of the spoon (for 1.65

m < x < 2.0 m), the component increases linearly and then there is a sudden drop off and non-linear deceleration around the rest of the spoon (for 1.16 m < x < 1.6 m). The drop off is unusual and represents the particle experiencing impact(s) with other particle(s). This is in contrast to the second run of the particle shown in Figure 8.12 (b), where vy increases linearly as the particle flows around the hood (for 2.13 m < x < 2.31 m), and a non-linear increase followed by linear decrease in vy as the particle flows around the spoon. The two runs of the particle in Figure 8.12 (b) show similar qualitative trends for vy to the analytical methods during free fall and impact with the spoon, and reveals that the uncertainty observed in the previous section regarding the aspect of free fall is due to the nature of the snapshots taken, which are a representation of the system at one instance in time, while the micro dynamic analyses show the motion history of the particle.

8.4.2 Single Hood Transfer Chute

Figure 8.13 (a) shows a particle that impacts twice upon the hood before free falling, rather than smoothly flowing around the hood element like the particle shown in Figure 8.13 (b). These differing flow attributes are the result of varying stream path locations for each particle. This can be seen when examining the horizontal velocity component in Figure 8.13 (a), where vx has a sudden decrease in magnitude (x = 3.38 m), while in Figure 8.13 (b) vx does not experience as large a jump. During the region 3.38 m < x < 3.62 m where the particle flows around the hood, for the first particle vx reduces only slightly, probably meaning that the particle was in little or no contact with the surrounding particles. In this region for the second particle vx fluctuates, firstly decreasing, then increasing, and then decreasing once again, meaning that particle interactions were taking place. The non-linear reduction in vx in the region 3.56 m < x < 3.62 m illustrates the effect of the particle flowing adjacent to the hood. The vertical velocity component trends in this case are similar for each particle. The trends shown by the particles with respect to positions and velocity components agree very well with the information generated using the analytical methods, Figure 8.9, which for the most part calculates the material stream path characteristics based upon the kinematics of a single element of mass, as mentioned.

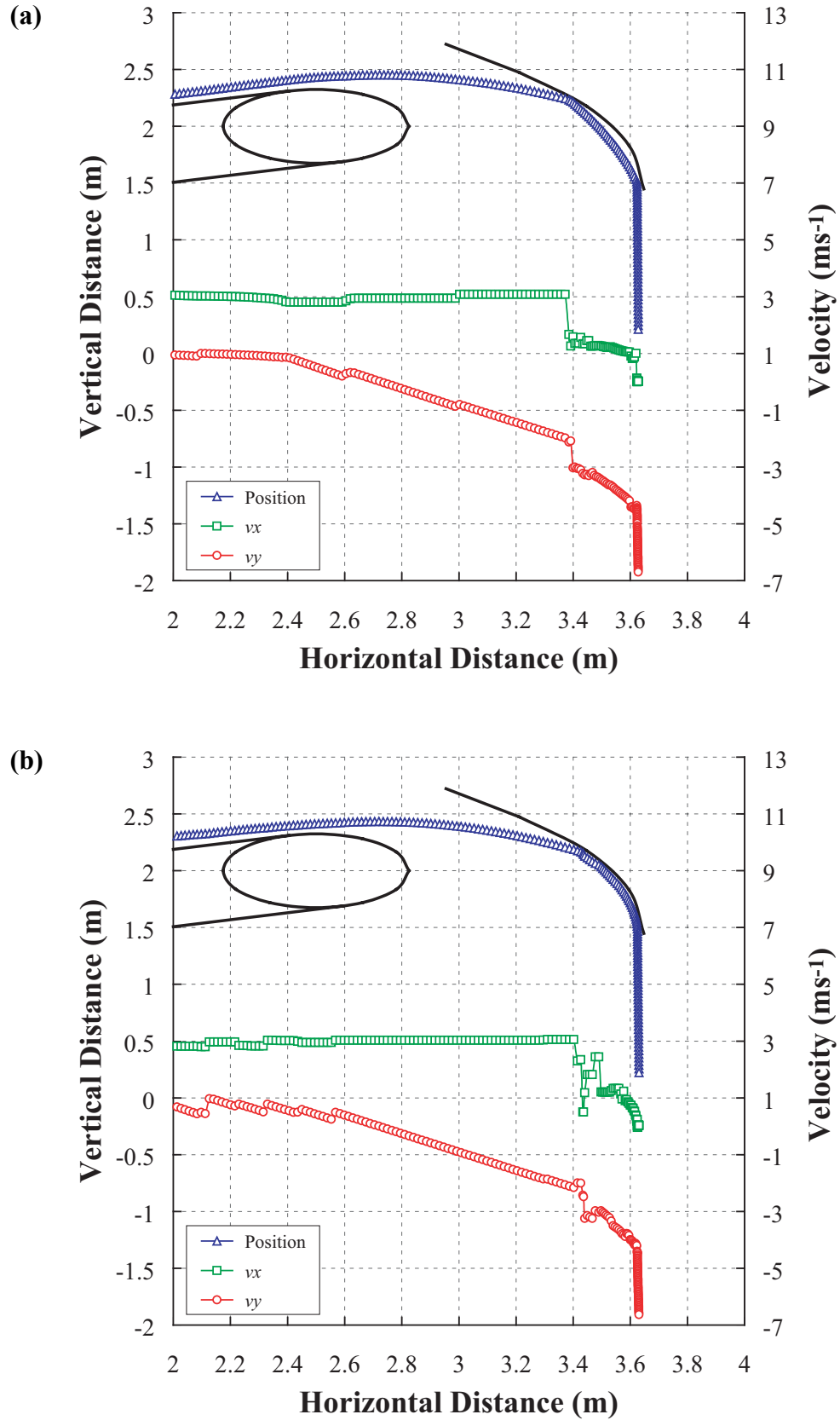

Figure 8.13 Two randomly selected particles from the single hood DEM simulation with positions, and horizontal and vertical velocity components. The particle numbers examined are **(a)** $i = 377$ and **(b)** $i = 801$

8.4.3 Conclusions

In summary, there are differences in the paths and velocity components of each individual particle, and analysis of the hood-spoon transfer has shown it is clear that the motion characteristics for each particle depend upon its location within the material stream. Analysis of the second transfer has emphasised this idea. The study of the micro dynamics of selected particles has shown that the particle dynamics within the flowing stream can be broadly separated into three areas: particles adjacent to the walls, particles within the flow, and particles on the surface of the flow. The particles adjacent to the walls tend to follow that path, and velocities are influenced primarily by their interactions with the wall, hence the velocity results of these particles resemble those produced by the analytical methods most closely. The particles within the flow have their motions dictated to them by their surrounding particles, and the velocity profiles produced are thus less smooth in nature, and can often have a jagged appearance. The particles on the surface of the flow are usually free flowing, however are the particles most likely to lose momentum if the material stream impacts a hood or spoon.

8.5 Additional Quantitative Considerations

Figures 8.14, 8.15 and 8.16 are screen captures that show elastic potential energy, inter-particle forces (including gravity) and particle torques respectively at times of (a) $t = 2.0$ s, (b) $t = 3.0$ s, (c) $t = 4.0$ s, and (d) $t = 5.0$ s for the hood-spoon transfer. Similarly for the single hood transfer, Figures 8.17, 8.18 and 8.19 are screen captures that show elastic potential energy, inter-particle forces (including gravity) and particle torques respectively at times of (a) $t = 2.0$ s, (b) $t = 3.0$ s, (c) $t = 4.0$ s, and (d) $t = 5.0$ s.

Note: Xu (1997) illustrated that due to strong localised distribution of forces, the inter-particle forces in particular, a logarithmic scale of base 10 in the force magnitude contours allows the details of the smaller magnitude forces to be highlighted. The reader must note that these very small force magnitudes are smaller than the large force

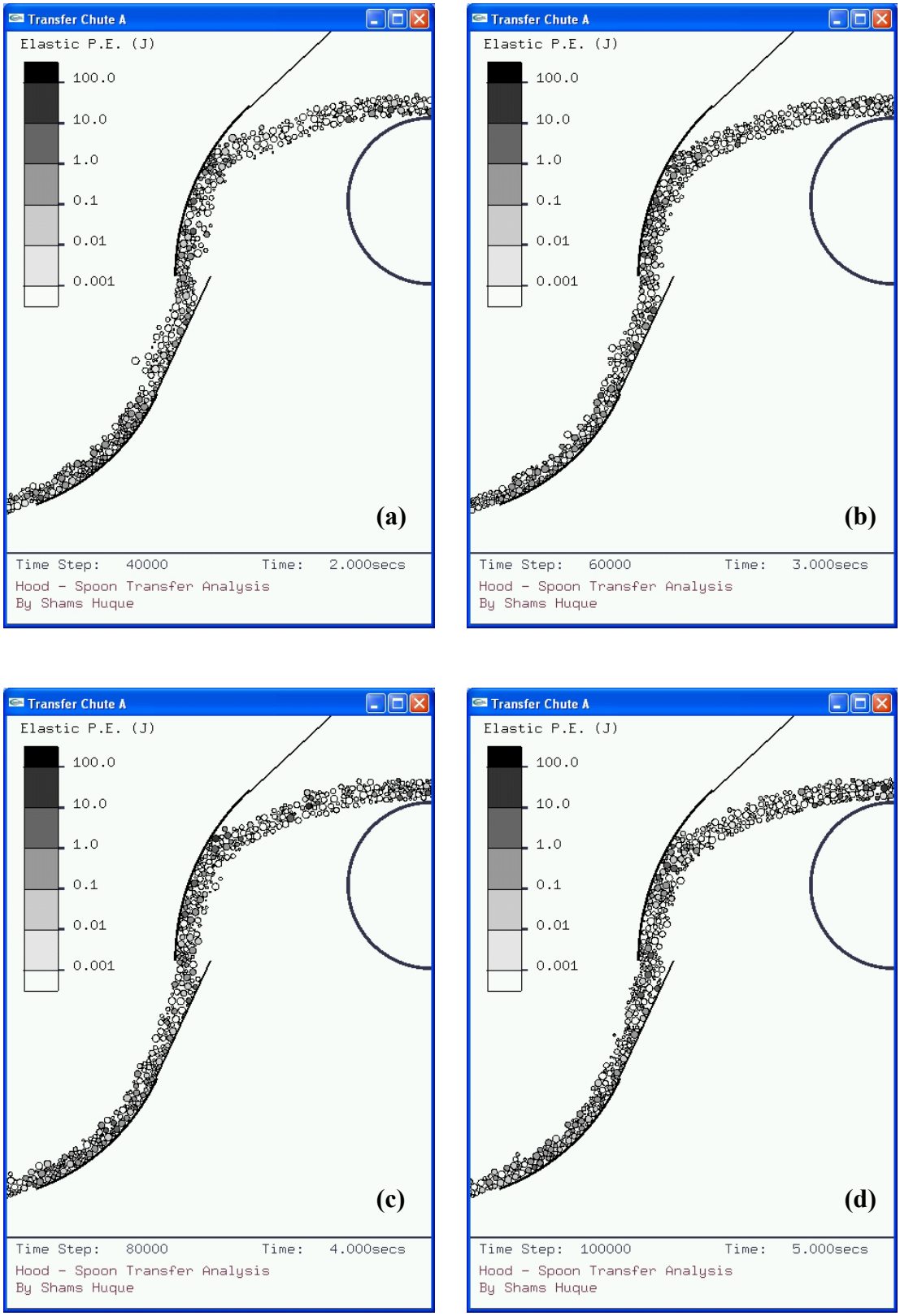

Figure 8.14 Screen captures that show the elastic potential energy (or strain energy) possessed by the particles for the first transfer system at times of **(a)** $t = 2.0$ s, **(b)** $t = 3.0$ s, **(c)** $t = 4.0$ s, and **(d)** $t = 5.0$ s.

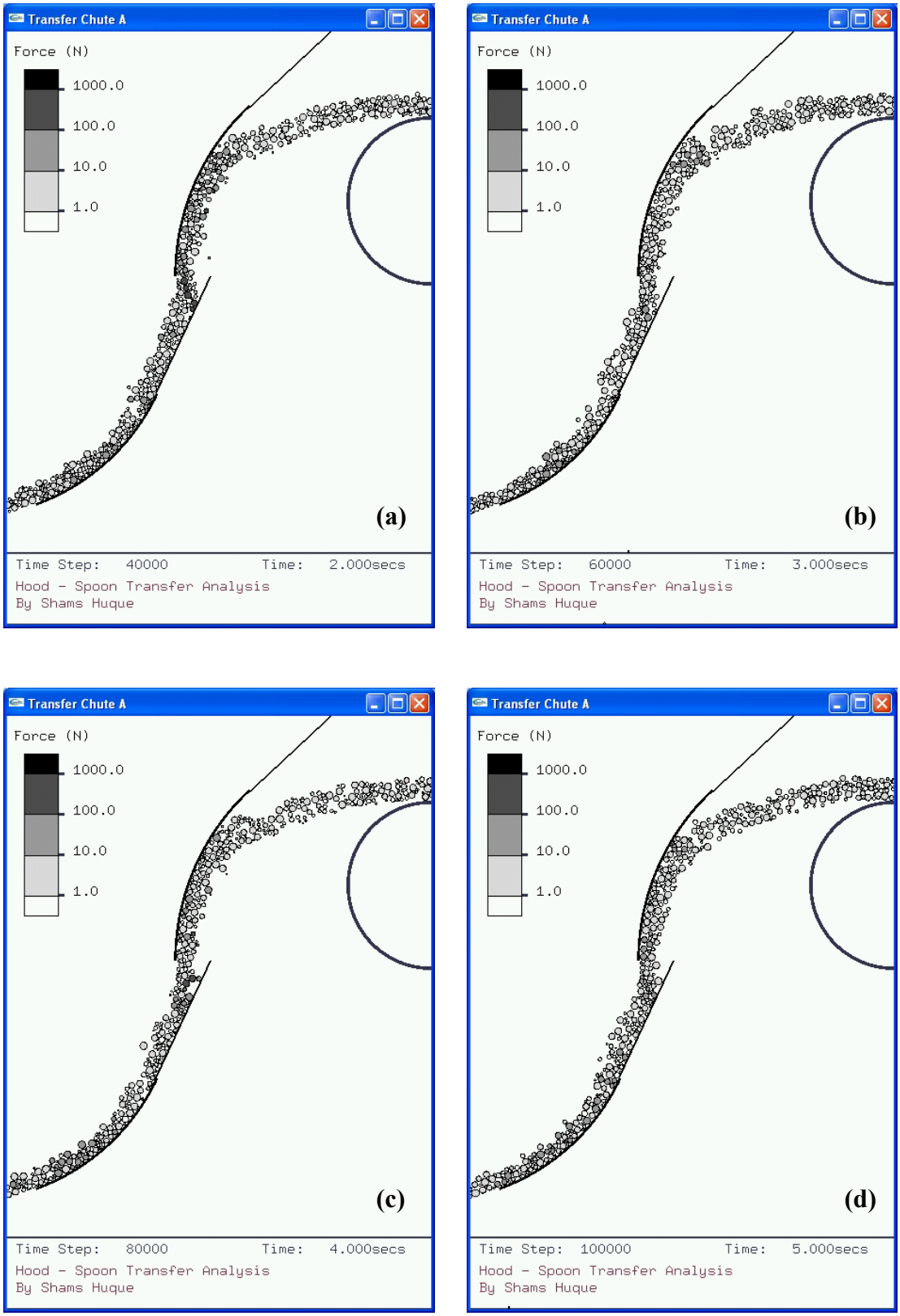

Figure 8.15 Screen captures that show the inter-particle forces (including gravity) possessed by the particles for the force transfer system at times of **(a)** $t = 2.0$ s, **(b)** $t = 3.0$ s, **(c)** $t = 4.0$ s, and **(d)** $t = 5.0$ s.

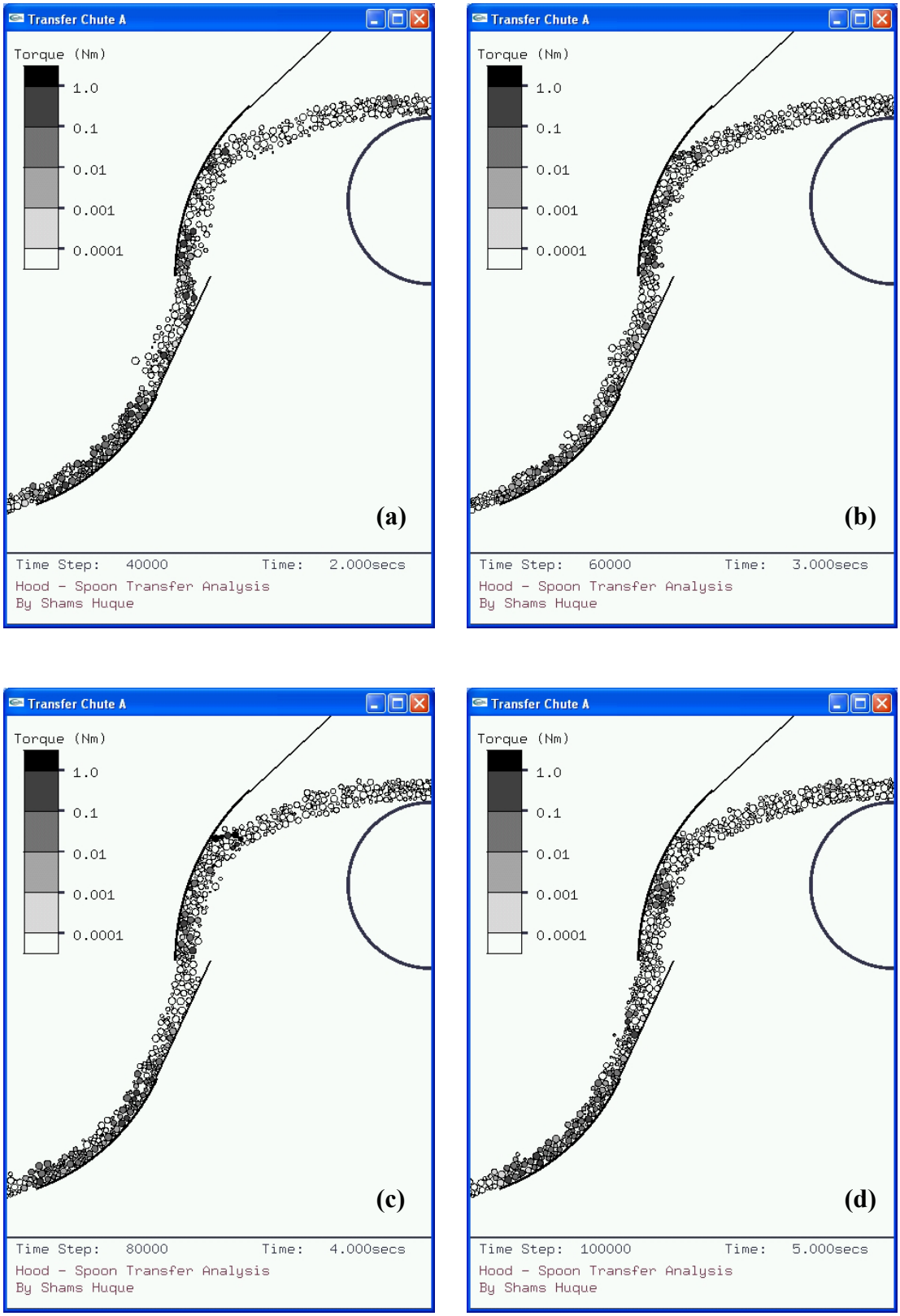

Figure 8.16 Screen captures that show the torques possessed by the particles for the first transfer system at times of **(a)** $t = 2.0$ s, **(b)** $t = 3.0$ s, **(c)** $t = 4.0$ s, and **(d)** $t = 5.0$ s.

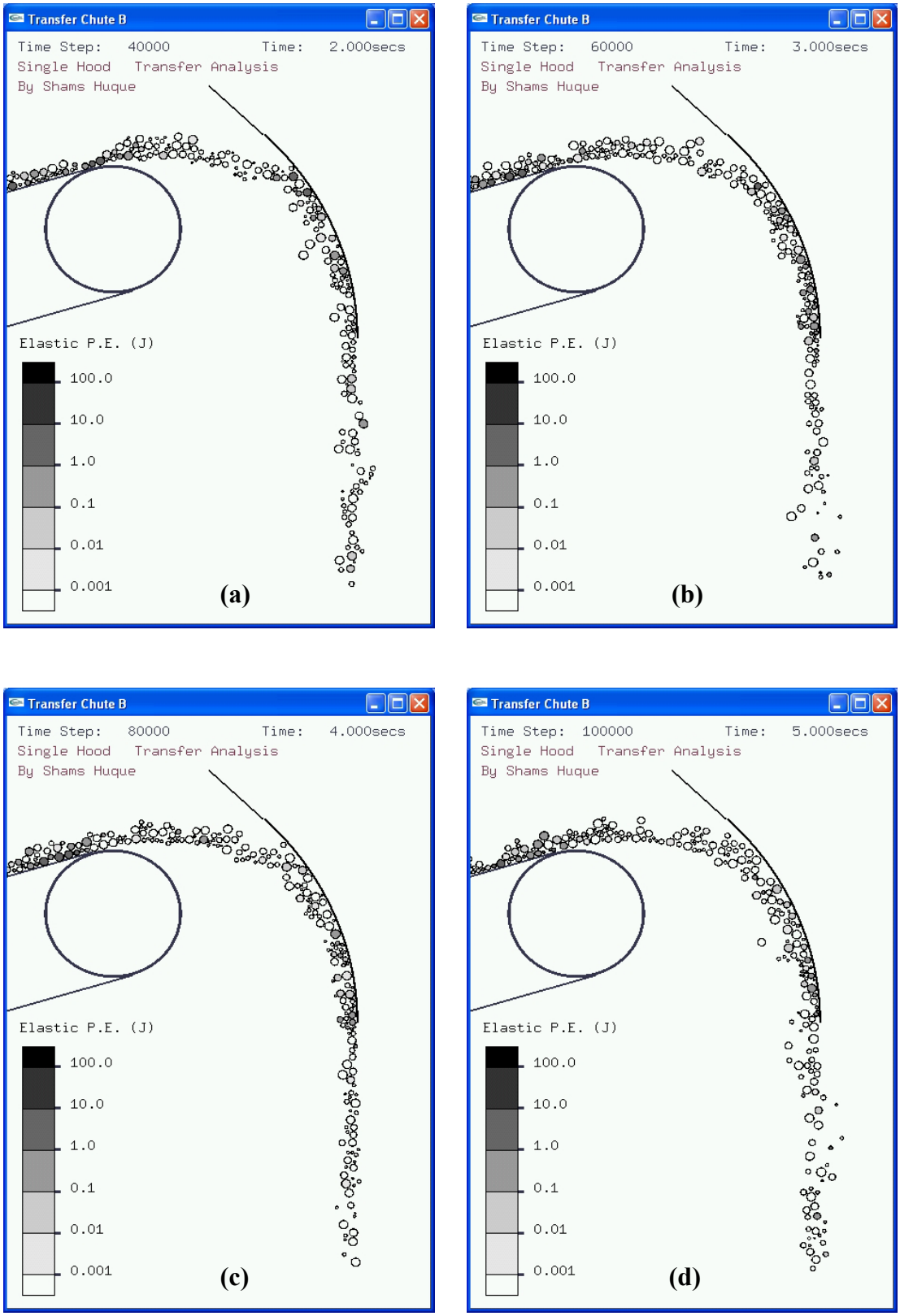

Figure 8.17 Screen captures that show the elastic potential energy (or strain energy) possessed by the particles for the second transfer system at times of **(a)** $t = 2.0$ s, **(b)** $t = 3.0$ s, **(c)** $t = 4.0$ s, and **(d)** $t = 5.0$ s.

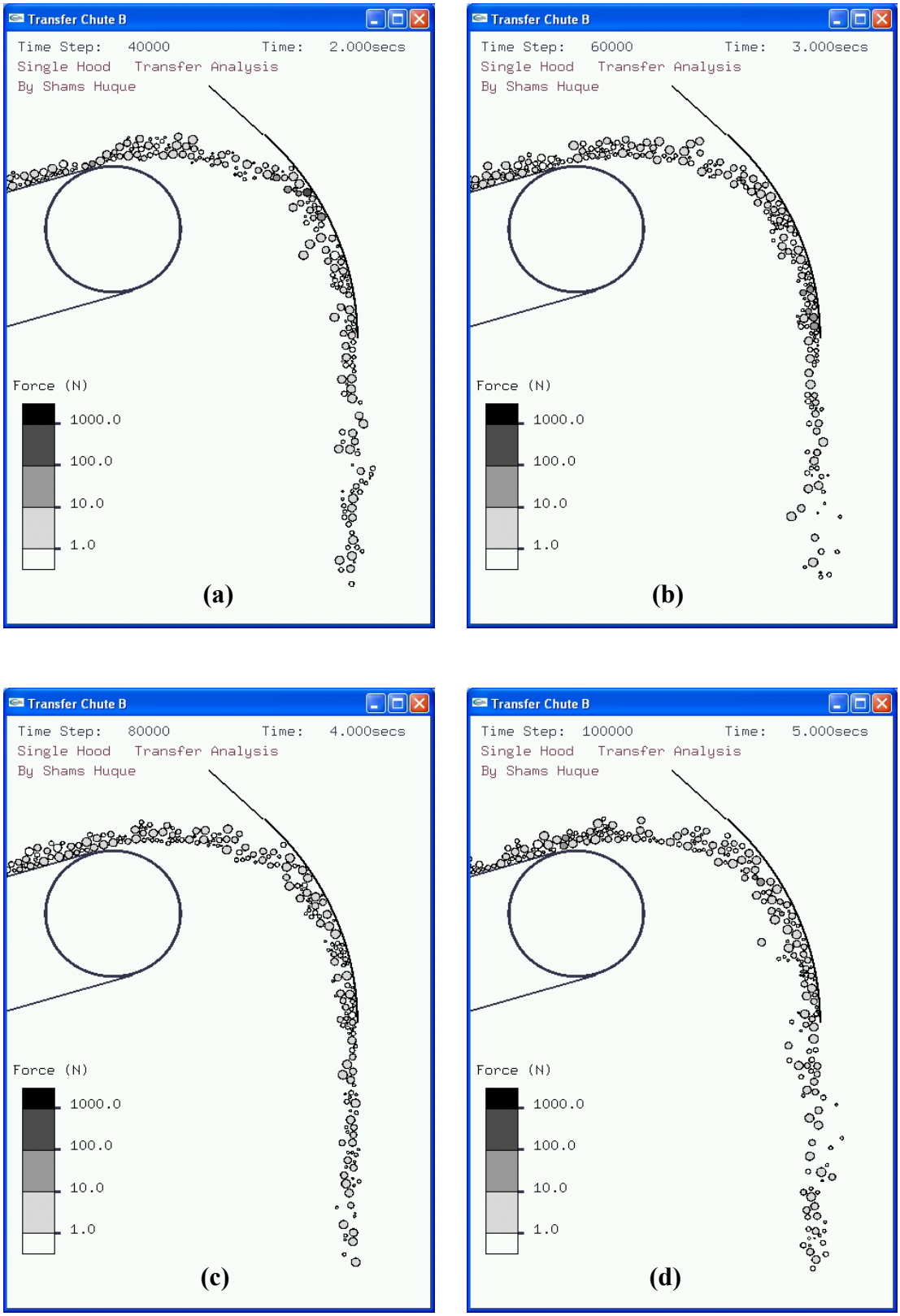

Figure 8.18 Screen captures that show the inter-particle forces (including gravity) possessed by the particles for the second transfer system at times of **(a)** $t = 2.0$ s, **(b)** $t = 3.0$ s, **(c)** $t = 4.0$ s, and **(d)** $t = 5.0$ s.

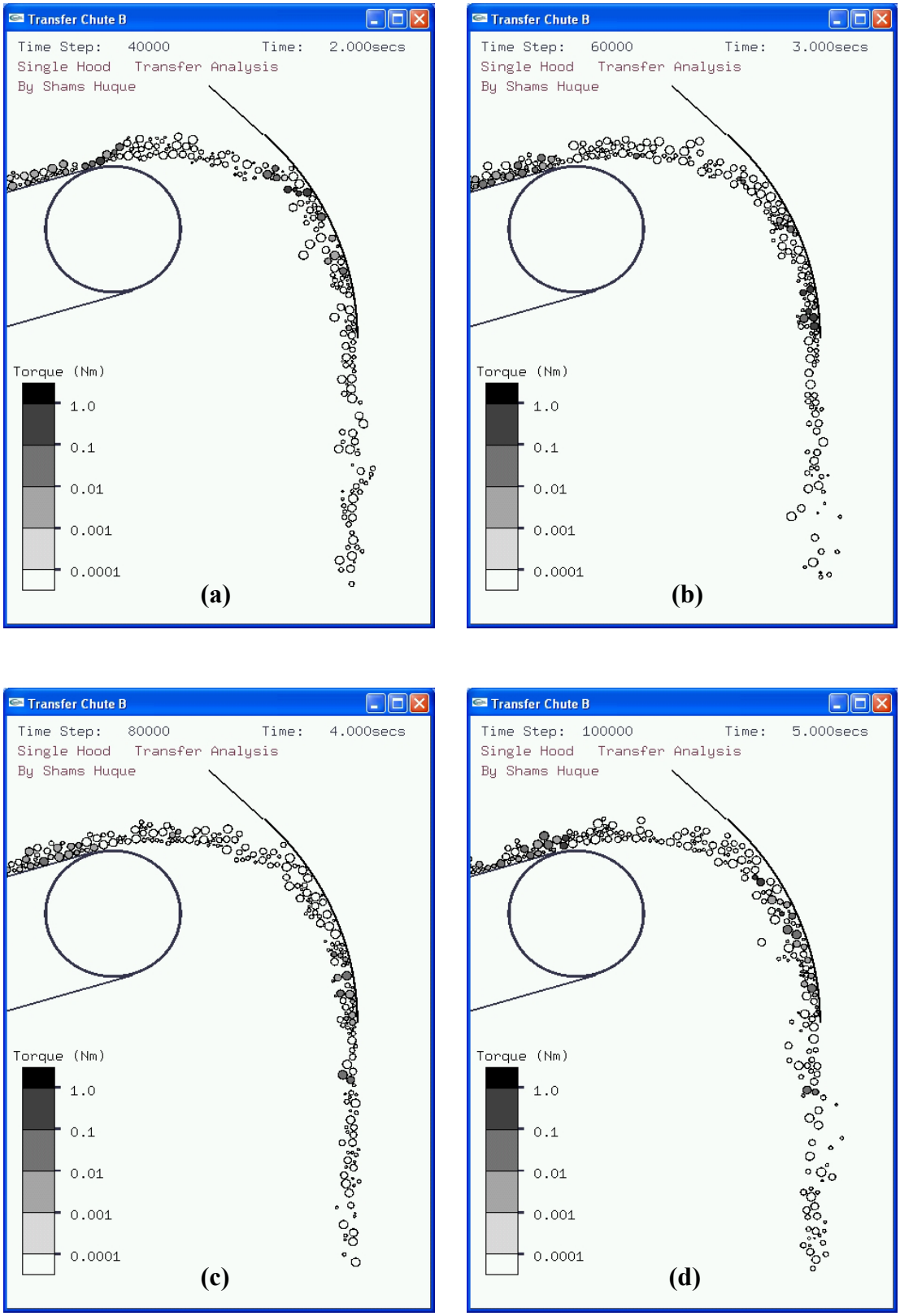

Figure 8.19 Screen captures that show the torques possessed by the particles for the second transfer system at times of **(a)** $t = 2.0$ s, **(b)** $t = 3.0$ s, **(c)** $t = 4.0$ s, and **(d)** $t = 5.0$ s.

magnitudes by many orders. This premise was also used for the elastic potential energy and torques resulting in base 10 logarithmic scales used for all the contours in this section.

8.5.1 Elastic Potential Energies

The concept of elastic potential energy was described in Chapter Six, and is fundamentally the energy stored in a particle from deformation. In the contours shown in Figure 8.14 and 8.17, the darker shades represent greater deformation, while the lighter shades represent little or no deformation. It can be seen that the greatest deformation occurs with particles in the regions of impact upon the hood and spoon, and also sliding with the band of particles adjacent to the chute walls and at the point of trajection and upon the belt having large deformations also. It is evident that the deformations in the particles lessen as we move outwards from the particle adjacent to the chute walls to the particles upon the flowing stream surface. Note that the deformations are not so pronounced for the second transfer case shown in Figure 8.17, as the material stream is not as thick and hence not tending to compress the particles as much as for the first transfer case illustrated in Figure 8.14.

8.5.2 Inter-Particle Forces

The reader will recall that the inter-particle force is composed of normal forces and tangential forces, and these forces and gravitational force concepts were described in Chapter Four. The inter-particle forces are also a function of the amount of deformation experienced by the particles. Figures 8.15 and 8.18 therefore show similar trends in the distribution of force magnitudes to that shown in the distribution of elastic potential energy in Figures 8.14 and 8.17, with particles in regions of impact generally showing greater forces, while the particles sliding adjacent to the curved portions of the hood and spoon also experiencing notable forces. The contour colouring again uses darker shades to represent greater magnitudes. Overall however it is difficult to extract useful information, particularly for the second transfer shown in Figure 8.18, as the localisation of forces is less apparent.

8.5.3 Particulate Torques

By omitting the normal force and gravitational force components of the inter-particle force, and decomposing the tangential component using Eq. (4.53) in Chapter Four, the particulate torques can be examined. Hence further insight can be gained into the flow of material around the chute elements, particularly with respect to the issue of internal shear. Figures 8.16 and 8.19 illustrate screen captures depicting the torques experienced by particles for the first and second transfers respectively. The captures show that in addition to the localised torque magnitudes, areas of greater torque (and therefore greater shear) experienced by the particles are in the regions of sliding flow, particularly in the curved portion of the spoon in Figure 8.16, where most particles are experiencing a degree of tangential interaction from neighbouring particles. This can partly be attributed to the fact that there is a higher coefficient of friction between particles than that for particle-wall interactions, hence the amount of particulate rotation allowable is greater and torques can be more pronounced. In this region, the weight of particles upon one another creates overlap effects that result in greater normal force, and hence raises the Coulomb friction limit. This concept is replicated to a lesser degree in the flow of material around the hood for both transfers. The particles also experience significant torques at the impact points of the particulate stream with hood and spoon. These observations, along with those gained from investigating the elastic potential energies and inter-particle forces support the notion of differing flowing regimes within the material stream.

8.6 Future Areas of Consideration

There are a number of additional areas to consider when examining transfer chutes. These aspects are beyond the scope of this thesis however are possible future directions for the current work and thus do merit a few brief remarks. Some of these issues are clarified further in Chapter Nine.

8.6.1 Wear upon Chute and Conveyor Belt

The issue of wear, on both the chute surfaces and also the receiving belt are major areas of interest. Quantifying such information in two dimensions is difficult, and hence shall not be explored here. For future DEM studies in three dimensions, the theory and computational processes detailed in the work of Hustrulid (1998) and Qiu & Kruse (1997a) can be used to examine wear issues. Although aspects of wear were unable to be measure in the present research, the velocity distributions summarised before implicitly convey information regarding areas of potential wear upon chute surfaces. The examination of wear has been extensively researched employing non-DEM means and particular references are detailed in Chapter Three.

8.6.2 Induced and Entrained Air Flow

The pressures and velocities of the air flow throughout the transfer process directly contribute to material loss and pollution, as detailed in the work of Huque et al. (2004). Quantifying such information allows an engineer to examine potential pollution effects in the transfer of materials, and therefore identify the best means of containing or reducing dust. The coupling of DEM and Computational Fluid Dynamics (CFD) is the only way to produce computer simulations capable of providing such information, and an increasing number of studies are utilising such numerical modelling techniques, such as the work of Xu (1997) and Xu & Yu (1997) in the area of gas-solid flows in fluidised beds.

8.6.3 Material Degradation

The issue of material degradation is of great importance in many conveying operations. Certainly for say crushing processes this is the chief purpose, however often the degradation of material is not desired. Examination of the force distributions in a simulation is one method of quantitatively observing the potential for degradation. In the present research the inter-particle forces were examined, and provide a means of identifying prospective degradation of materials. However, a much better representation of latent comminution is possible if particle breakage mechanics can be incorporated into the DEM model. Such models have been developed by Kruse (2000, 2003) for

simulations of gyration crushers. By modelling particle breakage, chute geometries promoting or reducing degradation could be identified with greater ease.

8.6.4 Chute Support Structure and Receiving Belt Aspects

Highly cohesive and dense materials can create very strong impact forces upon chute systems, and the supporting structure needs to be chosen to be able to withstand these forces at a minimum of cost. As the forces acting on the chute walls can be obtained from DEM, using force equilibrium processes the optimal placement of support structure elements and appropriate sizes can be determined. An examination of the forces acting upon the chute structure during material transfer has been investigated by Arnold and Hill (1991b) using experimental techniques. Another area of concern in industry is tracking of the conveyor belt. Mistracking occurs when the lateral force of the material impacting the belt overcomes the naturally tendency of the belt to stay within the troughing region set by the idler system. Mistracking also occurs when the belt has not been centrally loaded, with the material centre of mass skewed to one side rather than lying midway between the edges of the belt. These issues were investigated by Hustrulid (1998) in his three-dimensional transfer station analyses.

8.7 Summary

Two chutes designed by The Gulf Group using the EasyFlow^{TM} transfer technology were examined. DEM was used to model the particulate flow through the chutes and screen captures of the simulations were presented for qualitative analysis. It was found that the curved chute elements maintain speed through the transfer very well for both chutes with minor stagnations occurring only around the impact zones.

Quantitative data captures at select times were also presented and for the first time in literature conventional analytical methods were also utilised to predict the velocity at each point of the particulate flow through the chutes. The comparison between the optimal analytical methods and the quantitative DEM data revealed that generally the flowing characteristics were similar, however closer scrutiny revealed lesser defined

regions of flow in the DEM simulations which could be attributed to the specific dynamic characteristics of individual particles in the DEM. The analytical methods on the other hand treated the stream as motion of a single element of mass and therefore could not model many of the idiosyncrasies arising from the DEM simulations.

To investigate this issue, for the first time in literature a study of the different regions of flow in a conveyor transfer was conducted by examining the micro dynamics, with the primary finding that particles behave differently according to their location within the particulate stream. The elastic potential energy was examined to see where the greatest deformations occurred, and the inter-particle forces (including gravity) were examined but did not reveal information as expected due to the low localisation of forces. On the other hand, the torques experienced by each particle revealed that regions of primary shear are experienced by the particles at impact points and around the curved portions of the chute elements. It was also observed that the particles experienced greater magnitudes of the elastic potential energy, inter-particle forces (including gravity) and torques at similar regions in the transfer.

Chapter Nine

CONCLUSIONS AND FUTURE WORK

9.1 Application of DEM in Industry

Chapter Four illustrated the increasing use of DEM to analyse multi-body systems in a variety of industrial areas, however there are still difficulties regarding computation times, even when using high-end computers. Experience has shown that the time to compile programs containing up to one million particles can sometimes take a number of weeks (Cleary, P. 2002, pers. comm., 22 July). Taking into account the allocation of resources (initialising calculation space and material parameters, personnel involvement, computing time), the final cost of producing one simulation can be very high. Any corrective measures are difficult to implement in a program once it has started compiling, and the usual course of action is to stop the process, make the changes, and then start compiling once again. Such a process is expensive for the company that is utilising the DEM product, and the author's work experience has shown that the time scales involved are not acceptable to industries, such as coal collieries.

Currently the costs of purchasing DEM software is exorbitant to many engineering companies who work in the area of mining, particularly smaller companies, or those who are not subsidised with research grants or other forms of sponsorship. The cost effectiveness of such products is evidenced by the relatively few numbers of technical and commercial papers published that illustrate applications of DEM to belt conveyor transfer points, an area well known to be very important in a materials handling system. As computer power increases however, the costs of DEM will become less and it is foreseeable that DEM will become a very powerful tool in the near future.

9.2 Remarks on Current DEM Work

The current work has shown that simulating particulate flow through transfer chutes in what was essentially a two-dimensional environment has its advantages, but also has its

flaws and limitations. The main advantage is obviously the greatly reduced compilation time compared to full three-dimensional systems, along with a smaller amount of work to initialise each transfer simulation, such as developing or reading boundary data. The primary drawback however is that the simulations were idealised to some extent and can only analyse systems that are subject to certain conditions, with factors such as differing particle shapes not accounted for. An area of weakness is that in the existing chutes in operation, the three dimensional boundary surfaces of the chute play an important role in characterising the material flow, particularly since the hood outer walls are convergent in nature for the first transfer. The current work cannot cater for the outer wall and increased inter-particle interactions. Three-dimensional DEM investigations into straight inclined chute flows, for example the work of Hanes & Walton (2000), have shown differing velocity regimes between the flowing particles in the centre of the flow and the particles adjacent to side walls. Additionally, the first transfer examined is an angled transfer of 90 degrees which was simplified to an inline (or non-angled) system using the reasoning in Chapter Seven. Angled transfers have further nuances in the particulate interactions such as non-uniform spoon entry velocities in the material footprint which could not be examined in the current work.

The reduced time factor for the current (two-dimensional) research would presently translate to monetary benefits for an industrial facility, however as computer power increases, this advantage decreases, and the development and application of three-dimensional simulations will become attractive. The research in the thesis is best viewed as the basis for future projects, with one of the aims being to provide a computer coding base from which expansions could be facilitated without requiring the need for a complete overhaul of the coding structure. Therefore the individual file structure within the FORTRAN coding reflected this with each area of the DEM formulation allocated separate files. Thus the fundamentals developed here for contact detection, time step selection, and force-displacement models only requires modification to a certain degree to advance the work, to say three-dimensions. Many of the idiosyncrasies and details pertinent to DEM modelling were also identified, particularly those with regards to the initialisation of the transfer chute simulations in Chapter Seven, ensuring similar debugging errors and system set up could potentially be solved/completed more rapidly in future. Additionally, the animation coding requires little advancement with the current set up allowing for three dimensional visualisations with minimal coding

changes, provided the input data files are in the same format. Within all of these areas however improvements could be made and these aspects shall now be described.

9.3 Conclusions

The transfer point is a critical component of any conveyor system, with the design of the complete chute system being of great importance. The initial portion of the project presented for the first time in literature a comprehensive overview of all of the available analytical methods available to design chute system components. Detailed comparisons and analyses of the most common analytical design methods, and recommendations for which method to use were established. Areas of further study were also identified, and it was found that most areas apart from the prediction of initial trajectory prediction were lacking in design methods. Those few design methods that are available such as for the impact plate in the upper section of the transfer, or for a gravity flow chute as can be used in the lower portion of a transfer, had design techniques that were lengthy and often difficult to implement.

The second portion of the research detailed the development of a computer code that utilises the Distinct Element Method (DEM) to simulate three-dimensional particles flowing in a two-dimensional environment. A background into DEM and its use in the area of conveyor transfers was presented, and the areas of research that were lacking in quantitative and qualitative analyses were identified. The DEM mathematical formulation was described such as the definitions of particles and boundaries, with common force-displacement models reviewed. The numerical methods such as the development of a contact detection scheme based upon work developed by Walsh (2004) and selection of the critical time step were also detailed. The coding of a pre-processor to facilitate the generation of the parameter data file and post-processor allowing animations of DEM particulate material were presented. Comprehensive testing was conducted to assess the validity of the computer code. The tests employed included testing of single particle contacts, testing of multiple particle contacts, and stability checking via energy dissipation, all of which produced results that demonstrate successful operation of the DEM code.

The third portion of the work illustrated the application of DEM to simulate two separate transfers currently in operation in industry and examine flow characteristics. The chute systems were originally designed by The Gulf Group using their EasyFlow™ technology. Screen captures of the animations illustrated the advantages of curved chute elements in maintaining material momentum through the transfer. Quantitative DEM velocity data were also captured and compared to the velocities predicted by the optimal (and experimentally verified) analytical methods, revealing the DEM to produce velocity regimes close to those of the analytical techniques. DEM has the advantage however of providing data in areas of interest that otherwise are difficult to examine in detail, such as the mechanisms involved during the flowing stream impact process with a chute element. DEM also identified that there are differing magnitudes of contact during the flow through a chute, something that the analytical methods cannot provide. The analytical methods however have the advantage of providing much faster solutions and are good for chute designs for free flowing material transfers.

The deficiencies of the current DEM simulations were primarily related to the nature of the two-dimensional system involved which limited the amount of information that could be extracted. These include among others: gross approximations for chute geometry for angled transfers, the lack of recognition for the three dimensional nature of the hood and spoon wall profiles, and the lack of conveyor belt transition effects in the material trajectory. Further insight into particulate flows is expected when the calculation domain is expanded to three-dimensions and the developments outlined earlier are implemented, thus with a great potential to solve transfer problems. The analytical methods on the other hand are not obsolete by any means, and provided time and care are taken to implement the design processes, chutes transferring free flowing materials can be designed with a high degree of success.

9.4 Future Work

The areas of future work for the research could be classified in two distinct areas: (1) further developing the analytical design techniques, and (2) further development of the DEM work. The deficiencies of the analytical techniques were described thoroughly in

Chapter Three, with three of the major shortcomings as follows. The first is the issue of design methods that are too lengthy and complicated for implementation, or at the other extreme of being too short and basic. Secondly, if two differing methods are used in sequence to design separate chute components (say graphical and analytical) problems can arise when using graphical output as analytical input and vice-versa. Thirdly, almost all analyses only considering free flowing materials, with cohesive materials not catered for. The aim when developing analytical methods for the future is to resolve these issues whilst also creating a method that would be desirable for industry personnel. Currently The Gulf Group has overcome many of these drawbacks via the use of their extensive database of chute designs and empirical data, however must resort to first principles and experience once again when designing a new chute.

The second area of consideration for future work is the advancement and expansion of the DEM and can be further broken down into two areas: (A) development of the computer code and DEM concepts to optimise the computing time and allow ease of use, and (B) development of the computer code and DEM concepts to a level allowing more realistic depiction of particulate flow through conveyor transfers. Considering the first statement (A), the major drawback currently is the time consumed when compiling a simulation and one method to reduce this is to optimise the contact detection scheme used. The current work utilised spheres in one plane and therefore the zone structured method using the upwind neighbour search outlined in Chapter Five was satisfactory. Future expansions to three-dimensions however would require a more efficient contact detection scheme, depending upon the particle shapes used and increased number of surfaces. An optimised contact detection method is mandatory to reduce computation times in complicated systems.

A more realistic portrayal of particulate flow through conveyor transfers using DEM could be achieved in a number of ways. Modelling cohesive and adhesive forces for particle-particle and particle-boundary contacts respectively will be advantageous, thus allowing wet or sticky materials to be modelled. Currently the work is limited to free flowing bulk commodities such as dry coal, and incorporation of such a feature would allow simulation of materials such as limestone to a certain degree. This modelling however must determine the relationship between these forces and real materials.

Currently the use of non-spherical particles is highly computational resource intensive, hence one way to model non-spherical particles is to create clusters of spheres. Variances in individual bulk material shapes during commodity conveying could be simulated to a degree by bonding spheres together to create approximations of non-round shapes, and hence also allowing breakage effects to be modelled. However, the computing resources required are still a drawback to its implementation. Continuum mechanics would allow the examination of air flows and entrainment issues and would be a useful too if coupled with DEM, as has been done in the area of gas-fluidised beds (Xu 1997, Xu & Yu 1997, Xu et al. 2000, 2001).

For the two-dimensional system in the current work, arcs were used to model curved surfaces. For three-dimensional transfer analyses such as those conducted by Qiu & Kruse (1997a, 1997b), curved surfaces were approximated by using many smaller triangular shapes. True curved surfaces would be ideal, though currently the numerical complexity and thus computational power are a hindrance, but it is an area for future thought. The current work could be advanced by incorporating equations to model ellipse and spline shapes, although the benefits would be little when compared to the major advantages gained by expanding the system environment to three-dimensions.

The pre- and post-processing stages of the DEM simulations could also be improved. One area of improvement is incorporating a module that allows physical boundaries to be generated directly from CAD drawings in the pre-processor. Such a feature would read DXF™ (Drawing Interchange File) files and negate the need for the current spreadsheet linkage. A substantial portion of the DEM initialisation time would be saved. In current DEM transfer chute applications for example, Dewicki (2003) and Dewicki & Mustoe (2002) utilise 3-D CAD to represent the chute boundary elements. The GUI for the post-processing stage is hindered by intricacies with regards to correctly animating the DEM data, some details of which were described in Chapter Seven. Part of this could be attributed to the code developed which was continually built upon as time progressed, and therefore may be inefficient. The GUI could be re-written to create a simpler, more flexible and robust user interface.

Once the DEM model has been further developed into three-dimensions, experimental work could provide the foundation for a series of material transfer studies. If the

simulation methods can reliably reproduce the bulk and surface measurements obtained from conventional experiments, it follows that the information within the flow domain obtained from the simulations will also be reliable (Vu-Quoc et al. 2000). Hence, a combined experimental/numerical approach is ideal.

Chapter Ten

REFERENCES AND BIBLIOGRAPHY

10.1 References

Allen, M. P. & Tildesley, D. J. 1987, *Computer Simulation of Liquids*, Oxford University Press, New York.

Alspaugh, M., Dewicki, G. & Quesenberry, E. 2002, *Computer Simulation Solves Conveyor Problems* [Online, Accessed 27 Mar. 2003].
URL: http://www.coalage.com/ar/coal_computer_simulation_solves/

Arnold, P. C. & Hill, G. L. 1989, 'Predicting the discharge trajectory from belt conveyors', *Third International Conference on Bulk Materials, Storage, Handling and Transportation*, Institution of Engineers Australia, Newcastle, Australia, pp. 131-135.

Arnold, P. C. & Hill, G. L. 1990a, 'Feeding coal to and from belt conveyors', *International Coal Engineering Conference*, Institution of Engineers Australia, Sydney, Australia, pp. 47-54.

Arnold, P. C. & Hill, G. L. 1990b, 'Predicting the discharge trajectory from belt conveyors', *Bulk Solids Handling*, vol. 10, no. 4, pp. 379-382.

Arnold, P. C. & Hill, G. L. 1991a, 'Conveyor transfer chute performance and design', *Paper for Presentation at 'Bulk 2000'*, Institute of Mechanical Engineers, London, U.K., pp. 157-165.

Arnold, P. C. & Hill, G. L. 1991b, 'Design of conveyor chutes with special attention to blockage, wear and conveyor direction change', *End of Contract Report, NERDDP Project No. 1188*, 123 pages.

Arnold, P. C. & Hill, G. L. 1991c, 'Predicting the discharge trajectory from belt conveyors', *Bionic Conference*, Johannesburg, South Africa.

Arnold, P. C. 1993, 'Transfer chutes engineered for reliable performance', *National Bulk Materials Handling Conference*, Institution of Engineers Australia, Yeppon, Australia, pp. 165-173.

Asmar, B. N., Langston, P. A., Matchett, A. J. & Walters, J. K. 2002, 'Validation tests on a distinct element model of vibrating cohesive particle systems', *Computers and Chemical Engineering*, vol. 26, no. 6, pp. 785-802.

Augenstein, D. A. & Hogg, R. 1978, 'An experimental study of the flow of dry powders over inclined surfaces', *Powder Technology*, vol. 19, pp. 205-215.

Bardet, J. P. 1998, 'Introduction to computational granular mechanics', in *Behaviour of Granular Materials*, (ed.) B. Cambou, CISM, Italy, 1998, pp. 99-169.

Barker, G. C. 1994, 'Computer simulations of granular materials', in A. Mehta, ed., *Granular Matter: An Interdisciplinary Approach*, Springer-Verlag, NY, pp. 35-83.

Barr, A. 1981, 'Superquadrics and angle-preserving transformations', *IEEE Computer Graphics and Applications*, vol. 1, pp. 11-23.

Belytschko, T., Yen, H.-J. & Mullen, R. 1979, 'Mixed methods for time integration', *Computer Methods in Applied Mechanics and Engineering*, vol. 17/18, pp. 259-275.

Benjamin, C. W. 1999, 'Rapid design approach to the zero-spillage transfer chute', *Australian Bulk Handling Review*, June/July, pp. 52-58.

Benjamin, C. W., Burleigh, A. C. & Nemeth, J. 1999a, 'Transfer chute design', *Bulkex '99, Bulk Materials Handling Conference*, Sydney, Australia, pp. 8.1-8.9.

Benjamin, C. W., Burleigh, A. C. & Nemeth, J. 1999b, 'Transfer chute design – a new approach using 3D parametric modelling', *Bulk Solids Handling*, vol. 19, no. 1, pp. 29-33.

Benjamin, C. W. 2001, 'The use of parametric modelling to design transfer chutes and other key components', *BELTCON 11: International Materials Handling Conference*, Johannesburg, South Africa.

Benjamin, C. W. & Nemeth, J. 2001, 'Transfer chute design for modern materials handling operations', *Bulk Solids Handling*, vol. 21, no. 1, pp. 31-34.

BFGoodrich Engineering Handbook: Conveyor and Elevator Belting, 6th edition, BF Goodrich Company.

Bingham, E. C. & Wikoff, R. W. 1931, 'The flow of dry sand through capillary tubes', *Journal of Rheology*, vol. 2, no. 4, pp. 395-400.

Binzon, W. 1985, 'The integrated approach to dust collection', *Bulk Solids Handling*, vol. 5, no. 4, pp. 859-864.

Booth, E. P. O. 1934, 'Trajectories from conveyors – method of calculating them corrected', *Engineering and Mining Journal*, vol. 135, no. 12, pp. 552-554.

BTR Conveyor Belt Manual, BTR Belting Limited.

Burnett, A. J. 2000a, 'Chutes for stacker reclaimers', *Bulk Solids Handling*, vol. 20, no. 3, pp. 295-301.

Burnett, A. J. 2000b, 'Chutes for stacker reclaimers – generation of a design method', *From Powder to Bulk: International Conference on Powder and Bulk Solids Handling*, ImechE Headquarters, London, UK, pp. 463-476.

Campbell, C. S. 1990, 'Rapid granular flows', *Annual Review of Fluid Mechanics*, vol. 22, pp. 57-92.

Campbell, C. S. & Brennen, C. E. 1985, 'Chute flows of granular material: some computer simulations', *Journal of Applied Mechanics, Transactions of the ASME*, vol. 52, pp. 172-178.

C.E.M.A. – Belt Conveyors for Bulk Materials, 1997, 5th edition, Conveyor Equipment Manufacturers Association, pp. 49-51, 326-342.

Charlton, W. H. & Roberts, A. W. 1970, 'Chute profile for maximum exit velocity in gravity flow of granular material', *Journal of Agricultural Engineering Research*, vol. 15, pp. 292-294.

Charlton, W. H., Chiarella, C. & Roberts, A. W. 1975, 'Gravity flow of granular materials in chutes: optimizing flow properties', *Journal of Agricultural Engineering Research*, vol. 20, pp. 39-45.

Chiarella, C. & Charlton, W. H. 1972, 'Chute profile for minimum transit time in gravity flow of granular material', *Journal of Agricultural Engineering Research*, vol. 17, pp. 149-153.

Chiarella, C., Charlton, W. H. & Roberts, A. W. 1974a, 'Gravity flow of granular materials: chute profiles for minimum transit time' *Paper presented at Symposium on 'Solids and Slurry Flow and Handling in Chemical Process Industries', AIChE, 77th National Meeting*, Pittsburgh, USA, 13 p.

Chiarella, C., Charlton, W. & Roberts, A. W. 1974b, 'Optimum chute profiles in gravity flow of granular materials: a discrete segment solution method', *Transactions of the ASME, Journal of Engineering for Industry*, paper no. 73-MH-A.

Choda, A. 1965, 'Gravity flow of noncohesive granular materials through restricted passages', Unpublished M E thesis, The University of New South Wales, Australia, School of Mechanical Engineering.

Choda, A. & Willis, A. H. 1967, 'Flow regimes in inclined ducts', *Transactions of the ASAE*, vol. 10, no. 1, pp. 136-138.

Cleary, P. W. & Sawley, M. L. 1999, 'Three-dimensional modelling of industrial granular flows', *Proceedings of the Second International Conference on CFD in the Minerals and Process Industries*, CSIRO, Melbourne, Australia, pp. 95-100.

Cleary, P. W. 1998a, 'Discrete element modeling of industrial granular flow applications', *TASK Quarterly – Scientific Bulletin,* vol. 2, no. 3, pp. 385-415.

Cleary, P. W. 1998b, 'The filling of dragline buckets', *Mathematical Engineering in Industry*, vol. 7, no. 1, pp. 1-24.

Cleary, P. W. 2000, 'DEM simulation of industrial particle flows: case studies of dragline excavators, mixing in tumblers and centrifugal mills', *Powder Technology*, vol. 109, no. 1, pp. 83-104.

Cleary, P. W. & Hoyer, D. 2000, 'Centrifugal mill charge motion and power draw: comparison of DEM predictions with experiment', *International Journal of Mineral Processing*, vol. 59, no. 2, pp. 131-148.

Cleary, P. W. 2001, 'Modelling comminution devices using DEM', *International Journal for Numerical and Analytical Methods in Geomechanics*, vol. 25, no. 1, pp. 83-105.

Cleary, P. W., Laurent, B. & Bridgewater, J. 2002, 'DEM prediction of flow patterns and mixing rates in a ploughshare mixer', *World Congress on Particle Technology 4*, Sydney, Australia.

Colijn, H. & Conners, P. J. 1972, 'Belt conveyor transfer points', *Transactions of the AIME*, vol. 252, pp. 204-210.

Cook, B. K. & Jensen, R. P. (eds.) 2002, *Geotechnical Special Publication No. 117, Discrete Element Methods: Numerical Modeling of Discontinua, Proceedings of the Third International Conference, Santa Fe, New Mexico*, American Society of Civil Engineers, Virginia, USA.

Cooper, P. & Arnold, P. C. 1995, 'Air entrainment and dust generation from a falling stream of bulk material', *KONA Powder and Particle*, no. 13, pp. 125-134.

Cundall, P. A. 1971, 'A computer model for simulating progressive, large-scale movements in blocky rock systems', *Proceedings Symposium International Society Rock Mechanics*, Nancy, vol. 2, no. 8.

Cundall, P. A. & Strack, O. D. L. 1979, 'A discrete numerical model for granular assemblies', *Geotechnique*, vol. 29, pp. 47-65.

Dewicki, G. 2003, 'Bulk material handling and processing – numerical techniques and simulation of granular material', *Bulk Solids Handling*, vol. 23, no. 2, pp. 1-4.

Dewicki, G. & Mustoe G. 2002, 'Bulk material belt conveyor transfer point simulation of material flow using DEM', *Proceedings of the Third International Conference on DEMs*, Santa Fe, New Mexico, pp. 1-11.

Di Renzo, A. & Di Maio, F. P. 2004, 'Comparison of contact force models for the simulation of collisions in DEM-based granular flow codes', *Chemical Engineering Science*, vol. 59, pp. 525-541.

Drake, T. G. & Walton, O. R. 1995, 'Comparison of experimental and simulated grain flows', *Transactions of the ASME, Journal of Applied Mechanics*, vol. 62, no. 1, pp. 131-135.

Dunlop Rubber Co., 1982, *Dunlop Conveyor Manual*, Dunlop Industrial Handbook, pp. 9.1-9.5.

'Dust control at conveyor transfer points', *Quarry Management*, vol. 20, no. 11, 1993, pp. 27-28.

Els, D. N. J. 2003, 'Force reductions in vibrated forced granular flows', *Unpublished PhD Thesis*, University of Stellenbosch, Matieland, South Africa.

Fincham, D. & Ralston, B. J. 1981, 'Molecular dynamics simulation using the CRAY-1 vector processing computer', *Computer Physics Communications*, vol. 23, pp. 127-134.

Firstbrook, J. 1983, 'Preferred design of transfer points', *Colliery Guardian*, pp. 263-272.

Gear, C. W. 1971, *Numerical Initial Value Problems in Ordinary Differential Equations*, Prentice-Hall, Englewood Cliffs, New Jersey.

Gibor, M. 1997, 'Dust collection as applied to the mining and allied industry', *Bulk Solids Handling*, vol. 17, no. 3, pp. 397-403.

Goldbeck, L. J. & Marti, A. D. 1996, 'Dust control at conveyor transfer points: containment, suppression and collection', *Bulk Solids Handling*, vol. 16, no. 3, pp. 367-372.

Goldbeck, L. J. 1996, 'Improving conveyor efficiency by controlling fugitive material', *Proceedings of the 58th American Power Conference*, Illinois Institute of Technology, Chicago, Illinois, pp. 1204-1208.

Golka, K. 1992, 'Discharge trajectories of bulk solids', *International Conference on Bulk Materials Handling and Transportation, Symposium on Freight Pipelines*, Wollongong, Australia, pp. 497- 503.

Golka, K. 1993a, 'Prediction of the discharge trajectories of bulk materials', *Bulk Solids Handling*, vol. 13, no. 4, pp. 763-766.

Golka, K. 1993b, 'The dynamics of a physical body over a circular path', *National Bulk Materials Handling Conference*, Institution of Engineers Australia, Yeppon, Australia, pp. 105-108.

Goodyear Handbook of Conveyor and Elevator Belting Section 11: Trajectory of Material Discharged over Conveyor Head Pulley, 1976.

Goudreau, G. L. & Taylor, R. L. 1972, 'Evaluation of numerical integration methods in elastodynamics', *Computer Methods in Applied Mechanics and Engineering*, vol. 2, pp. 69-97.

Haff, P. K. & Werner, B. T. 1986, 'Computer simulation of the mechanical sorting of grains', *Powder Technology*, vol. 48, no. 3, pp. 239-245.

Hanes, D. M. & Walton, O. R. 2000, 'Simulations and physical measurements of glass spheres flowing down a bumpy incline', *Powder Technology*, vol. 109, no. 1, pp. 133-144.

Hemeon, W. C. L. 1962, *Plant and Process Ventilation*, 2nd edition, The Industrial Press, NY.

Hilber, H. M. & Hughes, T. J. R. 1978, 'Collocation, dissipation and 'overshoot' for time integration schemes in structural dynamics', *Earthquake Engineering and Structural Dynamics*, vol. 6, no. 1, pp. 99-117.

Hilber, H. M., Hughes, T. J. R. & Taylor, R. L. 1977, 'Improved numerical dissipation for time integration algorithms in structural dynamics', *Earthquake Engineering and Structural Dynamics*, vol. 5, no. 3, pp. 283-292.

Hogue, C. 1998, 'Shape representation and contact detection for discrete element simulations of arbitrary geometries', *Engineering Computations*, vol. 15, no. 3, pp.374-390.

Hogue, C. & Newland, D. 1994, 'Efficient computer simulation of moving granular particles', *Powder Technology*, vol. 78, pp. 51-66.

Hoffman, J. D. 1992, *Numerical Methods for Engineers and Scientists*, McGraw Hill USA.

Hoomans, B. P. B., Kuipers, J. A. M., Briels, W. J. & Van Swaaij, W. P. M. 1996, 'Discrete particle simulations of bubble and slug formation in a two-dimensional gas-fluidised bed: a hard sphere approach', *Chemical Engineering Science*, vol. 51, no. 1, pp. 99-118.

Hughes, T. J. R. & Liu, W. K. 1978, 'Implicit-explicit finite elements in transient analysis: stability theory', *Transactions of the ASME: Journal of Applied Mechanics*, vol. 45, pp. 371-374.

Hulbert, G. M. 1992, 'Explicit momentum conserving algorithms for rigid body dynamics', *Computers & Structures*, vol. 44, no. 6, pp. 1291-1303.

Huque, S. T., Robertson, M., Nemeth, J. & Bryant, P. 2004, 'An introduction to Gulf – Clean Air Technology (G - CAT)', *Eighth International Conference on Bulk Materials, Storage, Handling and Transportation*, Institution of Engineers Australia, Wollongong, Australia, 2004.

Hustrulid, A. I. 1998, 'Transfer station analysis', *Bulk Material Handling by Conveyor Belt II, SME Annual Meeting + Exhibit*, Orlando, Florida.

Hustrulid, A. I. & Mustoe, G. G. W. 1996, 'Engineering analysis of transfer points using discrete element analysis', *Bulk Material Handling by Conveyor Belt*, SME.

Jensen, R. P., Bosscher, P. J., Plesha, M. E. & Edil, T. B. 1999, 'DEM simulation of granular media-structure interface: effects of surface roughness and particle shape', *International Journal for Numerical and Analytical Methods in Geomechanics*, vol. 23, pp. 531-547.

Johnson, K. L. 1985, *Contact Mechanics*, Cambridge University Press, Cambridge.

Komodromos, P. I. & Williams, J. R. 2002, 'Utilization of Java and Database Technology in the Development of a Combined Discrete and Finite Element Multibody Dynamics Simulator', *Proceedings of the Third International Conference on DEMs*, Santa Fe, New Mexico, pp. 118-124.

Korzen, Z. 1980, 'Effect of deflector plates on the discharge of material transported on belt conveyors', *Aufbereitungs-Technik*, no. 11, pp. 552-557.

Korzen, Z. 1984a, 'Effects of pressure and flow originating from bulk materials on stationary chutes belonging to conveying systems', *Aufbereitungs-Technik* , no. 8, pp. 464-473.

Korzen, Z. 1984b, 'On the discharge process of belt conveyors', *f + h – fördern und heben*, vol. 34, no. 5, pp. 380-388.

Korzen, Z. 1986, 'Dynamic flow properties of bulk material on rotating impact drums of conveyor systems', *Aufbereitungs-Technik*, vol. 27, no. 9, pp. 512-522.

Korzen, Z. 1988, 'The dynamics of bulk solids flow on impact plates of belt conveyor systems', *Bulk Solids Handling*, vol. 8, no. 6, pp. 689-697.

Korzen, Z. 1989, 'Mechanics of belt conveyor discharge process as affected by air drag', *Bulk Solids Handling*, vol. 9, no. 3, pp. 289-297.

Kremmer, M. & Favier, J. F. 2001a, 'A method for representing boundaries in discrete element modelling – Part I: geometry and contact detection', *International Journal for Numerical Methods in Engineering*, vol. 51, pp. 1407-1421.

Kremmer, M. & Favier, J. F. 2001b, 'A method for representing boundaries in discrete element modelling – Part II: kinematics', *International Journal for Numerical Methods in Engineering*, vol. 51, pp. 1423-1436.

Kruse, D. J. 2000, 'Applications and advances of the discrete element method in the material handling industry', *Bulk Materials Handling by Conveyor Belt III*, SME Publication, pp.133-143.

Kruse, D. J., *Conveyor Belt Transfer Chute Modeling and other Applications using the Discrete Element Method in the Material Handling Industry* [Online, Accessed 31 Mar. 2003].
URL: http://www.ckit.co.za/Conveyor/Papers/Troughed/Conveyor/Conveyor.htm

Langston, P. A., Tüzün, U. & Heyes, D. M. 1994, 'Continuous potential discrete particle simulations of stress and velocity fields in hoppers: transition from fluid to granular flow', *Chemical Engineering Science*, vol. 49, no. 8, pp. 1259-1275.

Langston, P. A., Tüzün, U. & Heyes, D. M. 1995, 'Discrete element simulations of granular flow in 2D and 3D hoppers: dependence of discharge rate and wall stress on particle interactions', *Chemical Engineering Science*, vol. 50, no. 6, pp. 967-987.

Langston, P. A., Tüzün, U. & Heyes, D. M. 1996, 'Distinct element simulation of interstitial air effects in axially symmetric granular flows in hoppers', *Chemical Engineering Science*, vol. 51, no. 6, pp. 873-891.

Lesburg, L., Zhang, X., Vu-Quoc, L. & Walton, O. R. 1997, 'Simplified tangential force-displacement models for a discrete element particle flow code', *Powders & Grains 97*, eds. R. P. Behringer, & J. T. Jenkins, Balkema, Rotterdam, pp. 307-310.

Lin, X. & Ng, T. T. 1995, 'Contact detection algorithms for three-dimensional ellipsoids in discrete element modelling', *International Journal for Numerical and Analytical Methods in Geomechanics*, vol. 19, pp. 653-659.

Lin, X. & Ng, T. T. 1997, 'A three-dimensional discrete element model using arrays of ellipsoids', *Geotechnique*, vol. 47, no. 2, pp. 319-329.

Liu, Z., Wypych, P. & Cooper, P. 1999, 'Dust generation and air entrainment in bulk materials handling – a review', *Powder Handling & Processing*, vol. 11, no. 4, pp. 421-425.

Liu, Z., Cooper, P. & Wypych, P. W. 2001, 'Velocity profile in air entrainment during free-fall of particles', *Seventh International Conference on Bulk Materials, Storage, Handling and Transportation*, Institution of Engineers Australia, Newcastle, Australia, vol. 2, pp. 841-849.

Lonie, K. W., 1989, 'The design of conveyor transfer chutes', *Third International Conference on Bulk Materials, Storage, Handling and Transportation*, Institution of Engineers Australia, Newcastle, Australia, pp. 240-244.

Low, A. G. L. 2000, 'Australian innovation solves age-old problem', *Bulk Solids Handling*, vol. 20, no. 3, pp. 380-381.

Low, A. G. L. & Verran, M. J. 2000, 'Physical modelling of transfer chutes – case studies and applications in bulk materials handling', *Bulkex 2000*, Melbourne, Australia, pp. 4.1-4.7.

Marcus, R. D., Baller, W. J. & Barthel, P. 1996, 'The design and operation of the WEBA chute', *Bulk Solids Handling*, vol. 16, no. 3, pp. 405-409.

Maynard, E. P. 2003, 'Designing transfer chutes to eliminate spillage and dusting', *Cement Handling – Bulk Solids Handling Special*, pp. 28-34.

McBride, B. 2000, 'Curved transfer chute – results of site trials and optimization', *From Powder to Bulk: International Conference on Powder and Bulk Solids Handling*, ImechE Headquarters, London, UK, pp. 411-418.

McCurdy, J. A. & Buelow, F. H. 1963, 'Flow characteristics of shelled corn through chutes', *Quarterly Bulletin*, Michigan State University, Agricultural Experimental Station, vol. 46, no. 2, pp. 175-185.

McIlvenna, P. & Mossad, R. 2003, 'Two dimensional transfer chute analysis using a continuum method', *Proceedings of the Third International Conference on CFD in the Minerals and Process Industries*, CSIRO, Melbourne, Australia, pp. 547-551.

M.H.E.A. – Guide to the Design of Transfer Chutes and Chute Linings, 1989, The Mechanical Handling Engineers Association, 93 pages.

M.H.E.A. – Recommended Practice for Troughed Belt Conveyors, 1986, The Mechanical Handling Engineers Association, pp. 33, 42-48.

Mindlin, R. D. 1949, 'Compliance of elastic bodies in contact', *Transactions of the ASME: Journal of Applied Mechanics*, vol. 16, pp. 259-268.

Mindlin, R. D. & Deresiewicz, H. 1953, 'Elastic spheres in contact under varying oblique forces', *Transactions of the ASME: Journal of Applied Mechanics*, vol.20, pp. 327-344.

Miranda, I., Ferencz, R. M. & Hughes, T. J. R. 1989, 'An improved implicit-explicit time integration method for structural dynamics', *Earthquake Engineering and Structural Dynamics*, vol. 18, no. 5, pp. 643-653.

Montagner, G. J., Charlton, W. H., Roberts, A. W. & Chiarella, C. 1974, 'Optimization, identification and control applied to gravity flow of grain in a storage bin, discharge chute system', *Proceedings of the IFAC Symposium on Automatic Control for Agriculture*, University of Saskatchewan, Canada, vol. D-6, pp. 1-15.

Morrison, J. N. Jr 1971, 'Controlling dust emissions at belt conveyor transfer points', *Transactions of the SME/AIME*, vol. 250, pp. 47-53.

Munjiza, A. & Andrews, K. R. F. 1998, 'NBS contact detection algorithm for bodies of similar size', *International Journal for Numerical Methods in Engineering*, vol. 43, no. 1, pp. 131-149.

Mustoe, G. G. W., Henriksen, M. & Huttelmaier, H-P. (eds.) 1989, *Proceedings of the 1st US Conference on Discrete Element Methods*, Golden, Colorado.

Mustoe, G. G. W. & Miyata, M. 2001, 'Material flow analyses of noncircular-shaped granular media using discrete element method', *Journal of Engineering Mechanics*, vol. 127, no. 10, pp. 1017-1026.

Mustoe, G. G. W., Miyata, M. & Nakagawa, M. 2000, 'Discrete element methods for mechanical analysis of systems of general shaped bodies', *Proceedings of the 5th International Conference on Computational Structures Technology*, Leuven, Belgium.

Nordell, L. K. 1994, 'Palabora installs curved transfer chute in hard rock to minimise belt cover wear', *Bulk Solids Handling*, vol. 14, no. 4, pp. 739-743.

Nordell, L. K. 2003, 'Modern ore transfer chute & belt feeder designs developed from discrete element modeling (DEM)', *BELTCON 12: International Materials Handling Conference*, Randburg, South Africa.

Nordell, L. K., *Particle Flow Modeling: Transfer Chutes and other Applications* [Online, Accessed 31 Mar. 2003].
URL: http://www.ckit.co.za/Conveyor/Papers/Dem/particle/particle.htm

Nordell, L. K. & Van Heerden, J. J. 1995, 'Technical innovation's extend life of palabora's main slope belt', *BELTCON 8: International Materials Handling Conference*, Johannesburg, South Africa.

O'Donovan, E. 2003, 'Predictable transfers at last! without trial and error', *Bulk Handling Review*, vol. 8, no. 1, pp. 51-52.

Ouadfel, H. & Rothenburg, L. 1999, 'An algorithm for detecting inter-ellipsoid contacts', *Computers and Geotechnics*, vol. 24, pp. 245-263.

Ove & Michael Brunius, 1995, 'Dust control and prevention of dust explosions in belt conveyor systems', *Bulk Solids Handling*, vol. 15, no. 2, pp. 265-269.

Page, J. 1991, 'Examples of good and bad chute design', *Bionic Conference*, Johannesburg, South Africa.

Parbery, R. D. & Roberts, A. W. 1986, 'On equivalent friction for the accelerated gravity flow of granular materials in chutes', *Powder Technology*, vol. 48, pp. 75-79.

Perkins, E. & Williams, J. R. 2001, 'A fast contact detection algorithm insensitive to object sizes', *Engineering Computations*, vol. 18, no. 1/2, pp. 48-61.

Potapov, A. & Campbell, C. S. 1998, 'A fast model for the simulation of non-round particles', *Granular Matter*, vol. 1, pp. 9-14.

Powell, G. 1995, 'Prediction of discharge trajectories from conveyors and chutes', B Eng (Mechanical) Thesis, The University of Wollongong, Wollongong, Australia, 1995.

Qiu, X. & Kruse, D. 1997a, 'Analysis of flow of ore materials in a conveyor transfer chute using discrete element method', *Proceedings of the 1997 ASME-ASCE-SES Joint Summer Meeting: Mechanics of Deformation and Flow of Particulate Materials*, pp. 395-404.

Qiu, X. & Kruse, D. 1997b, 'Design of conveyor chute using discrete element method', *4th U.S. National Congress on Computational Mechanics*, San Francisco, California.

Quentrec, B. & Brot, C. 1973, 'New method for searching for neighbours in molecular dynamics computations', *Journal of Computational Physics*, vol. 13, pp. 430-432.

Rabindra Nath Ojha, 1993, 'Impact forces in design of material handling plants and equipment', *Bulk Solids Handling*, vol. 13, no. 2, pp. 330-334.

Rajamani, R. K., Mishra, B. K., Venugopal, R. & Datta, A. 2000, 'Discrete element analysis of tumbling mills', *Powder Technology*, vol. 109, pp.105-112.

Rapaport, D. C. 1980, 'The event scheduling problem in molecular dynamic simulation', *Journal of Computational Physics*, vol. 34, pp.184-201.

Rappen, A. 1986, 'Equipment for belt conveyor transfer points', *Solidex 86: Solids Handling Conference: 'Modern Technology in Bulk Solids Handling'*, Harrogate, England, pp. D15-D26.

Rappen, A. 1994, 'Dust suppression in comparison with other dedusting processes', *Bulk Solids Handling*, vol. 14, no. 2, pp. 333-338.

Roberts, A. W. 1967, 'The dynamics of granular material flow through curved chutes', *Mechanical and Chemical Engineering Transactions*, Institution of Engineers, Australia, vol. MC3, no. 2, pp. 216-224.

Roberts, A. W. 1969, 'An investigation of the gravity flow of noncohesive granular materials through discharge chutes', *Transactions of the ASME: Journal of Engineering for Industry*, vol. 91, no. 2, 1969, pp. 373-381.

Roberts, A. W. & Arnold, P. C. 1971, 'Discharge-chute design for free-flowing granular materials', *Transactions of the ASAE*, pp. 304-308, 312.

Roberts, A. W. & Montagner, G. J. 1975, 'Flow in a hopper discharge chute system', *Chemical Engineering Progress*, vol. 71, no. 2, pp. 71-72.

Roberts, A. W. 1979, 'Transfer chutes', in: *Feeder Loads and Transfer Chutes*, Bulk Solids Handling Research Associates, Australia.

Roberts, A. W. & Scott, O. J. 1981, 'Flow of bulk solids through transfer chutes of variable geometry and profile', *Bulk Solids Handling*, vol. 1, no. 4, pp. 715-727.

Roberts, A. W., Ooms, M. & Scott, O. J. 1984, 'Surface friction and wear in the storage, gravity flow and handling of bulk solids', *Proc. Inst. Conference 'War on Wear', Wear in the Mining and Mineral Extraction Industry*, Instn. of Mech. Engrs., Nottingham, U.K., pp. 123-134.

Roberts, A. W. & Ooms, M. 1985, 'Some aspects of surface friction, adhesion and wear in the gravity flow, handling and belt conveying of bulk solids', *BELTCON 3: International Materials Handling Conference*, Johannesburg, South Africa, pp. 1-43.

Roberts, A. W., Ooms, M. & Bennett, D. J. 1987, 'Bulk solid conveyor belt interaction in relation to belt cleaning', *Bulk Solids Handling*, vol. 7, no. 3, pp. 355-362.

Roberts, A. W. 1988, 'Friction, adhesion and wear in bulk materials handling', *Proceedings AntiWear 88,* The Royal Society London, Inst. of Metals, I. Mech. E.

Roberts, A. W., Ooms, M. & Wiche, S. J. 1989, 'Concepts of boundary friction, adhesion and wear in bulk solids handling operations', *Third International Conference on Bulk Materials, Storage, Handling and Transportation*, Institution of Engineers Australia, Newcastle, Australia, pp. 349-358.

Roberts, A. W. 1990, 'Storage and handling of coal – a state of the art review', *Mining Technology*, vol. 72, no. 832, pp. 37-49.

Roberts, A. W., Ooms, M. & Wiche, S. J. 1990, 'Concepts of boundary friction, adhesion and wear in bulk solids handling operations', *Bulk Solids Handling*, vol. 10, no. 2, pp. 189-198.

Roberts, A. W., Ooms, M. & Wiche, S. J. 1991, 'Concepts of boundary friction, adhesion and wear in bulk solids handling', *Bionic Conference*, Johannesburg, South Africa.

Roberts, A. W. 1991, 'Bulk solids handling – recent developments and future directions', *Bulk Solids Handling*, vol. 11, no. 1, pp. 17-35.

Roberts, A. W. & Wiche, S. J. 1993, 'Prediction of lining wear life of bins and chutes in bulk solids handling operations', *Tribology International*, vol. 26, no. 5, pp. 345-351.

Roberts, A. W. 1997a, 'Concepts of feeder design and performance in relation to loading bulk solids onto conveyor belts', *Mechanical handling Systems, Master of Engineering Practice Module Course Notes*, Centre for Bulk Solids and Particulate Technologies, Surfers Paradise, pp. 633-663.

Roberts, A. W. 1997b, 'Notes on conveyor discharge', *Belt Conveying, Master of Engineering Practice Module Course Notes*, Centre for Bulk Solids and Particulate Technologies, Perth, pp. 764-771.

Roberts, A. W. 1997c, 'Ship loader coal chute', *Belt Conveying, Master of Engineering Practice Module Course Notes*, Centre for Bulk Solids and Particulate Technologies, Perth, pp. 772-779.

Roberts, A. W. 1998a, 'Particle technology – reflections and horizons: an engineering perspective', *Chemical Engineering Research and Design*, vol. 76, part A, pp. 775-796.

Roberts, A. W. 1998b, 'Transfer chute performance and design', *Mechanical Handling Systems, Master of Engineering Practice Module Course Notes*, Centre for Bulk Solids and Particulate Technologies, Perth, pp. 799-828.

Roberts, A. W. & Wiche, S. J. 1999, 'Interrelation between feed chute geometry and conveyor belt wear', Bulk Solids Handling, vol. 19, no. 1, pp. 35-39.

Roberts, A. W. 2000, 'Developments in belt conveying technology and associated feeding of bulk solids', *From Powder to Bulk: International Conference on Powder and Bulk Solids Handling*, ImechE Headquarters, London, UK, pp. 377-410.

Roberts, A. W. 2001, 'Chute design considerations for feeding and transfer', *BELTCON 9: International Materials Handling Conference*, South Africa, pp. 1-24.

Roberts, A. W. 2004, 'Chute design considerations for feeding and transfer', *Paper presented at Bulkex 2004 Exhibition*, Darling Harbour, Sydney Australia.

Rothenburg, L. & Bathurst, R. J. 1991, 'Numerical simulation of idealized granular assemblies with plane elliptical particles', *Computers and Geotechnics*, vol. 11, no. 4, pp. 315-329.

Royal, T. A. & Craig, D. A. 2001, 'Effective chute design', *Seventh International Conference on Bulk Materials, Storage, Handling and Transportation*, Institution of Engineers Australia, Newcastle, Australia, vol. 2, pp. 589-595.

Rozentals, J. 1983, 'Rational design of conveyor chutes', *BELTCON 2: International Materials Handling Conference*, Johannesburg, South Africa.

Rozentals, J. 1991, 'Flow of bulk solids in chute design', *Bionic Conference*, Johannesburg, South Africa.

SA Catalog 66 Manual, Stephens-Adamson MFG. CO.

Sabina, W. E., Stahura, R. P. & Swinderman, R. T. 1984, 'Conveyor Transfer Stations: Problems & Solutions', *Coal Technology '84: 7th International Coal and Lignite Utilization Conference*, Vol. I & II, Houston, USA, pp. 437-501.

Sabina, W. E., Stahura, R. P. & Swinderman, R. T. 1992, 'Chute problem checklist', *Bionic Conference*, Johannesburg, South Africa.

Sadd, M. H., Adhikari, G. & Cardoso, F. 2000, 'DEM simulation of wave propagation in granular materials', *Powder Technology*, vol. 109, pp. 222-233.

Sadd, M. H., Tai, Q. & Shukla, A. 1993, 'Contact law effects on wave propagation in particulate materials using distinct element modeling', *International Journal of Non-Linear Mechanics*, vol. 28, no. 2, pp. 251-265.

Savage, S. B. 1979, 'Gravity flow of cohesionless granular materials in chutes and channels', *Journal of Fluid Mechanics*, vol. 92, Part 1, pp. 53-96.

Schäfer, J., Dippel, S. & Wolf, D. E. 1996, 'Force schemes in simulations of granular materials', *Journal de Physique*, vol. 6, no. 1, pp. 5-20.

Scott, O. J. & Choules, P. R. 1993a, 'Mining industry belt conveyor transfer station design', *National Bulk Materials Handling Conference*, Institution of Engineers Australia, Yeppon, Australia, pp. 175-184.

Scott, O. J. & Choules, P. R. 1993b, 'The use of impact plates in conveyor transfers', *Tribology International*, vol. 26, no. 5, pp. 353-359.

Scott, O. J. 1997, 'Conveyor transfer chute design', *Belt Conveying, Master of Engineering Practice Module Course Notes*, Centre for Bulk Solids and Particulate Technologies, Perth, pp. 740-762.

Seville, J., Tüzün, U. & Clift, R. 1997, *Processing of Particulate Solids*, Blackie Academic & Professional, London, UK.

Snow, C. L. 1991, 'Degradation control in transfer chutes', *Bionic Conference*, Johannesburg, South Africa.

Stahura, R. P. 1992, 'Dollars and sense: rebuilding conveyor transfer points to cut fugitive material and improve operations', *4th International Conference on Bulk Materials Handling and Transportation: Symposium on Freight Pipelines*, Wollongong, Australia, pp. 509-513.

Streett, W. B., Tildesley, D. J. & Saville, G. 1978a, 'Multiple time step methods and an improved potential function for molecular dynamics simulations of molecular liquids', in *Computer Modelling of Matter*, ed. P. Lykos, ACS Symposium Series, vol. 86, American Chemical Society, Washington, pp. 144-158.

Streett, W. B., Tildesley, D. J. & Saville, G. 1978b, 'Multiple time-step methods in molecular dynamics', *Molecular Physics*, vol. 35, no. 3, pp. 639-648.

Stuart-Dick, D. & Royal, T. A. 1991, 'Streamlined design of chutes to handle bulk solids', *Bionic Conference*, Johannesburg, South Africa.

Stuart-Dick, D. & Royal, T. A. 1992, 'Design principles for chutes to handle bulk solids', *Bulk Solids Handling*, vol. 12, no. 3, pp. 447-450.

Sundstrom, P. & Benjamin, C. W. 1993, 'Innovations in transfer chute design', *National Bulk Materials Handling Conference*, Institution of Engineers Australia, Yeppon, Australia, pp. 191-195.

Swinderman, R. T. 1994, 'Engineering your belt conveyor transfer point', *Powder and Bulk Engineering*, pp. 43-49.

Swope, W. C., Andersen, H. C., Berens, P. H. & Wilson, K. R. 1982, 'A computer simulation method for the calculation of equilibrium constants for the formation of physical clusters of molecules: Application to small water clusters', *Journal of Chemical Physics*, vol. 76, no. 1, pp. 637-649.

Taylor, L. M. & Preece, D. S. 1989, 'Simulation of Blasting Induced Rock Motion using Spherical Element Models', *Presented at 1st US Conference on Discrete Element Methods, Golden, Colorado*, eds. G. G. W. Mustoe, M. Henriksen, & H-P Huttelmaier.

Thomas, L. R. 1993, 'Transfer point sealing systems to control fugitive material', *National Bulk Materials Handling Conference*, Institution of Engineers Australia, Yeppon, Australia, pp. 185-189.

Thompson, S. M. 1983, 'Use of neighbour lists in molecular dynamics', *CCP5 Newsletter*, No. 8, pp. 20-28.

Tooker, G. E. 1985, 'Establishing design criteria for fugitive dust collection', *Bulk Solids Handling*, vol. 5, no. 4, pp. 865-869.

Tooker, G. E. 1992, 'Controlling fugitive dust emissions in material handling operations', *Bulk Solids Handling*, vol. 12, no. 2, pp. 227- 232.

Toxvaerd, S. 1982, 'A new algorithm for molecular dynamics calculations', *Journal of Computational Physics*, vol. 47, no. 3, pp. 444-451.

Trees, J. 1962, 'A practical investigation of the flow of particulate solids through sloping pipes', *Transactions of the Institute of Chemical Engineers*, vol. 40, no. 5, pp. 286-296.

Tsuji, Y., Kawaguchi, T. & Tanaka, T. 1993, 'Discrete particle simulation of two-dimensional fluidized bed', *Powder Technology*, vol. 77, pp. 79-87.

Tsuji, Y., Tanaka, T. & Ishida, T. 1992, 'Lagrangian numerical simulation of plug flow of cohesionless particles in a horizontal pipe', *Powder Technology*, vol. 71, pp. 239-250.

Ullmann, A. & Dayan, A. 1998, 'Exhaust volume model for dust emission control of belt conveyor transfer points', *Powder Technology*, vol. 96, no. 2, pp. 139-147.

User's Manual for Display III^{TM} *– Version 6.0* 1995, vol. II, E.M.R.C. (Engineering Mechanics Research Corporation), Michigan, USA

Vemuri, B. C., Chen, L., Vu-Quoc, L., Zhang, X. & Walton, O. 1998, 'Efficient and accurate collision detection for granular flow simulation', *Graphical Models and Image Processing*, vol. 60, no. 6, pp. 403-422.

Verlet, L. 1967, 'Computer "experiments" on classical fluids. I. Thermodynamical properties of Lennard-Jones molecules', *Physical Review*, vol. 159, no. 1, pp. 98-103.

Vu-Quoc, L. & Zhang, X. 1999a, 'An accurate and efficient tangential force-displacement model for elastic frictional contact in particle-flow simulations', *Mechanics of Materials*, vol. 31, no. 4, pp. 235-269.

Vu-Quoc, L. & Zhang, X. 1999b, Erratum to: 'An accurate and efficient tangential force-displacement model for elastic frictional contact in particle-flow simulations' [Mechanics of Materials, vol. 31, no. 4, pp. 235-269], *Mechanics of Materials*, vol. 31, no. 11, pp. 761-762.

Vu-Quoc, L., Lesburg, L. & Zhang, X. 2004, 'An accurate tangential force-displacement model for granular-flow simulations: Contacting spheres with plastic deformation, force-driven formulation', *Journal of Computational Physics*, vol. 196, no. 1, pp. 298-326.

Vu-Quoc, L., Zhang, X. & Lesburg, L. 2001, 'Normal and tangential force-displacement relations for frictional elasto-plastic contact of spheres', *International Journal of Solids and Structures*, vol. 38, no. 36-37, pp. 6455-6489.

Vu-Quoc, L., Zhang, X. & Walton, O. R. 2000, 'A 3-D discrete-element method for dry granular flows of ellipsoidal particles', *Computer Methods in Applied Mechanics and Engineering*, vol. 187, no.3, pp. 483-528.

Walsh, M. A. 2004, 'Simulation of granular materials', *Unpublished PhD Thesis*, University of Wollongong, Wollongong, Australia.

Walton, O. R. 1982a, 'Explicit particle dynamics model for granular materials', *Numerical Methods in Geomechanics*, Edmonton, Z. Elsenstein, ed., A. A. Balkema, Rotterdam, vol. 3, pp. 1261-1268.

Walton, O. R. 1982b, 'Particle-dynamics calculations of shear flow', *Mechanics of Granular Materials: New Models and Constitutive Relations, Proceedings of the U.S./Japan Seminar on New Models and Constitutive Relations in the Mechanics of Granular Materials*, Ithaca, New York, eds. J. T. Jenkins & M. Satake, Elsevier, Amsterdam, pp. 327-338.

Walton, O. R. 1990, 'Computer simulation of rapidly flowing granular solids', *Proceedings of the Second International Symposium for Science on Form*, KTK Scientific Publishers, Tokyo, pp. 175-189.

Walton, O. R. 1992, 'Numerical simulation of inelastic frictional particle-particle interactions', in Roco, ed., *Particulate Two-Phase Flow*, Ch. 25, Butterworth-Heinemann, Boston, pp. 884-911.

Walton, O. R. 1993a, 'Numerical simulation of inclined chute rows of monodisperse, inelastic, frictional spheres', *Mechanics of Materials*, vol. 16, pp. 239-247.

Walton, O. R. 1993b, 'Simulation of gravity flow of granular materials', *MEET'N'93 Joint ASCE-ASME-SES Conference*, 6-9 June, University of Virginia, Charlottesville, Virginia, USA.

Walton, O. R. 1994, 'Effects of interparticle friction and particle shape on dynamic angles of repose via particle-dynamics simulation', *Mechanics and Statistical Physics of Particulate Materials*, June 8-10, La Jolla, California, USA.

Walton, O. R. & Braun, R. L. 1986a, 'Stress calculations for assemblies of inelastic spheres in uniform shear', *Acta Mechanica*, vol. 63, pp. 73-86.

Walton, O. R. & Braun, R. L. 1986b, 'Viscosity, granular-temperature and stress calculations for shearing assemblages of inelastic, frictional disks', *Journal of Rheology*, vol. 30, no. 5, pp. 949-980.

Walton, O. R. & Braun, R. L. 1993, 'Simulation of rotary-drum and repose tests for frictional spheres and rigid sphere clusters', *Proceedings of DOE/NSF Workshop on Flow of Particulates and Fluids*, Sept. 29-Oct. 1, Ithaca, NY, USA.

Walton, O. R., Maddix, D. M., Butkovich, T. R. & Heuzé, F. E. 1991, 'Redirection of dynamic compressive waves in materials with nearly orthogonal and random joint sets', pp. 65-73.

Wang, C-Y. & Liang, V-C. 1997, 'A packing generation scheme for the granular assemblies with planar elliptical particles', *International Journal for Numerical and Analytical Methods in Geomechanics*, vol. 21, no. 5, pp. 347-358.

Wang, C-Y., Wang, C-F. & Sheng, J. 1999, 'A packing generation scheme for the granular assemblies with 3D ellipsoidal particles', *International Journal for Numerical and Analytical Methods in Geomechanics*, vol. 23, no. 8, pp. 815-827.

Weakly, L. A. 2000, 'Passive enclosure dust control system', *Bulk Materials Handling by Conveyor Belt III*, SME Publication, pp. 107-112.

Weiss, M. 1992, 'A practical approach to dust control for special applications', *Bulk Solids Handling*, vol. 12, no. 2, pp. 233-236.

Wightman, C., Moakher, M., Muzzio, F. J. & Walton, O. 1998, 'Simulation of flow and mixing of particles in a rotating and rocking cylinder', *AIChE Journal*, vol. 44, no. 6, pp. 1266-1276.

Williams, J. R., & Mustoe, G. G. W. (eds.) 1993, *Proceedings of the Second International Conference on Discrete Element Methods (DEM), The Massachusetts Institute of Technology*, MIT Press, Boston, USA.

Williams, J. R. & O'Connor, R. 1995, 'A linear complexity intersection algorithm for discrete element simulation of arbitrary geometries', *Engineering Computations*, vol. 12, no. 2, pp. 185-201.

Wolf, E. F. & Von Hohenleiten, H. L. 1945, 'Experimental study of the flow of coal in chutes at the riverside generating station', *Transactions of the ASME*, vol. 67, pp. 585-599.

Wolf, E. F. & Von Hohenleiten, H. L. 1948, 'Flow of coal in chutes', *Mechanical Engineering*, vol. 70, pp. 313, 314, and 335.

Xu, B. H. 1997, 'Numerical simulation of the gas-solid flow in fluidized beds', *PhD Thesis*, The University of New South Wales, Sydney, Australia.

Xu, B. H. & Yu, A. B. 1997, 'Numerical simulation of the gas-solid flow in a fluidised bed by combining discrete particle method with computational fluid dynamics', *Chemical Engineering Science*, vol. 52, no. 16, pp. 2785-2809.

Xu, B. H., Yu, A. B., Chew, S. J & Zulli, P. 2000, 'Numerical simulation of the gas-solid flow in a bed with lateral gas blasting', *Powder Technology*, vol. 109, no. 1, 2000, pp. 13-26.

Xu, B. H., Feng, Y. Q., Yu, A. B., Chew, S. J. & Zulli, P. 2001, 'A numerical and experimental study of the gas-solid flow in a fluid bed reactor', *Powder Handling & Processing*, vol. 13, no. 1, pp. 71-76.

Zhang, R., Mustoe, G. G. W. & Nelson, K. R. 1993, 'Simulation of hydraulic phenomena using the discrete element method', *Proceedings of the 2nd International Conference on Discrete Element Methods (DEM), The Massachusetts Institute of Technology*, eds. J. R. Williams, & G. G. W. Mustoe, IESL Publications, pp. 189-200.

Zhang, X. & Vu-Quoc, L. 2000, 'Simulation of chute flow of soybeans using an improved tangential force-displacement model', *Mechanics of Materials*, vol. 32, pp. 115-129.

10.2 Bibliography

Angel, E. 1997, *Interactive Computer Graphics: A Top-Down Approach with OpenGL*, Addison-Wesley, Reading.

Astle, D. & Hawkins, K. 2001, *OpenGL Game Programming*, Prima Tech, Rocklin.

Buss, S. R. 2003, *3-D Computer Graphics: A Mathematical Introduction with OpenGL*, Cambridge University Press, New York, USA.

Glaeser, G. & Stachel, H. 1999, *Open Geometry: OpenGL + Advanced Geometry*, Springer-Verlag, Rensselaer, NY, USA.

Harriger, A. R., Lisack, S. K., Gotwals, J. K. & Lutes, K. D. 1999, *Introduction to Computer Programming with Visual Basic 6: A Problem-Solving Approach*, Que E & T, Indianapolis.

Jung, D. G. & Kent, J. 2000, *Debugging Visual Basic: Troubleshooting for Programmers*, Osborne/McGraw-Hill, Berkeley.

Kilgard, M. J. 1996, *OpenGL Programming for the X Window System*, Addison-Wesley Developers Press, Reading.

McCarter, D. 2000, *David McCarter's VB Tips and Techniques*, APress, Emeryville.

Meriam, J. L. & Kraige, L. G. 1993, *Engineering Mechanics Volume 1: Statics*, 3rd edition, John Wiley & Sons, Canada.

Nyhoff, L & Leestma, S. 1996, *FORTRAN 77 for Engineers and Scientists with an Introduction to Fortran 90*, 4th edition, Prentice-Hall International, New Jersey.

Shreiner, D. (ed.) {OpenGL Architecture Review Board} 2000, *OpenGL Reference Manual: The Official Reference Document to OpenGL, version 1.2*, 3rd edition, Addison-Wesley, Reading.

Siler, B. & Spotts, J. 2002, *Special Edition using Visual Basic .NET*, Que/Hemel Hempstead/Prentice Hall, Indianapolis.

Stephens, R. 2000, *Visual Basic Graphics Programming: Hands-On Applications and Advanced Color Development*, 2nd edition, Wiley Computer Publishing, New York.

Woo, M., Neider, J., Davis, T. & Shreiner, D. {OpenGL Architecture Review Board} 1999, *OpenGL Programming Guide: The Official Guide to Learning OpenGL, version 1.2*, 3rd edition, Addison-Wesley, Harlow.

Wright, R. S. Jr & Sweet, M. 2000, *OpenGL SuperBible*, 2nd edition, Waite Group Press, Indianapolis.

Zak, D. 2001, *Programming with Microsoft Visual Basic 6.0*, Enhanced edition, Course Technology/Thomson Learning, Boston.

Appendix I

PROJECT GANTT CHARTS

I.1 Overview

It was envisaged that the project would be completed within 36 months. However as mentioned in Chapter One, there were unforseen circumstances and the final project completion time was almost 44 months. The first Gantt chart (Figure I.1) details the preliminary timeline completed during the early stages of the research, while the second (Figure I.2) was compiled during the finishing stages of the research. There are many differences, and these differences along with the lack of detail in the first chart can be attributed to the inexperience of the author during the early stages of the project.

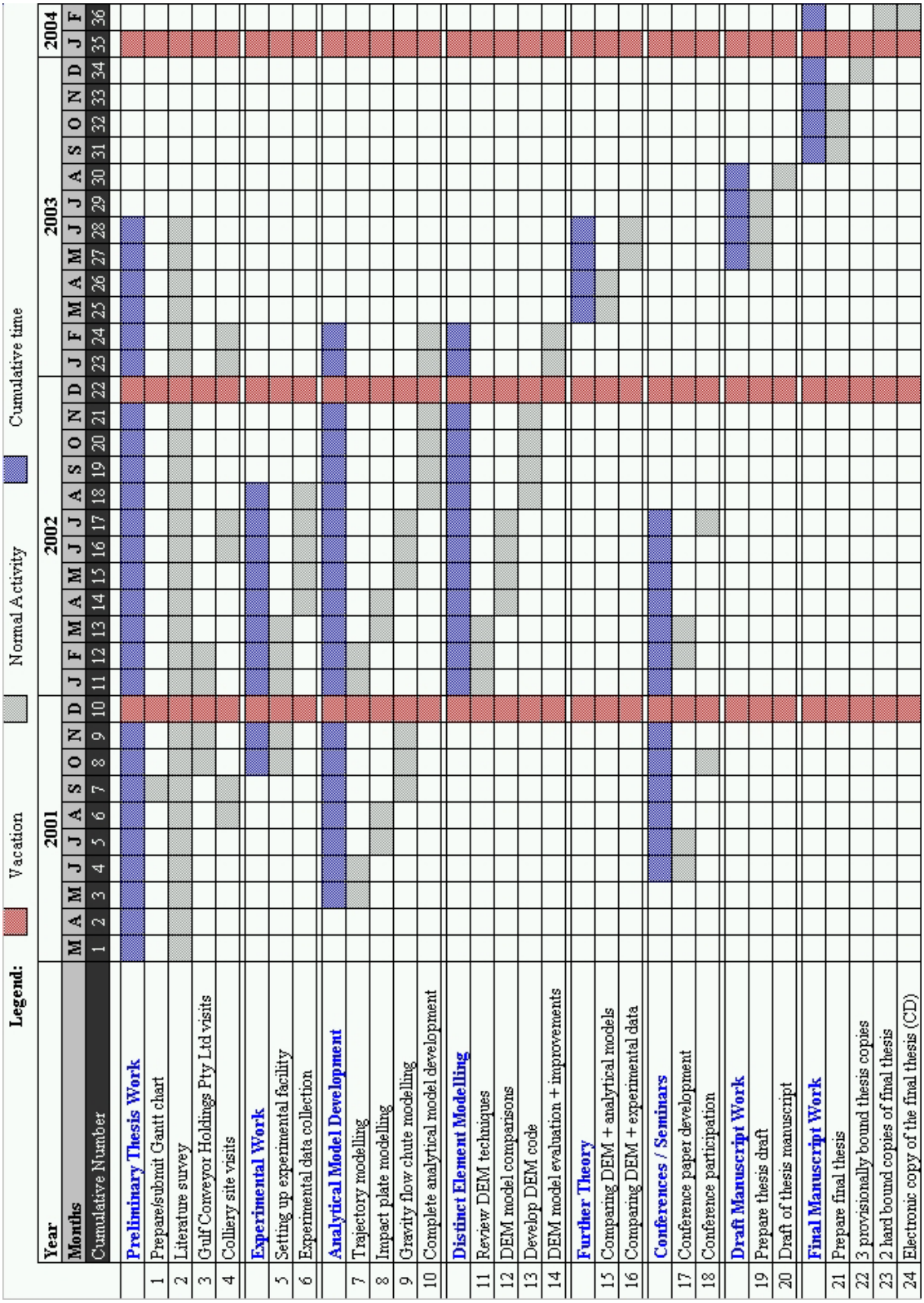

Figure I.1 Initial Gantt Chart

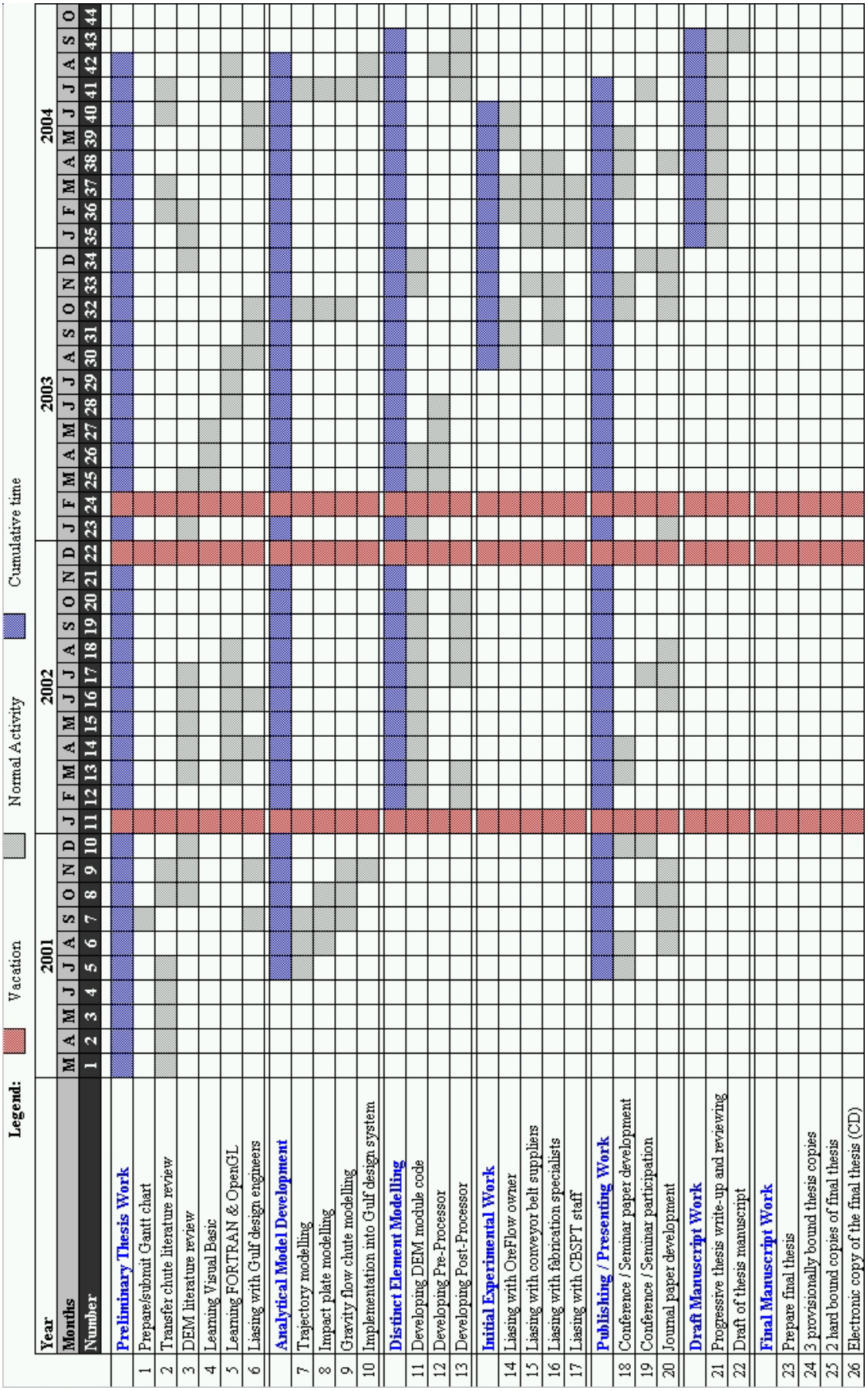

Figure I.2 Final Gantt Chart

Appendix II

EXPANDED IMPLEMENTATION OF TFD MODEL

II.1 Introduction

In the current work, the one-dimensional tangential force-displacement model (TFD) approximated by Walton & Braun (1986b) is used, and the implementation was described in Section 4.3.5.3. However the implementation theory of the two-dimensional (surface) TFD model of Walton (1993a) for three-dimensional DEM systems is derived here for future work purposes. The derivation is readily useable in the current work by letting the perpendicular tangential displacement component equal zero, however extra time and work would be required to code the relevant parameters and therefore the model was not coded.

As detailed in Chapter Four, modelling of the full Mindlin-Deresiewicz theory in a multi-body simulation is impractical (Els 2003), and therefore models have been developed that provide good approximations, such as the one-dimensional Walton & Braun (1986b) model. Walton (1993a) extended this one-dimensional approximation into a two-dimensional (surface) model, where the tangential displacement parallel to the current friction force $\Delta\delta_{t,||}$ and the displacement perpendicular to the existing friction force $\Delta\delta_{t,\perp}$ are considered separately. The tangential friction force F_t is set equal to the vector sum of $F_{t,\perp}$ and $F_{t,||}$, and checked to ensure it does not exceed the total friction force limit given by the Coulomb law. After contact occurs between particles, tangential forces build up non-linearly resulting in displacements in the tangent plane of contact.

In the tangential direction, let F_t^N and F_t^{N+1} be the tangential force magnitude at time t^N and time t^{N+1} respectively. The relationship between F_t^N and F_t^{N+1} is given by the

following incremental formula (Drake & Walton 1995, Vemuri et al. 1998, Vu-Quoc et al. 2000, Walton 1993a, Walton & Braun 1986b):

$$F_t^{N+1} = F_t^N + K_t^N \, \Delta\delta_t^N \tag{II.1}$$

where K_t^N is the tangential stiffness coefficient at time t^N and $\Delta\delta_t^N$ is the incremental tangential displacement at time t^N. The calculation of the term $\Delta\delta_t^N$ will be shown shortly. The effective tangential stiffness K_t^N in the direction parallel to the existing friction force is a function of the normal force F_n^N, the tangential force F_t^N, and F_t^*, which is the value of the tangential force F_t at the last turning point, as follows (Hanes & Walton 2000, Vemuri et al. 1998, Vu-Quoc et al. 2000, Walton 1993a, Walton & Braun 1986b, Walton et al. 1991):

$$K_t^N = \begin{cases} K_t^0 \left(1 - \dfrac{F_t^N - F_t^*}{\mu F_n^N - F_t^*}\right)^b & (for\ F_t\ increasing), \\ K_t^0 \left(1 - \dfrac{F_t^* - F_t^N}{\mu F_n^N + F_t^*}\right)^b & (for\ F_t\ decreasing), \end{cases} \tag{II.2}$$

where K_t^0 is the initial tangential stiffness and μ is the coefficient of friction. The value of F_t^* starts as zero (initial loading) and is subsequently set to the value of the tangential force F_t, whenever the magnitude changes from increasing to decreasing, or vice versa. The model assumes that in each time step, the normal force changes only by a small amount that will not significantly influence tangential force.

II.2 Implementation

The implementation of this frictional TFD model into the DEM simulation code involves some algebraic and vector manipulations. This is because the direction of the surface normal at contact changes continuously during a typical contact (Walton 1993a). The time step size in the simulations will be small hence the displacements from one

time step to the next are relatively small. The vector quantities are difficult to apply however in the computer code directly. Therefore the necessary working to manipulate the equations into a more useable form is also shown here. For the following work, the basic equations for implementation were taken from relevant sources, and these are both referenced and marked by (♦). The superscripts N-1, N, and N+1 refer to time t^{N-1}, t^{N}, and t^{N+1} respectively.

We let $\hat{\mathbf{k}}_{ij}^{N}$ be the current unit vector pointing from the centre of sphere i to the centre of sphere j:

$$\hat{\mathbf{k}}_{ij}^{N} = \frac{\mathbf{r}_j^N - \mathbf{r}_i^N}{\left\| \mathbf{r}_j^N - \mathbf{r}_i^N \right\|} \tag{II.3}$$

where $\mathbf{r}_i^N$ and $\mathbf{r}_j^N$ are position vectors of the two spheres of radii R_i and R_j. The vector $\hat{\mathbf{k}}_{ij}^{N}$ is also the unit normal at the contact point. This unit vector will be manipulated to give a form that is simpler to implement. Let:

$$\mathbf{r}_i^N = x_i^N \mathbf{i} + y_i^N \mathbf{j} \tag{II.4}$$

$$\mathbf{r}_j^N = x_j^N \mathbf{i} + y_i^N \mathbf{j} \tag{II.5}$$

where $\{x_i^N, y_i^N\}$ and $\{x_j^N, y_j^N\}$ are the horizontal and vertical components for the position vector for particles i and j respectively. From Eq. (II.4) and (II.5) the following algebraic expression can be created:

$$\mathbf{r}_j^N - \mathbf{r}_i^N = \left(x_j^N - x_i^N\right)\mathbf{i} + \left(y_j^N - y_i^N\right)\mathbf{j} \tag{II.6}$$

Also let:

$$dx^N = x_j^N - x_i^N \tag{II.7}$$

$$dy^N = y_j^N - y_i^N \tag{II.8}$$

then substituting Eq. (II.7) and (II.8) into Eq. (II.6) gives:

$$\mathbf{r}_j^N - \mathbf{r}_i^N = dx^N \mathbf{i} + dy^N \mathbf{j} \tag{II.9}$$

Substituting Eq. (II.9) into Eq. (II.3) gives:

$$\hat{\mathbf{k}}_{ij}^N = \frac{dx^N \mathbf{i} + dy^N \mathbf{j}}{\left\| dx^N \mathbf{i} + dy^N \mathbf{j} \right\|} \quad \Rightarrow \quad \hat{\mathbf{k}}_{ij}^N = \frac{dx^N \mathbf{i} + dy^N \mathbf{j}}{\sqrt{\left(dx^N\right)^2 + \left(dy^N\right)^2}} \tag{II.10}$$

Let:

$$\left(dn^N\right)^2 = \left(dx^N\right)^2 + \left(dy^N\right)^2 \tag{II.11}$$

Substituting Eq. (II.11) into Eq. (II.10) and simplifying gives:

$$\hat{\mathbf{k}}_{ij}^N = \left(\frac{dx^N}{dn^N}\right)\mathbf{i} + \left(\frac{dy^N}{dn^N}\right)\mathbf{j} \quad \Rightarrow \quad \hat{\mathbf{k}}_{ij}^N = cn^N \mathbf{i} + sn^N \mathbf{j} \tag{II.12}$$

where:

$$cn^N = \left(dx^N / dn^N\right) \tag{II.13}$$

$$sn^N = \left(dy^N / dn^N\right) \tag{II.14}$$

This form of the unit vector $\hat{\mathbf{k}}_{ij}^N$ is simpler to implement in the DEM computer code. Now in general, the direction of the normal at contact changes continuously, therefore the tangential force vector at time t^N has to be adjusted as follows. Let $\mathbf{F}_{t,old}^N$ be the tangential force vector at the end of the previous time step. Referring to Figure II.1, the current tangential force vector $\mathbf{F}_t^N$ at time t^N is computed by projecting the vector $\mathbf{F}_{t,old}^N$ onto the current tangent plane to sphere *i* having normal $\hat{\mathbf{k}}_{ij}^N$ (Walton 1993a):

$$\mathbf{F}_{t,0}^{N} = \hat{\mathbf{k}}_{ij}^{N} \times \mathbf{F}_{t,old}^{N} \times \hat{\mathbf{k}}_{ij}^{N} \quad \Rightarrow \quad \mathbf{F}_{t,0}^{N} = \mathbf{F}_{t,old}^{N} - \hat{\mathbf{k}}_{ij}^{N}\left(\hat{\mathbf{k}}_{ij}^{N} \cdot \mathbf{F}_{t,old}^{N}\right) \qquad \text{(II.15}\blacklozenge\text{)}$$

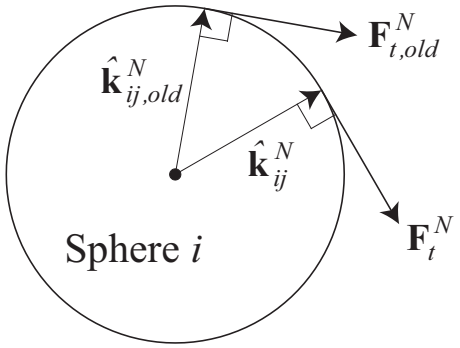

Figure II.1 Direction change of tangential force (adapted from Vu-Quoc et al. 2000)

Separating $\mathbf{F}_{t,old}^{N}$ into horizontal and vertical components:

$$\mathbf{F}_{t,old}^{N} = F\_x_{t,old}^{N}\mathbf{i} + F\_y_{t,old}^{N}\mathbf{j} \qquad \text{(II.16)}$$

and then by substituting Eq. (II.12) and (II.16) into Eq. (II.15) we get:

$$\begin{aligned}\mathbf{F}_{t,0}^{N} &= F\_x_{t,old}^{N}\mathbf{i} + F\_y_{t,old}^{N}\mathbf{j} \\ &\quad - \left(cn^{N}\mathbf{i} + sn^{N}\mathbf{j}\right)\left[\left(cn^{N}\mathbf{i} + sn^{N}\mathbf{j}\right)\cdot\left(F\_x_{t,old}^{N}\mathbf{i} + F\_y_{t,old}^{N}\mathbf{j}\right)\right]\end{aligned} \qquad \text{(II.17)}$$

Rearranging Eq. (II.17) gives:

$$\mathbf{F}_{t,0}^{N} = F\_x_{t,old}^{N}\mathbf{i} + F\_y_{t,old}^{N}\mathbf{j} - \left(cn^{N}\mathbf{i} + sn^{N}\mathbf{j}\right)\left[cn^{N}F\_x_{t,old}^{N} + sn^{N}F\_y_{t,old}^{N}\right] \qquad \text{(II.18)}$$

If we let:

$$F\_const_{t,const}^{N} = cn^{N}F\_x_{t,old}^{N} + sn^{N}F\_y_{t,old}^{N} \qquad \text{(II.19)}$$

then substituting Eq. (II.19) into Eq. (II.18) and simplifying gives:

$$\mathbf{F}_{t,0}^{N} = \left(F\_x_{t,old}^{N} - cn^{N} F_{t,const}^{N}\right)\mathbf{i} + \left(F\_y_{t,old}^{N} - sn^{N} F_{t,const}^{N}\right)\mathbf{j} \tag{II.20}$$

Simplifying further:

$$\mathbf{F}_{t,0}^{N} = F\_x_{t,0}^{N}\mathbf{i} + F\_y_{t,0}^{N}\mathbf{j} \tag{II.21}$$

where:

$$F\_x_{t,0}^{N} = F\_x_{t,old}^{N} - cn^{N} F_{t,const}^{N} \tag{II.22}$$

$$F\_y_{t,0}^{N} = F\_y_{t,old}^{N} - sn^{N} F_{t,const}^{N} \tag{II.23}$$

The following two identities are required for the next step in the process:

$$F\_mag_{t,old}^{N} = \left\| \mathbf{F}_{t,old}^{N} \right\| = \sqrt{\left(F\_x_{t,old}^{N}\right)^2 + \left(F\_y_{t,old}^{N}\right)^2} \tag{II.24}$$

$$F\_mag_{t,0}^{N} = \left\| \mathbf{F}_{t,0}^{N} \right\| = \sqrt{\left(F\_x_{t,0}^{N}\right)^2 + \left(F\_y_{t,0}^{N}\right)^2} \tag{II.25}$$

which are the magnitudes of $\mathbf{F}_{t,old}^{N}$ and $\mathbf{F}_{t,0}^{N}$ respectively. The projected friction force $\mathbf{F}_{t,0}^{N}$ is normalised to the old magnitude, so that $\left\| \mathbf{F}_{t}^{N} \right\| = \left\| \mathbf{F}_{t,old}^{N} \right\|$, to obtain a new virgin loading for the friction force $\mathbf{F}_{t}^{N}$ (Walton 1993a):

$$\mathbf{F}_{t}^{N} = \left\| \mathbf{F}_{t,old}^{N} \middle/ \mathbf{F}_{t,0}^{N} \right\| \mathbf{F}_{t,0}^{N} \tag{II.26♦}$$

Substituting Eq. (II.24) and (II.25) into Eq. (II.26) gives:

$$\mathbf{F}_{t}^{N} = \left(\frac{F\_mag_{t,old}^{N}}{F\_mag_{t,0}^{N}} \right)\left(F\_x_{t,0}^{N}\mathbf{i} + F\_y_{t,0}^{N}\mathbf{j}\right) \tag{II.27}$$

Simplifying further:

$$\mathbf{F}_t^N = F\_x_t^N \mathbf{i} + F\_y_t^N \mathbf{j} \tag{II.28}$$

where:

$$F\_x_t^N = \left(F\_mag_{t,old}^N \; F\_x_{t,0}^N\right) \Big/ F\_mag_{t,0}^N \tag{II.29}$$

$$F\_y_t^N = \left(F\_mag_{t,old}^N \; F\_y_{t,0}^N\right) \Big/ F\_mag_{t,0}^N \tag{II.30}$$

By letting:

$$F\_mag_t^N = \left\| \mathbf{F}_t^N \right\| = \sqrt{\left(F\_x_t^N\right)^2 + \left(F\_y_t^N\right)^2} \tag{II.31}$$

we can manipulate the unit vector in the direction of the virgin loading $\hat{\mathbf{t}}_{ij}^N = \mathbf{F}_t^N \Big/ \left\| \mathbf{F}_t^N \right\|$ to a more useable form:

$$\hat{\mathbf{t}}_{ij}^N = F\_x_{t,u}^N \mathbf{i} + F\_y_{t,u}^N \mathbf{j} \tag{II.32}$$

where:

$$F\_x_{t,u}^N = F\_x_t^N \Big/ F\_mag_t^N \tag{II.33}$$

$$F\_y_{t,u}^N = F\_y_t^N \Big/ F\_mag_t^N \tag{II.34}$$

Observing Eq. (II.15) and (II.26) it can be seen that the magnitude of $\mathbf{F}_t^N$ is the same as that of $\mathbf{F}_{t,old}^N$, whereas the direction of $\mathbf{F}_t^N$ is that of the projection of $\mathbf{F}_{t,old}^N$ into the tangent plane with normal $\hat{\mathbf{k}}_{ij}^N$.

The relative surface displacement vector $\Delta\boldsymbol{\delta}_t^N$ at time t^N is given by (Walton 1993a):

$$\begin{aligned} \Delta\boldsymbol{\delta}_t^N = & \left[\hat{\mathbf{k}}_{ij}^N \times \left(\mathbf{v}_j^{N-1/2} - \mathbf{v}_i^{N-1/2}\right) \times \hat{\mathbf{k}}_{ij}^N \right. \\ & \left. + R_i \left(\omega_i^{N-1/2} \times \hat{\mathbf{k}}_{ij}^N\right) + R_j \left(\omega_j^{N-1/2} \times \hat{\mathbf{k}}_{ij}^N\right)\right] \Delta t \end{aligned} \tag{II.35♦}$$

where $\{\mathbf{v}_i^{N-1/2}, \mathbf{v}_j^{N-1/2}\}$ are the velocity vectors and $\{\omega_i^{N-1/2}, \omega_j^{N-1/2}\}$ are the angular velocity vectors of spheres *i* and *j* respectively, all at time $t^{N-1/2}$ and Δt the time step size. The following approximation is made (Vu-Quoc et al. 2000):

$$\left(\mathbf{v}_j^{N-1/2} - \mathbf{v}_i^{N-1/2}\right)\Delta t \approx \Delta\mathbf{r}_{ij}^N = \mathbf{r}_{ij}^N - \mathbf{r}_{ij}^{N-1} \qquad \text{(II.36}\blacklozenge\text{)}$$

in Eq. (II.35) for $\Delta\boldsymbol{\delta}_t^N$ in the implementation for the TFD model. The term $\Delta\mathbf{r}_{ij}^N$ is the change in the relative position vector during the last time step, and is resolved into horizontal and vertical components for simpler algebraic manipulation:

$$\Delta\mathbf{r}_{ij}^N = \Delta r\_x^N\mathbf{i} + \Delta r\_y^N\mathbf{j} \qquad \text{(II.37)}$$

where:

$$\Delta r\_x^N = dx^N - dx^{N-1} \qquad \text{(II.38)}$$

$$\Delta r\_y^N = dy^N - dy^{N-1} \qquad \text{(II.39)}$$

Now substituting Eq. (II.12) and (II.37) into Eq. (II.35) gives:

$$\begin{aligned}\Delta\boldsymbol{\delta}_t^N &= \left(\Delta r\_x^N\mathbf{i} + \Delta r\_y^N\mathbf{j}\right)\\ &\quad - \left(cn^N\mathbf{i} + sn^N\mathbf{j}\right)\left[\left(cn^N\mathbf{i} + sn^N\mathbf{j}\right)\cdot\left(\Delta r\_x^N\mathbf{i} + \Delta r\_y^N\mathbf{j}\right)\right]\\ &\quad + \left[R_i\left(\omega_i^{N-1/2}\mathbf{k}\times\left(cn^N\mathbf{i} + sn^N\mathbf{j}\right)\right)\right.\\ &\quad \left. + R_j\left(\omega_j^{N-1/2}\mathbf{k}\times\left(cn^N\mathbf{i} + sn^N\mathbf{j}\right)\right)\right]\Delta t\end{aligned} \qquad \text{(II.40)}$$

Resolving dot products and cross products:

$$\begin{aligned}\Delta\boldsymbol{\delta}_t^N &= \left(\Delta r\_x^N\mathbf{i} + \Delta r\_y^N\mathbf{j}\right)\\ &\quad - \left(cn^N\mathbf{i} + sn^N\mathbf{j}\right)\left(cn^N\Delta r\_x^N + sn^N\Delta r\_y^N\right)\\ &\quad + \left[R_i\omega_i^{N-1/2}\left(cn^N\mathbf{j} - sn^N\mathbf{i}\right) + R_j\omega_j^{N-1/2}\left(cn^N\mathbf{j} - sn^N\mathbf{i}\right)\right]\Delta t\end{aligned} \qquad \text{(II.41)}$$

Performing some factorisation:

$$\begin{aligned}\Delta\boldsymbol{\delta}_t^N = &\left[\Delta r\_x^N - \Delta r\_x^N\left(cn^N\right)^2 - \Delta r\_y^N cn^N sn^N\right]\mathbf{i}\\ &+\left[\Delta r\_y^N - \Delta r\_y^N\left(sn^N\right)^2 - \Delta r\_x^N cn^N sn^N\right]\mathbf{j}\\ &+\left(cn^N\mathbf{j} - sn^N\mathbf{i}\right)\left[R_i\omega_i^{N-1/2} + R_j\omega_j^{N-1/2}\right]\Delta t\end{aligned} \tag{II.42}$$

Grouping horizontal and vertical terms together and simplifying yields:

$$\Delta\boldsymbol{\delta}_t^N = \Delta\delta x_t^N\mathbf{i} + \Delta\delta y_t^N\mathbf{j} \tag{II.43}$$

where:

$$\begin{aligned}\Delta\delta x_t^N = &\left[\Delta r\_x^N - \Delta r\_x^N\left(cn^N\right)^2\right.\\ &\left.- \Delta r\_y^N cn^N sn^N - sn^N\left(R_i\omega_i^{N-1/2} + R_j\omega_j^{N-1/2}\right)\Delta t\right]\end{aligned} \tag{II.44}$$

$$\begin{aligned}\Delta\delta y_t^N = &\left[\Delta r\_y^N - \Delta r\_y^N\left(sn^N\right)^2\right.\\ &\left.- \Delta r\_x^N cn^N sn^N + cn^N\left(R_i\omega_i^{N-1/2} + R_j\omega_j^{N-1/2}\right)\Delta t\right]\end{aligned} \tag{II.45}$$

The incremental tangential displacement must now be resolved into two components. Vu-Quoc et al. (2000) summarises the reasoning as follows. Recall that $\hat{\mathbf{t}}_{ij}^N$ (Eq. (II.32)) is the direction of the projection of $\mathbf{F}_{t,old}^N$ on the tangent plane having normal $\hat{\mathbf{k}}_{ij}^N$ (Eq. (II.12)). The direction $\hat{\mathbf{t}}_{ij}^N$ is considered as the direction of continuing application of the tangential force $\mathbf{F}_t^N$. Therefore the loading history in the TFD model is to be applied in this direction. On the other hand, the direction that lies in the same tangent plane, and is perpendicular to $\hat{\mathbf{t}}_{ij}^N$ is considered to correspond to a new virgin loading of tangential force, as mentioned previously. As shown in Figure II.2, the incremental tangential displacement $\Delta\boldsymbol{\delta}_t^N$ is therefore decomposed into two components, one along $\hat{\mathbf{t}}_{ij}^N$ and the other in the tangent plane and perpendicular to $\hat{\mathbf{t}}_{ij}^N$:

$$\Delta\boldsymbol{\delta}_t^N = \Delta\boldsymbol{\delta}_{t,||}^N + \Delta\boldsymbol{\delta}_{t,\perp}^N \tag{II.46}$$

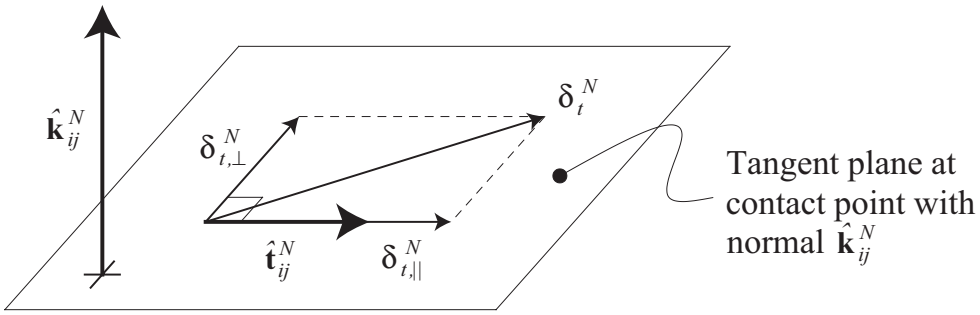

Figure II.2 Decomposition of the incremental tangential displacement $\Delta\boldsymbol{\delta}_t^N$ at time t^N (adapted from Vu-Quoc et al. (2000))

The displacement parallel to the friction force in the previous time step is (Walton 1993a):

$$\Delta\boldsymbol{\delta}_{t,||}^{N} = \left(\Delta\boldsymbol{\delta}_{t}^{N} \cdot \hat{\mathbf{t}}_{ij}^{N}\right)\hat{\mathbf{t}}_{ij}^{N} \qquad \text{(II.47}\blacklozenge\text{)}$$

Substituting Eq. (II.32) and (II.43) into Eq. (II.47) gives:

$$\Delta\boldsymbol{\delta}_{t,||}^{N} = \left[\left(\Delta\delta x_{t}^{N}\mathbf{i} + \Delta\delta y_{t}^{N}\mathbf{j}\right)\cdot\left(F\_x_{t,u}^{N}\mathbf{i} + F\_y_{t,u}^{N}\mathbf{j}\right)\right]\left(F\_x_{t,u}^{N}\mathbf{i} + F\_y_{t,u}^{N}\mathbf{j}\right) \qquad \text{(II.48)}$$

Resolving the dot product gives:

$$\Delta\boldsymbol{\delta}_{t,||}^{N} = \left[\Delta\delta x_{t}^{N} F\_x_{t,u}^{N} + \Delta\delta y_{t}^{N} F\_y_{t,u}^{N}\right]\left(F\_x_{t,u}^{N}\mathbf{i} + F\_y_{t,u}^{N}\mathbf{j}\right) \qquad \text{(II.49)}$$

Simplifying gives:

$$\Delta\boldsymbol{\delta}_{t,||}^{N} = \Delta\delta p_{const}^{N}\left(F\_x_{t,u}^{N}\mathbf{i} + F\_y_{t,u}^{N}\mathbf{j}\right) \qquad \text{(II.50)}$$

where:

$$\Delta\delta p_{const}^{N} = \Delta\delta x_{t}^{N} F\_x_{t,u}^{N} + \Delta\delta y_{t}^{N} F\_y_{t,u}^{N} \qquad \text{(II.51)}$$

Simplifying further we finally get:

$$\Delta\boldsymbol{\delta}_{t,||}^{N} = \Delta\delta p\_x^{N}\mathbf{i} + \Delta\delta p\_y^{N}\mathbf{j} \tag{II.52}$$

where:

$$\Delta\delta p\_x^{N} = \Delta\delta p_{const}^{N} F\_x_{t,u}^{N} \tag{II.53}$$

$$\Delta\delta p\_y^{N} = \Delta\delta p_{const}^{N} F\_y_{t,u}^{N} \tag{II.54}$$

The displacement perpendicular to the old friction force is (Walton 1993a):

$$\Delta\boldsymbol{\delta}_{t,\perp}^{N} = \Delta\boldsymbol{\delta}_{t}^{N} - \Delta\boldsymbol{\delta}_{t,||}^{N} \tag{II.55♦}$$

Substituting Eq. (II.43) and (II.52) into Eq. (II.55) gives:

$$\Delta\boldsymbol{\delta}_{t,\perp}^{N} = \left(\Delta\delta x_{t}^{N}\mathbf{i} + \Delta\delta y_{t}^{N}\mathbf{j}\right) - \left(\Delta\delta p\_x^{N}\mathbf{i} + \Delta\delta p\_y^{N}\mathbf{j}\right) \tag{II.56}$$

Grouping together horizontal and vertical terms:

$$\Delta\boldsymbol{\delta}_{t,\perp}^{N} = \left(\Delta\delta x_{t}^{N} - \Delta\delta p\_x^{N}\right)\mathbf{i} + \left(\Delta\delta y_{t}^{N} - \Delta\delta p\_y^{N}\right)\mathbf{j} \tag{II.57}$$

Simplifying further we finally get:

$$\Delta\boldsymbol{\delta}_{t,\perp}^{N} = \Delta\delta r\_x^{N}\mathbf{i} + \Delta\delta r\_y^{N}\mathbf{j} \tag{II.58}$$

where:

$$\Delta\delta r\_x^{N} = \Delta\delta x_{t}^{N} - \Delta\delta p\_x^{N} \tag{II.59}$$

$$\Delta\delta r\_y^{N} = \Delta\delta y_{t}^{N} - \Delta\delta p\_y^{N} \tag{II.60}$$

If the value of the normal force $\mathbf{F}_n^N$ changes from one time step to the next, then the value of $\mathbf{F}_t^*$ in Eq. (II.2) is scaled in proportion to the change in normal force (Walton 1993a):

$$F_t^* = F_t^* \frac{\left\| \mathbf{F}_n^{N+1} \right\|}{\left\| \mathbf{F}_n^N \right\|} \qquad \text{(II.61}\blacklozenge\text{)}$$

The effective incremental tangential stiffness K_T^N is determined from Eq. (II.2) with the new scaled value for F_t^* in Eq. (II.61) above substituted in for the old F_t^*. The component of the tangential force along the direction $\hat{\mathbf{t}}_{ij}^N$ is incremented from the projected tangential force $\mathbf{F}_t^N$ in the same direction as Eq. (II.26) (Vu-Quoc et al. 2000):

$$\mathbf{F}_{t,||}^{N+1} = \mathbf{F}_t^N + K_T^N \ \Delta\boldsymbol{\delta}_{t,||}^N \qquad \text{(II.62}\blacklozenge\text{)}$$

Substituting Eq. (II.28) and (II.52) into Eq. (II.62) gives:

$$\mathbf{F}_{t,||}^{N+1} = \left(F\_x_t^N \mathbf{i} + F\_y_t^N \mathbf{j}\right) + K_T^N \left(\Delta\delta p\_x^N \mathbf{i} + \Delta\delta p\_y^N \mathbf{j}\right) \qquad \text{(II.63)}$$

Grouping horizontal and vertical components together:

$$\mathbf{F}_{t,||}^{N+1} = \left(F\_x_t^N + K_T^N \ \Delta\delta p\_x^N\right)\mathbf{i} + \left(F\_y_t^N + K_T^N \ \Delta\delta p\_y^N\right)\mathbf{j} \qquad \text{(II.64)}$$

Walton (1993a) describes the following. If both of the conditions $\Delta\boldsymbol{\delta}_t^N \cdot \hat{\mathbf{t}}_{ij}^N < 0$ and $F_t^N + \left(\Delta\boldsymbol{\delta}_t^N \cdot \hat{\mathbf{t}}_{ij}^N\right) K_T^N < 0$ are simultaneously true then, in effect, the direction of $\mathbf{F}_{t,||}^N$ has reversed, and in the model the sign of the effective 'remembered' turning point F_t^* is changed (i.e. F_t^* is replaced by $-F_t^*$) for the next time step.

The displacement perpendicular to the existing friction force is assumed to have no pre-existing surface strain, therefore the perpendicular component of the tangential force in

the tangent plane with normal $\hat{\mathbf{k}}_{ij}^{N}$ is calculated as an initial increment (virgin loading) as (Vu-Quoc et al. 2000):

$$\mathbf{F}_{t,\perp}^{N+1} = K_T^0 \; \Delta\boldsymbol{\delta}_{t,\perp}^{N} \qquad \text{(II.65}\blacklozenge\text{)}$$

Substituting Eq. (II.58) into Eq. (II.65) gives:

$$\mathbf{F}_{t,\perp}^{N+1} = K_T^0 \left(\Delta\delta r\_x^N \mathbf{i} + \Delta\delta r\_y^N \mathbf{j}\right) \qquad \text{(II.66)}$$

Simplifying:

$$\mathbf{F}_{t,\perp}^{N+1} = K_T^0 \; \Delta\delta r\_x^N \mathbf{i} + K_T^0 \; \Delta\delta r\_y^N \mathbf{j} \qquad \text{(II.67)}$$

Finally the tangential force is set equal to the vector sum of (Walton 1993a):

$$\left(\mathbf{F}_t^{N+1}\right)' = \mathbf{F}_{t,||}^{N+1} + \mathbf{F}_{t,\perp}^{N+1} \qquad \text{(II.68}\blacklozenge\text{)}$$

which is the counterpart of Eq. (II.46). Substituting Eq. (II.64) and (II.67) into Eq. (II.68) gives:

$$\begin{aligned}\left(\mathbf{F}_t^{N+1}\right)' = &\left(F\_x_t^N + K_T^N \; \Delta\delta p\_x^N\right)\mathbf{i} + \left(F\_y_t^N + K_T^N \; \Delta\delta p\_y^N\right)\mathbf{j} \\ &+ K_T^0 \; \Delta\delta r\_x^N \mathbf{i} + K_T^0 \; \Delta\delta r\_y^N \mathbf{j}\end{aligned} \qquad \text{(II.69)}$$

Grouping horizontal and vertical components together:

$$\begin{aligned}\left(\mathbf{F}_t^{N+1}\right)' = &\left(F\_x_t^N + K_T^N \; \Delta\delta p\_x^N + K_T^0 \; \Delta\delta r\_x^N\right)\mathbf{i} \\ &+ \left(F\_y_t^N + K_T^N \; \Delta\delta p\_y^N + K_T^0 \; \Delta\delta r\_y^N\right)\mathbf{j}\end{aligned} \qquad \text{(II.70)}$$

The value given by Eq. (II.70) is checked to ensure it does not exceed the friction limit, i.e.:

$$\left\| \left(\mathbf{F}_t^{N+1} \right)' \right\| \leq \mu \left\| \mathbf{F}_n^{N+1} \right\| \tag{II.71}$$

and if it does it is scaled back so its magnitude equals that limit. In other words, the final updated tangential force at time t^{N+1} is set to be (Vu-Quoc et al. 2000):

$$\mathbf{F}_t^{N+1} = min\left(\left\| \left(\mathbf{F}_t^{N+1} \right)' \right\|, \left\| \mu \, \mathbf{F}_n^{N+1} \right\| \right) \frac{\left(\mathbf{F}_t^{N+1} \right)'}{\left\| \left(\mathbf{F}_t^{N+1} \right)' \right\|} \tag{II.72♦}$$

Appendix III

EXAMPLES OF INPUT FILES

III.1 Parameter Input File

In this section an example is given of a parameter data input file. As detailed in Chapter Five, this file is required so that the DEM program can be compiled. An example of a data input file is shown below. It basically provides the parameters to simulate the free fall of 5000 particles within square shaped boundary geometry.

```
*TITLE
Simulation Example - 5000 Particle Free Fall (Shams Huque 29-12-03)
*MAX STEPS, TIME STEP TO BEGIN AVERAGING
      1000000         0
*DRAWING : FIRST STEP,LAST STEP,INCREMENT
        0      1000000        100
*TIME STEP
   .500E-07
*PARTICLE FILLING TYPE : binary OR random
random
*{DIAMETER,+/-VARIANCE,DENSITY} (RAND) OR {DIAMETER,PERCENTAGE,DENSITY} (BIN)
   .031E+00   0.019  9.00E+02
*COEFFICIENT OF FRICTION (PMU) --> PP,PW
   .300E+00   .200E+00
*INITIAL NUMBER OF PARTICLES
        5000
*DIMENSIONS OF THE CALCULATIONAL SPACE (X-LENGTH,Y-LENGTH)
   1.00E+01   1.00E+01
*NORMAL STIFFNESS PARAMETERS (K1N) --> PP,PW
   .100E+08   .100E+08
*SHEAR STIFFNESS PARAMETERS (EKS) --> PP,PW
   .100E+08   .100E+08
*COEFFICIENT OF RESTITUTION --> PP,PW
   .200E+00   .200E+00
*SURFACE TYPE
smooth
*FLOW TYPE
chute
*NUMBER OF CALCULATIONAL BOXS IN THE X & Y DIRECTIONS
         200         200
RANDOM SEED FOR RANDOM NUMBER GENERATOR (INTEGER VALUE)
         7
*FORMAT TYPE OF DRAW.OUT FILE : formatted, unformatted OR none
formatted
*NEW(1) OR RESTART(0) SIMULATION,TIME-STEP FOR WRITING RESTART FILE
         1      50000
*start of Particle Positioning (top left) - x_start,y_start
   .100E+01   0.90E+01
*beta,L_particles
   .00E+01   .50E+01
*dilation factor of particles
   .110E+01
```

```
*Initial X-Velocity,Y-Velocity of particles
   .000E+00  .000E+00
*Indicate if symmetry occurs in the model (0)-No Symmetry (1)-Symmetry
         1
*Lines to be removed and at what time step (no_removed),(Line no, Time Step)
         0
         5   200000
*Line numbers and time steps to record boundary force profiles
         4        6          8
       100  1000000      10000
```

III.2 Boundary Input File

In addition to the parameter input file, a boundary input file is required so that the DEM program can be compiled. The following is an example of a boundary input data file and the geometry that results is similar to the first transfer chute simulation shown in Chapter Seven. As can be seen the unique data structure is that described in Chapter Five resulting from use of the Finite Element Program.

```
** EMRC/DISPLAY NEUTRAL FILE <TITLE> INFORMATION **
EMRC/DISPLAY  NEUTRAL FILE DATA  ( 9/15/2002)
** EMRC/DISPLAY NEUTRAL FILE <GLOBAL DESCRIPTOR DATA> **
        77         1
         9         0
** EMRC/DISPLAY NEUTRAL FILE <GRID DATA> INFORMATION **
         1         2
         1         0
0.0000000E+00  0.0000000E+00  0.0000000E+00
** EMRC/DISPLAY NEUTRAL FILE <LINE DATA> INFORMATION **
         2         4
         1         0         0         1
0.0000000E+00  0.0000000E+00  0.0000000E+00  0.0000000E+00  0.0000000E+00
0.0000000E+00  0.0000000E+00  0.0000000E+00  0.0000000E+00  0.0000000E+00
6.0000000E+00  0.0000000E+00
         2         4
         2         0         0         1
0.0000000E+00  0.0000000E+00  0.0000000E+00  0.0000000E+00  0.0000000E+00
0.0000000E+00  0.0000000E+00  0.0000000E+00  0.0000000E+00  7.0000000E+00
0.0000000E+00  0.0000000E+00
         2         4
         3         0         0         1
0.0000000E+00  6.0000000E+00  0.0000000E+00  0.0000000E+00  0.0000000E+00
0.0000000E+00  0.0000000E+00  0.0000000E+00  0.0000000E+00  7.0000000E+00
6.0000000E+00  0.0000000E+00
         2         4
         4         0         0         1
7.0000000E+00  0.0000000E+00  0.0000000E+00  0.0000000E+00  0.0000000E+00
0.0000000E+00  0.0000000E+00  0.0000000E+00  0.0000000E+00  7.0000000E+00
6.0000000E+00  0.0000000E+00
         2         4
         5         0         0         1
5.0000000E+00  6.0000000E+00  0.0000000E+00  0.0000000E+00  0.0000000E+00
0.0000000E+00  0.0000000E+00  0.0000000E+00  0.0000000E+00  5.0000000E+00
3.1319110E+00  0.0000000E+00
```

```
         2         4
         6         0         0         1
3.5000000E+00  3.0000000E+00  0.0000000E+00  0.0000000E+00  0.0000000E+00
0.0000000E+00  0.0000000E+00  0.0000000E+00  0.0000000E+00  7.0000000E+00
3.0000000E+00  0.0000000E+00
         2         4
         7         0         0         1
3.5000000E+00  2.0000000E+00  0.0000000E+00  0.0000000E+00  0.0000000E+00
0.0000000E+00  0.0000000E+00  0.0000000E+00  0.0000000E+00  7.0000000E+00
2.0000000E+00  0.0000000E+00
         2         4
         8         0         0         1
0.0000000E+00  0.4239270E+00  0.0000000E+00  0.0000000E+00  0.0000000E+00
0.0000000E+00  0.0000000E+00  0.0000000E+00  0.0000000E+00  7.0000000E+00
0.4239270E+00  0.0000000E+00
         2         4
         9         0         0         1
3.0610000E+00  3.6400000E+00  0.0000000E+00  0.0000000E+00  0.0000000E+00
0.0000000E+00  0.0000000E+00  0.0000000E+00  0.0000000E+00  2.4349612E+00
3.0562094E+00  0.0000000E+00
         2         4
        10         0         0         1
2.1999350E+00  2.0557175E+00  0.0000000E+00  0.0000000E+00  0.0000000E+00
0.0000000E+00  0.0000000E+00  0.0000000E+00  0.0000000E+00  1.8787451E+00
1.3669236E+00  0.0000000E+00
         2         4
        11         0         0         3
2.4349612E+00  3.0562094E+00  0.0000000E+00  2.1994490E+00  2.7670996E+00
0.0000000E+00  2.0507575E+00  2.4251327E+00  0.0000000E+00  1.9999350E+00
2.0557175E+00  0.0000000E+00
         2         4
        12         0         0         3
1.1683070E+00  0.7159270E+00  0.0000000E+00  1.4598363E+00  0.8676876E+00
0.0000000E+00  1.7021536E+00  1.0897304E+00  0.0000000E+00  1.8787451E+00
1.3669236E+00  0.0000000E+00
         2         4
        13         0         0         3
4.0000000E+00  2.5000000E+00  0.0000000E+00  3.9330127E+00  2.7500000E+00
0.0000000E+00  3.7500000E+00  2.9330127E+00  0.0000000E+00  3.5000000E+00
3.0000000E+00  0.0000000E+00
         2         4
        14         0         0         3
3.5000000E+00  3.0000000E+00  0.0000000E+00  3.2500000E+00  2.9330127E+00
0.0000000E+00  3.0669873E+00  2.7500000E+00  0.0000000E+00  3.0000000E+00
2.5000000E+00  0.0000000E+00
         2         4
        15         0         0         3
3.0000000E+00  2.5000000E+00  0.0000000E+00  3.0669873E+00  2.2500000E+00
0.0000000E+00  3.2500000E+00  2.0669873E+00  0.0000000E+00  3.5000000E+00
2.0000000E+00  0.0000000E+00
         2         4
        16         0         0         3
3.5000000E+00  2.0000000E+00  0.0000000E+00  3.7500000E+00  2.0669873E+00
0.0000000E+00  3.9330127E+00  2.2500000E+00  0.0000000E+00  4.0000000E+00
2.5000000E+00  0.0000000E+00
** EMRC/DISPLAY NEUTRAL FILE <END-OF-DATA> **
```

Appendix IV

ASSEMBLY DRAWINGS OF GULF TRANSFERS

IV.1 Overview

This section contains the AutoCAD® assembly drawings and additional three-dimensional SolidWorks™ images for the two transfer chute systems analysed in Chapter Seven and Chapter Eight. The first set of images (Figures IV.1 to IV.5) details the hood-spoon transfer system, and illustrates a top view, side views and cutaway views. The second set (Figures IV.6 to IV.9) details the transfer chute comprising a single hood, and also illustrates a top view, side views, and a cutaway view. The assembly drawings (Figures IV.10 and IV.11) are also presented though with selected confidential information omitted.

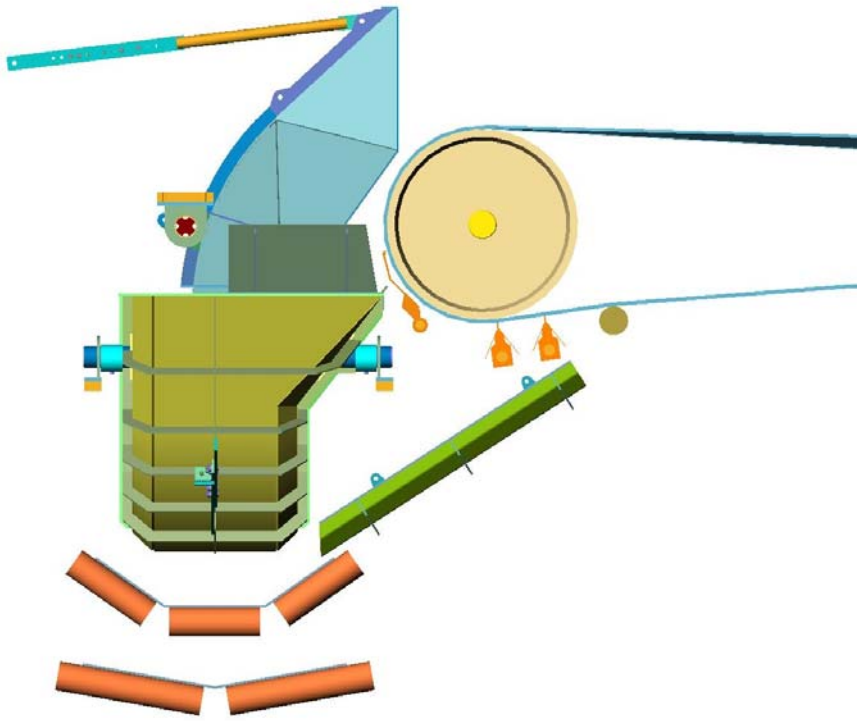

Figure IV.1 Image depicting hood-spoon transfer chute system

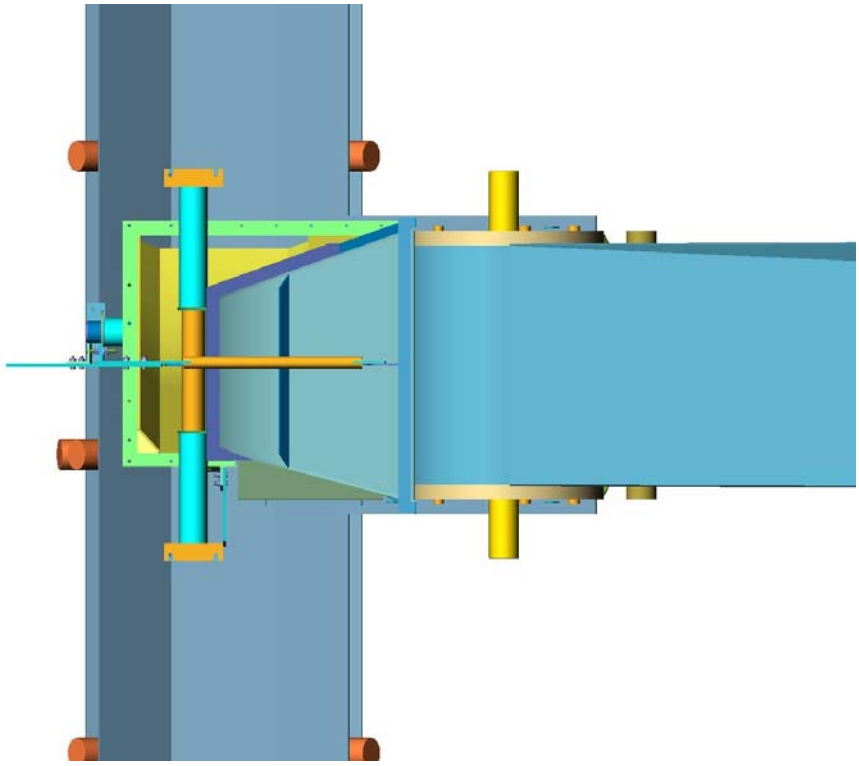

Figure IV.2 Image depicting hood-spoon transfer chute system

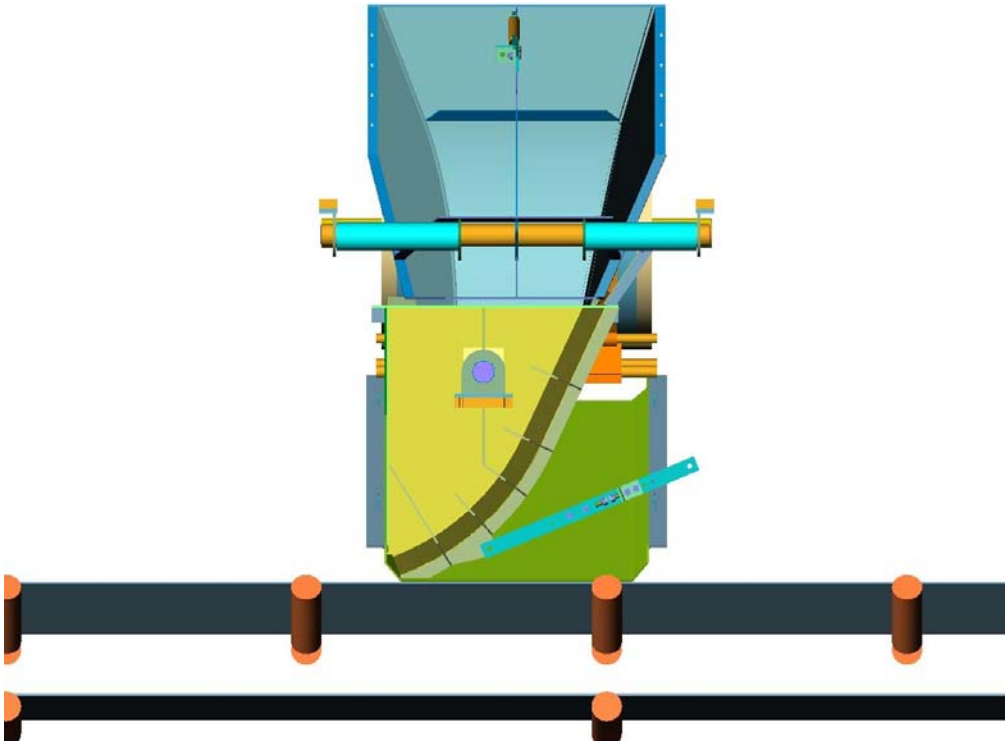

Figure IV.3 Image depicting hood-spoon transfer chute system

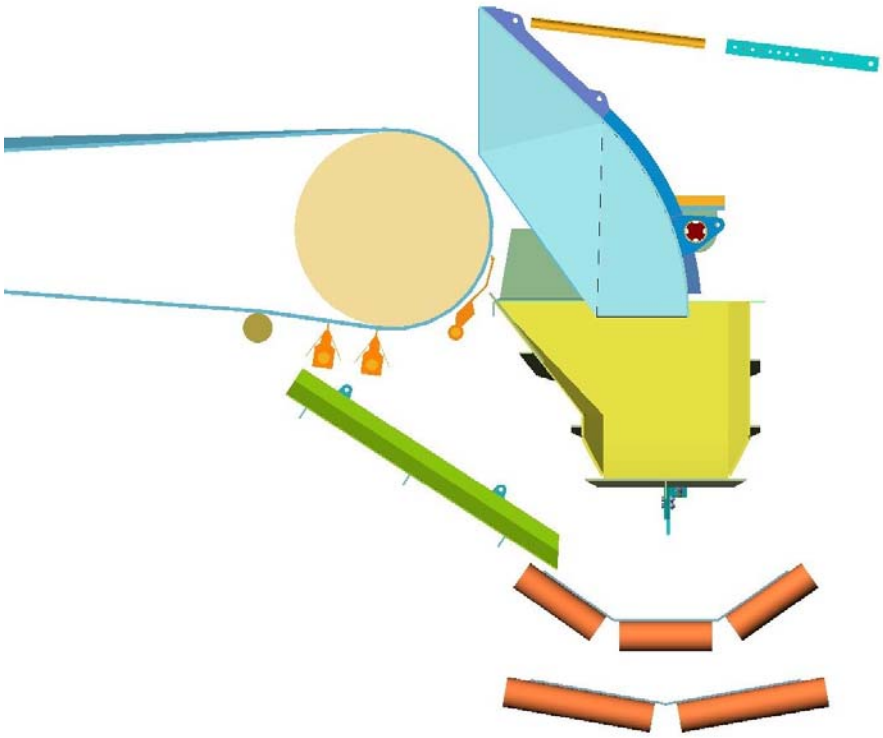

Figure IV.4 Image depicting hood-spoon transfer chute system

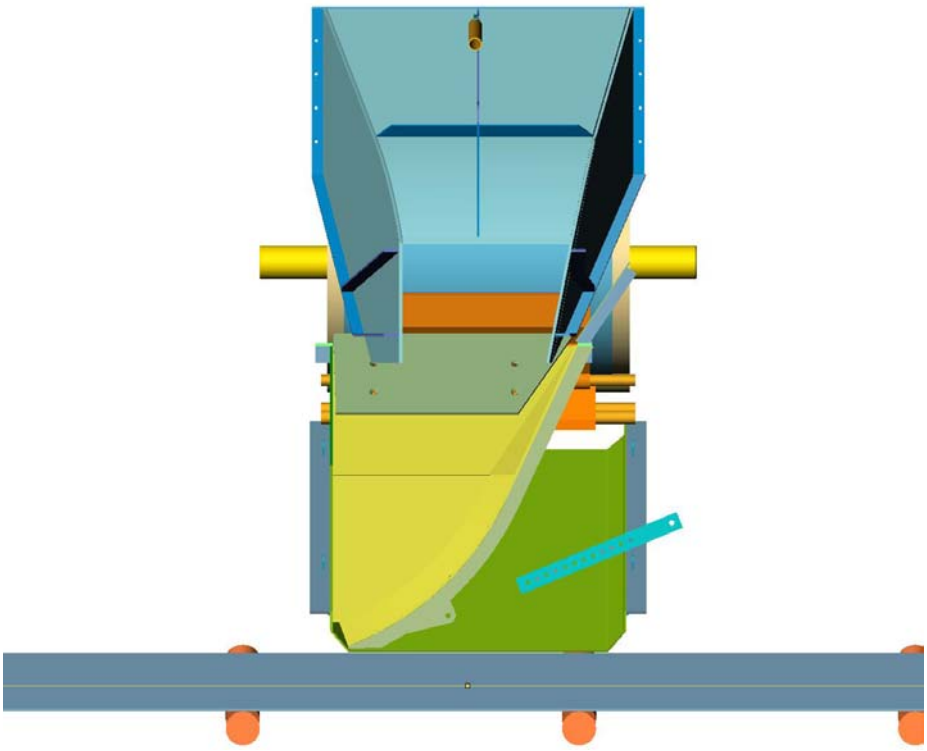

Figure IV.5 Image depicting hood-spoon transfer chute system

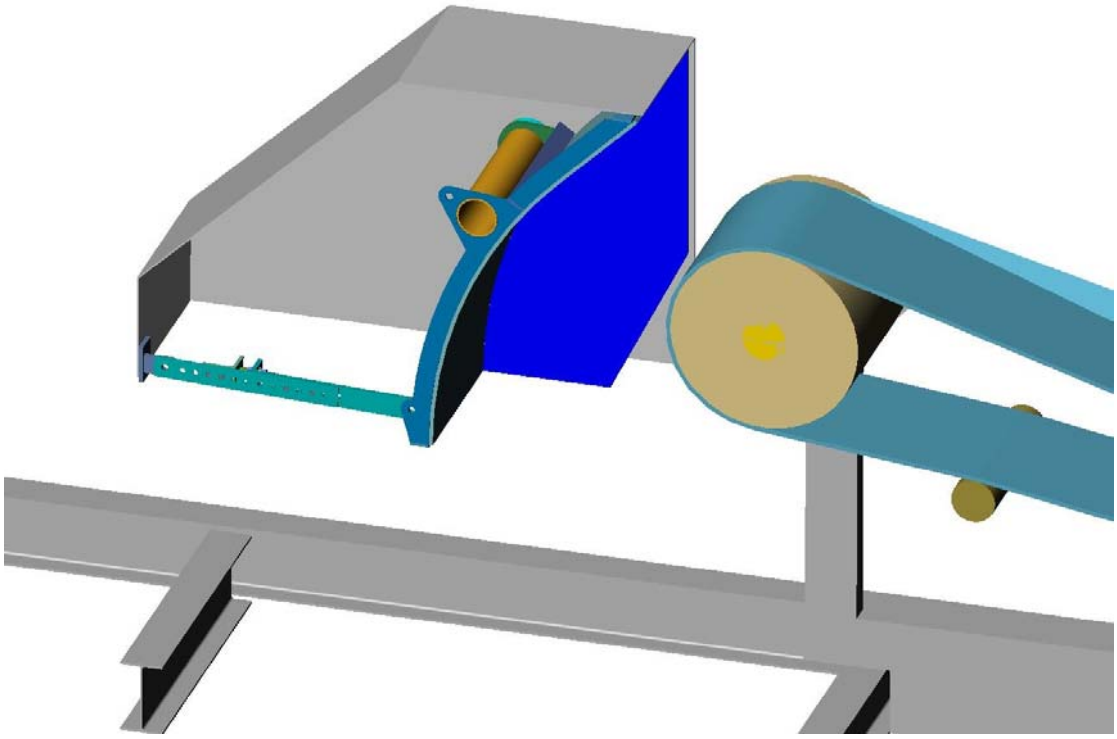

Figure IV.6 Image depicting single hood transfer chute system

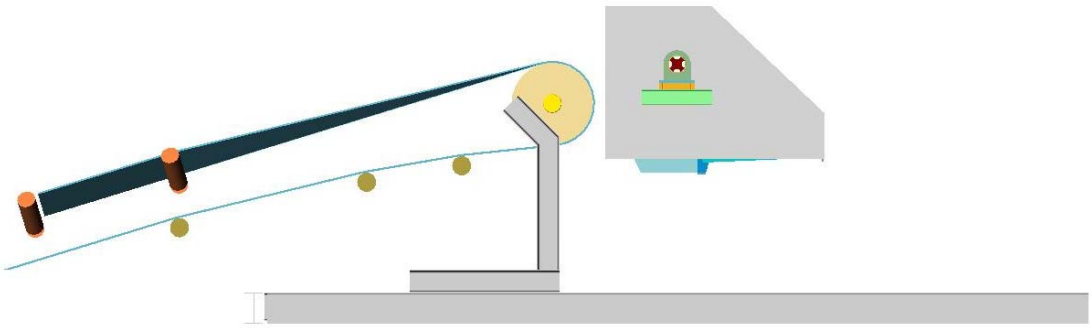

Figure IV.7 Image depicting single hood transfer chute system

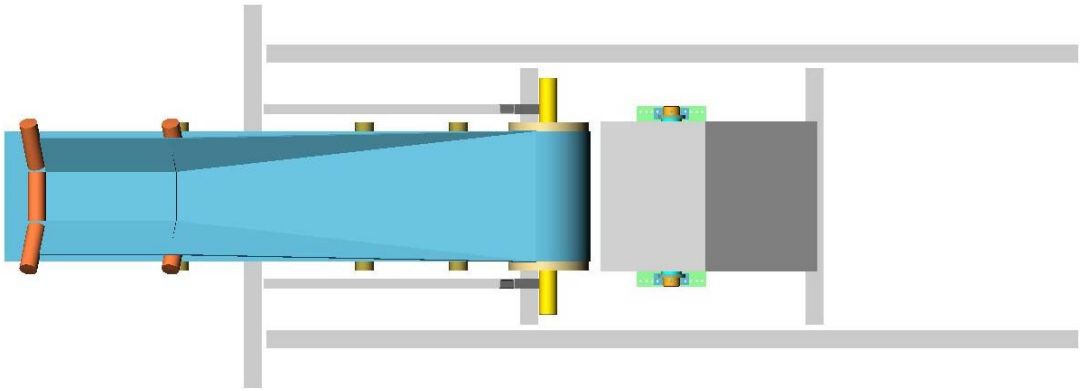

Figure IV.8 Image depicting single hood transfer chute system

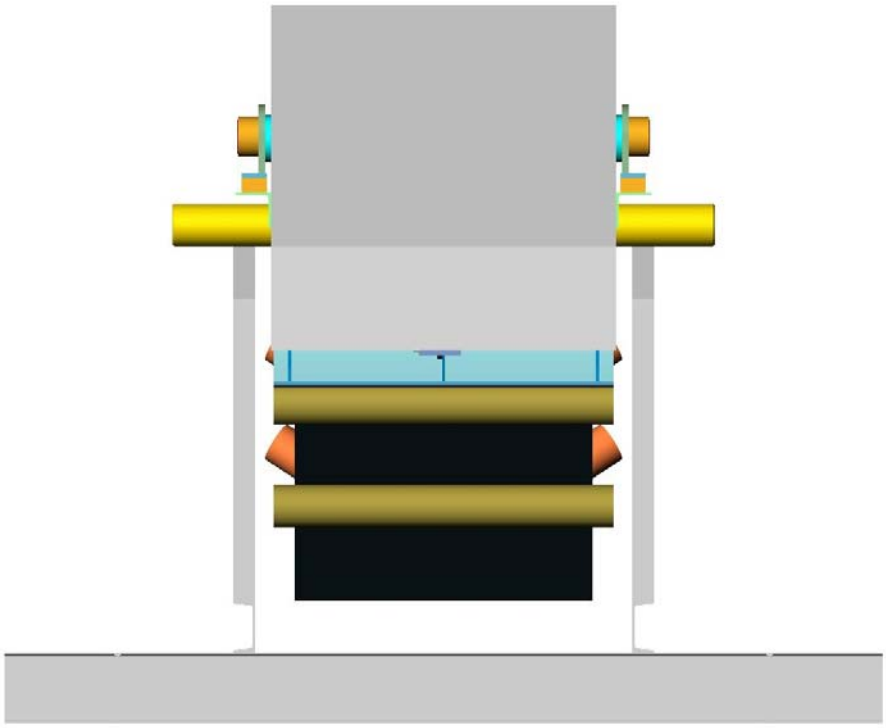

Figure IV.9 Image depicting single hood transfer chute system

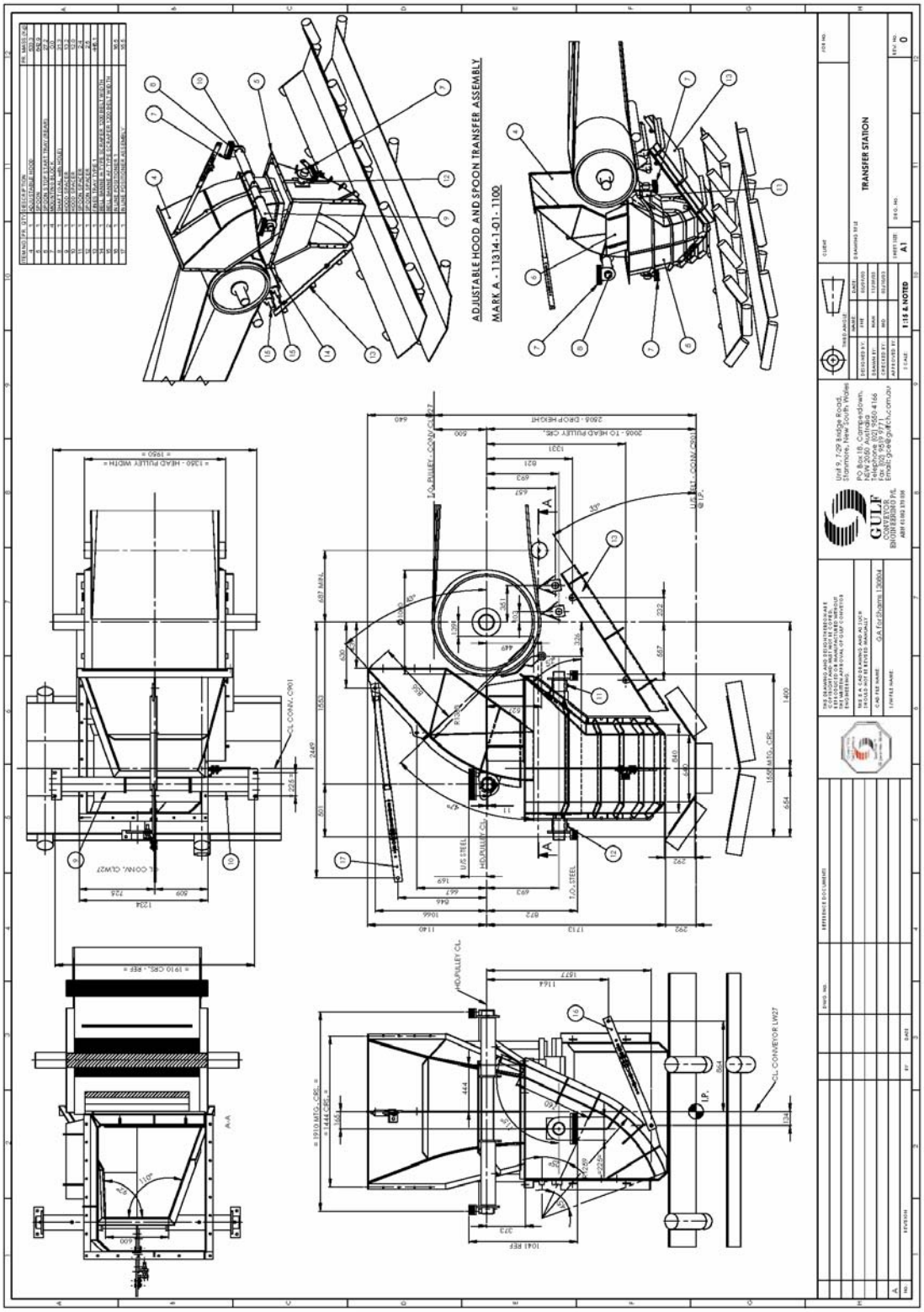

Figure IV.10 Assembly drawing for hood-spoon transfer chute

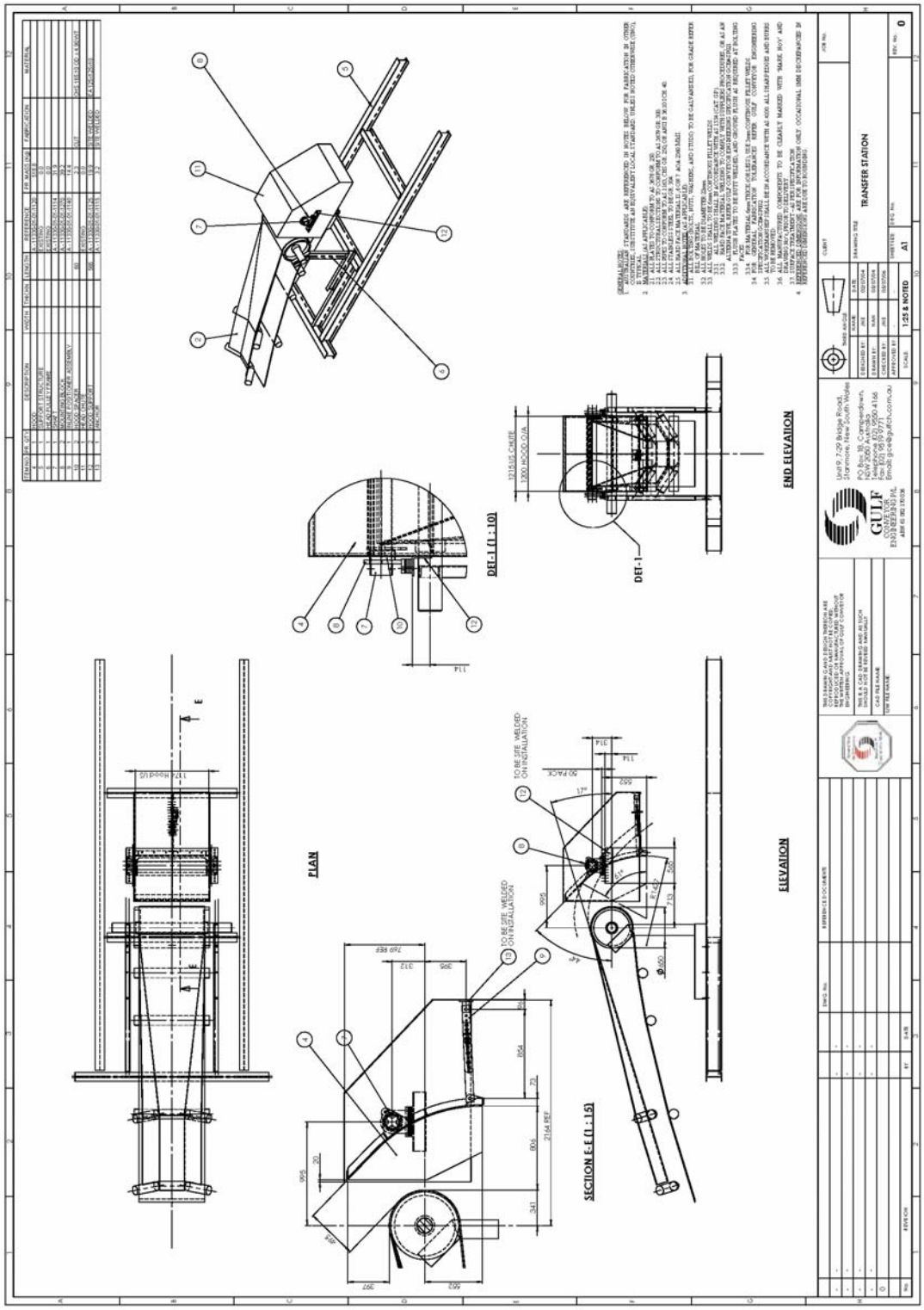

Figure IV.11 Assembly drawing for single hood transfer chute

Appendix V

SCREEN CAPTURES OF ENTIRE CALCULATION SPACE

V.1 Overview

This section illustrates examples of screen captures taken of the entire calculation space of the simulations in Chapter Seven and Eight. The primary focus of Chapter Seven and particularly Chapter Eight was to examine the transfer of materials hence the captures of the whole calculation space were not incorporated into those discussions. The first four captures (Figures V.1 to V.4) show the hood-spoon transfer system at times t = 2.0 s, t = 3.0 s, t = 4.0 s, and t = 5.0 s respectively, while the second four captures (Figures V.5 to V.8) show the single hood transfer chute system at times t = 2.0 s, t = 3.0 s, t = 4.0 s, and t = 5.0 s respectively. The particles have been colour coded according to speed.

An interesting observation is the seemingly stochastic nature of the particles re-entering the domain for the first transfer. However, as the examination of energy in Chapter Seven showed, over time there is a pattern of particles re-entering the calculation space. The particle re-entry in the second transfer is readily apparent.

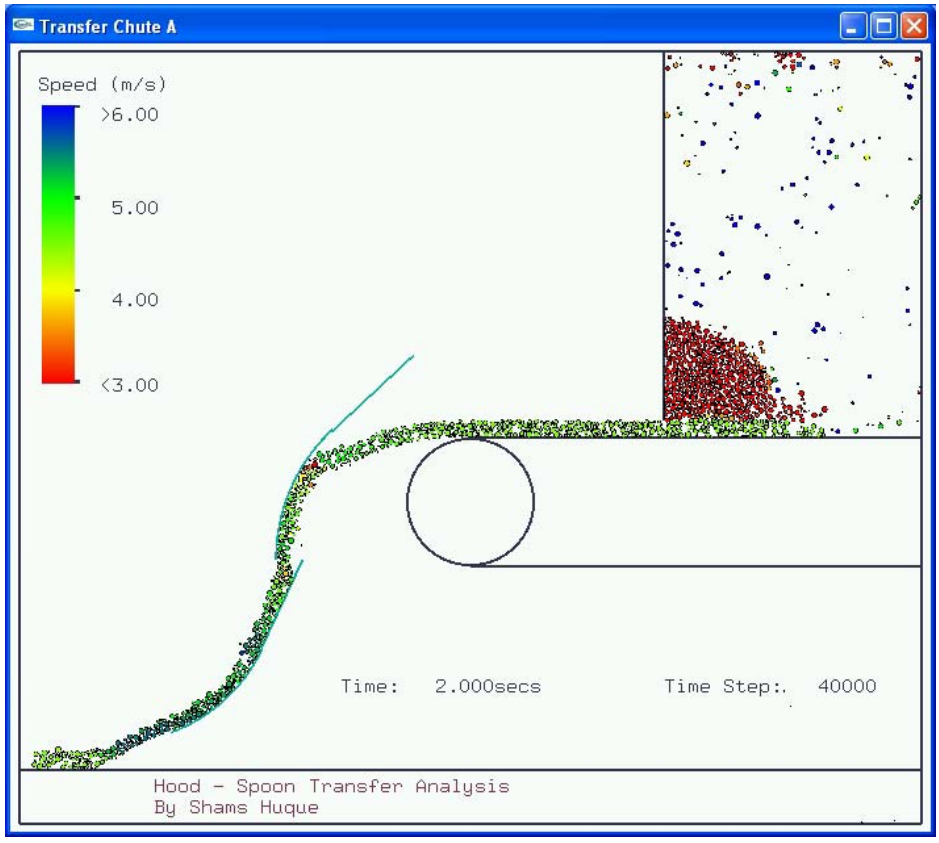

Figure V.1 Capture of entire calculation space for first transfer taken at $t = 2.0$ s

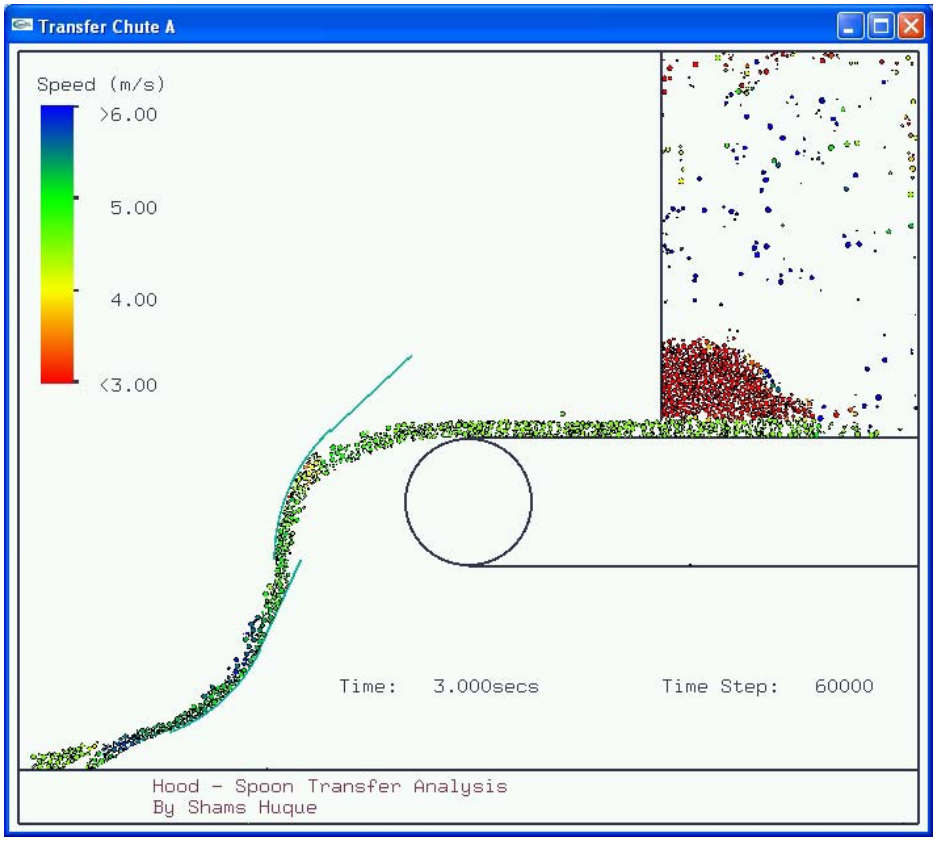

Figure V.2 Capture of entire calculation space for first transfer taken at $t = 3.0$ s

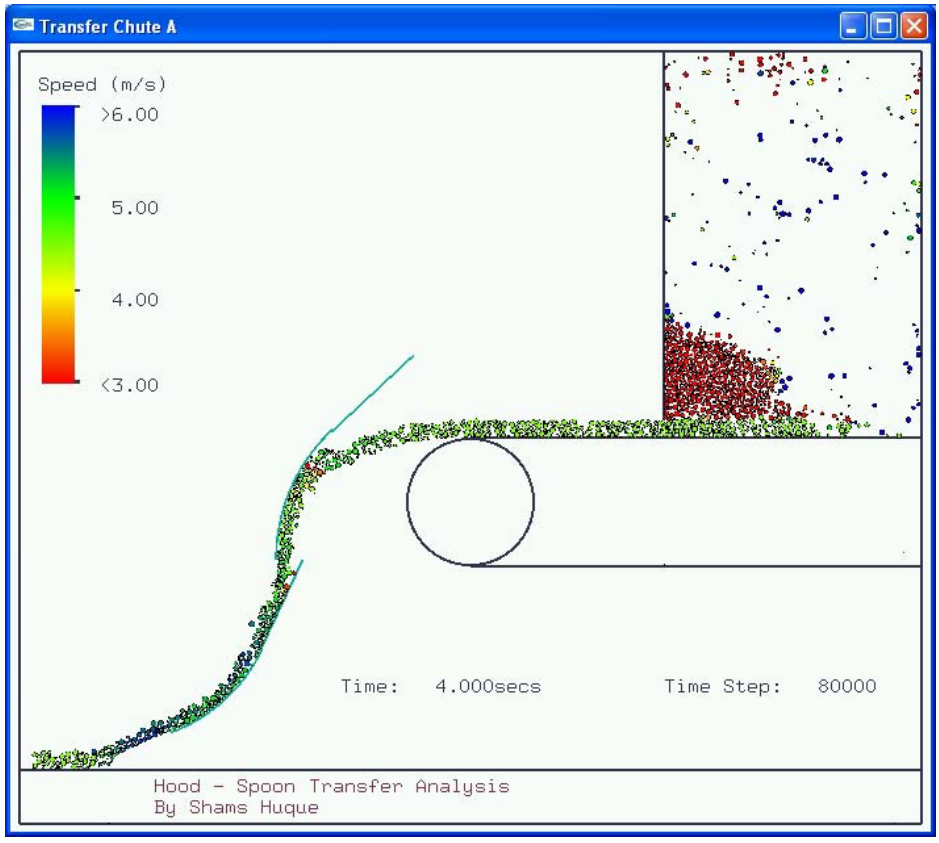

Figure V.3 Capture of entire calculation space for first transfer taken at $t = 4.0$ s

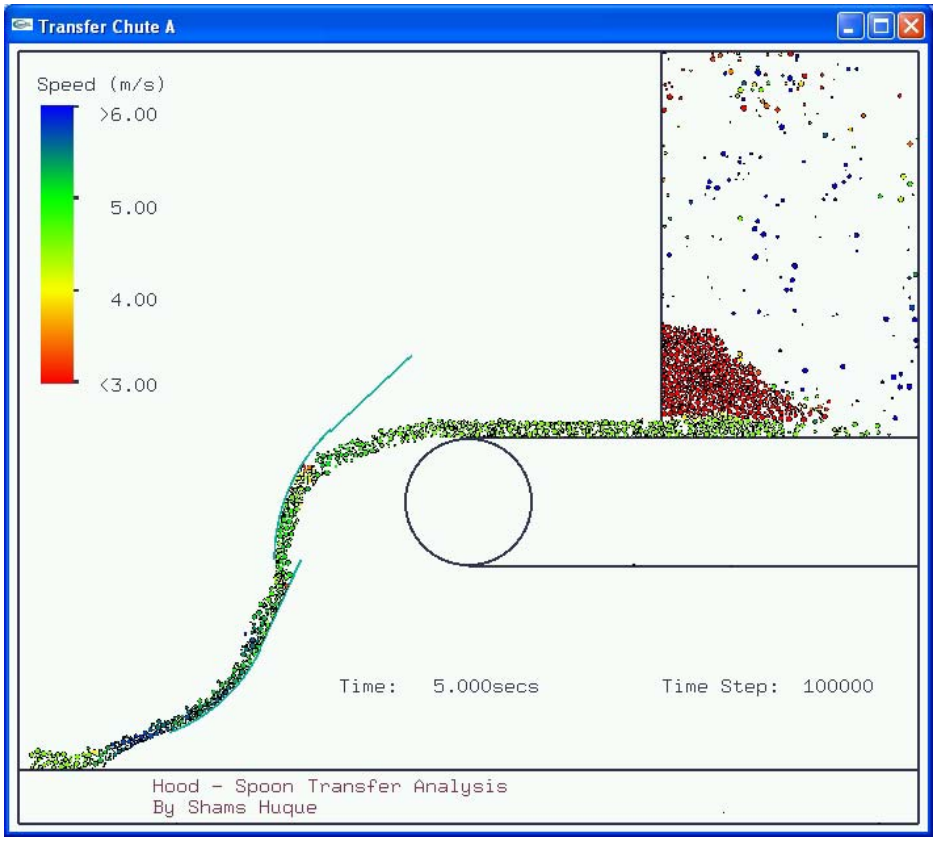

Figure V.4 Capture of entire calculation space for first transfer taken at $t = 5.0$ s

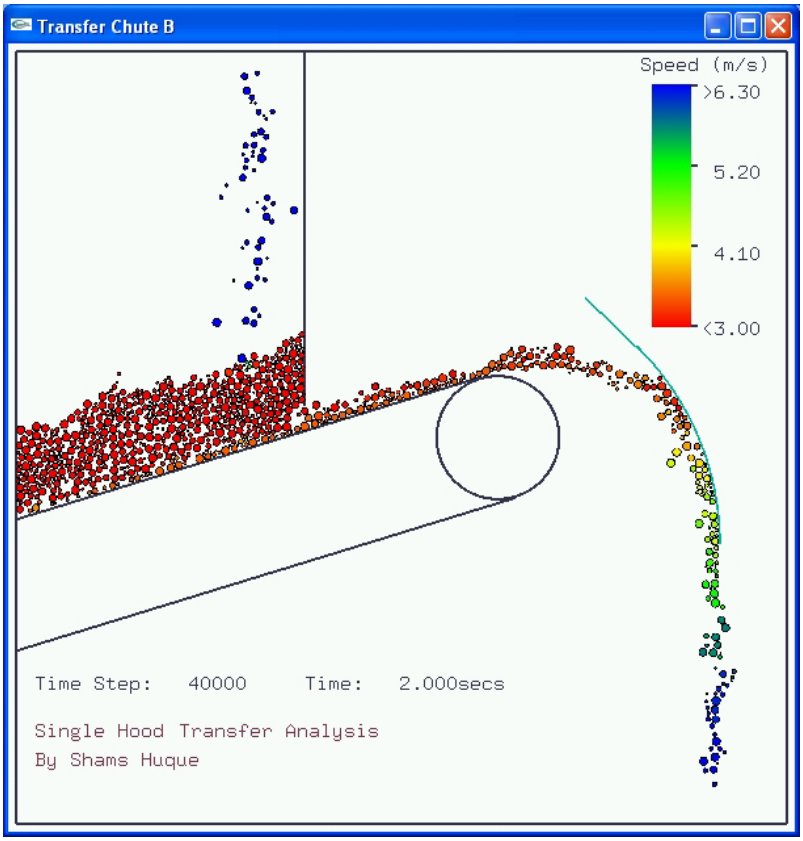

Figure V.5 Capture of entire calculation space for second transfer taken at $t = 2.0$ s

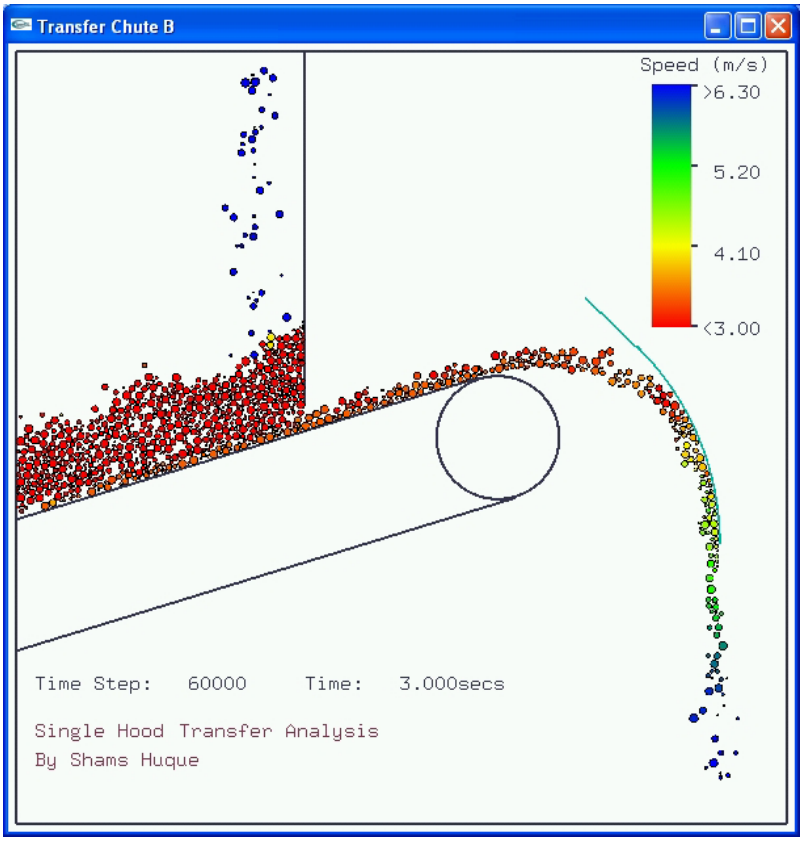

Figure V.6 Capture of entire calculation space for second transfer taken at $t = 3.0$ s

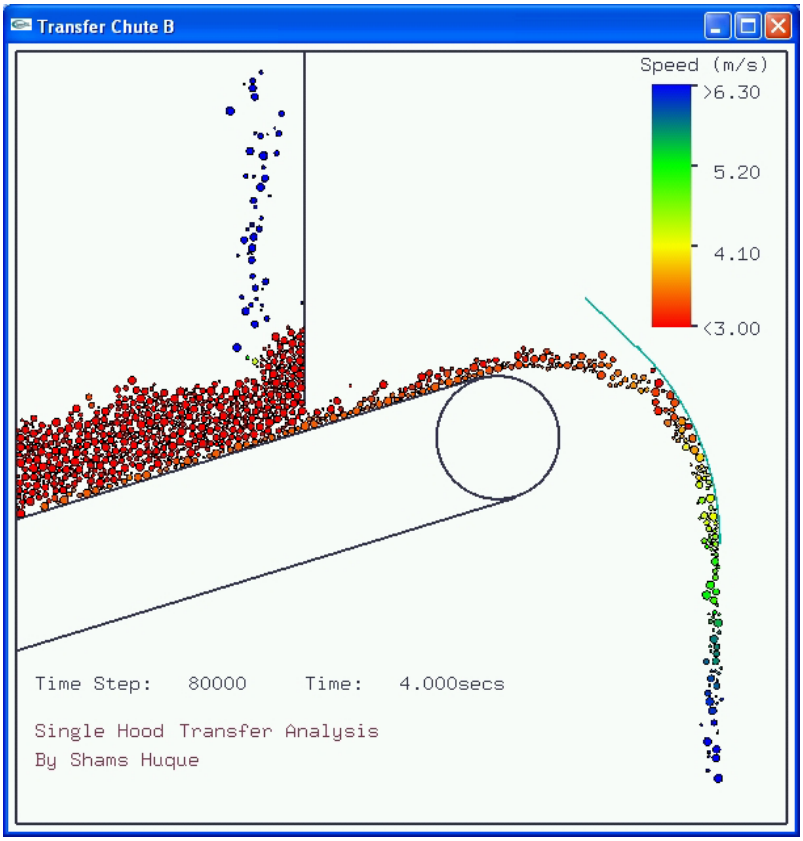

Figure V.7 Capture of entire calculation space for second transfer taken at $t = 4.0$ s

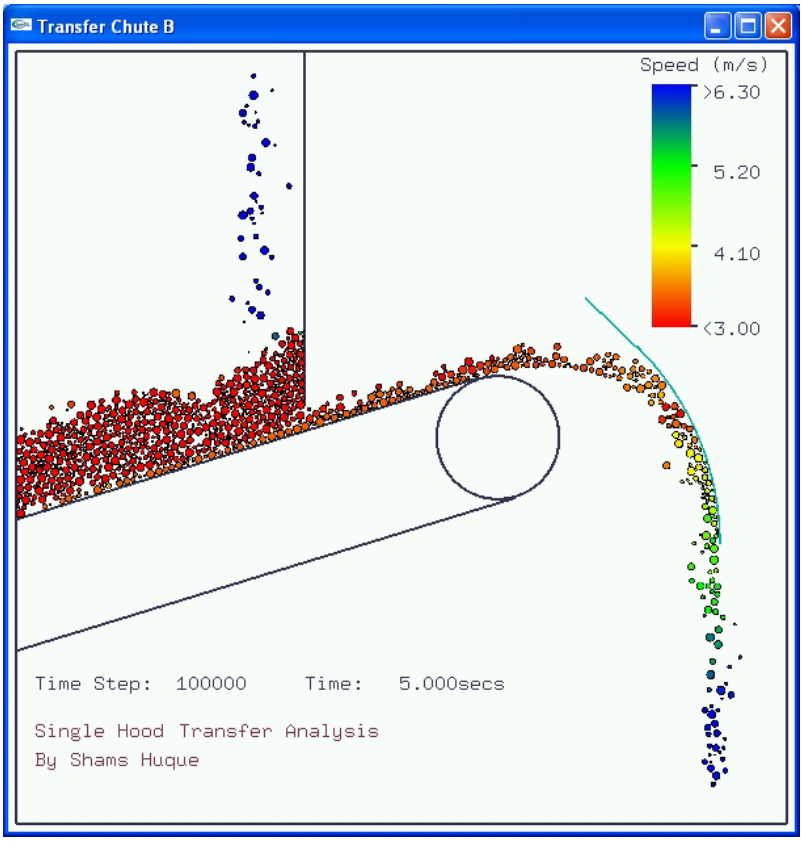

Figure V.8 Capture of entire calculation space for second transfer taken at $t = 5.0$ s